Thomas Kemper

Vom Fachbereich VI

(Geographie/Geowissenschaften)

der Universität Trier

zur Verleihung des akademischen Grades

doctor rerum naturalium

(Dr. rer. nat.)

genehmigte Dissertation

Reflectance Spectroscopy for Mapping and Monitoring of Metal Mining related Contamination
A Case Study of the Aznalcóllar Mining Accident, Spain

Betreuender:

Univ.-Prof. Dr. Joachim Hill

Berichterstattende:

Univ.-Prof. Dr. Joachim Hill

Univ.-Prof. Dr. Jean-Frank Wagner

Datum der wissenschaftlichen Aussprache: 21. Februar 2003

Trier, 2003

Acknowledgements

A study like the one presented here is always the product of collaboration of many people. Hence, I would like to take the opportunity to thank everybody who participated in one way or the other to this work.

Without PROF. DR. JOACHIM HILL, I probably never would have started this study. He suggested writing my thesis of diploma with data provided by the Joint Research Centre (JRC), which was actually the starting point of my interest in imaging spectroscopy. He followed closely the development of the thesis and contributed with numerous fruitful comments and ideas.

The original idea of the project has been encouraged and developed together with STEFAN SOMMER. He undoubtedly deserves the first 'thank you': without his ideas, criticism, hints, and countless discussions, the study never would have come to the final successful stage. He shared his profound knowledge in geology and the analysis of imaging spectroscopy data with me and allowed the work to grow also after the end of my grant.

During the time of my grant I could work together with DR. JAVIER GARCIA-HARO, who gave me deep insight in the mysteries of spectral mixture analysis. With the development of his unmixing tool he contributed strongly to the realization of this thesis.

When visiting the Remote Sensing Department of the University of Trier, I received several hints and criticism particularly from DR. THOMAS UDELHOVEN, DR. PATRICK HOSTERT and ACHIM RÖDER; they focussed my view on many details and pitfalls.

During the time of my research grant I was always well received by all the colleagues in the Land Management Unit and later the Soil & Waste Unit and I enjoyed very much the multinational working environment. Thanks to the Unit heads of the Soil & Waste Unit, GIOVANNI BIDOGLIO and JEAN MEYER-ROUX from the Land Management Unit for their acceptance and support to bring the study to a successful end.

The discussions with DR. ERIK PUURA encouraged me a lot to link the sludge abundances with geochemical models.

I also express my gratitude to the people, who joint the field campaigns. Only with their help and enthusiasm all the data could be collected. HELEN PREISSLER, WOLFGANG MEHL and KLAAS SCHOLTE contributed to the collection of spectroscopic data; DR. MARCO D'ALESSANDRO, FABRIZIO SENA and their team

collected the soil samples under the hot Andalusian summer sun. Together with FRANCO BO, they also signed responsible for the geochemical analysis.

The OFICINA TECHNICA DEL CORREDOR VERDE of the Consejería de Medio Ambiente is gratefully acknowledged for their support in the delivery of validation data and other valuable information.

The reviews of JILLIAN CROCKER, BERN ECKHARDT, DR. PAMELA KENNEDY and ALISON MUNRO improved a lot the understanding of the thesis.

Finally, I would like to thank particularly ANNETTE FIETZ. She supported me always during the time of this project and stepped back with her own interests, whenever parts of the work had to be reviewed or discussed, or GIS related problems to be solved. However, besides the scientific support, she also gave me the stamina to finish this thesis.

Table of contents

ACKNOWLEDGEMENTS III

TABLE OF CONTENTS V

SUMMARY IX

ZUSAMMENFASSUNG XIII

1 INTRODUCTION 1

2 OBJECTIVES AND WORKFLOW OF THE STUDY 5

3 THE AZNALCÓLLAR CASE 11

3.1 The Aznalcóllar Mine – Geological setting and mine operation 11

3.2 Geochemical processes and hazards of metal mining waste 15
3.2.1 The pyrite weathering process 16
3.2.2 Toxicity and mobilisation of heavy metals 18

3.3 The accident 19

3.4 Geo-environmental setting of the affected area 23

3.5 Clean up/remediation 28

4 PRINCIPLES OF REFLECTANCE SPECTROSCOPY 31

4.1 Electromagnetic radiation 31

4.2 Interaction of electromagnetic radiation with matter 33
4.2.1 Electronic processes 33
4.2.2 Vibrational processes 36
4.2.3 Scattering processes 37

4.3 Spectral properties of selected materials related to the study 39
4.3.1 Iron oxides, hydroxides, sulphates and sulphides 39
4.3.2 Soils 40

4.3.3 Vegetation 41

4.4 Use of imaging spectroscopy 42
4.4.1 Principle of imaging spectroscopy 43
4.4.2 Atmospheric interactions 44
4.4.3 Extraction of semi quantitative information on a sub-pixel level 47

4.5 Summary 48

5 DATA ACQUISITION AND AVAILABILITY 49

5.1 General data availability 49

5.2 Field data collection 50
5.2.1 Soil sampling 50
5.2.2 Field spectrometry 53

5.3 Imaging spectroscopy data acquisition 54
5.3.1 Sensor description 54
5.3.2 Data set description 54
5.3.3 Data preprocessing 56

5.4 Laboratory analysis 58
5.4.1 Laboratory spectrometry 58
5.4.2 Methods for geochemical analysis 58
5.4.3 Geochemical analysis results 58

6 LABORATORY SPECTROSCOPY FOR QUANTIFICATION OF RESIDUAL CONTAMINATION AND OTHER SOIL CONSTITUENTS 67

6.1 Multivariate calibration 67

6.2 Generation of an artificial mixture series of sludge and soil 68

6.3 Data pretreatment 72
6.3.1 Soil component scaling 72
6.3.2 Spectral resampling 73
6.3.3 Transformation of spectra 74

6.4 Building models using multivariate calibration 83
6.4.1 Multiple Linear Regression (MLR) 84
6.4.2 Partial Least Squares Regression (PLSR) 86
6.4.3 Artificial Neural Networks (ANN) 88
6.4.4 Results and discussion of modelling 93
6.4.5 Modelling other element groups 106

6.4.6 Modelling heavy metal concentration for subsequent year 108
6.4.7 Modelling with field and image spectra 108

6.5 Conclusions 116

7 IMAGING SPECTROSCOPY FOR QUANTIFICATION OF RESIDUAL CONTAMINATION 119

7.1 Addressing the problems of mixed pixels 119

7.2 The variable multiple endmember approach 120

7.3 Linear spectral mixture analysis with standardised variables 122

7.4 Identification of endmembers 124

7.5 Results 130
7.5.1 Derivation of residual sludge distribution for the year 1999 130
7.5.2 Derivation of residual sludge abundance and pyrite oxidation products for the year 2000 133

7.6 Conclusions 135

8 TRANSFORMATION OF ABUNDANCES INTO QUANTITATIVE INFORMATION FOR REMEDIATION MANAGEMENT 137

8.1 The artificial mixture series as a link between abundances and contamination 137

8.2 Quantification of residual contamination and assessment of acidification risk 138

8.3 Validation SMA maps against conventional methods 142

8.4 Conclusion 146

9 CONCLUSIONS AND RECOMMENDATIONS 149

10 LITERATURE 155

ANNEX 173

A. Description of sampling sites 174

B. HyMap sensor setup 182

C. Geochemical analysis 1999 184

D. Geochemical analysis 2000 195

E. Soil profiles 202

F. Sludge abundance 1999 204

G. Mineral abundance 2000 205

H. Sludge derivatives 1999 206

LIST OF FIGURES 207

LIST OF TABLES 213

LIST OF ACRONYMS 217

LEBENSLAUF 218

Summary

Acid drainage from weathering of mining wastes can harmfully impact the quality of drinking water and the health of riparian ecosystems. The task of identification and monitoring of such contamination sources is often costly and time consuming, if it is done conventionally with field sampling and laboratory analysis. While measurements of chemical and physical parameters can determine pollution levels at point locations, they do not give insight into their spatial structure. This can be achieved only to a certain extent with spatial interpolation algorithms. However, the quality of these interpolations is highly dependent of the number and distribution of the sampling points.

Reflectance spectroscopy is usually applied in the laboratory, but it can be applied also directly in the field and provides means for fast non-destructive measurements. Extended to hyperspectral airborne remote sensing it provides the potential of spatial observations of affected areas at different spatial resolutions. However, meaningful physical/chemical properties cannot be measured directly, both field spectra and remote sensing observations have to be calibrated with other measurements of chemical and physical properties.

In the present study, the possibilities of reflectance spectroscopy and airborne hyperspectral remote sensing for the qualitative and quantitative assessment of heavy metal contamination and the acidification risk related to the Aznalcóllar mining accident in SW Spain were evaluated. The data were collected in the two years after the accident, which happened in 1998. They consist of three types: soil samples taken from profiles along different transects, spectral field measurements with a portable spectrometer and hyperspectral images acquired with the HyMap sensor covering the entire affected area.

The results of the chemical analysis are in line with the results of other research groups, and confirm that after the first clean up the contamination is still very high, particularly in the northern part. The second clean up and remediation campaign improved the situation effectively by a re-cleaning and addition of acidity neutralizing products for fixation of heavy metals. In areas, where the remediation was not finished yet, the contamination problems worsened due to the oxidation of pyritic sludge, which produced acidity that mobilised heavy metals allowing them to penetrate into the soil profile.

In a mixture experiment, soil was contaminated with sludge for a better understanding of its influence on soil reflectance. A strong decrease in albedo could be observed with increasing sludge content and a wide iron absorption feature is becoming the main absorption feature centred near 1.0 µm. There was a strong linear correlation between

the depth of this absorption and heavy metal concentration, which allowed an estimation of heavy metals for laboratory data.

Multivariate calibration was chosen for improving these results and extending them to the full spectral range, including also other soil constituents. Multivariate calibration has the advantage that it is not based on a known physical assumption, but only on the data available. Stepwise multiple linear regression (MLR), partial least squares regression (PLSR) and artificial neural networks (ANN) were tested for their ability to estimate heavy metal concentrations based on their reflectance spectra. The spectra were transformed using different techniques in order to enhance important spectral features. Furthermore, they were spectrally degraded to evaluate the effect of wavelength reduction with regard to the predictive power of the models. The three methods worked equally well with a slightly better performance of PLSR, which was eventually selected for further modelling. With respect to the transformations and resampling, the best results were obtained with vector-normalised spectra with ten nm spectral resolution. The prediction quality of the various constituents was very different. Best results were obtained for those elements directly related to the accident, e.g. heavy metals. Also within the heavy metal group a clear separation could be observed. The quality of prediction improves with the stability of the heavy metals; the very mobile elements such as Cd, Cu and Zn cannot be predicted significantly, because they were not directly linked to the tailings sludge.

The application of chemometric models to field and image data was only partially successful. Field spectra were strongly influenced by surface crusts, but calibration with field spectra provided good results. Instead, the prediction of heavy metals with image spectra failed due to the strong influences of vegetation (green and dry), surface roughness and crusting (caused by pyrite oxidation) on a single pixel.

Spectral mixture analysis (SMA) accounts for this heterogeneity in the pixels and allowed a spatial estimation of contamination. Using an iterative approach with multiple endmember (EM) sets and standardised variables, it was possible to separate sludge related spectral information from background contributions.

The semi-quantitative abundance information derived from could be turned into quantitative information incorporating the mixture series into the SMA. These results provided the link between sludge abundance and sludge weight, allowing as a consequence calculation of the amount of residual sludge per pixel, the acidification potential and other parameters important for remediation planning. Validation against an independent data set analysed with conventional methods showed that the results obtained from the image are very reliable and allow a much higher level of detail than the interpolation of the conventional data. In the subsequent year it was possible to identify jarosite mixed with copiapite and ferrihydrite as indicators for oxidation of pyrite; gypsum was detected as an indicator for neutralisation of acidity by the remediation efforts.

The application of laboratory, field and imaging spectroscopy for providing quantitative information about the contamination levels in their spatial context is a good complement to conventional methods. The advantage is the reduction of the time and labour-intensive geochemical analysis because after the model calibration, further samples can be analysed directly with the chemometric models. Furthermore, the spatial distribution can be mapped with imaging spectroscopy data helping in a more precise remediation planning. However, the availability of field and imaging spectrometers has today only experimental character, which limits at the moment the application as screening tool.

Zusammenfassung

Bei der Verwitterung von Abbraum aus der Erz-Förderung bilden sich oft saure Sickerwässer (engl. *acid mine drainage*) durch Oxidationsprozesse. Diese Sickerwässer können Schwermetalle mobilisieren, die mit den Erzlagerstätten assoziert sind, und Grundwasser und Fliessgewässer kontaminieren. Die Erfassung und Überwachung der Kontaminationsquellen ist langwierig und kostspielig wenn sie mit konventionellen Methoden (Bodenprobennahme und Laboranalytik) durchgeführt wird. Zudem geben diese punktuellen Messungen nur zu einem geringen Teil Einblick in die räumliche Verteilung der Kontamination. Häufig wird versucht durch geostatistische Interpolationsmethoden die räumliche Struktur besser zu charakterisieren. Die Qualität der Interpolation ist allerdings sehr stark von der Anzahl und der Verteilung der Probenpunkte beeinflusst.

Reflektionsspektroskopie bietet eine sinnvolle Verbesserung zur Bereitstellung der gefragten Information. Ein Reflektionsspektrometer misst die von einem Objekt reflektierte Strahlung und erlaubt mit Hilfe von material-spezifischen Absorptionen Aussagen über dessen Zusammensetzung. Sie kann in der Regel ohne grössere Probenvorbereitung genutzt und sowohl im Labor als auch vor Ort eingesetzt werden. Darüber hinaus bieten luftgestützte abbildende Spektrometer, die ein Reflektionsspektrum für jedes Bildpixel erzeugen, die Möglichkeiten einer flächenhaften Darstellung.

In der vorliegenden Studie wurde die Anwendung von Labor-, Feld- und abbildender Spektroskopie zur Kartierung und Quantifizierung der Kontamination durch schwermetallhaltigen Pyrit-Schlamm nach einem Minenunfall westlich von Sevilla (Spanien) untersucht. Durch den Dammbruch eines Staubeckens im April 1998 wurde eine Fläche von mehr als 4000 ha mit Flotationsrückständen verseucht. Angesichts der Nähe zum Doñana Nationalpark, der eines der wichtigsten europäischen Feuchtgebiete beheimatet, wurden umgehend grossräumige Reinigungsmassnahmen gestartet, die allerdings eine beträchtliche Restkontamination zurückliessen. Zur Charakterisierung dieser Restkontamination und deren Enwicklung in einem räumlichen und zeitlichen Kontext wurden 1999 und 2000 zwei Messkampagnen durchgeführt. Im Untersuchungsgebiet wurden umfangreiche Bodenproben gesammelt und deren Reflektion zuvor vor Ort mit einem Feldspektrometer gemessen. Zeitgleich fanden Befliegungen mit dem HyMap Sensor, einem abbildenden Spektrometer, statt. Die Bodenproben wurden im Labor auf ihre Gehalte an Schwermetallen, Schwefel, Eisen und sonstigen Elementen analysiert und erneut spektral vermessen.

Die geochemischen Laboranalysen bestätigten die Ergebnisse anderer Forschergruppen, die vor allem für den Nordteil des Untersuchungsgebietes eine hohe Restkontamination

festgestellt hatten. Zwar verbesserte sich die Situation zwischen der ersten und der zweiten Messkampagne durch eine wiederholte Reinigungsaktion und weitere Sanierungsmassnahmen deutlich, aber in einigen Teilen kam es durch beginnende Oxidationsprozesse zu einer Mobilisierung der Schwermetalle; insbesondere die Gehalte von Arsen erhöhten sich im Bodenprofil beträchtlich.

Für die Modellierung der Schwermetallgehalte mit Hilfe der Reflektionsspektren ist das Verständnis des Einflusses des Pyrit-Schlammes auf die Bodenreflektion von Bedeutung. Deshalb wurde eine künstliche Mischreihe erstellt, bei der nicht-kontaminierte Böden aus dem Untersuchungsgebiet mit dem Pyrit-Schlamm in verschiedenen Gewichtsanteilen gemischt wurden. Mit Erhöhung des Schlamm-Anteils konnte ein starker Rückgang der Gesamtalbedo und die Ausbildung einer weiten Eisenabsorptionsbande bei 1 µm beobachtet werden. Zwischen der Tiefe dieser Bande und dem Schlammgehalt bestand eine hohe Korrelation, die eine signifikante Bestimmung der Schwermetalle für die Labordaten ermöglichte.

Die Labordaten und die Mischreihe bildeten die Grundlage für weitere Modellierungen, um die Bestimmung der Schwermetalle anhand der spektralen Reflektion zu verbessern. Neben multipler linearer Regression und „Partial Least Squares Regression“ wurden künstliche neuronale Netze getestet. Zur Verbesserung der Modellierungen wurden die Reflektionsspektren mit Hilfe von verschiedenen Methoden transformiert, um dadurch wichtige Absorptionsbereiche zu betonen. Ausserdem wurden die hochaufgelösten Bandbreiten zusammengefasst, um dadurch die Anzahl der Variablen in den Modellen zu reduzieren.

Die Ergebnisse der drei Modellierungs-Methoden waren insgesamt sehr ähnlich; aufgrund der etwas besseren und stabileren Ergebnisse wurde schliesslich „Partial Least Squares Regression“ für die weitere Modellierung ausgewählt. Durch die Transformation der Spektren liessen sich die Ergebnisse deutlich verbessern; generell erwiesen sich vektor-normalisierte Spektren mit einer Bandbreite von 10 nm am vorteilhaftesten. Allerdings zeigten sich beträchtliche Unterschiede in der Modellierungsqualität für die verschiedenen Elemente. Die besten Ergebnisse wurden für diejenigen Elemente erzielt, die direkt mit dem Unfall im Zusammenhang stehen, vor allem Schwermetalle. Aber auch innerhalb dieser Gruppe gab es starke Unterschiede. Dabei erhöhte sich die Qualität der Ergebnisse mit der Stabilität (im Sinne von Mobilisierbarkeit) der Schwermetalle. So wurden für die stabilen Elemente Pb (R^2=0.942), Hg (R^2=0.932) und Sb (R^2=0.924) die besten Ergebnisse erzielt. Hingegen konnten Cd, Cu und Zn nicht zufriedenstellend berechnet werden, da sie früher in Lösung gehen und dementsprechend nicht so stark mit dem Pyrit-Schlamm korrelieren. Eine Übertragung der Labormodelle auf die Feldspektren und die abbildenden Spektrometerdaten war nur bedingt möglich. Die vor Ort gemessenen Spektren waren stark von dünnen, oberflächlichen Krusten verändert, die sich negativ auf die Qualität der Ergebnisse auswirkten. Die Anwendung auf Spektren des abbildenden Spektrometers war nicht erfolgreich, da der Einfluss von grüner und

trockener Vegetation, Oberflächenrauhigkeit und Oberflächenverkrustung auf das Reflektionssignal zu stark waren.

Auf eine derartige Heterogenität im Subpixelbereich zielt die spektrale Mischungsanalyse (engl. *Spectral Mixture Analysis*) ab, mit der sich die Anteile der Materialien, die zur Reflektion eines Pixels beitragen (die sog. *Endmember*), bestimmen lassen. Dadurch können die Restschlammgehalte in dieser Studie flächenhaft dargestellt werden. Es wurde ein iteratives Verfahren mit multiplen „Endmembern" benutzt, was den Vorteil hat, dass für jedes Pixel spezifische Lösungen gefunden werden können. Ausserdem wurde anstelle von Reflektionswerten mit standardisierten Spektren gearbeitet, die, wie schon bei der vorher beschriebenen Modellierung, den spektralen Kontrast zwischen belasteten und unbelasteten Böden verstärken. Diese semiquantitativen Ergebnisse konnten mit Hilfe der spektralen Mischungsanalyse der künstlichen Mischreihe in quantitative Information umgewandelt werden. Die Entmischungsergebnisse zeigten eine klare nicht-lineare Beziehung zwischen prozentualem Anteil am Reflektionssignal und Gewichtsprozent des Pyritschlamms. Über diese Beziehung, die sich durch ein Polynom zweiten Grades abbilden liess, konnten sowohl Karten der Schwermetalle und anderer Elemente wie auch der Restschlammenge erstellt werden. Mit Hilfe von geochemischen Modellen liess sich daraus das Versauerungspotential, das für die Sanierungsmassnahmen von Bedeutung ist, bestimmen. Die Daten wurden mit Hilfe eines unabhängigen, konventionellen Datensatzes validiert und zeigten, dass die aus den Bildspektren abgeleiteten Gehalte sehr gut mit den konventionell bestimmten Werten übereinstimmen und gegenüber einer Interpolation mit dem konventionellen Datensatz ein sehr viel genaueres Bild der Restkontamination zeichnen.

Im darauffolgenden Jahr konnten mit Hilfe der spektralen Mischungsanalyse verschiedene Indikatorminerale für die Oxidation von Pyrit identifiziert werden. Diese Sekundärminerale fanden sich vor allem in jenen Bereichen, in denen die Sanierungsmassnahmen noch nicht abgeschlossen waren. Sie waren dort mit Gips assoziiert, der durch die Reaktion der freigesetzten Säure mit dem eingebrachten Kalk entstand und eine direkte Folge der Sanierungmassnahmen ist.

Insgesamt bietet der kombinierte Einsatz von Labor-, Feld- und abbildender Spektrometrie zur Kartierung und Quantifizierung der Kontamination nach einem Minenunfall eine sinnvolle Ergänzung zu herkömmlichen Untersuchungsmethoden. Der Vorteil des Einsatzes liegt in der Reduzierung der zeit- und kostenintensiven geochemischen Laboranalyse und geostatistischer Modellierung, denn nach der Kalibrierung können weitere Proben direkt mit den chemometrischen Modellen bestimmt werden. Diese Bestimmung kann unter Umständen sogar direkt vor Ort durchgeführt werden. Darüberhinaus lässt sich die räumliche Verteilung mit Hilfe der abbildenden Spektrometerdaten kartieren, was eine zielgerichtetere Planung der Sanierungsmassnahmen ermöglicht. Abbildende Spektrometer könnten auch für die

weitere Überwachung von Oxidationsprozessen und potentieller Versauerung im betroffenen Gebiet eingesetzt werden.

Um allerdings im Falle eines Unfalls als Screening und Monitoring-Tool zur Verfügung zu stehen, müssen vor allem auch flugzeuggetragene abbildende Spektrometer schnell und zuverlässig bereitgestellt werden können. Im Moment ist das in Europa noch nicht hinreichend gewährleistet, da die Anzahl von wirklich operationell einsetzbaren Systemen noch zu gering ist. Für das Monitoring könnten hingegen weltraumgestützte hyperspektrale Systeme bei gleichzeitig relativ hoher räumlicher Auflösung neue Möglichkeiten eröffnen.

1 Introduction

Mining for the extraction of metals has been used in many areas throughout the world and in some places for thousands of years. Today mining is, on the one hand, an important sector in global economy, and, on the other hand, mining activities are some of the most far-reaching and intensive disturbances of the ecological balance on a worldwide basis (Sol et al. 1999). Mining operations generally progress through different stages, starting with the exploration for assessment of the size and economic value of the deposit to the exploitation by extraction of minerals and disposal of overburden and waste rock. The extracted ore is processed by smelting or refining on site or at a different location. Finally, at the end of its productive phase the mine is closed. At every stage of operations mining activities have a wide range of environmental impacts. They can be the source of both acute pollution, releasing large, often concentrated amounts of pollutants in a short time (due to accidents) and diffuse pollution, a rather constant emission of relatively low concentrations during a longer period of time (Table 1.1, Sol et al. 1999).

Management of tailings, which is a ground rock waste product that remains after the desired metal minerals have been removed from the ore, is one of the most significant environmental aspects of mining operations (World Bank 1998). Failure of tailings containments can have serious adverse environmental consequences. Only in the past ten years, a large number of mining accidents have happened worldwide; some of them will be mentioned in the following paragraph to explain the far-reaching consequences they may have on the environment and human health: In 1992, a damburst at the Summitville Gold Mine in Colorado/USA caused the complete loss of aquatic life along a 25 km stretch of the Alamosa River. In 1993, masses of sludge and rubble buried a gold miner's settlement in Ecuador causing the deaths of 24 people. In 1994, a similar accident at the Harmony Gold Mine in South Africa killed 17 people and destroyed 80 houses. In 1995, 2.5 million cubic meters of cyanide solution from the Omai Gold Mine in Guyana contaminated the river Essequibo causing massive loss of aquatic life. In 1996, on Marinduque Island in the Phillippines, 3 million tonnes of poisonous sludge from a copper mine flowed into the river Boac flooding 20 villages (ICOLD 2001). In 1998, the collapse of the tailings pond in Aznalcóllar, Spain, left several thousands of hectares in the Guadiamar floodplain contaminated with pyritic sludge with high concentrations of trace metals, endangering the Doñana National Park (Grimalt et al. 1999). In January 2000, cyanide contaminated water with some tailings were released in Baia Mare, Romania, into the Tisza river, a tributary of the Danube, killing all aquatic life up to its confluent with the Danube (UNEP/OCHA 2000).

Table 1.1. Potential environmental impacts of mining (Sol et al. 1999)

Environmental impacts
Destruction of natural habitat at the mine site and waste disposal site
Destruction of adjacent habitats as a result of emissions and discharges
Destruction of adjacent habitats arising from influx of settlers
Changes in river ecology due to siltation and flow modification
Alteration of water tables
Change in land form
Land degradation due to inadequate rehabilitation after closure
Land instability
Danger from failure of structures and dams
Abandoned equipment, plant and buildings
Pollution impacts
Drainage from mining sites, including acid mine drainage
Sediment run-off from mining sites
Pollution from mining operations in riverbeds
Effluent from mineral processing operations
Sewage effluent from the site
Oil and fuel spills
Soil contamination from treatment residues and spillage of chemicals
Pollutants leached from tailings, disposal areas and contaminated soils
Air emissions from mineral processing operations
Dust emissions from sites near living areas or habitats
Release of methane from mines
Occupational health impacts
Handling of chemicals, residues and products
Dust inhalation
Fugitive emissions within the plant
Air emissions in confined spaces from transport, blasting, combustion
Exposure to asbestos, cyanide, mercury or other toxic materials
Exposure to heat, noise, vibration
Physical risk at the plant or site
Resource Issues
Effects on ground water and surface water resources
Effects on fisheries
Loss of forestry resources
Agricultural land losses

In Europe particularly the Aznalcóllar and Baia Mare accidents have increased public awareness of the environmental and safety hazards of mining activities, which since a long time have been considered a major problem in the mining provinces in North America and Australia (U.S. Bureau of Mines 1994, Harries 1997). The U.S. Environmental Protection Agency (EPA) estimated that 45 billion tons of mining and mineral processing waste had been generated in the United States and about one billion tons would continue to be generated each year (U.S. Environmental Protection Agency 1985). Much of this waste is left in inactive or abandoned mine sites, whose number (between 100 000 and 500 000) and extent varies widely with often little or no field evidence (Peters 1995). However, metal mining activities are also an issue within Europe with considerable metal mining activity carried out in four EU member states (Finland, Greece, Sweden and Spain), while minor mining sites are active in Austria, France, Ireland and Portugal. In other Member States, past mining activities have left abandoned mines and waste disposals that need to be monitored and managed to avoid environmental damages. Solely in Europe, evidence of significant accidental pollution problems caused by leakage and spillage from mine tailings lagoons and by abandoned mines (acid mine streams) can be found in at least five Member States (Spain, Italy, Portugal, Sweden and United Kingdom) (Sol et al. 1999). In central and eastern Europe the mining sector plays even a more important role. The production in the former communist countries, some of them becoming EU member states, was very high until the collapse of the political and economic system in 1989 and the beginning of the nineties. Many mining sites were closed abrupt without adequate measures to prevent pollution. In spite of the significance of the problem and of the existence of active or inactive mining sites throughout the European territory, no inventory of active and abandoned metal mining sites exists at a European level, nor have common guidelines for the national mining legislation been defined so far. Moved by the latest accidents in Europe, the European Commission started in March 2001 a debate with the Communication COM 664 on “Safe operation of mining activities: a follow-up to recent mining accidents” (European Commission 2000), in order to amend existing EU environmental legislation. The objective of the debate is the definition of measures that can prevent the negative impacts of mining activities, and the development of a new element of EU environmental legislation regulating all the aspects of mining waste management, in particular the operation of tailings lagoons. In general, the literature reveals a lack of precise spatial and substance-dynamic information and an urgent need for an inventory of metal mining activities and abandoned mine sites. Special interest should be given to those sites producing acid mine drainage (AMD), which is the result of iron sulphide oxidation (Nordstrom 1982). Production of broken waste rock and tailings by mining operations expose large amounts of pyrites and other sulphides to the effects of water and oxygen. Pyrite oxidation is one of the most acid producing natural weathering processes, in which heavy metals (HM) are mobilised and released into the river system and the groundwater. It is these dissolved HMs that constitute the most dangerous emissions of metal mining, due to their strong toxicity to most forms of life. Where pyrite oxidation is active, the impact is highly visual – colours of yellow, orange

and red line affected streams (Anderson & Robbins 1998, Figure 1.1). This led early on to the application of remote sensing for mineral identification and analysis of mining impacts. Early studies by Alexander et al. (1973), Chase & Pettyjohn (1973) and Schubert & McLeod (1973) described the use of Landsat1 MSS data (ERTS-1) to evaluate the damage caused by strip mining in Maryland, Ohio and Pennsylvania. Peters (1983) used airborne multispectral data for detection of the iron minerals goethite and hematite. Further development of sensor technology led to the construction of imaging spectrometers, which have been used for mineral exploration since the eighties (Collins et al. 1983). However, they are also used for the assessment of mining impacts and the remediation of abandoned mining sites. The identification and mapping of acid generating minerals using imaging spectroscopy is documented in a large number of papers (e.g. Fenstermaker & Miller 1994, Swayze et al. 1996, Farrand 1997, Farrand & Harsanyi 1997, Clark et al. 1998, Reinhäckel & Krüger 1998, Ferrier 1999, Swayze et al. 2000).

Figure 1.1. Acid Mine Drainage at Rio Agrio, Spain

2 Objectives and workflow of the study

The principal objective of this study is to assess the potential of the combined application of ground and airborne reflectance spectroscopy for the mapping, impact assessment and monitoring of metal mining related contamination. The work is based upon data sets collected in the Aznalcóllar test area that had been affected by a tailings pond accident releasing large amounts of heavy metal bearing pyrite sludge into the environment.

Given the large volumes and extent of contaminated materials in mining waste a strong demand for spatial information about distribution and severity of environmental pollution from metal mining is given.

Previous studies (e.g. Swayze et al. 2000) showed that the major advantage of reflectance spectroscopy and particularly imaging spectrometry is the ability to provide a synoptic view on the spatial distribution of minerals indicating semi-quantitatively the occurrence of hazardous waste material released to the environment. Furthermore, it offers the potential to assess the state of the processes related to AMD based on the diagnostic absorption features in the spectral reflectance signatures of secondary minerals formed during these processes.

This may particularly help to overcome typical problems of ground surveys due to the discontinuous spatial distribution of contaminated material creating problems in geostatistical interpolation and spatialisation of geo-chemical models. Thus, conventional geochemical modelling of contamination typically based on raster sampling, laboratory geochemical analysis and geostatistical spatial modelling, may be planned in a more focussed, time and cost efficient way and complemented by more frequent up-dates by information derived from multiple scale reflectance spectroscopy. This is particularly important in the case of mining accidents with a sudden release of contamination affecting wide areas as happened in the Aznalcóllar area. In such cases fast responses to minimize the impact of the accident are required.

Reflectance spectroscopy could be used for a fast screening of residual contamination by providing quantitative information about the concentration of contaminants in their spatial context. This would allow estimation of the potential acidification risk and acidity buffering needs as input for a remediation plan. Furthermore, repeated airborne surveys could provide evidence for acidification through identification of indicator minerals for AMD. Hence, reflectance spectroscopy provides faster spatially and temporally more detailed information than can be obtained with conventional assessments within the same time. Once applied successfully, this method could be adapted to other mining accidents.

On the small-scale level reflectance spectroscopy can be applied as a fast non-destructive method for the characterization and quantification of the contamination. In agriculture and food research it is used for similar purposes and became known as near infrared analysis (NIRA) (Williams & Norris 1987, Massart et al. 1998, Hildrum et al. 1992). It is based on the assumption that the concentration of a constituent is proportional to a combination of several absorption features. Relatively few researchers have extended the methods for the extraction of soil/sediment related information. Ben-Dor & Banin (1990, 1994) have used this method for the prediction of different soil constituents. Malley & Williams (1997) determined the heavy metal contamination in lake sediments using multivariate methods. Udelhoven & Schütt (2000) used artificial neural networks for the chemical characterization of sediments. Kooistra et al. (2001) used partial least squares regression for the estimation of soil contamination in floodplain sediments. This study applies different multivariate methods and artificial neural networks to predict soil constituents related to the mining accident.

The macroscopic level, which obviously refers to the imaging spectroscopy data, is analysed with Spectral Mixture Analysis (SMA), which is a means of determining the relative abundances of materials represented in multispectral imagery based on the materials' spectral characteristics. The reflectance at each pixel of the image is assumed to be a linear combination of the reflectance of each material present within the pixel (e.g. Adams et al. 1986; Thomson and Salisbury 1993, Hill et al. 1995, Roberts et al. 1998). In this study SMA is applied to the image data for sub-pixel determination of residual sludge and sludge derivatives, which result from sludge oxidation.

Using two different approaches, multivariate calibration and spectral mixture analysis, a quantitative estimation of soil contamination with laboratory and field spectra as well as with hyperspectral airborne imagery to obtain precise soil contamination information is envisaged.

In order to reach the principle objectives special emphasis should be given to the following points:

- Exploration of correlation between soil constituents and soil spectral reflectance with a special emphasis on components related to the Aznalcóllar mining accident. A particular interest focuses on the investigation of properties which are not directly related to spectral absorption features, but which are highly relevant to describe the contamination status in an environmental context (e.g. heavy metals).
- Development and test of models for the prediction of soil constituents with the help of reflectance spectra. The methods should be robust and simple in order to keep the models transferable to data measured in the field or with the imaging spectrometer. The methods include multivariate statistics and artificial neural networks. A detailed pre-processing precedes the modelling that takes advantage of different filtering and transformation methods to enhance important features.

- Assessment of the possibilities to transfer the developed models to spectra measured in the field and extracted from imaging spectroscopy data, which would allow production of contamination maps for the most important heavy metals (As, Cd, Cu, Hg, Pb, Sb, Zn) and driving variables for acidification (Fe and S).
- Evaluation of spectral mixture analysis for extraction of abundances of residual sludge and its weathering products. The SMA is achieved with advanced unmixing approaches based on multiple endmember sets and standardised variables.

The working steps necessary to derive the quantitative spatial information about the residual contamination are outlined in Figure 2.1. The work consists of two parts, the laboratory/field spectral analysis and the imaging spectroscopy data analysis. The division in two parts is imposed mainly by the different data processing steps. However, there are several links between laboratory/field data analysis and imaging spectroscopy data analysis.

For the laboratory/field spectral analysis, soil samples collected during the field campaigns were geochemically analysed and spectrally measured (*in situ* and in laboratory). This data set, consisting of chemical concentrations and spectral reflectance, was used for the estimation of the soil constituents based on the spectral properties of the samples. Field spectra were used for the in-flight calibration of the imaging spectroscopy data and were inserted into a spectral database as potential endmembers for the SMA. Furthermore, an artificial mixture series was built with soil samples and pure sludge. This data set was analysed using spectral mixture analysis in order to obtain the relation between sludge abundance and concentration of heavy metals.

The imaging spectroscopy data were radiometrically and geometrically corrected and converted into georeferenced reflectance images. SMA was used for the determination of abundances of different endmembers that contribute to the reflectance of a pixel. The derived sludge abundance maps show the spatial distribution of sludge visible at the surface. The relation between sludge abundance and heavy metal concentration derived from the mixture series could then be used for calculation of contamination maps. Based on a geochemical model the potential acidification risk and acidity buffering needs could be estimated as input for a remediation plan. For data of the following year, the adapted SMA focused on identification of indicator minerals for acidification.

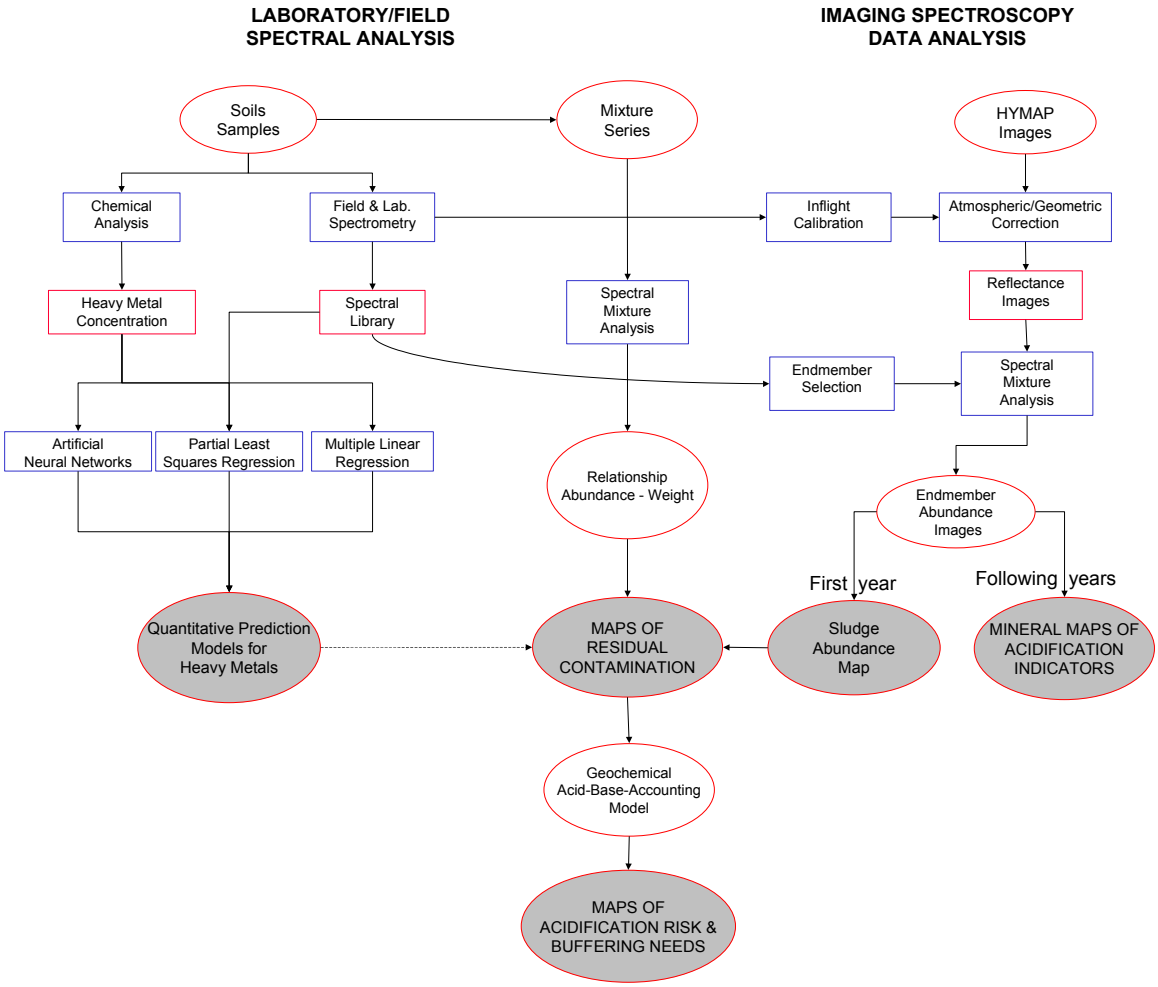

Figure 2.1. Flowchart of fundamental work steps and products of the thesis

Deriving quantitative information about soil contamination with reflectance spectroscopy comprises a wide range of competences. On the one hand the geochemical processes and the remediation actions related to the accident have to be understood. On the other hand the derivation of quantitative information from laboratory, field and image data has to be managed. Therefore, the first chapter introduced to the topic of metal mining related contamination and the contribution of remote sensing for identification of such contamination.

The following chapter 3 presents the Aznalcóllar case study. It provides general information about the study area, the mining activities and the processes related to pyrite oxidation and contamination of heavy metals. Furthermore, the accident and its impact are described and finally the remediation work and concept is explained.

Chapter 4 introduces the fundamentals of reflectance spectroscopy, which are necessary to understand how reflectance spectroscopy can provide qualitative and quantitative information about materials. The spectral properties of materials related to the study are described and the use of imaging spectroscopy is presented.

Chapter 5 starts with a description of the data set used in this study. This includes the data collection in the field, the acquisition and the pre-processing of the hyperspectral imagery and the methodologies, which were used to chemically analyse the soil samples and to measure the spectral data including the corrections of these data. The chapter also includes the presentation of the results of the geochemical laboratory analysis.

Chapter 6 deals with analysis of the relationship between soil composition as derived from the geochemical analysis and soil reflectance measured in the laboratory. It presents and analyses an artificial mixture series of sludge and soil to assess the influence of sludge on the soil reflectance. The chapter describes the methods used for the prediction of soil constituents based on their spectral reflectance, and finally, it presents and discusses the results obtained.

Chapter 7 shows the application of spectral mixture analysis to the imaging spectroscopy data for derivation of the spatial distribution of the residual contamination and the identification of oxidation products.

Chapter 8 demonstrates how the derived abundances can be turned into quantitative maps of heavy metals, potential acidification risk and other parameters important in the remediation planning process and validates the results with an independent data set.

Finally, in chapter 9 the results are evaluated and recommendations are given for the application of reflectance spectroscopy as a screening tool for future cases of accidental contamination related to metal mining.

3 The Aznalcóllar case

The Aznalcóllar mine-tailings spill was one of the largest environmental pollution accidents recorded in Spanish history (Grimalt et al. 1999, WWF 2002). The impact of the accident was particularly severe, because it occurred in the surroundings of the Doñana National Park, one of the biggest wetlands in Europe and an important refuge for migrating waterfowl. The park is protected by national and international laws and conventions (UNESCO - Man and Biosphere Reserve, Natural World Heritage Site and RAMSAR site (Wetland of International Importance), UNESCO 1972, 1994).

The study area is located in the region of Andalucía, SW Spain, approximately 30 km west of Sevilla. The Aznalcóllar mining area is located on the foothills of the Sierra Morena. From Aznalcóllar, the contaminated area extends southbound along the Rio Agrio and Rio Guadiamar, the last tributary of the Rio Guadalquivir (Figure 3.1).

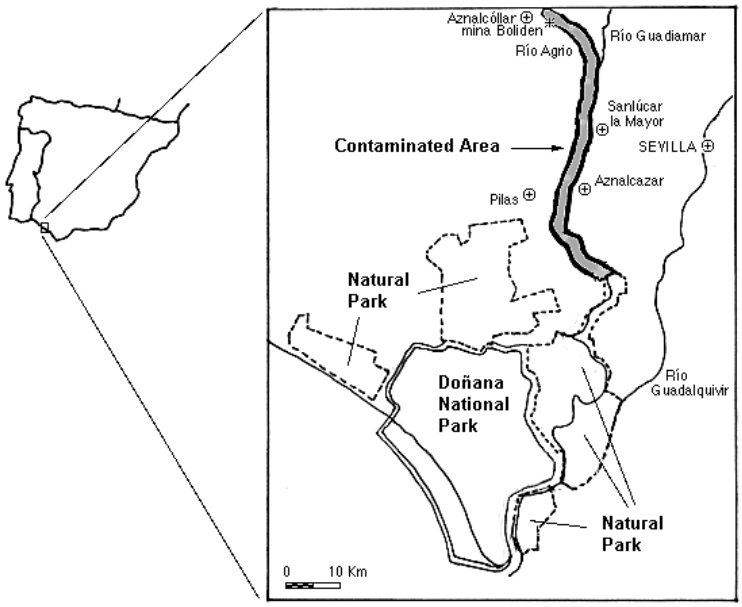

Figure 3.1. Sketch of the study area

3.1 The Aznalcóllar Mine – Geological setting and mine operation

The Aznalcóllar mine is part of the Iberian Pyrite Belt (IPB), which extends from southern Portugal into central south Spain on 250 km length and 25-70 km width. The IPB is considered one of the most important reserves of non-ferrous metals in Europe,

that include the massive sulphide deposits of Rio Tinto, Aljustrel, Neves Corvo, Tharsis, Sotiel and Aznalcóllar.

All these deposits are typical representatives of so called Volcanogenic Massive Sulphide deposits (VMS). VMS belong to the large class of concordant massive sulphide deposits. They typically, if not exclusively occur within geological domains, which can be defined by the presence of submarine volcanic rocks (Lydon 1988). The paleo-geographic tectonic setting of the IPB is considered a hercynian convergent plate margin in island arc or continental margin position. Although the immediate host rocks to the deposits are most commonly associated with rocks of direct volcanic origin, other sedimentary marine lithologies with no volcanic affiliation such as shales or greywackes are by no means rare (Lydon 1988).

This typical lithology is clearly represented in the hercynian sequence of upper paleozoic rocks of the South Portuguese Zone, which hosts the Pyrite Belt. It consists of Late Devonian to Middle Carboniferous rocks, covered in places by Tertiary-Quarternary terrace and alluvial deposits (Figure 3.2). According to Olivera (1990), the IPB can be divided into a southern parautochthonous branch and a northern autochthonous branch. For the southern branch hosting the mine the successions are relatively well established and can be distinguished in three litho-stratigraphic formations:

1. Phyllitic Quarzite (PQ) formation – late Devonian:
    - shale and quartz sandstone, rare conglomerate and a 30 m thick top sequence containing bioclastic carbonate lenses and nodules with fauna and conodonts from middle to late Famennian
2. Volcano-Sedimentary (VS) sequence – late Famennian to early late Visean:
    - The thickness of the VS varies between 100 and 600 m, but only exposed in the IPB. The VS sequences are:
        - VA1 a lowermost rhyolitic sequence with fine to coarse-grained pyroclastics and lava
        - VA2 a second rhyolitic sequence with pyroclastics and lava
        - VA3 a third rhyolitic sequence with reworked tuff and siliceous shale
    - Basic lava, locally pillowed, intercalated between VA1 and VA3; basic dykes and sills injected into the lower part of the complex probably represent feeder zones
    - A bed of purple-blue shale is orming a marker horizon immediately below VA3
    - A pelite black shale and sandstone sequence, which contains beds of jasper and rare limestone, interstratified with VA1 and VA2 volcanics.
3. Turbidite formation – Culm facies or Baixo Alentejo flysch group:

- The Turbidite formation is forming a detrital cover graduating in SW direction and is lying diachronoussly over the other series. Several basin formations are distinguished on the basis of sedimentological and paleontological criteria.

The massive sulphides are hosted by the VS sequence, either directly in the black shale, which is the most common situation, or resting on acidic volcanic facies, though commonly separated from the acidic volcanics by a thin pelitic layer.

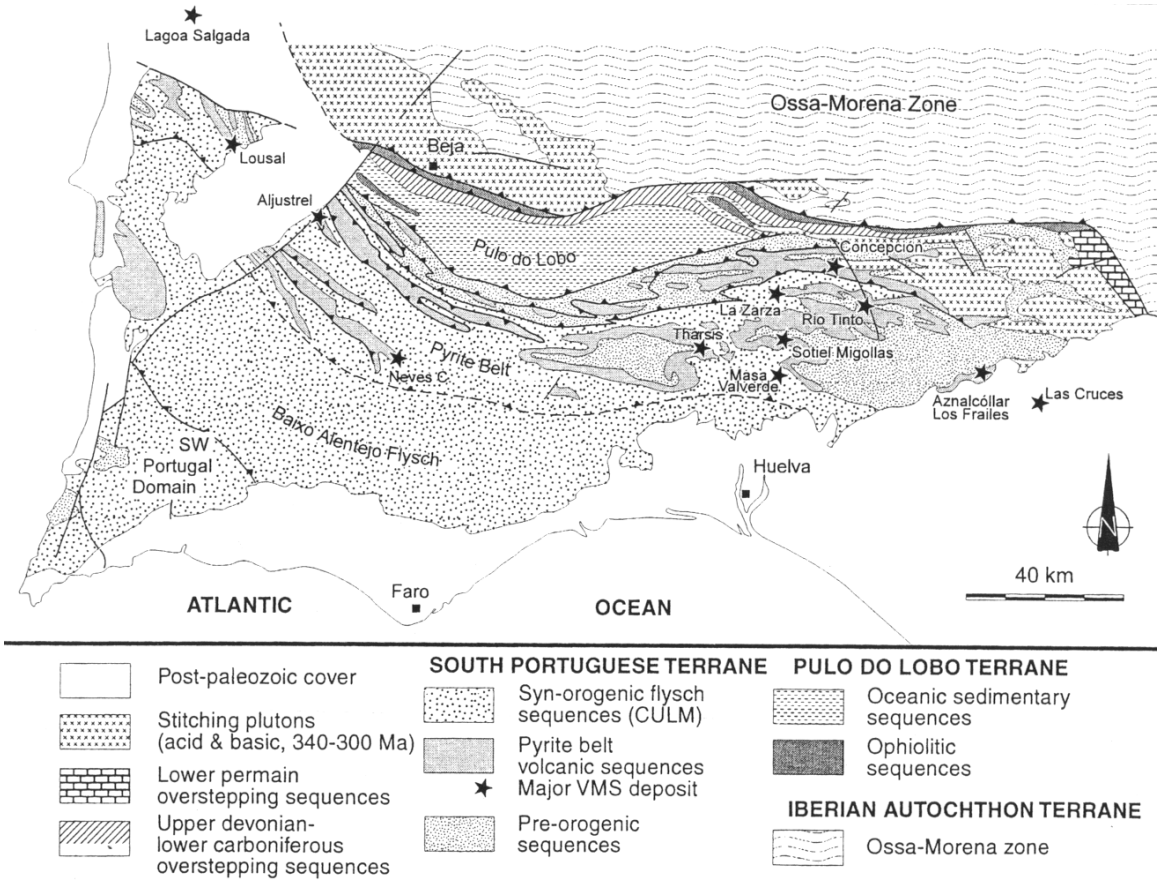

Figure 3.2. Major structural units and tectonostratigraphic domains in the South Portuguese Zone and location of the major volcanogenic massive sulphide deposits of the Iberian Pyrite Belt (from Leistel et al. 1998)

The Aznalcóllar mining district is located on the eastern edge of the Iberian Pyrite Belt (IPB) (Figure 3.3). The PQ crops out mainly N of the mining complex with tectonised contacts with the overlying VS sequence. The characteristic lithofacies include alternating Devonian shales and sandstones.

The VS complex is present in Aznalcóllar in two sequences: the Southern Sequence (SS) and the Aznalcóllar-Los Frailes Sequence (AFS). The SS is located outside the mineralised area and is mainly pelitic, containing some carbonate rocks and basic

volcanites. The AFS comprises the massive sulphides in the study area. The sequence is subdivided into two felsic sub-units, known as Upper and Lower Sequences. They are correlated with the two main volcanic episodes in the area. In the Lower Sequence crystalline tuffs, vitric, tuffs and black shales with massive sulphides can be distinguished. In the Upper Sequence dacite porphyries, purple tuffites and felsic epiclastites are found.

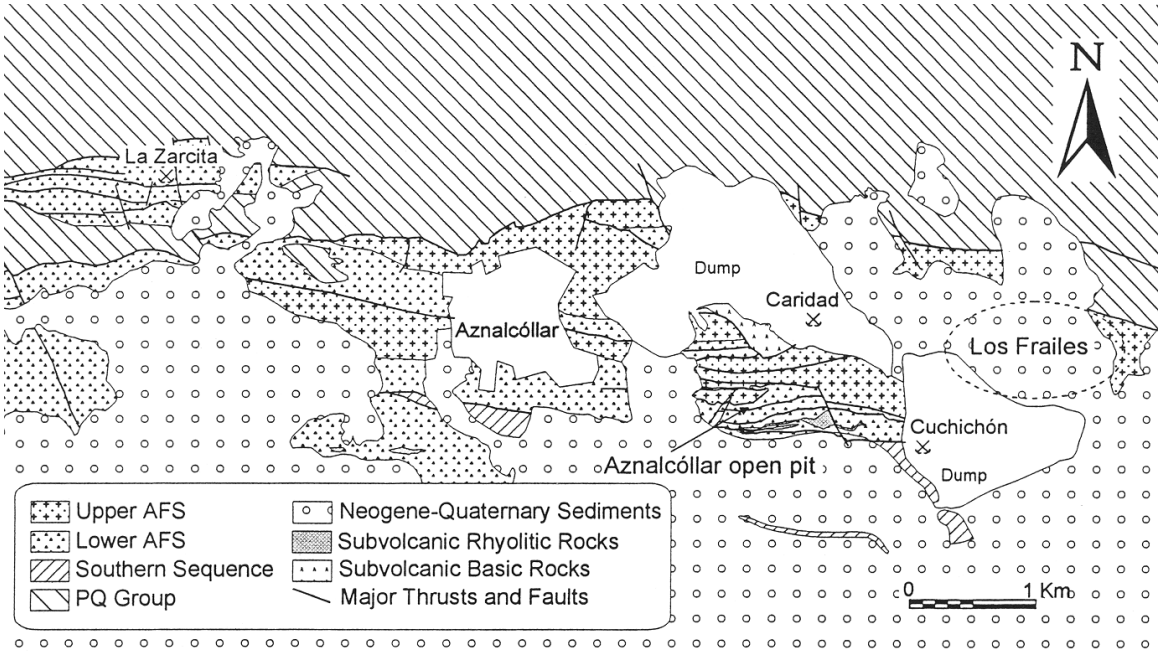

Figure 3.3. Geological Map of the Aznalcóllar mining district (from Almodóvar et al. 1998)

As in other deposits in the IPB, the massive sulphides are characterised by a limited number of major minerals (pyrite, sphalerite, chalcopyrite, galena) together with a wide variety of minor species (Strauss 1965, Marcoux et al. 1996, Almodóvar et al. 1998).

According to their mineral composition, three ore types can be distinguished in the area: polymetallic, pyritic and cu-pyritic. Pyrite is the most common mineral in all three types, showing a wide range of textures including framboidal, colloform, replacement, banded, idiomorphic and recrystallisation. The polymetallic ores are characterised by sphalerite, and galena with minor portions of tetrahedrite, arsenopyrite, chalcopyrite and less frequent minerals like bournonite, boulangerite, stannite and cassiterite. The cu-pyrites consist of chalcopyrite and different Bi-minerals like native bismuth, bismuthinite, nuffieldite, Bi-meneghinite and jaskoskiite (Almodóvar et al. 1998). These associations are, however, rare in massive sulphides and more common in the stockwork zones.

More detailed information on the geology of the IPB is found in the review of Leistel et al. (1998); the Aznalcóllar mining district is described detailed in Almodóvar et al. (1998) and the references therein.

In the IPB mining activities are widely spread and some mines have been in operation since Roman times. Boliden-Apirsa, a multinational Swedish-Canadian-Spanish consortium had acquired the Aznalcóllar mine in 1987, while the mine had been in exploitation for a considerable number of years already. In 1996, a new opencast pit was opened with an ore body of an estimated potential of 50 million tons and the planned annual production was 400,000 tons of concentrate.

The mine produces zinc-, silver-, lead- and copper-concentrates from a pyritic ore body. The ore, which also contains arsenic, cadmium, thallium and other metals in lower concentrations, is broken in the mine installations and milled down to a rather fine grain. Then, different metal compounds are separated from this fine-grained ore with the help of a flotation process, where water is used, to which sulphur dioxide, calcium hydroxide, copper-sulphate-pentahydrate and an organic compound are added as agents, in order to promote flotation.

This extraction procedure produces huge amounts of acidic waste and tailings. These tailings were discharged into an artificial pond. The pond covered a surface of about 1.5 km² and contained, at the time of the accident, about 31 million tons of sludge. Around this pond, a dam had been erected in 1974 to contain the tailings; the dam was regularly increased, as more quantities of tailings were added. The main material that was used for the construction of the dam came from the mining activity itself. At the time of the accident, the dam had an altitude of approximately 25 m.

The main aspects to be controlled in such dams are wall resistance and water draining. Poor structure and resistance of the dam or formation of water lenses by inadequate control of water drainage may lead to rupture of the tailings reservoir under overpressure of the water pockets. Aguilar Campos had already reported these problems in 1995 for the Aznalcóllar dam (in Grimalt et al. 1999). Already several times before the last accident heavy metal pollution by mine effluent leaks occurred in the Agrio and Guadiamar rivers (Cabrera et al. 1984, 1987, Arambarri et al. 1996).

3.2 Geochemical processes and hazards of metal mining waste

As mentioned before, mining of metallic sulphide ore deposits, like the deposits of the IPB, generates huge amounts of mining waste. The waste produces acidic water through chemical reaction of surface water with sulphur-bearing minerals (mainly pyrite), resulting in sulphuric acid. HMs can be leached from natural and waste rocks that are exposed to the acid water. AMD and the related HM mobilisation is a major threat to the quality of water and soil resources throughout the world (USDA Forest Service 1993).

3.2.1 The pyrite weathering process

The formation of AMD is a complex geochemical microbially mediated process that is controlled by several factors. AMD is produced primarily by the oxidation of the iron disulfide mineral pyrite. A complex series of chemical reactions is initiated when surface mining activities expose waste rock to an oxidizing environment. These reactions are analogous to geologic weathering, which takes place over extended time-periods (hundreds of years). However, the rates are orders of magnitudes faster than in natural weathering systems. The accelerated rates release huge amounts of acidity, which allows the associated HMs to get mobile and releases them into the environment. The sequence of pyrite reactions was described by Singer and Stumm (1970):

$$2\,FeS_2 + 7\,O_2 + 2\,H_2O \rightarrow 2\,Fe^{2+} + 4\,SO_4^{2-} + 4\,H^+ \qquad \text{Eq. 3.1}$$

$$4\,Fe^{2+} + O_2 + 4\,H^+ \rightarrow 4\,Fe^{3+} + 2\,H_2O \qquad \text{Eq. 3.2}$$

$$4\,Fe^{3+} + 12\,H_2O \rightarrow 4\,Fe(OH)_3 + 12\,H^+ \qquad \text{Eq. 3.3}$$

$$FeS_2 + 14\,Fe^{3+} + 8\,H_2O \rightarrow 15\,Fe^{2+} + 2\,SO_4^{2-} + 16\,H^+ \qquad \text{Eq. 3.4}$$

The first equation (Eq. 3.1) describes the reaction of pyrite with water and oxygen to produce ferrous iron, sulphate and acidity. In the second step (Eq. 3.2) ferrous iron is converted to ferric iron. This second reaction term has been termed the “rate determination” step for the overall process (Singer and Stumm 1970). This conversion is significantly accelerated by microbial action. Several species of bacteria that are widespread in the environment, principally Thiobacillus ferroxidans, have shown to increase the iron conversion rate by a factor of 100 to 10^6 times (Singer and Stumm 1970, Nordstrom 1982). The activity of these bacteria is pH dependent with optimal conditions in the range of pH 2 to 3. Thus, once the pyrite oxidation and acid production has started, conditions for the bacteria are favourable to further accelerate the reaction rate (Nordstrom 1982). The third step (Eq. 3.3) involves the hydrolysis of ferric iron with water to form solid ferric hydroxide and the release of more acidity. As this reaction is controlled by pH, ferric hydroxide precipitates only at pH values above 3.5. The fourth step (Eq. 3.4) involves the oxidation of additional pyrite by ferric iron. The ferric iron is generated in the steps one and two. This cyclic propagation of acid generation continues until the supply of ferric iron or pyrite is exhausted (Nordstrom 1982).

The acidic water formed by sulphide oxidation can precipitate a large suite of relatively soluble and insoluble Fe-bearing secondary minerals, whose speciation is controlled by pH, degree of oxidation, moisture content, and solution composition (Bigham et al. 1992). It is these secondary minerals that can be identified and possibly quantified with remote sensing techniques (Swayze et al. 1996). Therefore, they are described in more detail. Nordstrom (1982) described the overall sequence of mineral reactions for pyrite oxidation (Figure 3.4).

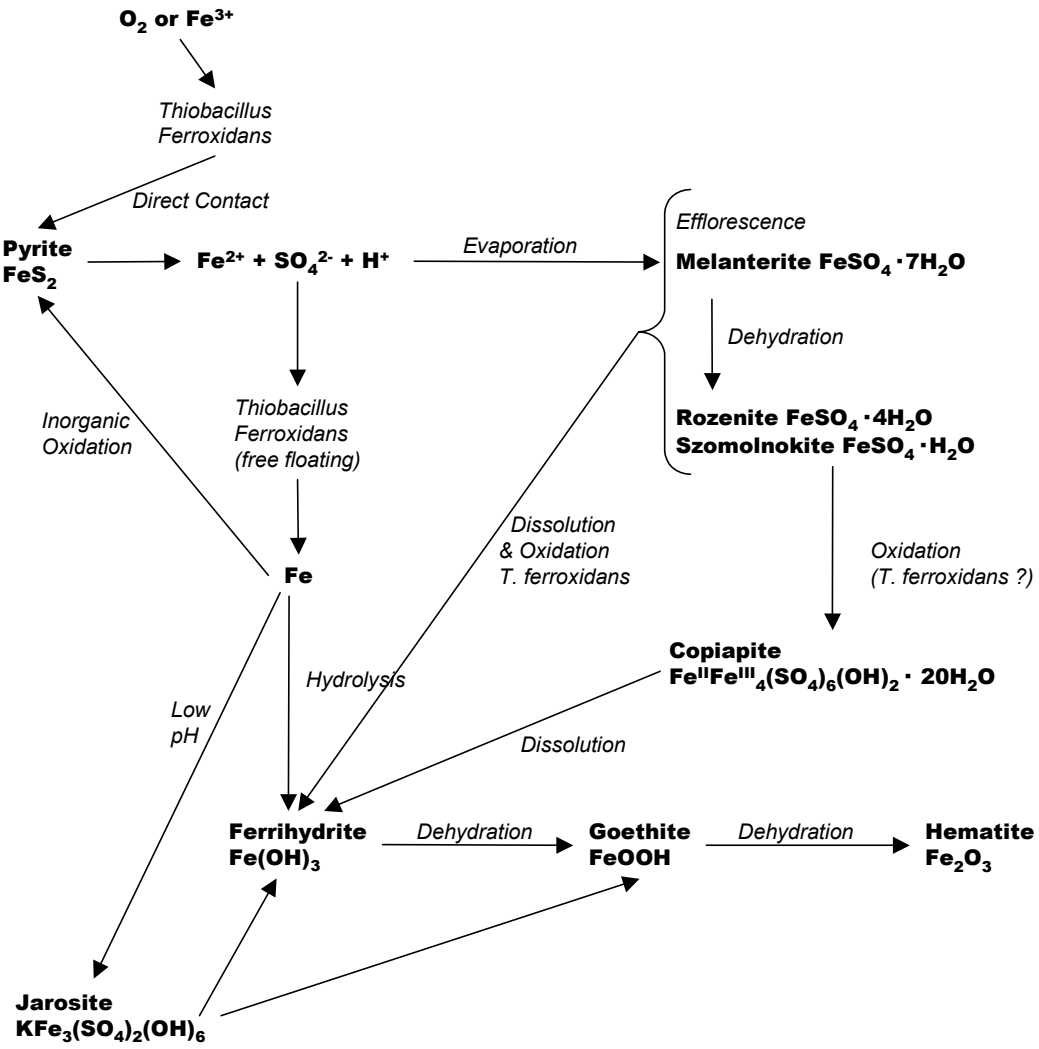

Figure 3.4. Overall sequence of mineral reactions for pyrite oxidation showing relationships between oxidising agents, catalysts and mineral products (from Nordstrom 1982)

Hydrated ferrous sulphate minerals develop on moist pyrite surfaces. When moisture evaporates saturation is first reached with respect to melanterite ($FeSO_4 \cdot 7\ H_2O$), which possibly dehydrates to either rozenite ($FeSO_4 \cdot 4H_2O$) or szomolnokite ($FeSO_4 \cdot H_2O$). If these minerals are still in contact with soil water or humid air and warm temperatures they oxidise to copiapite ($Fe^{2+}Fe_4^{3+}(SO_4)_6(OH)_2 \cdot 2H_2O$). When iron becomes fully oxidised in acid mine waters it eventually reaches saturation with respect to either ferrihydrite ($Fe(OH)_3$) or jarosite ($KFe_3(SO_4)_2(OH)_6$). Jarosite is stable at lower pH levels than ferrihydrite. When jarosite weathers or is exposed to dilute waters with higher pH it will gradually decompose to ferrihydrite or goethite (FeOOH). Goethite possibly dehydrates to hematite (Nordstrom 1982). The more soluble sulphates are most commonly formed during dry periods as evaporation promotes the rise of subsurface waters to the uppermost soil layers by capillary action. The water becomes progressively concentrated and the salts precipitate in an efflorescence, which is an

important step preceding the precipitation of more common insoluble minerals such as jarosite or goethite. Under more humid conditions, the ferrous ion is oxidised to ferric ion catalysed by bacterial action and eventually forms jarosite or ferrihydrite depending on the acidity. Because jarosite forms under more acidic conditions then do schwertmannite, ferrihydrite, and goethite, the relative distributions of these minerals can provide a remote sensing basis for locating potential acid producing areas (Swayze et al. 2000).

The overall quality of the weathering products is a product of two competing processes: the formation of acidity from pyrite weathering and the generation of alkalinity from dissolution of carbonates and other basic materials. The acid-producing process can proceed very rapidly with few chemical constraints. In contrast, dissolution or reaction rates of many common minerals are generally slow due to solubility limitations. Production of alkalinity tends to attain a constant value or level off with time so that the rate of acid production may commonly exceed the production of alkalinity.

More detailed description of pyrite weathering and AMD can be found e.g. in Alpers & Blowes (1994) or Plumlee & Lodgson (1999).

3.2.2 Toxicity and mobilisation of heavy metals

Generally, ore deposits consist only of a certain number of major minerals, but with a large variety of secondary minerals. Massive sulphide ores are typically dominated by pyrite with associated sulphides of trace elements (e.g. Cu, Zn, Pb), which are often the actual mined commodity. These trace elements are also often referred to as heavy metals (HMs) if their density is more than 6 g/cm³ (Alloway 1999). For simplification, in this study also arsenic is included into the heavy metal group even if the density is less than 6 g/cm³. Among all chemical contaminants, trace elements are considered to be of a specific ecological, biological and health significance (Kabata-Pendias & Pendias 1984). Table 3.1 lists the ranges found in soils and the critical concentrations above which toxic effects may occur.

Table 3.1. Ranges of natural occurence and critical concentrations of different trace metals (*Bowen H.J.M. 1979, ** Kabata-Pendias & Pendias 1992)

Element	Range* [ppm]	Critical Concentrations** [ppm]
As	0.1 – 40	20 – 50
Cd	0.01 – 2.0	3 – 8
Cr	5 – 1500	75 – 100
Cu	2 – 250	60 – 125
Hg	0.01 – 0.5	0.3 – 5
Mn	20 – 10000	1500 – 3000
Ni	2 – 750	100
Pb	2 – 300	100 – 400
Sb	0.2 – 10	5 – 10
Zn	1 - 900	70 – 400

High concentrations of HMs do not necessarily impose an acute toxicity risk. In soils with a neutral or alkaline pH value, the solubility of HMs (and therefore their toxicity) is limited. However, with increasing soil acidity (e.g. caused by AMD), the trace elements get into solution. Cadmium becomes soluble already with values lower than pH 6.5. Table 3.2 lists the boundary values for beginning mobility for some trace metals (Blume & Brümmer 1991).

Table 3.2. Boundary pH values for beginning mobility of trace metals (Blume & Brümmer 1991)

Trace Element	Boundary pH value
As	4.5 – 4.0
Cd	6.5
Cr	4.5 – 4.0
Cu	4.5
Hg	4.0
Ni	5.5
Pb	4.0
Sb	4.0
Zn	6.0 – 5.5

More detailed information on the behaviour and toxicity of different trace elements can be found in Kabata-Pendias & Pendias (1984) and Alloway (1999).

Consequently, the complex process of mine waste weathering and particularly pyrite oxidation has strong potential to affect the environment and human health because the mobilised HMs associated with the mine waste may pollute soil and aquifers and thus eventually enter the food chain. Hence, a primary objective for mine waste management is to avoid or minimise the spread and the oxidation of the waste material at any time. This includes the handling during extraction, transport, processing and deposition.

3.3 The accident

Sometime during the night of the 24th and 25th of April 1998 a 50 m wide breach was opened in the dam of the tailings pond (Figure 3.5). Approximately 4 million m³ of acidic water and 2 million m³ of toxic sludge (1.3 to 1.9 million tons) were released into the Agrio and Guadiamar rivers. The sudden release overflowed the floodplain of both rivers approximately 400 m on both sides of the rivers, depending on the elevation of the different river terraces (Figure 3.6). The mud layer left after the flood accumulated 40 km along the rivers with a thickness of 1.7 m in the surroundings of the dam and a few centimetres further down the river. The toxic flood affected an area of 4286 ha of land and the sludge covered an area of 2616 ha (Table 3.3, Coopers & Lybrand 1998), mostly agricultural land and flood or marsh plains (Figure 3.8).

Figure 3.5. Breach of the broken tailings pond dam (from Aguilar et al. 2000)

Figure 3.6. Aerial view of Rio Agrio floodplain after the accident. View to NW (from Aguilar et al. 2000)

Table 3.3. Landcover types affected by the accident (Coopers & Lybrand 1998)

Land type	Area [ha]
Herbaceous crops	999
Herbaceous crops under plastic	172
Fruit and olive trees	261
Rice fields	481
Marsh pastures	315
Pasture	176
Non-worked crop land	154
Water flows, marsh and barren soil	1729

While the toxic flow left 62 % of the spilled tailings in the first 13 km downstream from the broken dam, most of the toxic water was retained in the *Entremuros* area with several urgently constructed dams, but some of the released amount of toxic water was conducted through the *Aguas Minimas* channel towards *Brazo de la Torre*, a side arm of the Guadiamar, and were discharged directly into the Guadalquivir river. The fish and shellfish population in the watercourses died due to burial, gill blocking or the drastic change in water quality (decrease of pH to values near 3 and low dissolved oxygen) (Grimalt et al. 1999).

From the measured concentrations in the sludge (Table 3.4, CSIC 1998, Simón et al. 1998, Cabrera et al. 1999) it could be calculated that the remaining sludge layer contained an estimated 16 000 t of lead and zinc, 10 000 t of arsenic, 4000 t of copper, 1000 t of antimony, 120 t of cobalt, 100 t of thallium and bismuth, 50 t of cadmium and silver, 30 t of mercury and 20 tons of selenium and other metals. Most of the metals occurred in insoluble sulphides, but oxidation processes of these sulphides started right after the accident (Figure 3.7).

Table 3.4. Average chemical concentrations of the sludge released by the accident. Measurements taken immediately after the accident from different locations (CSIC 1998)

Element	Mean Concentration [ppm]	Standard Deviation [ppm]
Iron	34.9 [%]	-
Sulphur	38.1 [%]	-
Lead	7996.1	2364.1
Zinc	7187.0	613.4
Arsenic	3113.5	1066.4
Copper	1993.2	195.5
Antimony	699.8	214.6
Barium	639.9	152.7
Bismuth	68.6	20.7
Thallium	54.2	12.6
Cobalt	47.3	7.9
Cadmium	29.4	5.3
Mercury	3.3	0.9

Figure 3.7. Sludge layer at Vado de Quemas, approx. 30 km downstream (from Aguilar et al. 2000). Note the bright efflorescent crusts on top of the sludge, which are the first oxidation indicators.

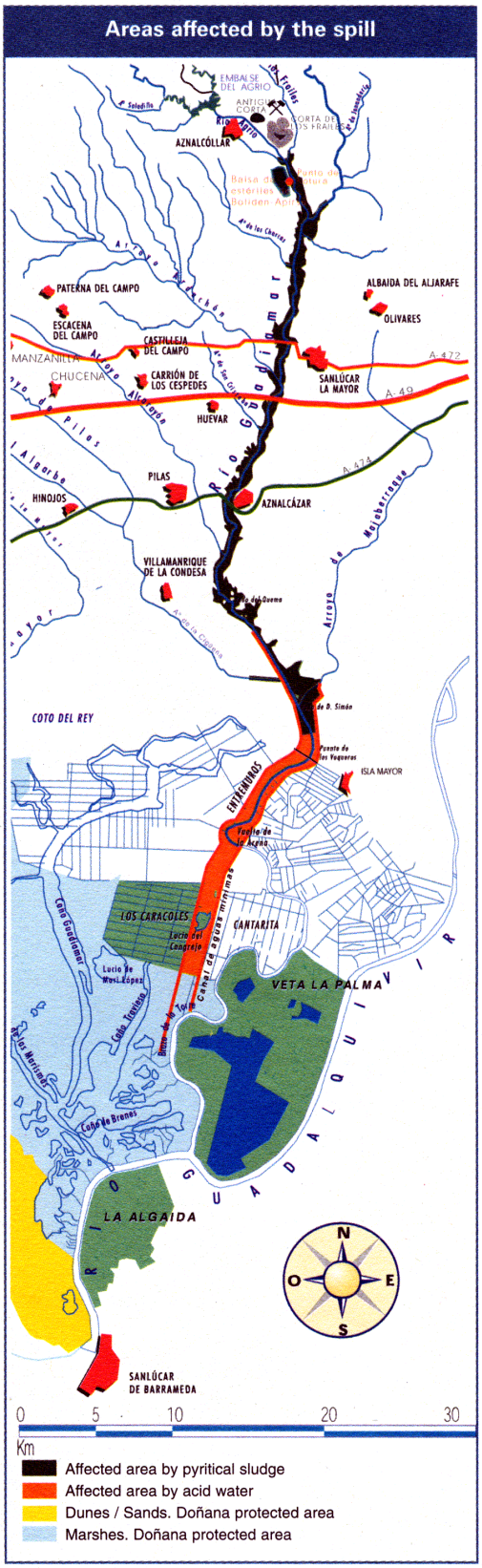

Figure 3.8. Area affected by the toxic spill (from WWF 2002)

3.4 Geo-environmental setting of the affected area

An understanding of the environmental context is indispensable for a risk assessment of the contamination. The vulnerability of soils is strongly dependent on their buffer potential, which is strongly controlled by the background geology. Therefore, in the following paragraph an overview of the climatological, geomorphological, pedological conditions and vegetation and land use is given.

The climate of the study area is a subhumid Mediterranean type with winter rains and harsh summer droughts. However, it still has some oceanic influence, which results in milder temperatures, higher air moisture and rainfall than further inland, although this influence is decreasing from South to North. The decrease in oceanic influence is overweighed by the terrain effects, which cause higher precipitation in the Sierra Morena area. The precipitation regime is characterised by a strong inter- and intra-annual irregularity. Yearly precipitation averages 565 mm, but can exceed 1000 mm or stay below 300 mm. Most of the precipitation (80 %) occurs in the October to March period with December and January maxima approaching 90 mm and no rain for July and August. The monthly average temperatures vary from 9° C in December and January to 27° C in July and August with an absolute maximum exceeding 40° C (Figure 3.9, Consejería de Medio Ambiente 1999).

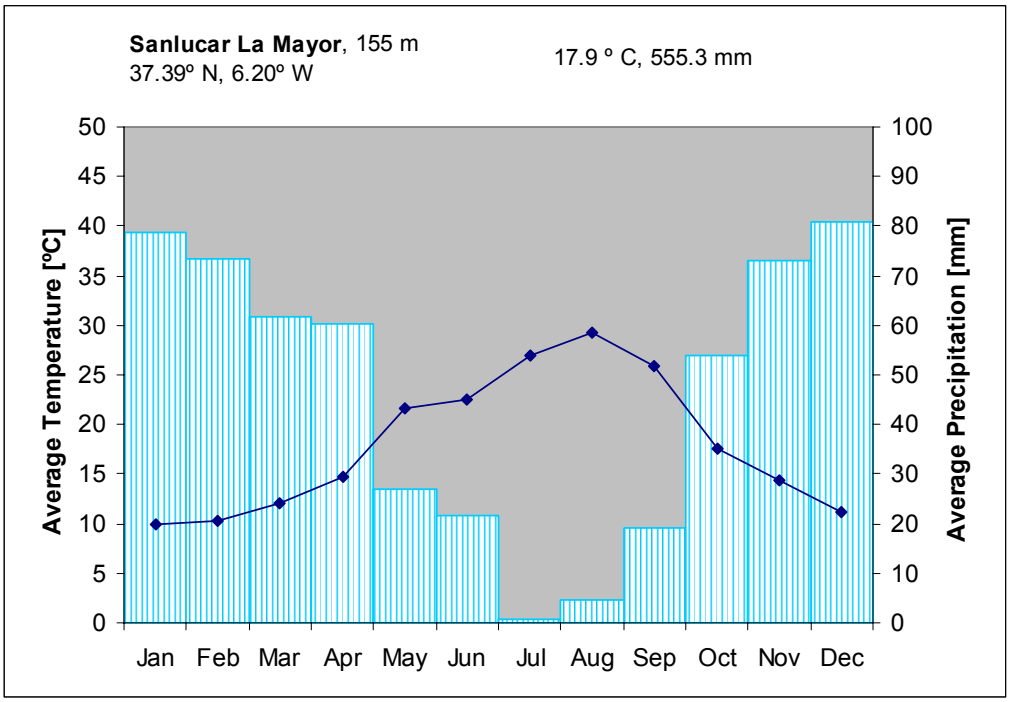

Figure 3.9. Climate diagram of Sanlucar la Mayor (Consejería de Medio Ambiente 1999)

The Guadiamar is the last big tributary to the Guadalquivir. However, it does not flow directly into the Guadalquivir, but splits up into the *Brazo de la Torre* arm, leading to the Guadalquivir, and the *Caño de Guadiamar*, which fed the salt marshes of the *Marismas* in case of floods. This circumstance is explained by the evolution of the Guadalqivir estuary, whose sediments forced the rivers continuously to change their riverbeds. Additionally, the anthropogenic influence has changed the net of watercourses in the last decades.

From a lithologic point of view, the Guadiamar watershed consists of three well distinguishable units. The superior section of the fluvial system is inserted in the southern edge of the *Sierra Morena*, which is characterised by outcroppings of material from the superior Palaeozoic and a strong folding tectonics in sub-meridional direction (Consejería de Medio Ambiente 1999). In this unit the volcano-sedimentary complex penetrated with the sulphuric mineralisation that is mined at the Aznalcóllar mine and all along the Iberian Pyrite Belt. The middle section, the *Campiñas* and the *Aljarafe*, of the river basin is underlain by Miocene blue marls and yellowish calcareous sands from the Pliocene/Pleistocene transition, and on Quaternary materials associated with fluvial dynamics. The latter represent coarse to fine detrital facies of fluvial terraces and alluvial plains. The lower section, the *Marismas*, as well as parts of the middle section are dominated by Holocene clays and loam (Gallart et al. 1999, Consejería de Medio Ambiente 1999).

The most recent distribution of sediments from a hydro-geomorphologic point of view is of particular interest for this work because a higher permeability may lead to a deeper intrusion of contamination. In the area affected by the mining accident, three sectors can be distinguished according to geomorphic characteristics and human impact. In the upper reach, along the first 15 km downstream from the tailings reservoir, the river comprises a 50 m wide, 2-3 m deep single meandering channel, and a 350 to 1000 m wide floodplain, which smoothly declines towards the main channel. It is built up mainly by point bar deposits, formed by gravels and medium to coarse sand textures, and overbank deposits with coarse to fine sand textures. Gravel and sand deposits are mined in open pits (Gallart et al. 1999).

The second reach, between *Las Doblas Bridge* and *Vado de Quema* (15 and 30 km downstream the reservoir), is characterised by a sudden change to a lower valley gradient. The low flow channel is a 30 m wide and 4-5 m deep single meandering channel. This channel is limited by natural levees, which are typical for suspended load rivers. The floodplain is 300-700m wide and is built up mainly by overbank deposits with sand and silt textures.

The lowest part affected by sludge reaches from *Vado de Quema* to Entremuros (30 to 45 km downstream). Where the Guadiamar enters the marshland, the natural river divided into two branches; the *Brazo de la Torre*, which flows in the western direction to the Guadalquivir and the *Caño de Guadiamar*, which crosses the Doñana marsh lands. However, the natural river system has been changed drastically to allow

agriculture. The *Brazo de la Torre* arm was abandoned and a straight low flow channel with an artificial levee along the right side was constructed to prevent flooding. This channel opens at the former junction of *Guadiamar-Brazo de la Torre* into a 1 km wide channel, called *Entremuros*, which is 34 km long and conveys the waters of the Guadiamar directly into the Guadalquivir (Gallart et al. 1999).

The flood produced by the failure of the tailings reservoir merely caused minor changes in river morphology due to the low gradient and the short flood peak discharge. The pyrite mud sedimentation generally occurred in the main channel and the floodplain. The flood wave reached the lower terrace, 4 m above the main channel, only at the confluent of Rio Agrio and Guadiamar. The pyrite thickness decreased from 50 cm at the reservoir to a few millimeters in the Entremuros area. The largest accumulations were found in the gravel pits. The impact of the clean up activities on the river morphology was much stronger. During the removal, also the topsoils with vegetation cover as well as most of the trees were removed, smaller fluvial landforms were destroyed and the main channel had to be transformed into an earth channel with a flat bottom and steep embankments (Gallart et al. 1999).

Soils are a complex and dynamic system generated by diverse factors. The most important ones are lithology, climate and biocenosis. The lithology provides the basic material; the climate determines the existence and characteristics of certain biocenosis, the alteration and erosion processes and finally, the biocenosis controls the biochemical change, provides organic matter and protects the surface from erosion. The factor time has to be added in terms of duration and history; duration is related to the time the soil has for its development and the history is related to paleo-soils that were formed during different climatic conditions (e.g. terra rossa). According to these specifications, the soils in the study area correspond to the Mediterranean edaphic zone, which is particularly in Andalucia a very heterogeneous zone due to a highly variable lithology and mesoclimate (Alba 1991). Three different edaphic units can be separated in the study area: Sierra Morena, Campiñas and Marisma.

The soils in the *Sierra Morena* are, apart from few calcitic outcrops, underlain mainly by silicatic material and form predominantly little developed soils with A-C type profiles. Leptosols and regosols are the most common. The leptosols are located in areas with very steep slopes and ridges that do not allow any accumulation of finer material and often show outcrops of bare rocks. The Regosols develop preferably on shists and granitic colluvial deposits. Depending on the parent material, they have a varying composition and are covered by *Matorral comunities* and, if agriculturally used, by olive groves or cereals. In less hilly terrain cambisols are common (Alba 1991).

In the central study area, catenas dominated by calcaric cambisols are widespread on gentle slopes on the Miocene material of the edges of the *Campiñas Altas*. They are associated with calcaric Regosols in steeper terrain and with Vertisols on the clayey foothills of the slopes. Chromic Luvisols or Terra rossa are located on the Pliocene sands of the Aljarafe and the higher terraces of the Guadiamar. They are relictic soils

from the hot interglacial, when intense weathering liberates iron and allowed rubification of the cambisols. The *Campiñas Bajas* with their clayey Miocene/Pliocene parent material are characterised by Vertisols, which have a strong swelling capacity during the rainy season and the formation of deep cracks during the dry season.

The *Marismas* are characterised by Fluvisols and Solonchaks, which had been subject to contamination already before the last accident (Cabrera et al. 1984, Ramos et al. 1994).

With respect to the affected area, the major part of the soils are calcic and eutric Fluvisols with minor areas of calcic and eutric Luvisols, calcic Vertisols, calcic Regosols and calcic or vertic Cambisols (Simón et al. 1998). The affected soils react very differently to the contamination, depending on their physical characteristics and their chemical properties. The soils may act as a filter that retains, transforms or even degrades the contaminants and therefore play an important role for the expansion and the development of the contamination. According to Simón et al. (1998), the soils in the area generally show a favourable behaviour towards the contamination with neutral to alkaline pH regime and high cation exchange capacity. However, there are two areas with different contamination characteristics CSIC (1998). There is on the one hand the area from the Las Doblas Bridge to Entremuros with pH values above 6.5, elevated calcite, clay and salt contents, characteristics which generally favour the buffering of acidity and the fixation of heavy metals. On the other hand, there is the very heterogeneous area from Aznalcóllar to the Las Doblas Bridge. The pH values are ranging from lower than three to seven, which means that one finds hyper acidic, acidic and neutral environments. The texture is lighter and the calcite content much lower (CSIC 1998). This means that this area is much more susceptible to contamination.

The natural vegetation shows a clear trisection in the N-S direction. The typical Mediterranean *Matorral* communities, predominated by low tree, shrub and herbaceous vegetation patterns, dominate the area north of Aznalcóllar. The vegetation cover is characterised by patches of *Dehesa*, oak and pine forests and different shrub associations (with *Arbutus unedo, Pistacia lentiscus*, *Cistus ssp*) (Consejería de Medio Ambiente 1999).

In the central part from Aznalcóllar to Vado de Quema the natural vegetation is practically absent due to the intense agricultural land use. Depending on the substratum cork oak (*Quercus suber)* and stone oak (*Quercus rotundifolia)* would be predominant species. The few spots of trees are limited to the vicinity of the rivers and agriculturally unusable land. The natural riparian vegetation is a gallery forest with poplar, willow, elm, ash and other trees, but in many areas, this typical Mediterranean forest was substituted by eucalyptus plantations. In the vicinity of Aznalcázar and Villamanrique de la Condesa extended pine forests are found (Consejería de Medio Ambiente 1999).

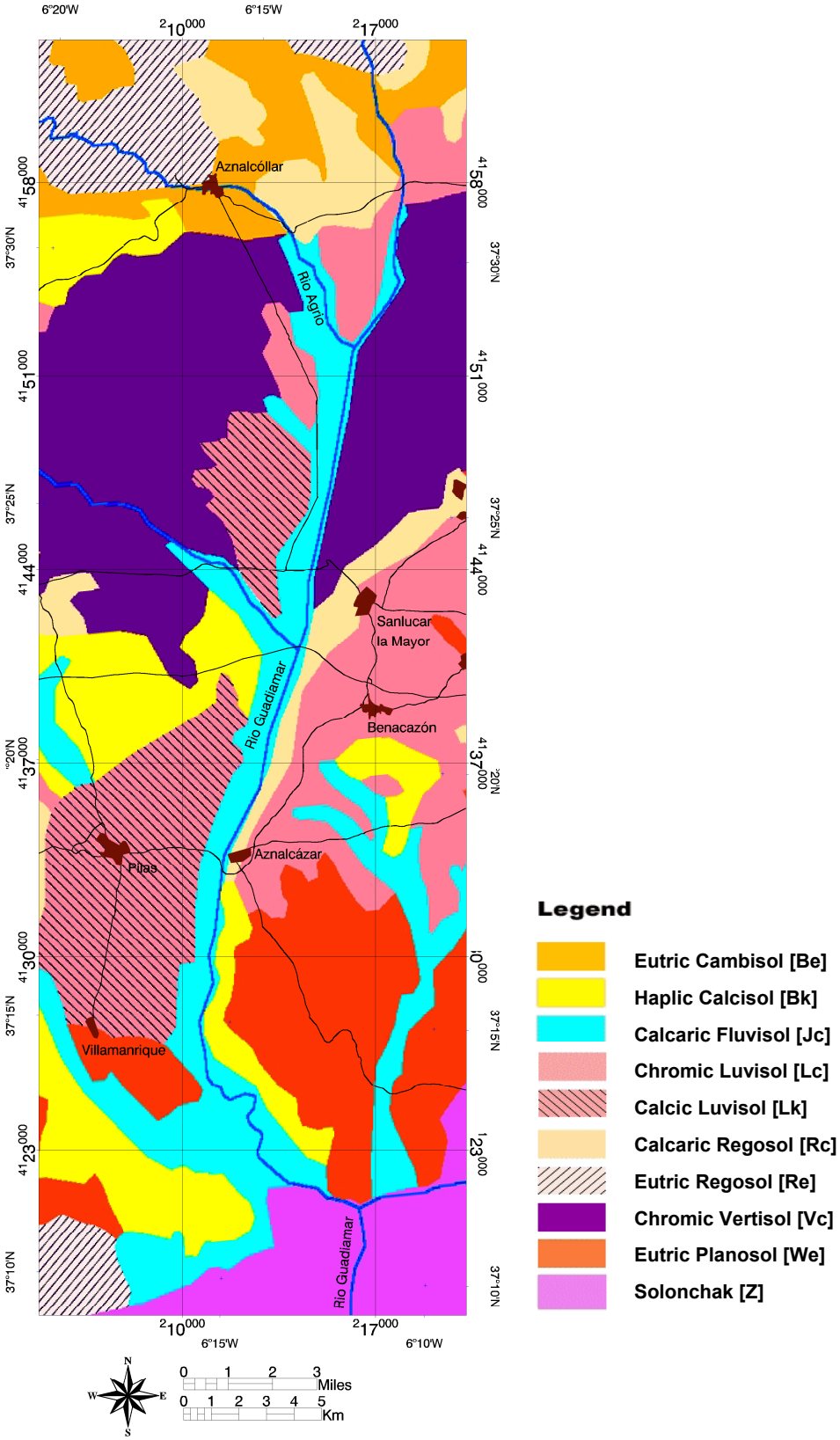

Figure 3.10. Soil map of the study area (derived from 'Mapa de suelos de Andalucía 1:400 000)

In the lower part, the natural vegetation consists of aquatic (reed, sedge) and halophytic (*Tamarix ssp*., *Salicornia ssp.*) vegetation. As well as the central zone, also the *Marismas* have been changed drastically due to agricultural land use. The natural vegetation in the area is differentiated in three types according to the level of inundation. The upper *Marisma* is dominated by *Salicornia ssp*. vegetation. Pastures characterize the middle *Marisma*, which is not affected by periodical inundations. The lower *Marisma* finally, with the highest humidity, is found in depressions and old abandoned water channels. The water in these depressions is often covered with swamp vegetation (García Novo (1981), Consejería de Medio Ambiente 1999).

As mentioned before, the study area is used intensively for agricultural production. Hence, the natural vegetation is repelled to small islands within the agricultural matrix. The central part between Aznalcóllar to Vado de Quema is dominated by dry land agriculture (*Secano*) with Crops, the areas in the South and along the river are characterised by irrigated fields (*Regadio*) with corn, sugar beets, cotton and rice. Furthermore, orchards and olive groves are common on the plateau of the Aljarafe (Consejería de Medio Ambiente 1999).

3.5 Clean up/remediation

The only way to prevent severe soil and ground water contamination, atmospheric pollution due to wind transportation of dried tailings and further surface water contamination due to soil lixiviation was the removal of the material left by the toxic flood, the neutralisation of the retained waters and the decommissioning of the failed dam.

The acidic water with high concentrations of cadmium, zinc, thallium, cobalt manganese and nickel was submitted to physical-chemical treatment in decanting ponds, where the pH was neutralised and heavy metal hydroxides were precipitated. Prior to release into the Guadalquivir estuary, solid substances were physically separated and the water diluted with non-toxic water. The treatment of accumulated toxic water was concluded in August 1998 (WWF 2002).

After the accident the tailings pond still contained 13 Mm^3 of tailings, which had to be prevented from further pollution. After some immediate emergency measures, the tailings pond was decommissioned by sealing the lagoon through an impermeable seepage cut-off wall around the north and east side of the dam and a hydraulic barrier including a back-pumping system on the inside of the cut-off wall (Eriksson & Adamek 2000).

The collection of tailings started slowly on May 3, 1998, eight days after the accident, using heavy machinery: 154 excavators and caterpillars, 491 trucks. In addition to the

sludge layer, also the topsoils were removed leaving behind barren soils and alluvial sands. The removed sludge and soils were disposed in the Aznalcóllar open-pit for sub-aqueous disposal. Most of the 300 m deep open-pit is situated below ground water level in *Visean Terranes* comprising folded and thrusted black shales and rhyolitic pyroclastites. This first removal campaign was completed in November 1998, just before the start of the rainy season. According to the Consejería de Medio Ambiente (2001), about 7 million m^3 of sludge and soil were deposited in the Aznalcóllar open-pit.

The use of heavy machinery and trucks left large amounts of toxic material on the ground and favoured a mixing of tailings and soils. This made a sampling campaign necessary to analyse the status of residual contamination. In March 1999 more than 1000 samples were taken and geochemically analysed. In areas with an elevated concentration additional 775 samples were taken in order to direct a second clean up. After identification of problematic areas a second clean- up was performed mainly in the northern part during which approximately 200 ha were re-cleaned and 1 million m^3 taken to the open pit.

After a further removal of sludge was not possible any more, areas that still had elevated heavy metal concentrations or low pH values were treated with substances that are able to fix heavy metals in more or less soluble products and improve the soil quality. Different materials were tested for their capacity to precipitate heavy metals and to raise the pH level of the acidic soils (García et al. 2000). Limestone ($CaCO_3$) was the parameter, which controlled fundamentally the precipitation of heavy metals. In non-carbonatic horizons the precipitation of Fe, regulated by cation exchange capacity (CEC), controlled the fixation of Cu, As and partly Tl. The clay content controlled the retention of Zn, Pb and Tl.

Alkaline lime-rich by-products from sugar refinement were distributed for neutralisation of acidity and precipitation of heavy metals, because its application is less aggressive than the one of pure limestone by lifting the pH level more gradually. Moreover, the high content of organic matter is a positive side effect. In order to improve the fixation of As, clayey soils from road construction rich in iron oxides, MnO_2 and $FeCl_3$ were applied. Finally, organic matter was distributed to improve the overall pedologic conditions after the topsoils had been removed during the clean up.

As a consequence of the accident the regional and the central government have launched two restoration programmes aiming at repairing the damages of the toxic flood and improving the ecological conditions in the whole Doñana area: the Guadiamar Green Corridor and the Doñana 2005 plans.

The Guadiamar Green Corridor project aims at a restoration of the Guadiamar basin and the establishment of an ecological corridor between the mountainous Sierra Morena and the littoral systems of Doñana. At the same time, the program intends to improve the quality of life for the inhabitants of the region by developing a socio-economical system

that is sustainable and integrated into the natural context (Consejería de Medio Ambiente 2000).

The marshland restoration project Doñana 2005 aims at a hydrologic regeneration of the watershed and riverbed flowing into the marshland of the Doñana national park in order to recover the hydrologic supply and to ensure the needed quantity and quality of water for the marshland ecosystem.

The accident had a great impact on Spanish society, which considers the Doñana a 'pearl' of nature conservation in Spain. Besides this the economic impact of the accident was also tremendous. The costs of the disaster remediation sum up to 377.7 million euro (M€) (WWF 2002). The mining company Boliden-Apirsa had expenses of 96 M€, which included clean up in the northern sector of Guadiamar (27 M€), acqusition of the harvest 1998 (11M€), the operations of the decommissioning of the tailings lagoon (41 M€) and the loss due to the interruption of the mining activity during 1998. The regional government of Andalusia made 145 M€ available for disaster remediation including clean up and acquisition of polluted land (48 M€) and land restoration (90 M€). The national government approved 136.7 M€. This includes 13 M€ for tailings removal and 15 M€ for treatment of the toxic waters and 93.7 M€ for the hydrologic regeneration plan.

The mining company recommenced mining one year after the accident, but in October 2000 the Spanish subsidiary Boliden-Apirsa of the Swedish-Canadian company went bankrupt and ceased mining. The mining company abandoned the Aznalcóllar mine in December 2001, suspending payments, dismissing 425 workers and leaving behind an environmental deficit of 298 M€ without undertaking an appropriate closure (WWF 2002).

4 Principles of reflectance spectroscopy

Reflectance spectroscopy is the study of light as a function of wavelength that has been reflected or scattered from a solid, liquid, or gas (Clark 1999). Spectroscopy has the advantage of being sensitive to both crystalline and amorphous materials, unlike some diagnostic methods such as X-ray diffraction. The other main advantage is that spectroscopy can be used at different scales, from the microscopic scale (laboratory) to macroscopic scales (earth remote sensing and planetary astronomy). Because spectroscopy is sensitive to many processes, spectra can be very complex. However, it is because of this sensitivity that spectroscopy has great potential as a diagnostic tool. Reflectance spectroscopy can be used without sample preparation, is non-destructive, and can be carried out remotely without direct contact to the object under investigation.

In reflectance spectroscopy (particularly in remote sensing), the electromagnetic radiation (EMR) serves as the main communication link between object and sensor. The interaction of EMR with materials on a 'macroscopic' level, including refraction, diffraction, and scattering effects, formed the basis of traditional remote sensing theory. However, hyperspectral research (hyperspectral imaging is another expression for imaging spectroscopy) and development has shifted the emphasis towards monitoring interactions of electromagnetic energy within molecules, crystal lattices, and cell structures (Goetz 1992a). This new perspective requires knowledge of quantum mechanics and the application of a 'particulate view' of electromagnetic energy (Hunt 1980).

Hence, the key of deriving information from spectroscopy data is the understanding of the interactions between electromagnetic energy and the surfaces being observed. This chapter discusses those issues. However, a single chapter cannot cover the topic of reflectance spectroscopy adequately. For more detailed information the reader is referred to Hunt (1980), Elachi (1987), Gaffey et al. (1993), Clark & Roush (1984), Clark (1999) and the references therein for more detailed discussions.

4.1 Electromagnetic radiation

Since the discovery of the composite nature of white light by Newton in 1664 the physical principles of spectroscopy in all ranges of wavelengths of electromagnetic radiation have been used to study the properties of terrestrial and extraterrestrial objects (Sturm 1992). Electromagnetic radiation is a dynamic form of energy that is capable of propagating through a vacuum and becoming apparent only by its interaction with matter (Suits 1983). Over time, two different concepts of electromagnetic radiation have been developed to describe the behaviour of radiation and its interactions with matter.

The classic concept treats electromagnetic radiation as a continuous transverse wave of oscillating magnetic and electric fields. The interaction of electromagnetic radiation with materials on a macroscopic level can be described by Maxwell's equations. This set of partial differential equations can be used for phenomena related to propagation, reflection, dispersion, diffraction and interference of electromagnetic radiation (Hunt 1980). However, with this concept only macroscopic optical behaviour can be described and predicted, but interactions at atomic and molecular levels have to be described using the quantum theory that treats electromagnetic radiation as a stream of discrete particles, which carry fixed amounts of energy (Hunt 1980). According to quantum theory, an atom or molecule can only exist at certain discrete energy levels and cannot have intermediate energy levels. In addition, energy can only be absorbed if the provided energy matches exactly the amount that is necessary to promote an atom or molecule from one energy state to a higher state. Similarly, electromagnetic radiation is emitted when an atom or molecule falls from an excited state to a lower-energy state.

The wave concept is used to describe the electromagnetic radiation. It is characterised with respect to frequency, wavelength, and wavenumber. The energy carried by a photon is precisely related to its associated wave frequency by the following equation:

$$E = h \cdot \nu \qquad \text{Eq. 4.1}$$

where E is energy, h is Planck's constant ($6.626 \cdot 10^{-34}$ J·s), and ν is the frequency. The frequency is a fundamental characteristic; as it is independent of the medium, the radiation passes through. The frequency is related to wavelength and the speed of radiation propagation in a medium:

$$\nu = c / \lambda \qquad \text{Eq. 4.2}$$

where λ represents wavelength and c is the speed of propagation (in a vacuum the speed of propagation is approximately $3 \cdot 10^8$ m $\cdot$ s^{-1}). The wavenumber is the reciprocal of the wavelength and gives the number of wave cycles per unit distance. The flux and reflectance of radiation are generally expressed as a function of wavelength (Clark 1999).

The radiance measured by a sensor (e.g. a spectrometer) is related to the irradiance on a Lambert surface by the following expression:

$$L_{(\lambda)} = \frac{R_{(\lambda)} E_{(\lambda)}}{\pi} \qquad \text{Eq. 4.3}$$

where $L_{(\lambda)}$ is the spectral radiance measured in W m^{-2} sr^{-1} μm^{-1}, $R_{(\lambda)}$ is the absolute spectral reflectance, and $E_{(\lambda)}$ is the irradiance from the light source (e.g. the sun).

The most commonly used term in remote sensing in the VIS to SWIR domain is bidirectional reflectance $\rho_{(\lambda)}$, which is the ratio of reflected radiance in direction toward the sensor to the irradiance in direction toward a portion of the source:

$$\rho_{\lambda}(\theta_i, \varphi_i, \theta_r, \varphi_r) = \frac{L_{\lambda}(\theta_r, \varphi_r)}{E_{i\lambda}(\theta_i, \varphi_i)} \qquad \text{Eq. 4.4}$$

where L_λ (θ_r, φ_r) is the radiance measured along the direction of observation (θ_r, φ_r) and $E_{i\lambda}(\theta_i, \varphi_i)$ is the incident irradiance of the light source along direction (θ_i, φ_i); θ is the zenith angle and φ the azimuth angle. In practice, the bidirectional reflectance $\rho_{(\lambda)}$ of an object is derived from the ratio of reflected object radiance to the reflected radiance of a standard under identical illumination geometry and irradiance.

The spectrum has been divided into different spectral or wavelength ranges. However, the extent of the spectral ranges is rather arbitrary and the decision as to where the divisions should be was made based on limits imposed by the human eye (visible range), the properties of optical materials, and the response limits of various sources and detectors. The common spectral ranges are: ultraviolet (UV, 0.001 – 0.4 μm), visible (VIS 0.4 – 0.7 μm), near-infrared (NIR, 0.7 – 3.0 μm), mid-infrared (MIR, 3.0 – 30 μm) and far-infrared (FIR, 30 μm – 1 mm). These spectral ranges are general in chemistry and physics (Lide 2000). However, in remote sensing literature the range from 0.4 to 1 μm is often referred to as visible/near-infrared region (VNIR) and the range from 1 to 2.5 is referred to as short wave infrared (SWIR) (Clark 1999).

4.2 Interaction of electromagnetic radiation with matter

The key to understanding how remotely sensed data could be used to recognize surface features lies in the way electromagnetic energy interacts with matter. When an electromagnetic wave interacts with matter, there are a number of mechanisms, which affect the properties of the resulting wave. Some mechanisms affect the entire spectrum, while others operate over a narrow band of the spectral region. The narrow band interactions are usually associated with electronic and vibrational molecular processes. These mechanisms are strongly affected by composition and crystalline structure and thus allow estimates of the target properties from the reflectance spectrum. The wide band mechanisms are usually associated with non-resonant electronic processes like reflection, transmission and scattering.

4.2.1 Electronic processes

Electronic processes are associated with electronic energy levels. Electrons in an atom can occupy only specific quantized orbits with specific energy levels. Electronic processes occur at shorter wavelengths (0.4 to 1.1 μm) since the energy necessary to lift an electron into a higher level is rather high. Many of the absorption features in the VIS and NIR, which are particularly important for remote sensing, are due to crystal field effects. However, other processes like charge transfer bands, conduction bands and colour centres occur and – even if not frequent – they are important for certain minerals.

The most common absorption process in mineral spectra is caused by the unfilled electron shells of transition elements (e.g. Ni, Cr, Fe, Ti). Amongst the transition

elements iron is the most important, because it is common in many minerals and hence practically all soils resulting from weathering of the parent materials (Clark 1999). When transition elements are bound in a crystal field, the energy levels are split. The split of orbital energy states allows the movement of electrons to a higher level by absorption of photons with the equivalent energy state (Burns 1993). The energy levels are primarily determined by the valence state of the atom (e.g. Fe^{2+}, Fe^{3+}), and by its coordination number and the symmetry of the site it occupies. Secondarily, they are determined by types of ligands formed (e.g. metal-oxygen), the extent of distortion of the metal ion site, and value of the metal-ligand interatomic distance (Hunt 1980).

The crystal field varies with the crystal structure from mineral to mineral and consequently the amount of splitting varies. The same ion (e.g. Fe^{3+}) produces different absorptions in different minerals due to the variable splitting, making specific mineral identification possible from spectroscopy (Clark 1999). For example, the Fe^{3+}-minerals goethite and hematite show a change in Fe^{3+}-absorption band position and shape with composition (Figure 4.1).

Absorptions caused by charge transfer bands refer to inter-element transitions, where the absorption of a photon causes an electron to move between neighbouring ions or ions and ligands. The transition can also occur between the same metal in different valence states, such as between Fe^{2+} and Fe^{3+}. Charge transfer bands are in general diagnostic in mineralogy. They are stronger by a factor 100 to 1000 than those of crystal fields; thus only in the short wavelengths enough energy is available and consequently the band centres of charge transfer bands occur in the ultraviolet, with wings of the absorption extending into the visible (Figure 4.1). Charge transfer bands are the main causes for the reddish colours of iron oxides and hydroxides (Clark 1999).

In metals and semiconductors the electrons are released entirely from attachment to particular atoms or ions. In metals the valence electrons are essentially equivalent, because they can freely exchange places. The energy levels form a continuum. Thus a metal can absorb radiation at any wavelength (Elachi 1987). In the case of semiconductors there is a splitting of the energy levels into two broad bands with a forbidden gap. The lower energy levels in the valence band are completely occupied. The upper conduction band is usually empty. The semiconductor cannot absorb photons with energy less than the gap energy. If the gap is small, all wavelengths in the visible spectrum can be absorbed (e.g. the dark, metal-like luster of silicon). If the band gap is large, no wavelength in the visible can be absorbed and the material is colourless (e.g. diamond). The conduction band of sulphur and cinnabar extend throughout the NIR, starting at about 0.6 µm. The valence band is located in the UV, only visible for Cinnabar in this example. The band gap of sulphur is located at about 450 nm causing its yellow colour, for cinnabar at 0.59 µm causing a red colour (Figure 4.2). The sharpness of the conduction band is a function of purity and crystallinity of the material.

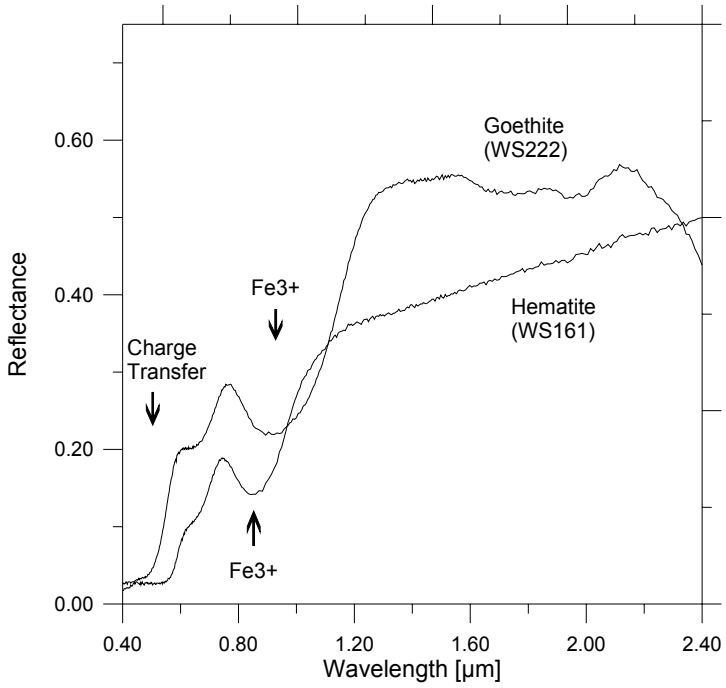

Figure 4.1. Reflectance spectra of the iron oxide hematite (Fe_2O_3) and iron hydroxide goethite (FeOOH) (from Clark et al. 1993). The wing of an intense charge transfer band in the UV is partly visible at wavelengths < 0.5 µm. The Fe^{3+}-absorption at about 1 µm is caused by variable energy splitting within the crystal structure.

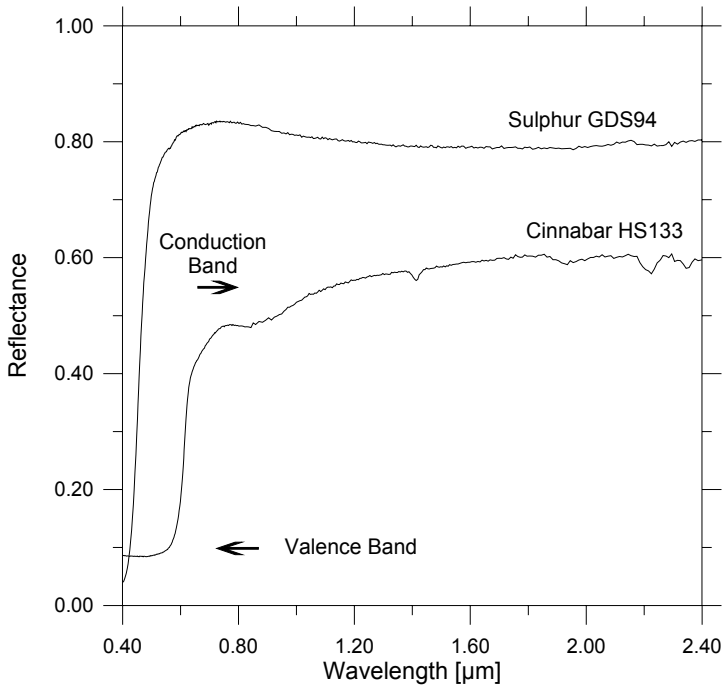

Figure 4.2. Reflectance spectra of sulphur (S) and Cinnabar (HgS) with a conduction band in the visible. The arrows indicate the level of the conduction and the valence band for cinnabar (from Clark et al. 1993).

4.2.2 Vibrational processes

The vibration of molecules consists of very small displacements of atoms from their equilibrium positions. The frequency of vibration depends on the strength of each bond in a molecule and the mass of each element in a molecule. In a molecule composed of N atoms, there are 3N possible modes of motion, because each atom has three degrees of freedom. Of these modes of motion, three constitute of rotation of the molecule as a whole, three constitute translation and 3N – 6 constitute independent types of vibration. Each motion leads to vibration at a classical frequency ν_i. The transitions between the ground state to a state only one energy level higher are called fundamental tones. These usually occur in the mid infrared (> 3µm) (Elachi 1987). Overtones occur when a vibrational mode transits from one energy state to a state more than one energy level above (or below) the original state. Combinations of fundamental and/or overtone transitions are called combination tones, which occur when the energy of an absorbed photon is split between more than one (fundamental and/or overtone) mode (Castellan 1983).

This will be demonstrated for the water molecule (Figure 4.3). It consists of three atoms that produce three fundamentals at ν_1 (symmetrical OH stretch at 3.106 µm), ν_2 (HOH bending 6.08 µm) and ν_3 (OH asymmetric stretch at 2.903 µm). The lowest order overtones correspond to the frequencies $2\nu_1$, $2\nu_2$ and $2\nu_3$ and to the wavelengths $\lambda_1/2$, $\lambda_2/2$ and $\lambda_3/2$. Overtones and combination tones of the fundamental modes occur in the near-infrared at 1.875, 1.454, 1.38, 1.135 und 0.942 µm (Elachi 1987).

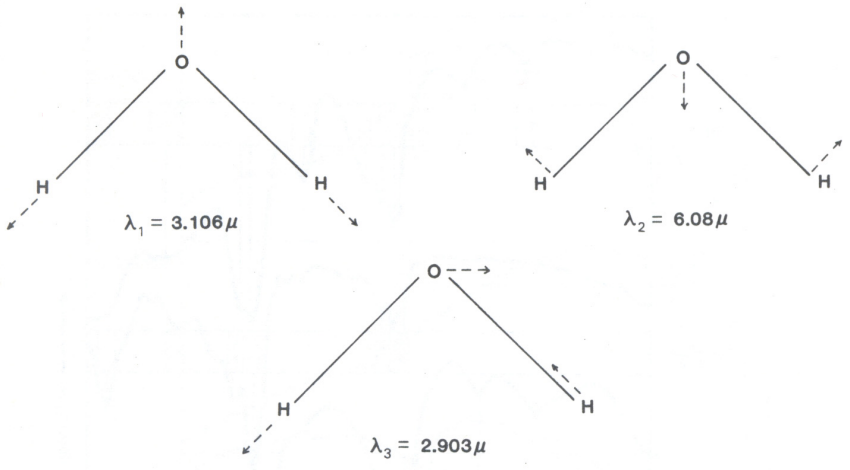

Figure 4.3. Fundamental vibrational modes of the water molecule (from Elachi 1987).

In the SWIR, vibrational features are very narrow and mineral-specific, which allows identification of many minerals. In minerals, OH^-, H_2O and CO_3^{2-} are the main oscillation units for overtones and AlOH, MgOH and FeOH the most important oscillation units for combination tones (Geerken 1991). Three examples of absorptions caused by these oscillation units are given for calcite, gypsum and jarosite in Figure 4.4.

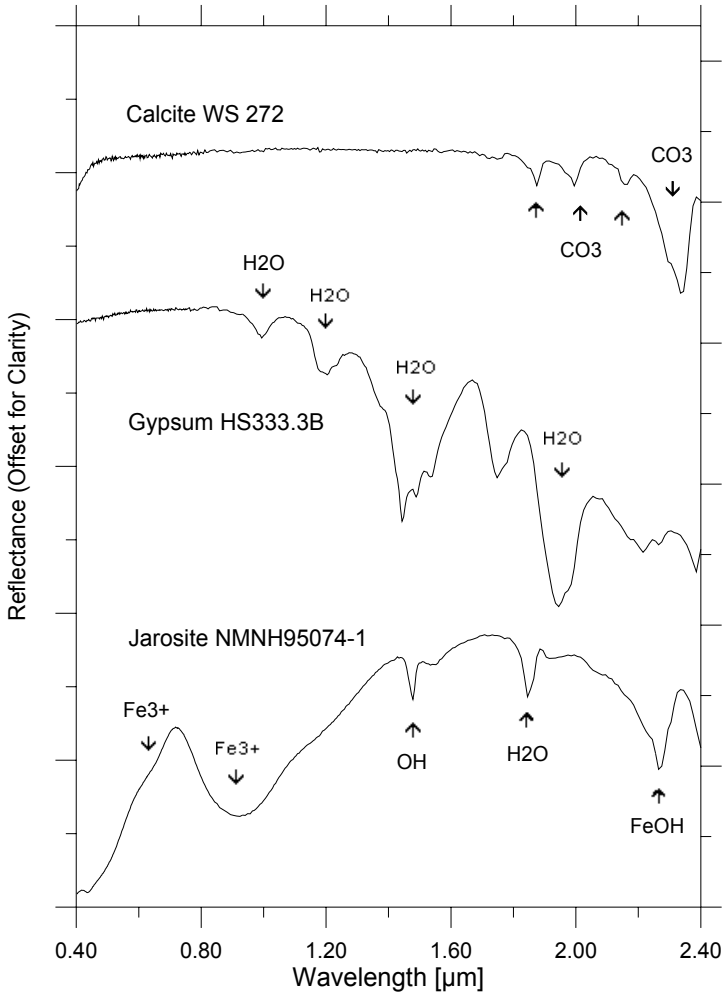

Figure 4.4. Reflectance spectra of calcite, gysum and jarosite, showing vibrational bands due to H_2O, OH, CO_3 (overtones) and FeOH (combination bands) (from Clark et al. 1993)

4.2.3 Scattering processes

Scattering is a key process, which makes reflectance spectroscopy possible. When photons enter a surface they are scattered one or more times. Some are absorbed from the surface and others are scattered from the surface to the sensor (Figure 4.5). However, the scattering processes make the information more complex, because it is basically a non-linear process, which makes the retrieval of quantitative information more difficult (Clark 1999).

Clark & Roush (1984) explained the reflectance of a particulate surface as a random walk. At each grain the photons encounter, a certain percentage is absorbed. If the encountered grain is bright, like a quartz grain, most photons are scattered and the random walk process continues many times. If the encountered grains are dark, like pyrite, the majority of photons are absorbed (the problem of mixtures is discussed in chapter 4.4.3).

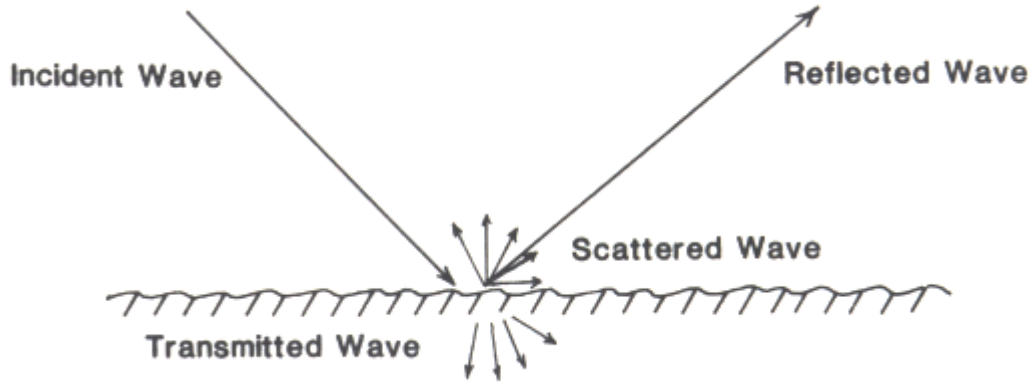

Figure 4.5. Wave interaction at an interface between two materials (from Elachi 1987)

The random walk process of photons scattering in a particulate surface also enhances weak absorption features, because at the wavelength of a weak absorption fewer photons are absorbed with each encounter with a grain, so the random walk process goes further and the greater path length will result in more absorption, thus strengthening the weak absorption in the reflectance spectrum. The amount of light scattered and absorbed by a grain is dependent on the grain size. A larger grain has a greater internal path, where photons may be absorbed. In a smaller grain there are proportionally more surface reflections than internal photon path lengths. If multiple scattering dominates, the reflectance decreases as the grain size increases (Clark & Roush (1984), Hapke (1993).

There have been various attempts to quantify the scattering process. The Kubelka-Munk theory was one of the first and is still used today (e.g. Clark & Roush (1984)). In chemical and food industries the use of absorption described as log(1/R), where R is reflectance, is very widespread (see also chapter 6). However, these approaches are useful only under controlled conditions, e.g. in laboratory. The independent theories of Hapke (1981), Goguen (1981) and Lumme & Bowell (1981) provided reasonable solutions to the complex radiative transfer problem of particulate surfaces. These theories provide for nonisotropic scattering of photons from particles, shadowing between particles and first surface reflection from grain surfaces. The theory of Hapke (1981, 1993) also provides for mixtures and has become the dominant theory in the remote sensing community (Clark 1999). With the Hapke (1981, 1993) reflectance theory and the optical constants of minerals, reflectance spectra of pure minerals at a single grain size, spectra of pure minerals with a grain size distribution and mineral mixtures with varying grain sizes can be computed. Clark & Roush (1984) showed that reflectance spectra could be inverted to derive quantitative information on the abundances and grain sizes of each component. The inversion of reflectance to quantitative abundance have been tested in laboratory mixtures (e.g. Johnson et al. (1992), Mustard & Pieters (1987a)) and some inversion attempts using imaging spectroscopy have been published (e.g. Mustard & Pieters (1987b), Adams et al. 1993).

4.3 Spectral properties of selected materials related to the study

All methodologies used for identification or quantification of materials based on spectral properties require a certain knowledge of the reflectance spectra of pure materials and of common natural mixtures in order to build an appropriate analysis strategy. As reported in chapter 3.2, the environmental risk of metal mining waste is related to the acidification and the associated HMs. However, they are only traceable due to the presence of secondary minerals as oxidation products of pyrite. Hence, the first group of materials described are pyrite and the most important secondary minerals.

The real world is a complex mixture of materials at just about any scale. Also in this study the pyrite was worked into the soil causing a mixture of different soil materials and sludge. Consequently, also soil reflectance will be described. Finally, there is the vegetation, which is in most areas present in more or less high concentrations.

4.3.1 Iron oxides, hydroxides, sulphates and sulphides

Iron oxides and hydroxides are in general very important for remote sensing, because they are ubiquitous and the iron ions tend to substitute other ions like Mg^{2+}, Al^{3+}, Si^{4+} or Mn^{2+} (Geerken 1991). They are of central importance for this study, because the sludge is composed mainly of the iron sulphide mineral pyrite and the secondary products are iron oxides and hydroxides. In the following, some of these minerals will be described with regard to their spectral reflectance and diagnostic absorption features (Figure 4.6).

The pyrite spectrum is an example for a strong conduction band that absorbs over the full spectrum equally strong due to the free electrons in the crystal structure. Jarosite has a narrow absorption at 0.43 µm caused by Fe^{2+}, which appears however sometimes weak due to saturated UV absorption. A weak diagnostic absorption for jarosite at 2.27 µm is due to a combination of OH stretch and Fe-OH bend. Features near 1.475 and 1.8 µm are related to OH and are common for sulphate spectra (Clark 1999). The absorption band at about 0.91 µm is related to Fe^{3+} electronic transitions. Copiapite has similar features as jarosite, like the 0.43 µm feature and the 1.475 µm OH absorption, but without the diagnostic OH stretch and Fe-OH bend at 2.27 µm. Ferrihydrite is characterised by OH/H_2O absorptions near 1.45 and 1.9 µm and the Fe^{3+} absorption centred near 1.0 µm. Goethite (FeO·OH) is one of the most common minerals, typically formed under oxidizing conditions and very often mixed with hematite. Goethite displays trans-opaque behaviour with an absorption edge near 0.55 µm caused by a conduction band. The ferric ion itself produces a wider absorption near 0.9 µm. Unlike other oxides, goethite does not produce any hydroxyl bands in the NIR (Hunt et al. 1971). Hematite (Fe_2O_3) is the anhydrous ferric oxide and has a similar spectral behaviour as goethite in that it displays the transition from opaque to transparent behaviour near 0.55µm. However, it has a narrower absorption near 0.9 µm at a slightly shorter wavelength than goethite (Clark 1999).

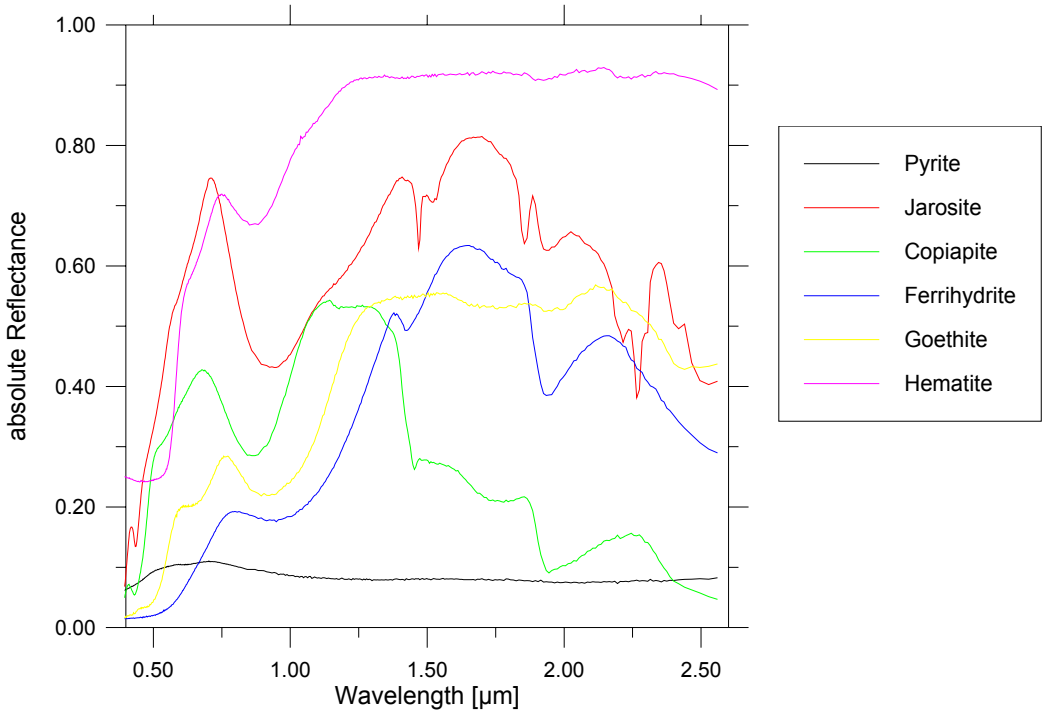

Figure 4.6. Spectra of iron oxide, iron hydroxide, iron sulphate and sulphide minerals related to pyrite oxidation (from Clark et al. 1993)

4.3.2 Soils

The spectral reflectance of soils is a combination of the spectral reflectance of its constituents. As such soil reflectance may be very variable depending on compositional factors such as mineralogy, organic matter, iron, water or salinity. Stoner and Baumgardner (1981) studied the spectral reflectance of 485 soil samples mainly from the U.S. They identified five characteristic curve shapes on the basis of visual inspection (Figure 4.7). Each shape is associated with certain soil characteristics. The classes are: organic dominated (organic carbon > 2%, iron oxide < 1%, fine texture), minimally altered (organic carbon < 2%, iron oxide < 1%), iron affected (organic carbon > 2%, iron oxide 1–4%), organic affected (organic carbon > 2%, iron oxide < 1%), iron dominated (iron oxides > 4%). More detailed information about reflectance of soils is found in the reviews of Baumgardner et al. (1985), Irons et al. (1989) and Ben-Dor et al. (1999).

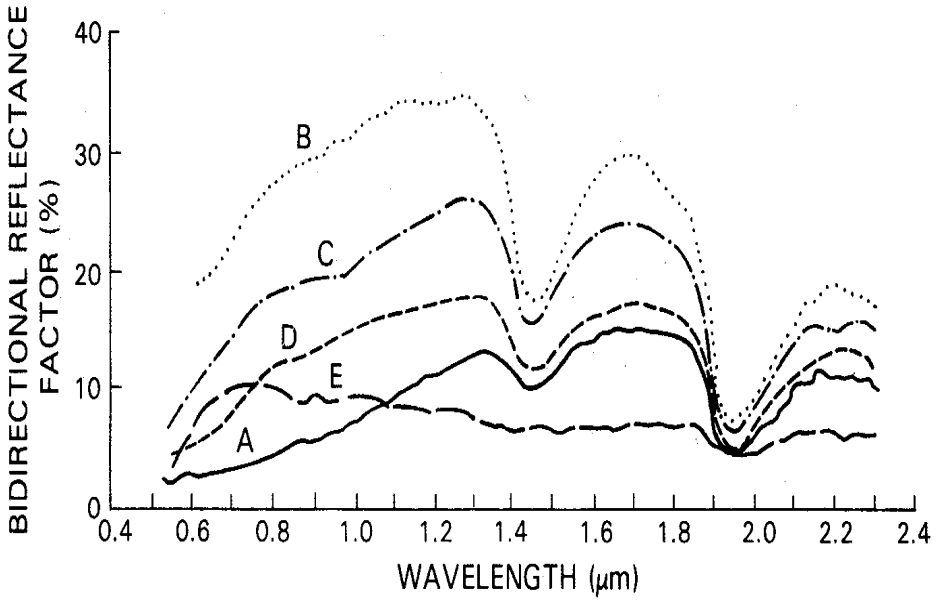

Figure 4.7. Reflectance spectra of mineral soils representing different soil characteristics: organic dominated (A), minimally altered (B), iron affected (C), organic affected (D) and iron dominated (E) (from Stoner & Baumgardner 1981)

4.3.3 Vegetation

Most remote sensing land applications have to consider the spectral reflectance of vegetation even if it is not the focus of the study, because vegetation is quasi omnipresent on the land surface. Spectra of vegetation have two general forms: green photosynthetic active or dry non-photosynthetic; between these two extremes exists a continuous range. Although the albedo may vary, the general shape of reflectance curves for green leaves is similar for all leaves, because all plants are made of the same basic components (Gates et al. 1965). Figure 4.8 shows spectra of green and dry vegetation. Foliar absorptions are caused primarily by photosynthetic pigments (mainly chlorophyll) in the visible spectrum below 1 μm and water, cellulose, and other carbon-based compounds in the infrared. Water dominates the leaf absorption in the NIR region; major water absorptions appear at 1.45 and 1.94 μm with secondary features at 0.96, 1.12, 1.54 and 2.2 μm (Knipling 1970, Weyer 1985). Dry vegetation is characterised by absorptions of cellulose (1.7, 1.77, 2.09, 2.227, 2.34 μm), lignin (1.7, 1.74, 2.13, 2.227 μm), tannin (1.65 μm) in the SWIR (Elvidge 1990). These features must also be present in green vegetation but they are masked by the stronger water absorptions.

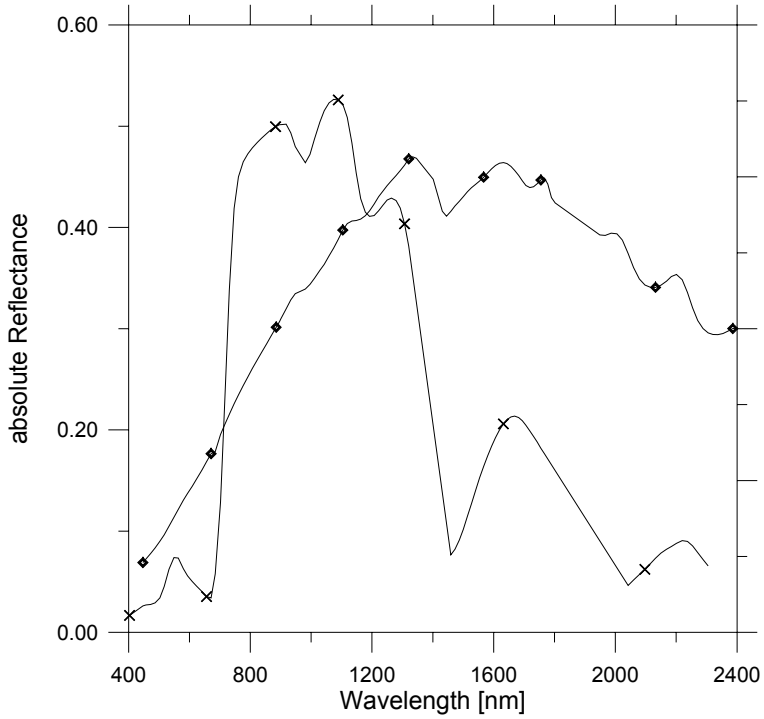

Figure 4.8. Typical spectra of photosynthetic active vegetation (×) and non-photosynthetic dry vegetation (◊)

4.4 Use of imaging spectroscopy

Supported by laboratory measurements and airborne campaigns, the relevance of imaging spectroscopy for the extraction of distinct spectral features contained in multi-spectral remotely sensed data sets has become apparent. The ability to acquire narrow-band spectra gives remote sensing more detailed information about the environment compared with broadband sensors (Rast 1991). As reported previously, most natural Earth surface materials have diagnostic absorption features in the 0.4 – 2.5 µm range of the reflected spectrum. Since the diagnostic features for each material are apparent over very narrow spectral bands, differences between materials can only be identified if the spectrum is sampled at a sufficiently high resolution. Imaging spectrometers have been recently developed as a new generation of airborne optical remote sensing systems specifically designed to acquire this hyperspectral information. Today, imaging spectrometry is widely used in environmental research (Hill & Megier 1992). In order to analyse imaging spectroscopy data in a proper way, the technical principles and the implications, which are arising when analysing imaging spectroscopy data, are discussed in this section.

4.4.1 Principle of imaging spectroscopy

Imaging spectroscopy for remote sensing involves the acquisition of image data in many contiguous spectral bands with an ultimate goal of producing laboratory quality reflectance spectra for each pixel in an image (Figure 4.9) (Goetz 1992b).

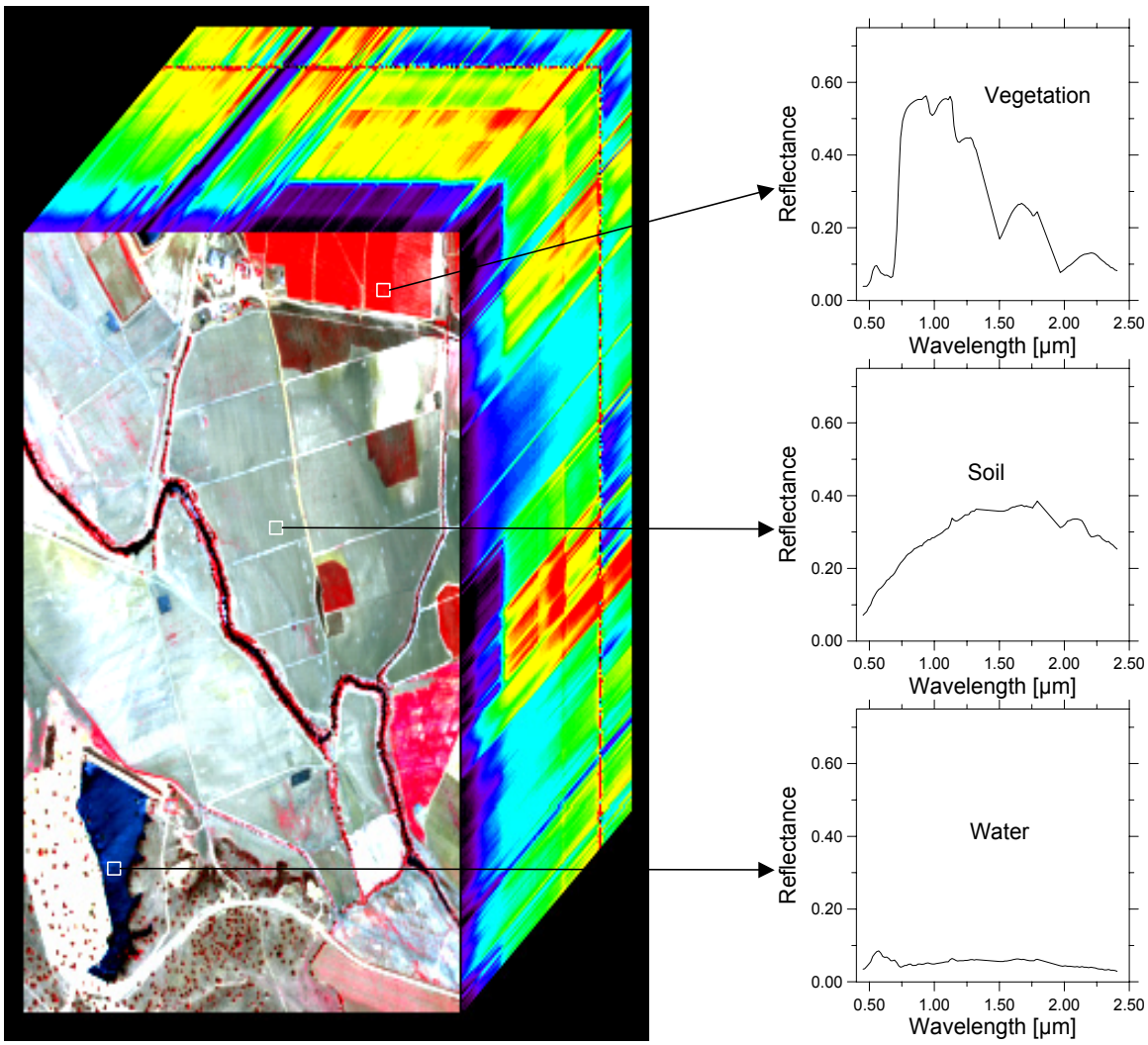

Figure 4.9. HyMap image data cube. Spatial data (x and y axes) represented as a three-band colour composite (R= band 25, G= band 17, B= band 9). The spectral data is represented by the z-axis in pseudocolour (rainbow) showing the first 64 out of 128 bands. Spectra on the right show extracted spectra from the data cube.

Imaging spectrometers were preceded by broadband multispectral sensors like Landsat MSS and TM or SPOT. These sensors with less than ten bands allow a mapping of surface materials only based on statistical classification techniques. The advances of technology led to the development of portable field spectrometers, which were initially used to verify and correct observations made with broadband sensors, and to establish

reference spectral databases. The first airborne spectrometer was built in the late seventies by Geophysical Environmental Research Company (GER, USA) as a profiling instrument with 500 bands but only a single scan line (Chiu & Collins 1978). The first airborne imaging spectrometer was developed in the early eighties by NASA's Jet Propulsion Laboratory (JPL). The Airborne Imaging Spectrometer (AIS) acquired data in 128 bands in the NIR between 0.9 and 2.4 µm in either 'tree' mode (0.9 – 2.1 µm) or 'rock' mode (1.2 – 2.4 µm) with a field of view of 3.7 ° (Goetz et al. 1985). In 1983, JPL started the construction of a new sensor; the Airborne Visible/Infrared Imaging Spectrometer (AVIRIS), is continuously in use since 1987. AVIRIS measures radiance through 224 contiguous spectral channels of 10 nm intervals across the spectrum from 0.4 to 2.4 µm (Green et al. 1998). With its high signal-to-noise ratio and its contiguous bandwidth of 10 nm it is still one of the best imaging spectrometers, although in the meantime a large number of imaging spectrometers is available (see Kramer (1994) for a list of available sensors).

4.4.2 Atmospheric interactions

When moving out of the laboratory, the most evident change is the illumination. The sun is the most important radiation source for most remote sensing applications and field spectroscopy measurements in the visible and infrared part of the spectrum. The radiation emitted at a temperature of 6000 K is measured with 1370 Watts/m² at top of the atmosphere and it is relatively stable. When passing the atmosphere a part of the solar energy is absorbed at specific wavelengths by atmospheric gases or scattered by molecules and aerosols. Strong absorptions are caused by atmospheric water vapour (at 0.95, 1.12, 1.4 and 1.9 µm), carbon dioxide (2.01 and 2.06 µm) and oxygen (0.76 µm) (Figure 4.10).

The atmospheric absorptions limit the use of optical remote sensing systems to relatively small transmission windows (Figure 4.11). With the available optical sensor techniques the spectral ranges 0.4 to 2.5 µm and 8 to 12 µm are used. However, the bandwidths in the range 8 to 12 µm (thermal range) are usually too wide for direct material identification due to the small amount of energy available. However, it has been shown that also in the wavelength range between 0.4 and 2.5 µm spectral diagnostic absorptions occur, which allow an identification of minerals and biochemical components of plants (Goetz 1992a).

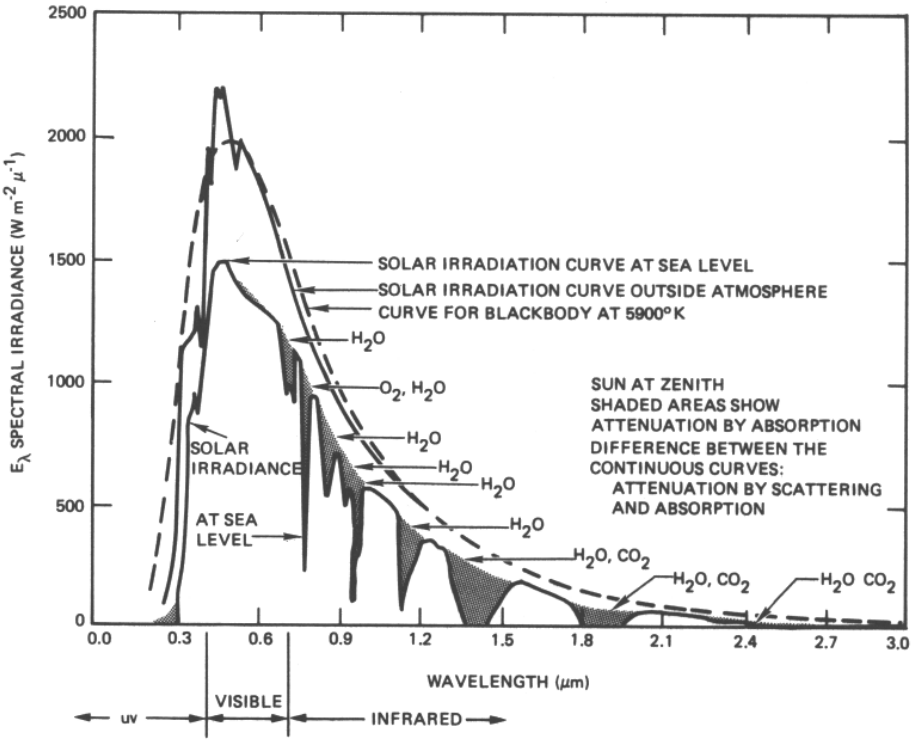

Figure 4.10. Solar radiation at top of atmosphere and on earth surface after selective absorption and scattering (from Elachi 1987)

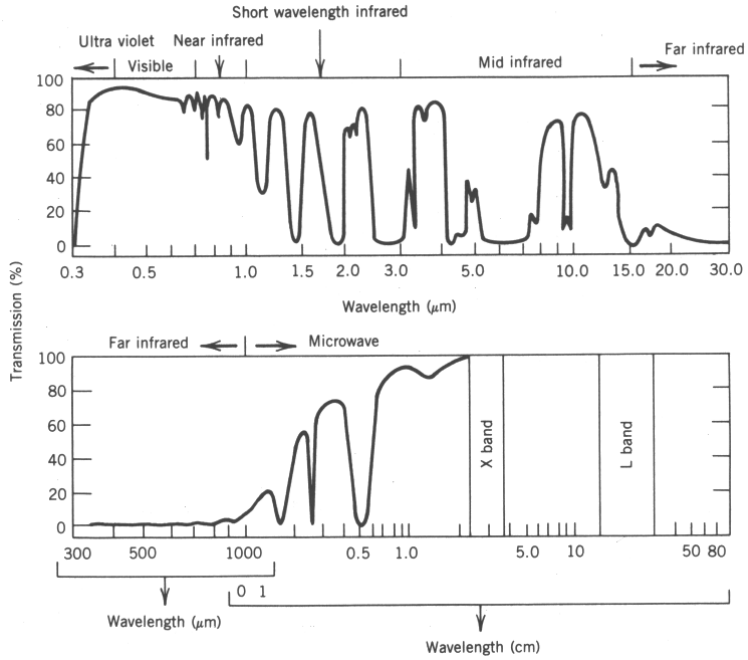

Figure 4.11. Transmission windows of the atmosphere (from Elachi 1987)

Figure 4.12 describes the interactions of incoming solar radiation and radiation reflected from the target with the atmosphere. Due to the absorption and scattering only a part of the direct solar radiation (50 – 80 %) arrives at the earth surface (1). The target is additionally illuminated by diffused solar radiation (skylight, 2), and, to a smaller extend, by already ground-reflected light that is again reflected back by aerosols in the lower atmosphere (3). The radiation measured at the sensor is a combination of target reflectance (4), path radiance (5) and radiance contributions from the environment of the target (6), which enter the field of view due to secondary scattering effects in the lower atmosphere (Hill 1993).

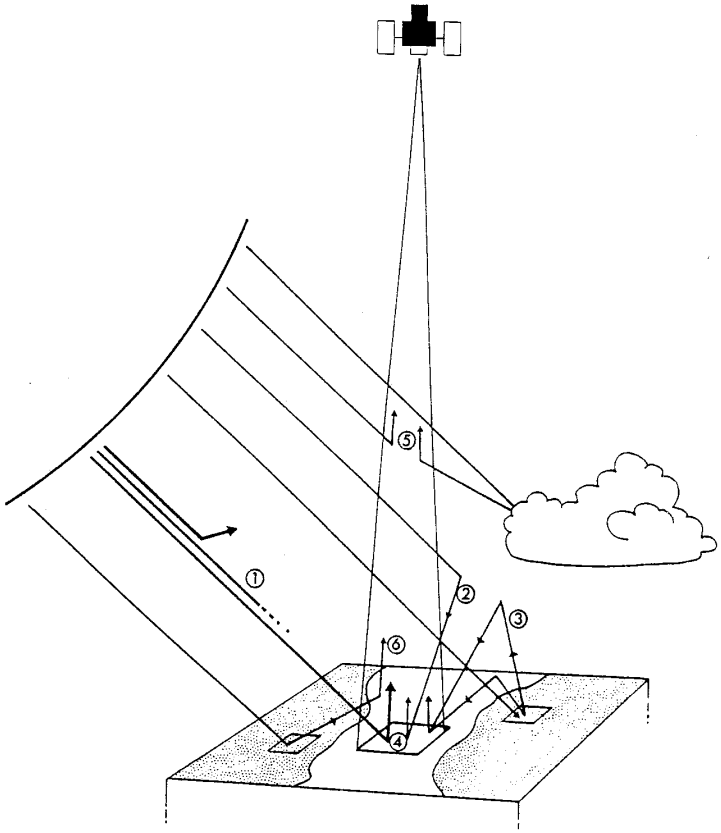

Figure 4.12. Interactions of incoming solar radiation with the atmosphere and contamination of radiance measured at the sensor (from Tanré et al. 1995)

The described atmospheric effects have to be corrected in order to retrieve the real surface reflectance. This is achieved for ground-based field measurements using a calibrated reference surface, which is measured under the same illumination conditions than the target and with which the target reflectance is estimated through division by the reference reflectance (see Eq. 4.4). Field measurements can be used for spectra derived with airborne instruments to apply the regression-based empirical line method described e.g. by Roberts et al. (1985) or Farrand et al. (1994). More complex radiative transfer

models try to describe the mentioned interactions of radiation with the atmosphere on its way from the source to the target and from the target to the sensor (e.g. Tanré et al. 1990, Vermote et al. 1997). They have been applied successful to data of satellite and airborne sensors (e.g. Hill 1993, Staenz & Williams 1997, Richter & Schläpfer 2001).

4.4.3 Extraction of semi quantitative information on a sub-pixel level

Spatial mixing of materials within the field of view (FOV) of a sensor down to the depth of penetration of the photons is the cause of spectral mixing. The concept of mixed pixel has been recognised for many years (e.g. Horwitz et al. 1975, Nash & Conel 1974), but the idea that mixing at a subpixel scale is a natural consequence of earth processes and an inherent feature of remote sensing data sets that can be exploited quantitatively has evolved only in the last two decades (e.g. Adams et al.1986, Smith et al. 1990; Thomson and Salisbury 1993; Hill et al. 1995, Roberts et al. 1998).

The basic premise of mixture modelling is that within a given field of view (FOV), the surface is dominated by a small number of materials, so called endmembers (EM), that have relatively constant spectral properties. Nash & Conel (1974) showed that the reflectance spectrum of a mixture is a systematic combination of the components of the mixture. The systematics is basically linear if the components are arranged in spatially distinct patterns, analogous to those of a checkerboard (Figure 4.13) (Singer & McCord 1979). In this case the scattering and absorption of electromagnetic radiation is dominated by a single component on the surface, and thus the spectrum of a mixed pixel is a linear combination of the EM spectra weighted by the areal coverage of each EM in the pixel (Mustard & Sunshine 1999). If, however, the components of interest are in an intimate mixture, like mineral grains in a soil or rock, the mixing systematics between the different components are non linear. The spectral properties of the different EMs become involved in this case, because the electromagnetic radiation interacts with more than one EM as it is multiply scattered in the surface. In an intimate mixture, the darker material dominates because photons are absorbed when they encounter a dark grain (Clark 1999). An example for an intimate mixture is the artificial mixture series, which is described in the chapter 6.2 and analysed later in chapter 8.1.

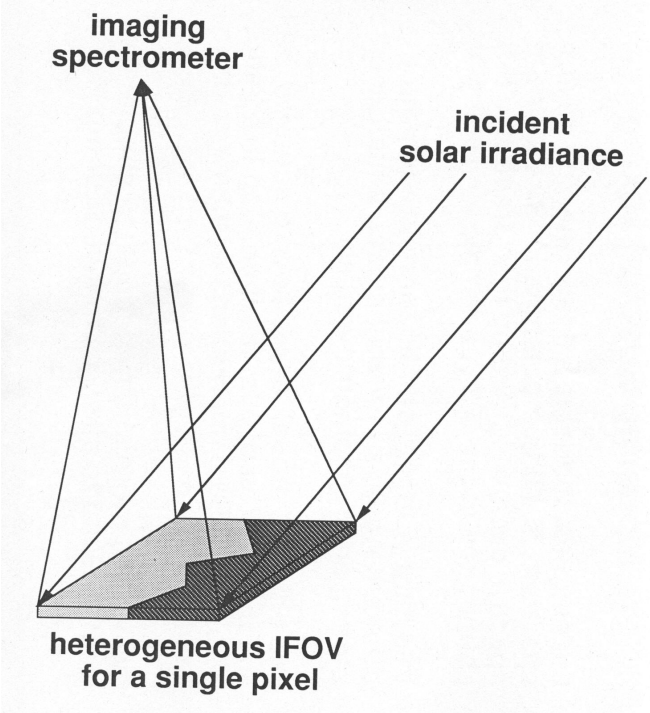

Figure 4.13. Spectral mixing is a consequence of integration of reflected radiation from a spatially mixed IFOV.

4.5 Summary

Reflectance spectroscopy can be used to derive significant information about materials with little or no sample preparation, because electromagnetic radiation reacts with the molecules of the materials causing specific absorption features in the reflectance spectrum. This principle works in the laboratory, in the field and even for airborne or spaceborne spectrometers. However, only for laboratory measurements controlled measurement conditions can be assumed. When measuring in the field or from an airborne system, the illumination of target by the sun is modified by the atmosphere. Moreover, the area over which the spectrum is integrated, is much more inhomogeneous causing mixtures of different materials in the field of view. Nevertheless it is possible to account for most of these modifications. Therefore spectroscopy is an excellent tool for all materials that exhibit distinct absorption features. Among these are iron oxides, iron hydroxides and sulphates, which are of central importance for the identification of residual contamination after the Aznalcóllar mining accident.

5 Data acquisition and availability

This work is based on a number of different digital and analogue data sets, which were collected during fieldwork or provided by the Consejería de Medio Ambiente.
In order to be able to develop models for the estimation of the quantitative composition of soils by means of reflectance spectroscopy, it is indispensable to have a large, meaningful reference data set that allows a profound statistical analysis. Hence, data were acquired during two intensive field campaigns in May/June 1999 and June/July 2000. Apart from the soil sampling, also spectral measurements with portable spectroradiometers were performed for a spectral characterisation of the area and for providing in-flight ground calibration data for the airborne flight campaigns, which took place at the same time.

This chapter describes the data sets acquired for and used in this thesis and describes the fundamental pre-processing steps, which are a prerequisite for later data analysis.

5.1 General data availability

The Consejería de Medio Ambiente, as one of the key actors in the management of the remediation, provided several data sets for this work (Figure 5.1). This data was used in the pre-processing of the imaging spectroscopy data and in the analysis of obtained results.

The digital terrain model (DTM) has a pixel resolution of 20 × 20 m². It was derived from elevation lines, which were converted into area-wide raster data. The digital elevation data are necessary for the geometric and radiometric correction of the imaging spectrometer data. The digital raster maps in 1:10.000 and 1:50.000 scales were used for the collection of ground control points for the geometric correction of the images.

Directly after the accident, an assessment of the extent of the sludge contamination was made. The resulting vector layer with the initial sludge contamination (volume, average, minimum and maximum thickness) was used for evaluation of the spatial results obtained with imaging spectroscopy data. Further vector layers included the major roads, villages and the borders of the green corridor.

The University of Granada performed a soil sampling and analysis campaign after the first clean up in order to assess the residual contamination. The 676 sampling points were chosen from a regular 400 × 400 m² grid. At each point five samples were taken from the corners and the centre of a 10 × 10 m² rectangle. The samples were taken with an auger from 0 to 10 cm depth and then analysed as a single sample (Consejería de Medio Ambiente 2001).

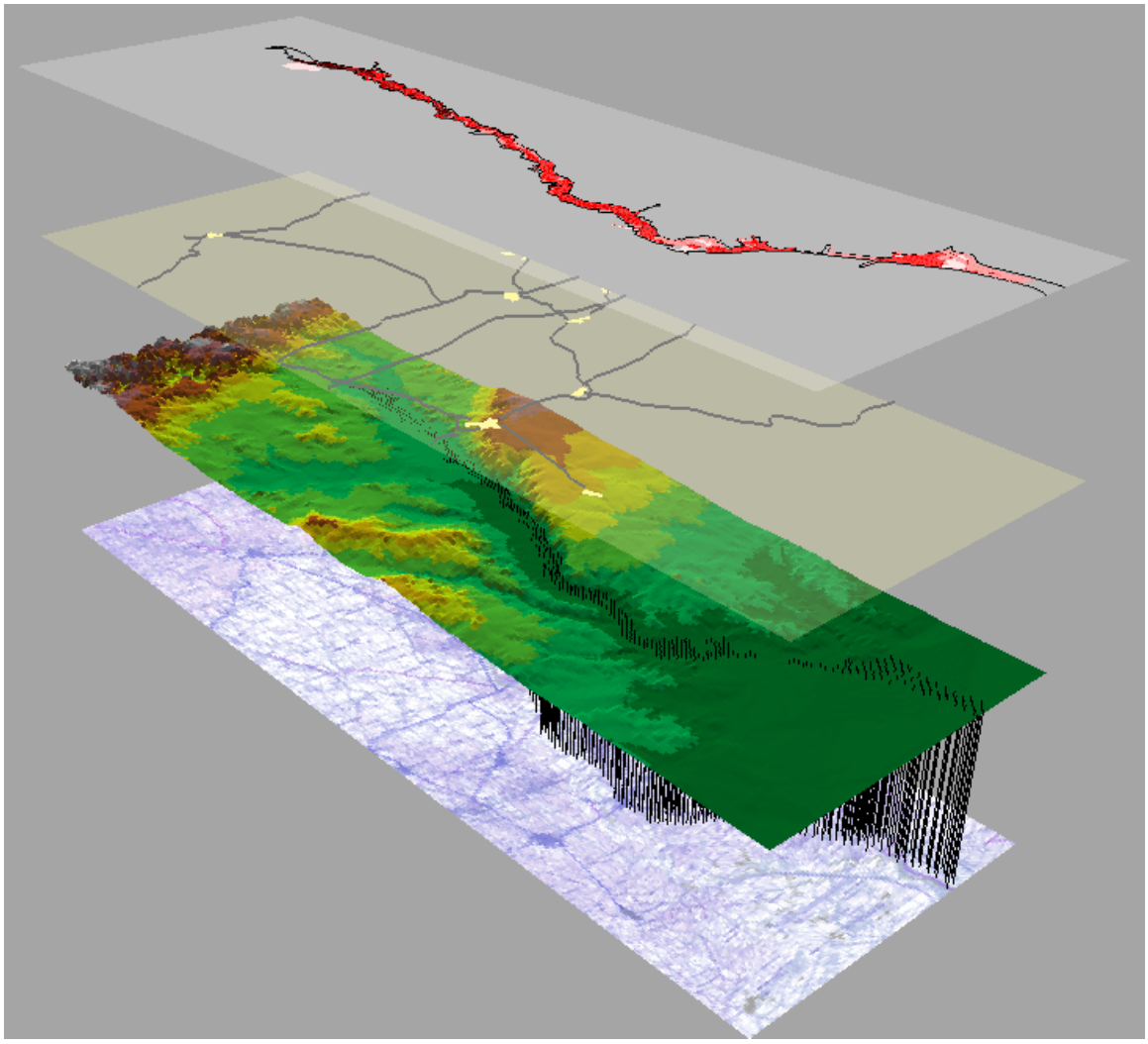

Figure 5.1. Data sets provided by Consejería de Mediombiente of the Junta de Andalucía. Base layer: raster maps 1:50.000; 2nd layer: digital terrain model with soil sampling points; 3rd layer: mayor roads and villages; 4th layer: distribution of sludge before remediation and borders of the green corridor.

5.2 Field data collection

5.2.1 Soil sampling

In the affected area, a total of seven test sites were selected for a detailed soil sampling. These sites were selected in such a way that they represent a broad range of both contamination levels and background soils. If possible, they were chosen in zones, where soil sampling had already taken place by other research groups (Figure 5.3). This could help in an interpretation of our own results, since the other measurements were taken before the remediation campaign (Cabrera et al. 1999, Simón et al. 1999, Simón

et al. 2001). Out of the six sites three are in the northern part (Mine North & South, Sobarbina), the remaining sites are located in the central and southern part. At the 'Las Doblas' site samples were only taken in 1999 and at Entremuros only in 2000. At each site, sampling transects, consisting of five to twelve points, were selected following possible contamination gradients. If possible, also areas that were not contaminated were included in the transects. Detailed maps of each sampling location are shown in Figure 5.2 and in Annex A. At each point, soil samples were taken at four different levels (0-2, 2-20, 20-40, 40-60 cm) (Figure 5.2). The surface samples were collected with a hoe from an area of approx. 50 × 50 cm². The lower horizons were sampled with an auger; 20 cm cores were used as sample material. Each sample was mixed and divided into two sub-samples. One was used for spectroscopic measurements, the other one for characterisation of soil chemical properties.

The location of each sampling point was marked using a differential global positioning system (Trimble Geoexplorer3®). This allowed a mapping of the sampling points in the hyperspectral images and for the sampling in the second year, which, if possible, was carried out on the same spots. However, in two areas it was not possible to sample due to a dense vegetation cover. It would have been possible to take soil samples, but not to make field measurements of the soil surfaces. At the Vado de Quemas site, new sampling points were selected in the vicinity. The Las Doblas site was irrecoverable and therefore a new site was established at the Entremuros site.

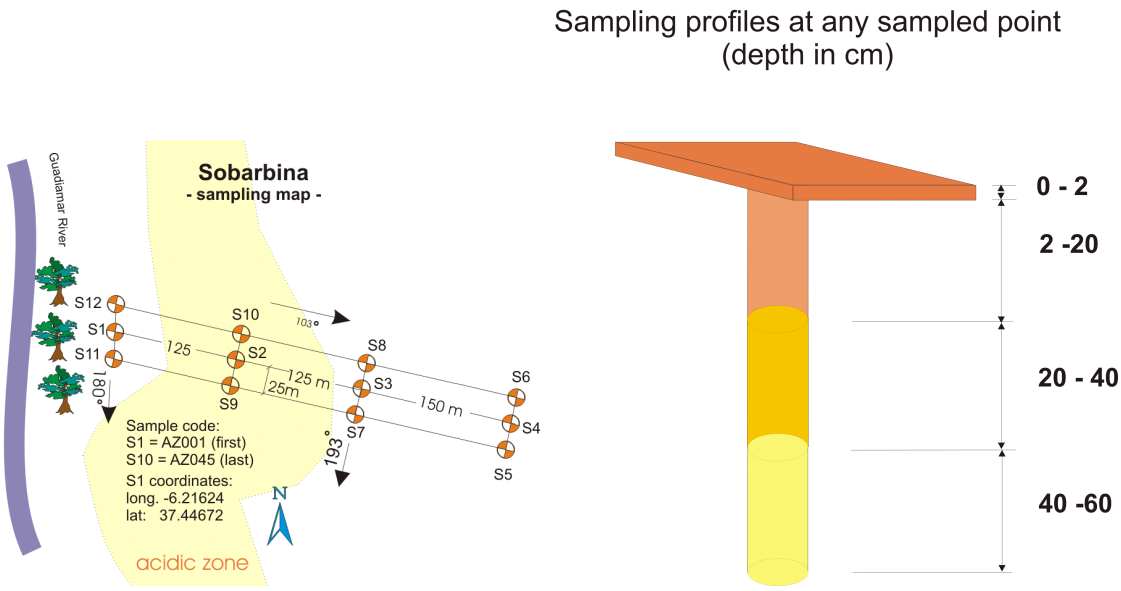

Figure 5.2. Soil sample map example from Sobarbina site (left). Soil sampling depth profile (right)

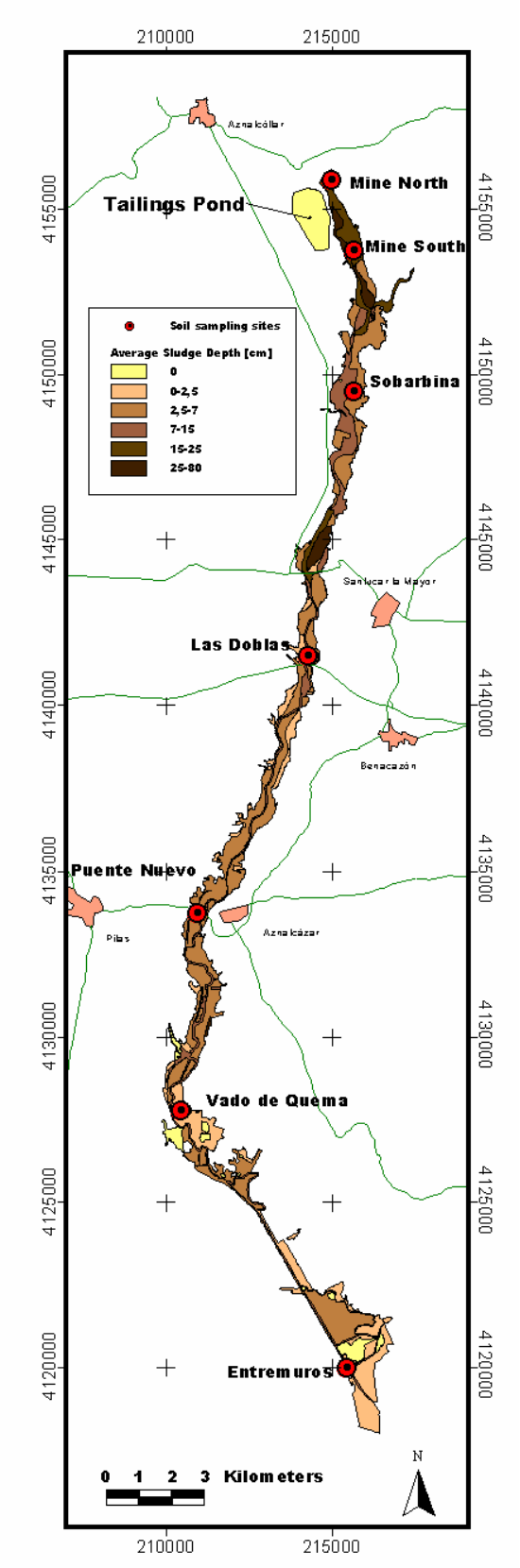

Figure 5.3. Soil sampling sites with sludge affected area (average sludge depth deposited after the accident from Consejería de Medio Ambiente 1999)

5.2.2 Field spectrometry

Two different spectroradiometers were used for the field measurements, the GER S-IRIS® in 1999 and the ASD FieldSpec FR® in 2000. The Single-field-of-view InfraRed Intelligent Spectroradiometer covers a spectral range from 370-3000 nm with 900 bands and a bandwidth between 1.3 and 4.8 nm. It is an opto-mechanical scanner with three dispersing gratings and a filter wheel across silicon and PbS detectors (Geophysical & Environmental Research Corp. 1993). ASD FieldSpec FR® is a portable spectroradiometer designed for field use with a sampling interval of 2 nm and a spectral resolution of 10 nm. It covers a spectral range from 350 to 2500 nm. The spectrometer has a line array of Si-photo-diodes in the VIS and NIR (350 to 1000 nm); the SWIR part is measured with two spectrometers with InGaAs detectors (Analytical Spectral Devices 1999). In the field, reflectance was measured relative to a sprayed $BaSO_4$ panel or to Spectralon®.

The field measurements were made mainly with the sun as the illumination source. In 2000, also the ASD High Intensity Reflectance Probe® was used, if the atmospheric conditions did not allow measurements with sun illumination. The ASD High Intensity Reflectance Probe® is designed for measuring small surfaces of not more than 60 mm with a built in light source (Analytical Spectral Devices 1999).

The purpose of the field measurements was the spectral measurements of the soil surfaces at the sampling points, a spectral characterisation of dominant surfaces in the entire area and in-flight calibration measurements for the correction of the hyperspectral images.

Apart from the measurements at the soil sampling sites (Figure 5.3), about 30 additional spectral measurement sites were selected based on their physiographic characteristics and their spectral variability. The description of the sites included exact locations using differential GPS, characterisation of the environment (geology, pedology, landcover), visual documentation (digital camera), information on conditions on the day of the site visit (weather, phenology, soil moisture), and spectral measurements of the spectrally dominant surfaces. The spectra measured at these sites were compiled to a spectral library. The in-flight calibration measurements were performed on spatial and spectral homogeneous sites of a size that covered several pixels in the hyperspectral images. In 1999, three areas in the northern part and in 2000 two areas in the southern part were selected. The field spectra were pre-processed to correct for influences imposed by systematic errors rather than material immanent changes in spectral reflectance. Furthermore, the spectra were transformed into absolute reflectance.

5.3 Imaging spectroscopy data acquisition

5.3.1 Sensor description

The data used in this thesis was collected with the HyMap Sensor. HyMap is a highly flexible airborne hyperspectral scanner. The system provides 128 wavebands over the range 403 – 2480 nm with a spectral resolution of 13 – 17 nm. Signal to noise ratio is quoted at 500:1 with spectral calibration precision similar to AVIRIS. Band to band registration is within $1/10^{th}$ of a pixel. The instrument is optimised for operating at a spatial resolution of 5 m, with a 2.3 km swath width; the spatial resolution can be improved to 3 m (approx. 1.3km swath), though this may be at the expense of signal to noise at SWIR wavelengths. The acquisition of 5 m resolution data is recommended, in order to maximise spectral data quality (Cocks et al. 1998). Spectral coverage is contiguous, except for the atmospheric water bands near 1.4 µm and 1.9 µm. Each module acquires 32 bands (Table 5.1).

Table 5.1. HyMap spectral specifications for 1999

Module	Spectral Range	Bandwidth Across Module	Average Spectral Sampling
VIS	0.40 - 0.89 µm	15 -16 nm	15 nm
NIR	0.89 - 1.35 µm	15 - 16 nm	15 nm
SWIR1	1.40 - 1.80 µm	15 - 16 nm	13 nm
SWIR2	1.95 - 2.48 µm	18 - 20 nm	17 nm

In 2000 the sensor was set up slightly different with only 126 bands and somewhat shifted band centres. Detailed information about spectral configuration of both years can be found in Annex B.

5.3.2 Data set description

The HyMap data were acquired on behalf of the JRC performed by DLR in parallel to the soil sampling campaigns. In order to cover the entire affected area (see Figure 5.3), it was necessary to record five flight strips, which were arranged in form of a ‘Z’ (Figure 5.4). Table 5.2 summarizes the flight dates, times and altitude. The weather conditions were excellent on both flight dates and the sensor worked properly. However, in 2000 the data recording was stopped too early, so that the calibration site in the Southern end of the flight strip and the nearby soil-sampling site were not recorded.

Table 5.2. Flight dates, time and altitude for 1999 and 2000

	1999	2000
Date	05.06.1999	28.06.2000
Time (UTC)	12:45 to 13:38	11:50 to 12:54
Altitude [m above ground]	3200	3350

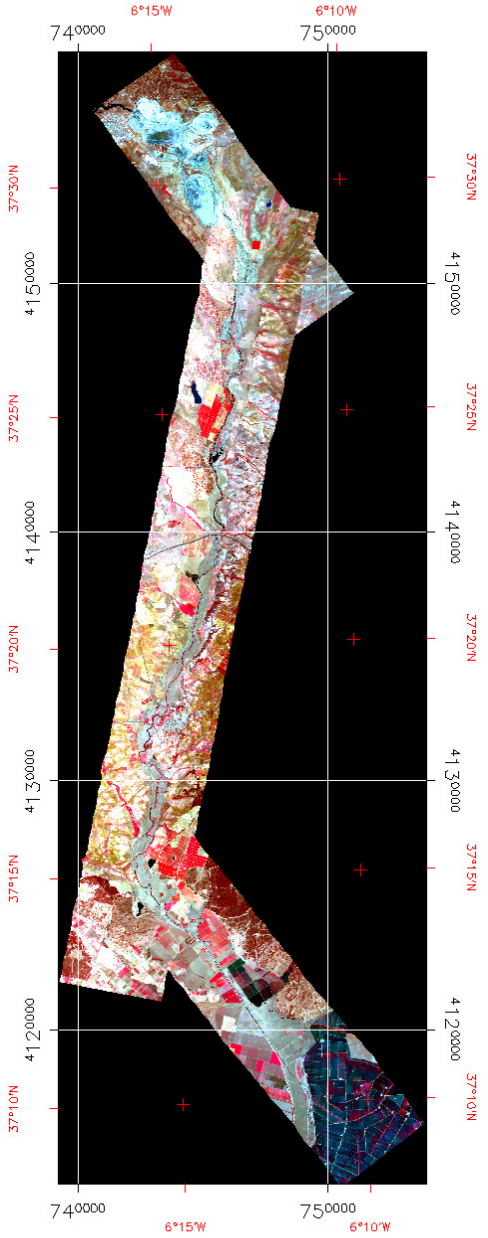

Figure 5.4. Georectified HyMap false colour composite (R = band41 (1.011 µm), G = band17 (0.671 µm), B = band9 (0.549 µm)) showing the full flightline

5.3.3 Data preprocessing

Geometric and radiometric effects account for main distortions present in imaging spectroscopy data and need to be corrected to allow a physics based image analysis.

The HyMap sensor is a scanning airborne system. The stability of such systems is much worse than that of spaceborne satellites. Geometric distortions occur due to variations of the flightpath as well as of attitude (given by roll, pitch and heading angles) of the airplane. These distortions cannot be corrected simply by traditional ground control point based georeferencing, because the movements of the airplane cannot be approximated satisfactorily by polynomial transformations of the image. A pixel-by-pixel transformation has to be performed instead, to account for the position and attitude of the plane during the scanning process (Schlaepfer et al. 1998).

The geometric correction, which was applied in this study, is based on a fully parametric orthorectification. The parametric geocoding procedure (Parge) strictly takes into account the aircraft and terrain geometry and uses a forward transformation algorithm to create orthorectified imaging spectrometry cubes (Schlaepfer & Richter 2001). The parametric geocoding requires a variety of input data, which include navigation data, which consist of position data (longitude, latitude, height) and attitude data (roll, pitch, heading) for each scan line, a digital terrain model (DTM) and general sensor information. A ground control point based procedure is used to recalibrate the offsets of the attitude data, which are given in relative angles. Combining this information, Parge exactly reconstructs the scanning geometry for each image pixel with accuracies down to one or two pixels, depending on the available input data.

The radiometric data (Digital Numbers, DN) acquired by the sensor cannot be directly linked to the radiance or reflectance of the field and laboratory measurements. In fact, the signal measured by the sensor is composed of sensor specific characteristics, effects related to the acquisition date and constellation (i.e. illumination, observation geometry, atmospheric phenomena and topographic variations) and target reflectance characteristics (Hill, 1993). Therefore, several steps are necessary in order to correct radiometric distortions of hyperspectral images:

- Sensor calibration
- Atmospheric correction
- Topographic correction with digital elevation model

In case of the HyMap sensor is radiometric calibration is not necessary, because the data are delivered already calibrated to at sensor radiance (Cocks et al. 1998).

The influence of the atmosphere on the radiance measured at the sensor has been described in chapter 4.4.2. The components that have to be taken into account are path radiance (radiation scattered by the atmosphere), reflected radiation from the viewed pixel, adjacency radiation (ground reflected from the neighbourhood into the view direction) and terrain radiation reflected to the pixel.

The radiometric correction is based on the geocoded, orthorectified image, which is obtained by the georectification described above. From this output the scan and azimuth angles are obtained. Then a combined atmospheric/topographic correction is performed with a database of look-up tables of atmospheric correction functions (path radiance, atmospheric transmittance, direct and diffuse solar flux) calculated with a radiative transfer code, which is based on MODTRAN4 (Berk et al. 1989). Additionally the terrain shape obtained from a digital elevation model is taken into account. (Richter & Schlaepfer 2001).

The data used in this study were delivered by DLR radiometrically and geometrically corrected, because at DLR the corrections are synchronised in a tool, which combines the two independent procedures for geometric and atmospheric processing. It is optimised with regard to specific characteristics of airborne imaging spectrometry data. A detailed description of the two procedures is found in Schlaepfer & Richter (2001) and Richter & Schlaepfer (2001).

The results of the atmospheric correction are shown in Figure 5.5 for two calibration sites used in 1999. The first pair of spectra matches well, some problems due to atmospheric interference occur at the 1.4 µm water absorption. In the NIR, (1.5 to 1.9 µm) some differences can be observed in overall albedo. The second pair exhibits the same water absorption features than the first pair. However, the image spectrum shows also absorptions at 0.9 and 1.1 µm, which can be also attributed to water absorptions of the atmosphere. The two examples show that it is still very difficult to account for all influences particularly when atmospheric conditions are changing within a scene.

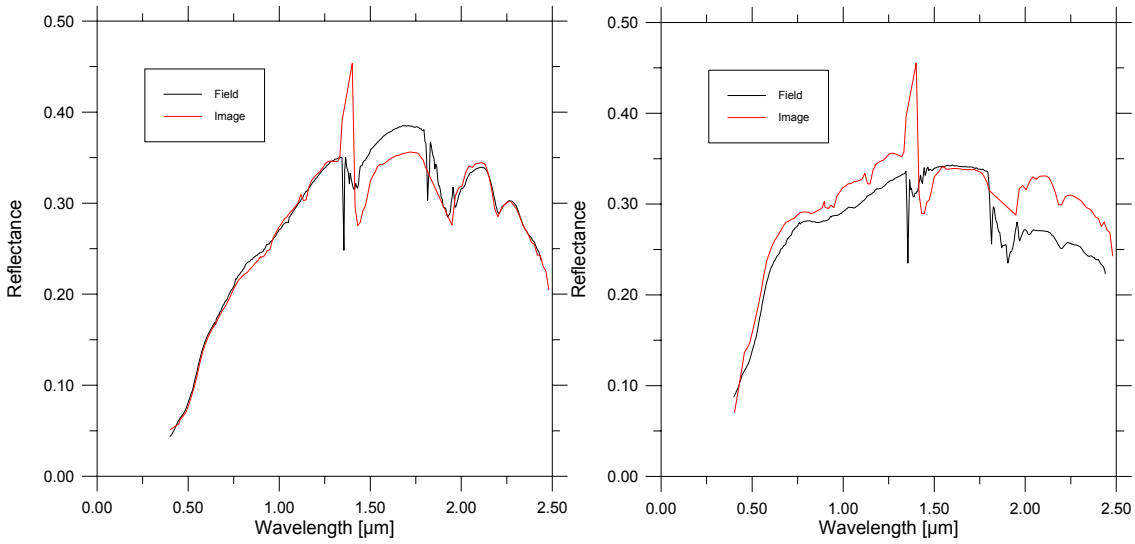

Figure 5.5. Comparison of averaged calibration measurements and averaged image spectra for two sites in 1999

5.4 Laboratory analysis

5.4.1 Laboratory spectrometry

The spectral reflectance of the collected soil samples was measured after they were dried at room temperature with an ASD FieldSpec FR®. Illumination was provided with ASD High Intensity Reflectance Probe® or with UNOMAT LX 801S- CP® Videolamp. Spectralon® was used as white standard. For the bidirectional measurements with the video lamp the illumination angle was 30º and the observation angle was 0º (vertical observation geometry). The distance lamp–sample was 30 cm, the distance sensor–sample 25 cm. In combination with an apex angle of 25º, it results in a circle of approx. 11 cm in diameter. The measurement setup was constructed in such a way that disturbing effects were limited. The samples were measured four times with a different field-of-view; each measurement was an average of 50 scans with the ASD Fieldspec.

5.4.2 Methods for geochemical analysis

Chemical analysis was provided by the Soil & Waste Unit of the Institute for Environment and Sustainability using the following methods:

- Major and trace elements (SiO_2, Al_2O_3, CaO, K_2O, Fe_2O_3, MgO, TiO_2, S, P_2O_5, Pb, Zn, Cu, Ni, Mn, Cr, Na, Cl, Sb) were estimated directly through X-ray fluorescence analysis (XRF)
- Mercury (Hg) was analyzed directly with atomic absorption spectrometry (AAS)
- Arsenic (As) was analyzed in solution, obtained by microwave acid digestion, by AAS with hydride generation
- Total Carbon C_{tot}, Hydrogen (H) and Nitrogen (N) were determined through combustion at 1000° C and gas-chromatography
- Organic Carbon Content (C_{org}) was estimated after acidification with hydrochloric acid, combustion at 1300° C and measurement of the carbon dioxide by an infrared detecting system
- Calcite was estimated by X-ray diffraction utilizing active dilution technique

5.4.3 Geochemical analysis results

5.4.3.1 Data analysis 1999

During the first sampling campaign in May/July 1999, 214 samples have been taken from 55 points. The first studies after the accident have shown that the main

contaminants, in descending order of concentrations, were Zn, Pb, Cu, As, Sb and Cd (Cabrera et al. 1999, Simón et al. 1999). Additionally, we found high concentrations of mercury. This is important, because it is one of the most toxic elements when released into the environment (Steinnes 1999). The concentration levels for the soils collected in 1999 are summarised in Table 5.3 (see Annex C for detailed information about single samples). The coefficient of variation (C.V.), or relative standard deviation, is particularly high for elements closely related to the mining accident (bold); this group includes most trace metals, sulphur and calcite. The high variation is caused by the irregular distribution of the sludge (and the related elements) after the first remediation campaign. The average values are close to or above critical concentrations at which toxic effects may be observed for most trace metals (Kabata-Pendias & Pendias 1984, see also Table 3.1).

Table 5.3. Descriptive statistics (minimum, maximum,mean, standard deviation and coefficient of variance) for all samples from 1999.

Element	*Min*	*Max*	*Mean*	*Stddev*	*C.V. %*
Al_2O_3 (%)	0.5	16.95	11.48	2.50	21.79
As (ppm)	**7**	**442**	**61.26**	**66.40**	**108.39**
CaO(%)	0.4	32.8	4.15	3.10	74.68
Calcite(%)	**0.46**	**42.42**	**4.52**	**4.86**	**107.52**
$C_{tot.}$ (%)	0.105	6.69	1.26	0.74	58.37
$C_{org.}$ (%)	0.1	3.28	0.73	0.41	56.28
Cd (ppm)	**0.05**	**14.803**	**1.26**	**1.70**	**134.36**
Cl (%)	0.02	0.15	0.03	0.02	76.46
Cr (ppm)	41	322.5	107.84	32.28	29.93
Cu (ppm)	17.5	521	120.44	84.08	69.81
Fe_2O_3 (%)	2.75	18.45	5.98	1.98	33.06
H (%)	0.24	1.6	0.51	0.17	33.54
Hg (ppm)	**0.01**	**13.9**	**0.45**	**1.14**	**255.06**
K_2O (%)	0.3	2.8	1.94	0.34	17.56
MgO (%)	0.6	6.65	1.88	0.57	30.47
Mn (ppm)	203.5	1177	734.52	188.16	25.62
N (%)	0.015	0.405	0.08	0.04	54.39
Na_2O (%)	0.05	6.4	2.67	1.34	50.17

Element	*Min*	*Max*	*Mean*	*Stddev*	*C.V. %*
Ni (ppm)	2	123.5	39.89	14.65	36.72
P_2O_5 (%)	0.055	0.605	0.12	0.04	36.67
Pb (ppm)	**17.5**	**3331.5**	**202.21**	**305.09**	**150.88**
S (%)	**0.01**	**19.34**	**0.77**	**2.28**	**294.36**
Sb (ppm)	196	3362	438.73	308.97	70.42
SiO_2 (%)	25.35	64.15	52.78	4.62	8.76
Ti O_2 (%)	0.315	1.225	0.89	0.14	16.13
Zn (ppm)	**94**	**3887**	**380.44**	**372.85**	**98.00**

However, the variability is also related to the fact that samples were taken from different depths and different sites. Therefore, it is necessary to have a more detailed look at the soil profiles and to compare profiles within the affected area with those from outside, which can be referred to as normal background contamination. Furthermore, the different sites have to be compared.

The trace metal concentrations are rapidly decreasing with increasing depth, but even the levels in 40 to 60 cm are still clearly above background values. This is demonstrated for selected HM in Figure 5.6 in comparison to uncontaminated soils of the area. The profiles are average profiles from nine contaminated and three uncontaminated soils taken at the Sobarbina site.

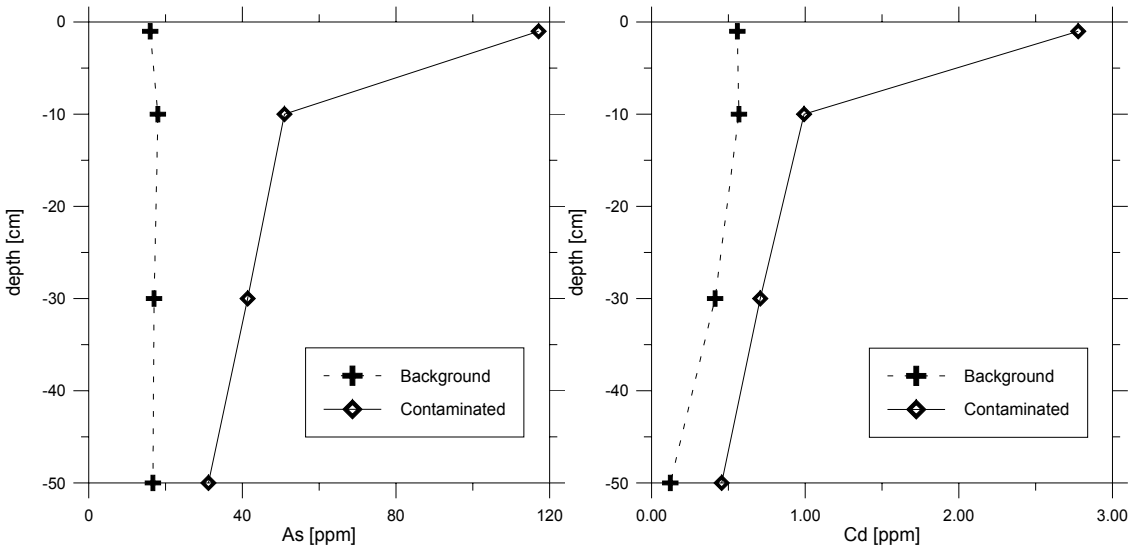

Figure 5.6. Average depth profiles from Sobarbina site for contaminated soils (solid) and uncontaminated soils (dashed). Arsenic (left), cadmium (right)

Generally, the highest surface contaminations are found in the northern part at the *Mine South* and *Sobarbina* sites (Table 5.4). The site *Mine North* is less contaminated due to its upstream location at the northern edge of contamination. The *Vado de Quema* site shows again higher contamination levels. Here, samples were taken from profiles on surfaces with the original sludge layers. Cabrera et al. (1999) found similar contamination patterns in their study.

Table 5.4. Average surface trace metal contaminations 1999 for all sites in ppm (Fe_2O_3 and S in percent).

Average (0-2cm)	*As*	*Cd*	*Cu*	*Fe_2O_3*	*Hg*	*Pb*	*S*	*Sb*	*Zn*
Mina Nord	101	2.31	143	6.40	1.19	213	0.54	453	536
Mine South	160	4.25	231	8.81	1.53	552	3.37	759	1003
Sobarbina	176	3.14	145	9.60	1.59	589	4.69	949	660
Las Doblas	124	2.27	200	7.29	0.80	338	1.47	600	558
Puente Nuevo	56	1.70	109	4.69	0.29	178	0.20	405	468
Quema	99	3.71	144	5.21	0.52	226	0.70	453	879

The correlation analysis of the analysed soil samples (Table 5.5) shows a clear separation between elements related to the accident and elements related to normal soil composition. The group of elements related to the accident is composed of the trace metals As, Cd, Cu, Hg, Pb, Sb and Zn and Fe_2O_3 and Sulphur. The latter can be attributed to the pyrite (Fe_2S) that made up 80 % of the sludge. The correlations within this group are not equally distributed. A strong group with equally strong correlations is made up of Fe_2O_3, Hg, Pb, S and Sb. As is correlated weaker with this group, but it is a link between this group and another group of Cd, Cu and Zn.

The elements related to normal soil composition are divided into four sub-groups; some of them forming groups of related soil components or processes. A group consisting of Al_2O_3, K_2O and SiO_2 can be attributed to the Al- and Si-oxides, which are the most abundant oxides in the earth crust (Hudson 1995) and consequently are major elements in soil composition. Mn and TiO_2 are not strongly correlated to the group of oxides, but they are also abundant soil components. Cr and Ni are trace metals, which are not particularly related to the mining accident. The group of Calcite, CaO, C_{tot}, C_{org}, N and P_2O_5 is related to the nutrients part of the soil, as Ca, N, P are plant nutrients and C_{tot} and C_{org} can be related to the organic matter component. Cl, H, MgO and Na_2O do not have strong correlations with any of the other elements.

Table 5.5. Correlation matrix of elements 1999. For more clarity only significant correlations (> 0.5, α = 0.05) are displayed

	Al_2O_3	As	$CaCO_3$	CaO	Cd	Cl	$C_{ORG.}$	Cr	$C_{tot.}$	Cu	Fe_2O3	H	Hg	K_2O	MgO	Mn	N	Na_2O	Ni	P_2O_5	Pb	S	Sb	SiO_2	TiO_2	Zn
Al_2O_3			-0.501	-0.522	-0.511									0.803		0.684								0.771	0.602	
As					0.738						0.731		0.768								0.730		0.784			0.523
Calcite	-0.501			0.938					0.827											0.728				-0.571	-0.640	
CaO	-0.522		0.938						0.782					-0.605						0.750				-0.634	-0.556	
Cd	-0.511	0.738								0.637	0.622		0.566								0.568	0.653	0.585			0.868
Cl										0.543	0.701										0.560	0.691	0.612			
Corg.									0.592			0.600					0.733									
Cr																			0.898							
Ctot.			0.827	0.782			0.592													0.731				-0.576		
Cu					0.637	0.543					0.598															0.679
Fe_2O_3		0.731			0.622	0.701				0.598			0.682					-0.584			0.803	0.879	0.852			0.558
H							0.600										0.614	-0.501								
Hg		0.768			0.566						0.682				0.592						0.864	0.820	0.858			
K_2O	0.803																		0.549					0.790		
MgO													0.592								0.559	0.580	0.536			
Mn	0.684																								0.732	
N							0.733					0.614														
Na_2O											-0.584	-0.501											-0.502			
Ni								0.898						0.549												
P_2O_5			0.728	0.750					0.731															-0.597		
Pb		0.730			0.568	0.560					0.803		0.864		0.559							0.860	0.967			
S	-0.509	0.704			0.653	0.691					0.879		0.820		0.580						0.860		0.893			0.515
Sb		0.784			0.585	0.612					0.852		0.858		0.536			-0.502			0.967	0.893				
SiO_2	0.771		-0.571	-0.634										0.790						-0.597						
TiO_2	0.602		-0.640	-0.556												0.732										
Zn		0.523			0.868					0.679																

5.4.3.2 Data analysis 2000

During the field campaign in June/July 2000, 132 samples have been taken from 70 points. However, because the results of 1999 showed that most of the contamination is found in the upper centimetres of the soil, and that for hyperspectral remote sensing only the first millimetres are visible, only one full depth profile per profile was taken.

In 2000, slightly different elements have been analysed. Additionally bismuth and thallium have been measured; total, organic and inorganic carbon and calcite were not obtained (Table 5.6, see Annex D for detailed information about single samples). The average concentrations for bismuth (Bi) and thallium (Tl) are above critical concentrations (Kabata-Pendias & Pendias 1984) and they show the same elevated C.V. values than all other elements related to the accident. Consequently, they can be considered contaminants related to the accident. The differences in C.V. between elements related to the accident and others are more pronounced than in 1999. This raised C.V. is probably caused by the different sampling strategy with more surface samples in 2000, which are generally higher contaminated.

Table 5.6. Descriptive statistics for all samples from 2000

Element	*Min*	*Max*	*Mean*	*Stdev.*	*C.V.*
Al_2O_3	3	19.4	14.00	3.50	25.02
As	**12.3**	**3070.9**	**223.89**	**479.65**	**214.24**
Bi	**0.3**	**49.5**	**2.94**	**7.40**	**251.82**
CaO	0.5	19.7	5.36	3.23	60.31
Cd	**0.06**	**17.03**	**1.60**	**2.18**	**136.54**
Cl	0.01	0.15	0.03	0.02	76.17
Cr	62	439	116.48	44.91	38.55
Cu	31	614	110.31	83.99	76.15
Fe_2O_3	3.75	24.6	6.90	3.62	52.43
Hg	**0.01**	**16.29**	**0.80**	**2.35**	**293.39**
K2O	0.23	3.3	1.99	0.63	31.81
MgO	0.2	6.35	2.02	1.11	55.18
Mn	136	3440	796.74	363.04	45.57
Na2O	0.05	3.5	1.69	0.80	47.40
Ni	6	48	34.31	8.08	23.54

Element	*Min*	*Max*	*Mean*	*Stdev.*	*C.V.*
P_2O_5	0.055	0.695	0.19	0.09	46.42
Pb	**25**	**3130**	**272.41**	**506.29**	**185.85**
S	**0.02**	**30.4**	**2.42**	**5.80**	**239.52**
Sb	**10**	**3840**	**343.83**	**642.24**	**186.79**
SiO_2	15.2	64.9	51.02	8.99	17.62
TiO_2	0.195	1.09	0.76	0.18	22.96
Tl	**0.18**	**46.8**	**2.87**	**7.43**	**259.22**
Zn	**68**	**5600**	**445.85**	**628.31**	**140.92**

The comparison between concentrations of the two years focuses on those elements that are related to the mining accident and which have shown a high variability (Figure 5.7). Generally, the concentrations decrease. Only for arsenic a considerable increase of concentrations can be observed at all sites. The iron and particularly the sulphur concentrations show an inconsistent behaviour. At two sites (*Mine South* & *Sobarbina*), the sulphur concentrations diminish by approx. 50 %, while they increase at the other sites between 40 and 220 %.

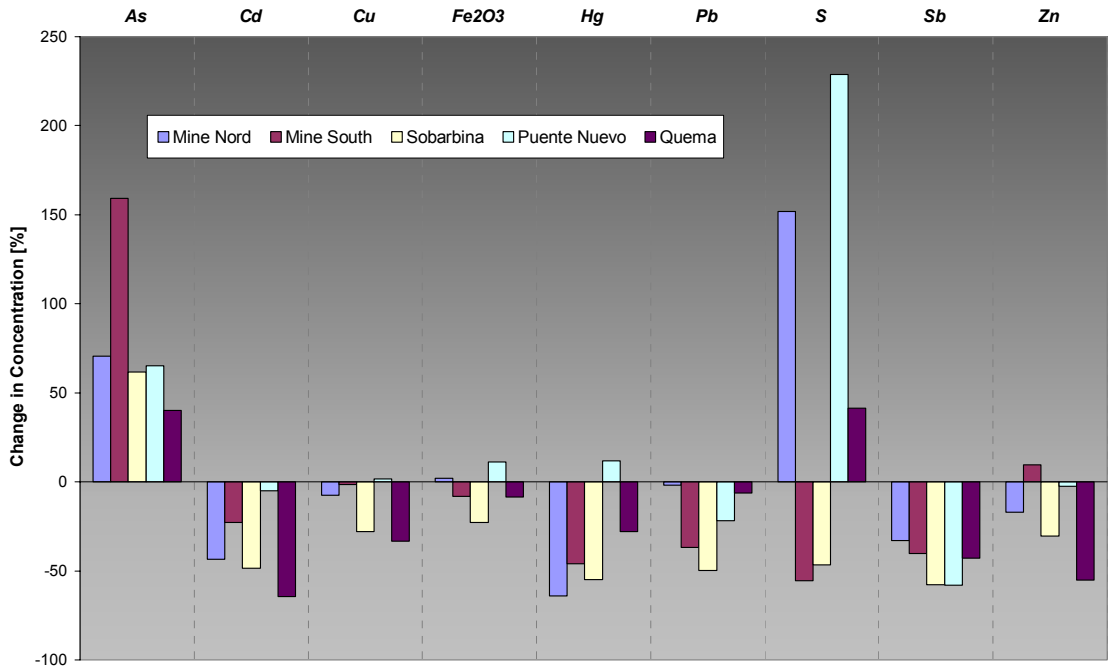

Figure 5.7. Differences in surface concentrations (in percent) between 1999 and 2000 for the sites, where sampling was possible in both years

Changes in the concentrations also appear in the depth profile, which can be caused by removal due to the remediation works, they may be washed away by surface runoff or they may be migrated into deeper horizons. Regarding the movement within the profile also an upward movement is possible, when elements in solution are transported upward due to capillary effects caused e.g. by a high evapotranspiration.

As mentioned above the concentrations for As increased considerably at all sites. Also the *Sobarbinas* depth profiles show an overall increase (Figure 5.8, for further profiles see Annex E). The strongest increase is observed at the surface, but also in the samples down to 40 cm. Fe and S concentrations also increase slightly at the surface and even more in the middle part of the profile indicating a downward movement. Similar changes can be observed for Pb and Hg, although the concentrations at the surface decrease. A general decrease can be observed for Cd, Cu, Sb and Zn. Only the surface concentrations are still above background levels.

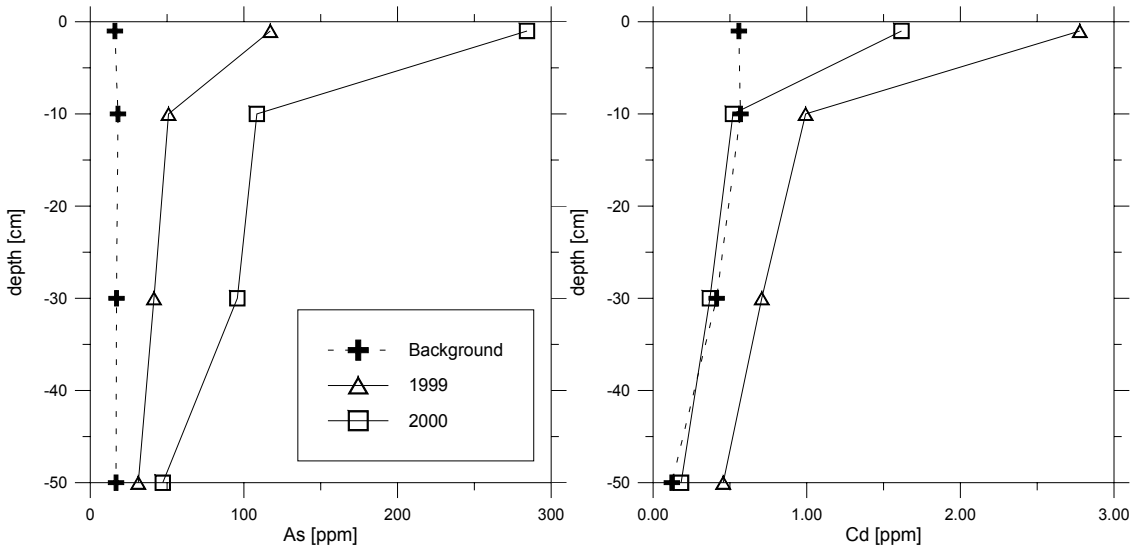

Figure 5.8. Comparison of soil depth profiles 1999 (triangle) and 2000 (square) and background (cross) from Sobarbina

5.4.3.3 Conclusion

The reference data set with more than 300 samples forms a good basis, on which the relationships between chemical composition and spectral reflectance can be built. The results obtained are in good agreement with the results obtained by other research groups. The data set is big enough to use the samples of both years separately for assessments of the temporal development of the contamination.

After the end of the first clean-up operation in June 1999 the contamination was partly still high, which corresponds accurately with the study of Galán et al. (2002). The average values of contaminated soils for all HM were still above average values of

background soils and the range of contamination values was very wide. The HM concentrations were rapidly decreasing with increasing depth, but even the levels in 40 to 60 cm were still clearly above background values, which showed that the HM had already affected deeper horizons. One year later in July 2000, the HM concentrations generally decreased. Only for arsenic a considerable increase of concentrations could be observed at all sites. It is also the only element, whose concentrations also in the depth profile rose significantly, indicating an increased mobility, which is most probably triggered by the intensified oxidation.

6 Laboratory spectroscopy for quantification of residual contamination and other soil constituents

As demonstrated in chapter 5 reflectance spectra are very rich in information, which allows inferring chemical or physical properties of material from a single spectrum. Sometimes, we can even use the visible spectrum and our own eyes to infer such properties. For example, we can estimate the ripeness of a banana at a glance just by its colour (yellow for ripe and green for unripe). Automatically, without any chemical test, we can assess how much of its starch has been converted to sugar.

In this chapter, the relationship between soil constituents and soil reflection is worked out and multivariate calibration is used to predict different soil constituents related to the mining accident using the spectra measured in the laboratory and in the field. An artificial mixture series of sludge and soil is developed and analysed for a better understanding of the effect of the contamination on the spectral reflectance and for having more control over influencing side effects.

6.1 Multivariate calibration

Using chemometric modelling we can formalize the process of correlating properties to spectra. In chemometrics, a discipline of analytical chemistry, this modelling is often referred to as multivariate calibration. Multivariate calibration is the collective term used for the development of a quantitative method for the reliable prediction of properties of interest (y_1, y_2, …, y_q) from a number of predictor variables (x_1, x_2, …, x_p). The goal of the calibration is to replace a measurement of the property of interest by one that is cheaper, faster, or better accessible, yet sufficiently accurate. Developing the calibration model includes stating of the objective of the study, designing the experiment (sample measurement, data treatment), choosing the type of model, estimating its parameters and finally assessing the precision of the predictions (Massart et al. 1998).

Multivariate calibration, in contrast to univariate calibration, involves more than one predictor variable, which opens up new opportunities for better prediction. It allows for example, the use of an entire spectrum rather than the signal at the ‘best’ wavelength. In principle, this may lead to improved predictions. However, it also opens the possibility to incorporate essentially non-informative spectral regions through random correlations in the calibration set, which are not based on physical relationships. Multivariate

calibration allows the estimation of more than one dependent property and the correction for undesired covariates (interferences). The latter allows for the separation of information relevant for the respective properties from non-relevant variation or random noise, and is a major motivation for multivariate calibration (Massart et al. 1998).

A major application of multivariate calibration is in analytical chemistry, specifically the development and application of quantitative predictive calibration models, e.g. for simultaneous determination of the concentrations of various analytes in a multi-component mixture, where one may choose from different spectroscopic methods (e.g. UV, IR, NIR, XRF). The application of near infrared analysis (NIRA) to analyse samples, needing little or no pre-treatment, has found widespread use in chemical and food industries (Williams & Norris 1987, Hildrum et al. 1992). The use of multivariate calibration in the field of environmental science particularly in the soil sciences is still limited. Relatively few researchers have extended the methods for the extraction of soil/sediment information. Ben-Dor & Banin (1990, 1994) have used this method for the prediction of different soil constituents. Malley & Williams (1997) determined the heavy metal contamination in lake sediments using multivariate methods. Udelhoven & Schütt (2000) used artificial neural networks for the chemical characterisation of sediments. Kooistra et al. (2001) used partial least squares regression for the estimation of soil contamination in floodplain sediments.

The ultimate goal of multivariate calibration is the indirect determination of a property of interest by measuring the predictor variables only. Therefore, it is not sufficient to describe the calibration data as adequate, but the model must be able to generalise unknown observations. The assessment of the optimum extent to which this is possible has to be done carefully. When the calibration model chosen is too simple (underfitting) systematic errors are introduced, when it is too complex (overfitting) large random errors may result.

In order to understand chemometric models a deeper understanding of the underlying chemistry and physics is as important as a set of statistical parameters describing the models. This means for spectral data that a basic understanding of spectra and their errors is useful and that spectral representation should be included in the utility of the data treatment (Geladi & Martens 1996a). Having this in mind, in the following section a mixture experiment is performed with exactly the purpose of understanding the relationship between sludge and reflectance.

6.2 Generation of an artificial mixture series of sludge and soil

The soil samples collected in the field were analysed in the laboratory as described above for their element composition, but the detailed quantitative analysis of the mineralogical composition could not be provided with the means of the laboratory. This

means that the sludge content of the samples can only be determined indirectly *via* the correlation between sludge and elements. However it is known that pyrite makes up 75 – 80 % of the sludge (Galán et al. 2002) that predominantly influences the spectral behaviour of the samples through its opacity and consequently absorption rather than the associated HMs or trace elements. This was the rationale for setting up an artificial mixture series, in order to assess under controlled conditions empirically the influence of the sludge on the overall reflectance of the soils. Non-contaminated samples (i.e. not affected by the accident) of the three most important soil types in the area were used for this experiment to add sludge in increasing weight percentage from 0 to 100 % (32 samples).

Already, the visual analysis of the measured soil spectra showed a large difference between contaminated and uncontaminated soils. Figure 6.1 shows the reflectance change for an uncontaminated soil with increasing sludge content. The most evident change was a strong decrease of overall albedo from a maximum reflectance of 53 percent to 14 percent. In particular, at longer wavelengths the spectrum levelled off strongly. Besides the general decrease in albedo, some changes in the absorption features are apparent. With the building up of a very wide absorption feature between 700 and 1400 nm the absorption features at 1400, 1900 and 2200 nm diminished and were almost extinguished at sludge concentrations above 50 weight-percent. Smaller absorption features disappeared even earlier.

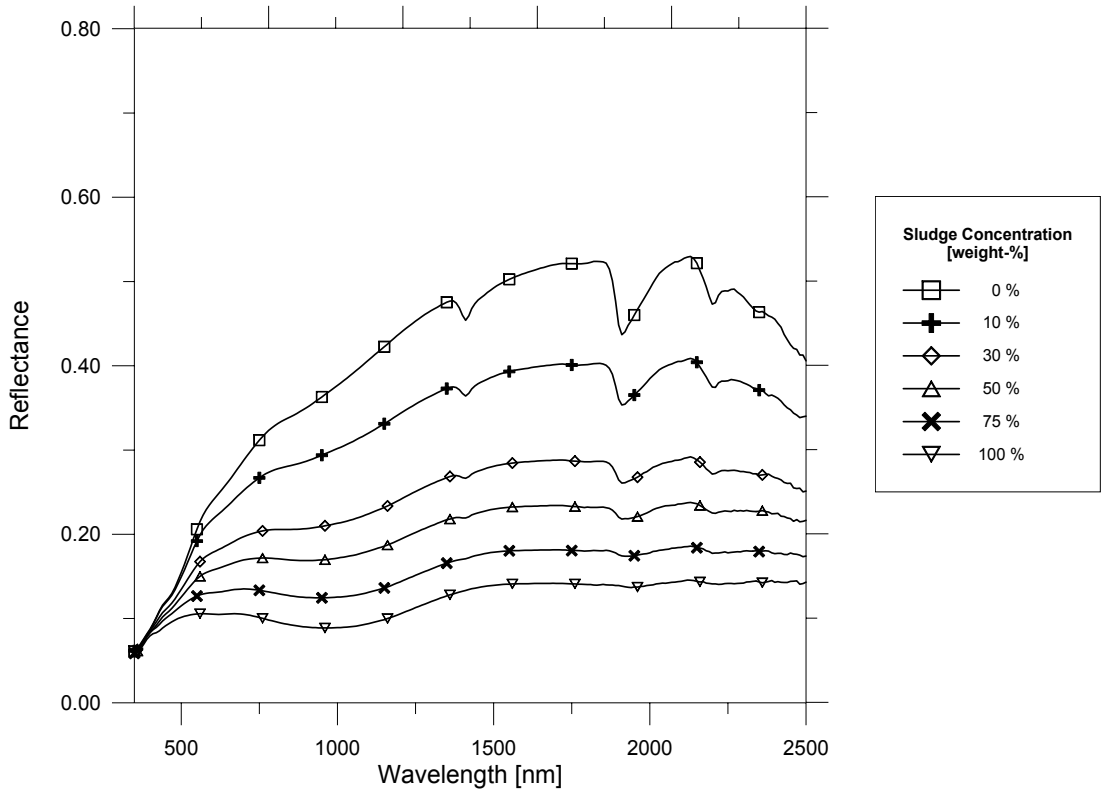

Figure 6.1. Spectra of mixture series of soil sample AZ086 (10 nm)

A means for a comparison of individual absorption features is the so-called continuum removal. Continuum removal normalizes reflectance spectra to allow comparison from a common baseline (Clark & Roush 1984). The continuum is a convex hull fit over the top of a spectrum utilizing straight-line segments that connect local spectral maxima (Figure 6.2). The first and last spectral data values are on the hull and therefore the first and last bands in the output continuum removed data file will be equal to 1.0.

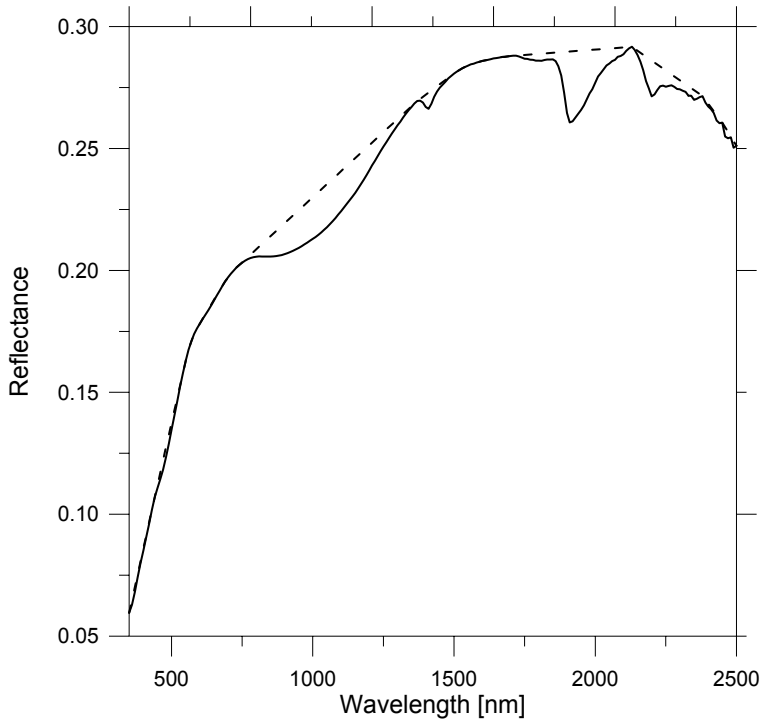

Figure 6.2. Soil AZ086 with 30 weight-% sludge and convex hull fit (dashed)

The continuum removed spectra of the mixture series are displayed in Figure 6.3. The main feature is the wide iron absorption centred at about 1000 nm, whose depth and width are increasing with increasing amount of sludge. The H_2O and OH features at 1400, 1900 and 2200 show the opposite behaviour; they are strongest with lowest sludge content. Also the iron absorptions between 400 and 500 nm are related to non-contaminated soils.

The strong link between depth of the iron absorption and sludge content allows the use of this relationship for the estimation of the sludge content. The strongest correlation for the samples of the mixture series was obtained at the maximum absorption depth at 1043 nm with a high coefficient of determination ($R^2 = 0.967$).

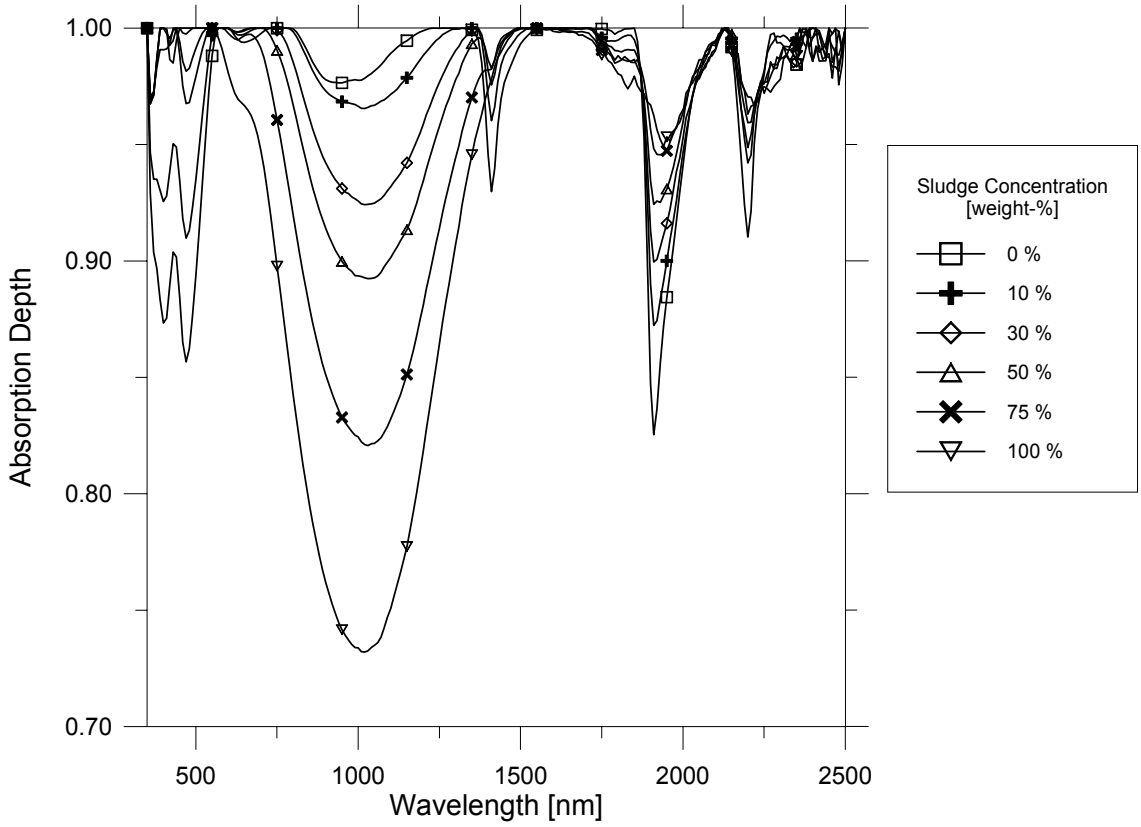

Figure 6.3. Continuum removed spectra of mixture series

This relationship is also apparent for all samples collected in 1999 (Figure 6.4). There is however, a group of samples that do not follow this trend. The spectral shape of these samples is different from the one of the mixture series. The maximum depth of absorption for these samples is shifted towards 948 nm, which can be related to the absorption of goethite or hematite. These samples are characterised by an elevated amount of Fe_2O_3. In fact, all samples were collected in the riverbed of the Rio Agrio and had a very coarse gravel texture with iron coatings, which were caused by the long-term acidic conditions in the riverbed rather than the accident. By removing these outliers a coefficient of determination of $R^2 = 0.851$ is obtained, which is however strongly controlled by the skewed distribution of the data. The application of this relationship to image data is difficult, because of the influence of green vegetation in this part of the spectrum and the amounts of Goethite in the soils.

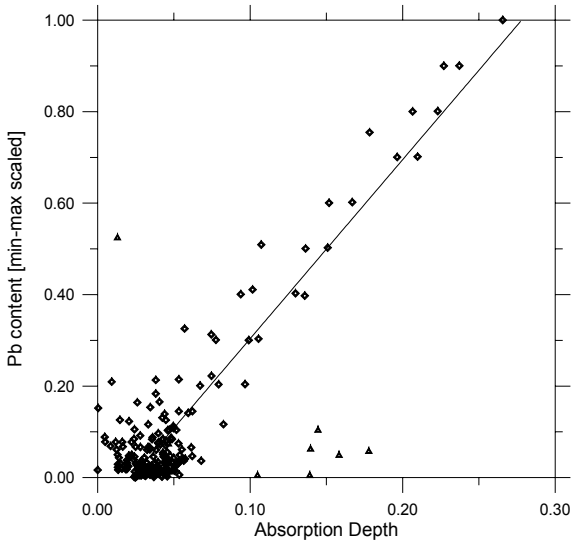

Figure 6.4. Relationship between absorption depth at 1043 nm and Pb content for 1999 samples. Outliers are marked as triangles (Δ)

6.3 Data pretreatment

The continuum removal procedure applied in the previous section has shown that it is possible to strongly enhance subtle features, which may be very important for the purpose of a study. Thus, this section applies different transformations to the spectra, but also to the geochemical data.

6.3.1 Soil component scaling

The data set of elements, which was chemically analysed, represents quite different properties of the soils, so that the metric differs substantially. This implies absolute values as well as variances. It becomes obvious, when checking again the descriptive statistics table (e.g. Table 5.3); trace metal concentrations are given in ppm, the soil matrix concentrations are given in percentage values and the C.V. values vary over a wide range. Both types of distortion may affect the statistically based multivariate methods and neural networks. Scaling the data to similar ranges can eliminate these differences (Otto 1999):

$$x_{ik}^{*} = \frac{x_{ik} - x_k(\min)}{x_k(\max) - x_k(\min)} \quad 0 \le x_{ik}^{*} \le 1 \qquad \text{Eq. 6.1}$$

where i = row index,

k = column index,

$x_k(\min)$ = column minimum

$x_k(\max)$ = column maximum.

6.3.2 Spectral resampling

The spectral resampling smoothes the spectra and reduces the number of wavelengths, which will be used later as independent variables in multivariate calibration, speeding up calculations and reducing the problems of over-fitting (Otto 1999). The resampling, termed 'spectral channel degradation technique', has been found effective for prediction of different soil properties (Ben-Dor & Banin 1994). Furthermore, the final goal is the application of multivariate calibration to airborne and eventually satellite imaging spectrometers, which usually have a bandwidth between 10 and 50 nm. Accordingly, the reflectance spectra were resampled from 1 nm to 5, 10, 20 and 50 nm spectral resolution at full width half maximum (FWHM) and HyMap band set, reducing the number of spectral bands from 2151 to 42, which smoothes the spectra and speeds up the calculations.

Table 6.1. Resampling width (FWHM) and resulting number of bands

FWHM [nm]	Number of bands
1	2151
5	431
10	216
20	108
50	42
HyMap	128

The spectral processing was performed using IDL/ENVI® software (Research Systems Incorporate 1999) using a gaussian model that takes into account the band centre and the FWHM spacing.

Figure 6.5 illustrates the effects of the resampling. They are best recognizable at the water and hydroxyl absorptions at 1400, 1900 and 2200 nm. The broader the bandwidth is, the wider and the more flattened out is the absorption feature. The close up of the SWIR region highlights these effects and show the filtering effect due to resampling. However, very broad bands are not able to resolve small absorption features like the weak carbonate absorption at 2350 nm.

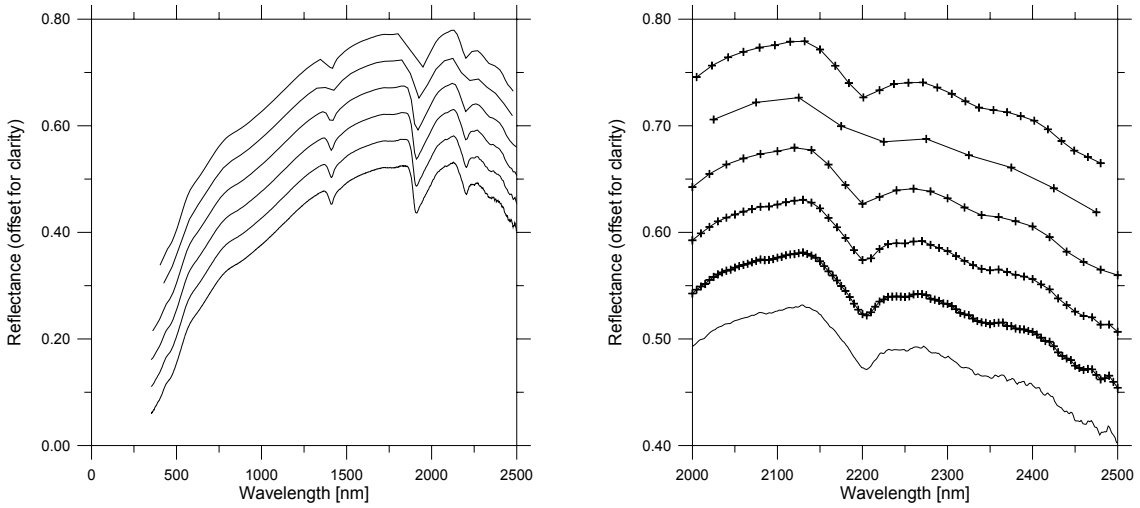

Figure 6.5. Resampling results for soil sample AZ086. Full spectrum (left), spectral subset with band centres (right). From bottom to top increasing bandwidth (1,5,10,20,50 nm), HyMap spectra on top

6.3.3 Transformation of spectra

After the spectral resampling, different data treatments were applied to each data set in order to enhance the spectral features that might be important in the modelling process. The reflectance data were transformed to absorption, standardised and vector-normalised spectra, first and second order derivatives using the Savitzky-Golay method.

6.3.3.1 Absorption

One of the keys to quantitative analysis in any scientific field is the assumption that the amounts (concentrations) of the constituents of interest in the samples are somehow related to the data from a measurement technique used to analyse them.

In chemometrics, the Beer-Lambert law is often used to exploit this correlation. The law states that there is an exponential dependence between the transmission of light through a substance and the concentration of the substance, and also between the transmission and the length of material that the light travels through. Thus, the concentration of a substance can be deduced from the amount of light transmitted by it. However, the law tends to break down at very high concentrations, especially if the material is highly scattering (e.g. in turbis solutions).

Nevertheless, the transformation of reflectance units into absorption is widely applied in chemometrics. Absorption is often preferred, because there is an almost linear relationship between the concentration of an absorbing component and its contribution to the log(1/R) value at the wavelength absorbed. Due to its logarithmic scale, absorption also accounts for scattering effects (Hruschka 1987).

Reflectance spectra are transformed into absorption units according to the following equation:

$$A = \log(1/R) \qquad \text{Eq. 6.2}$$

where A = Absorption

R = Reflectance.

After the transformation, the spectra appear mirrored and stretched. The absorption features that are negative peaks in reflectance units appear as slightly enhanced positive peaks (Figure 6.6).

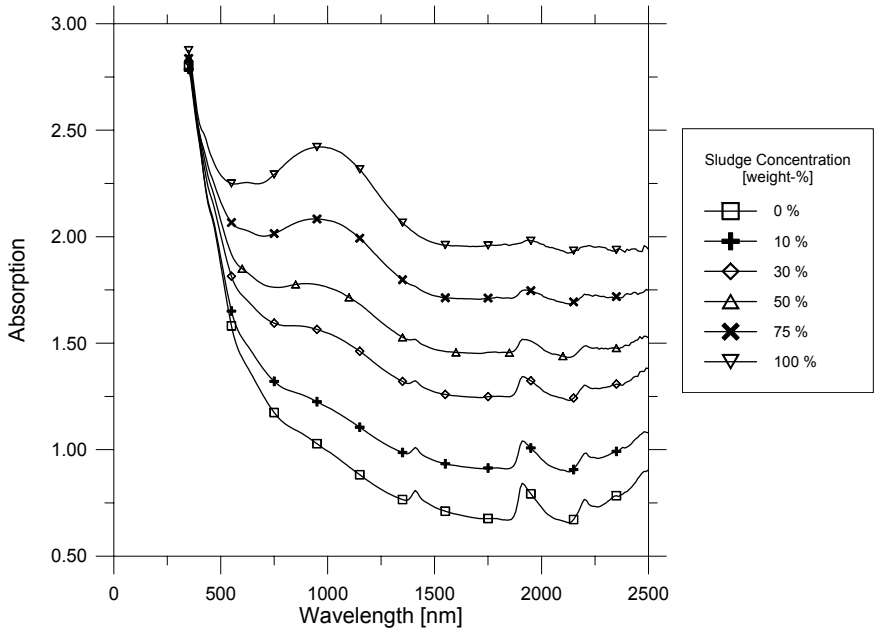

Figure 6.6. Absorption spectra of examples from mixture series (10 nm). See Figure 6.1 for original reflectance spectra

6.3.3.2 Standardisation

The standardisation transforms the data to a set of data with a mean of zero and a standard deviation of one:

$$x_{ik}^{*} = \frac{x_{ik} - \overline{x_k}}{s_k} \qquad \text{Eq. 6.3}$$

where i = row index,

k = column index,

$\overline{x_k}$ = column mean,

$s_k = \sqrt{\frac{\sum_{i=1}^{n}\left(x_{ik} - \overline{x_k}\right)}{n-1}}$, where n = number of objects

Figure 6.7 shows an example of standardised spectra of the mixture series. This standardisation transforms the data to a set of percentage variations about the mean value, which allows matching of the data in a manner independent of the reflectance scale (Mackin et al., 1991). This procedure overcomes the problems of brightness variations due to grain size retaining and even enhancing the information due to the spectral shape, such as gradient and absorption bands. This is particularly true for the sludge spectrum, which is spectrally flat when it is not transformed, but shows a well defined, strong absorption centred at about 1000 nm.

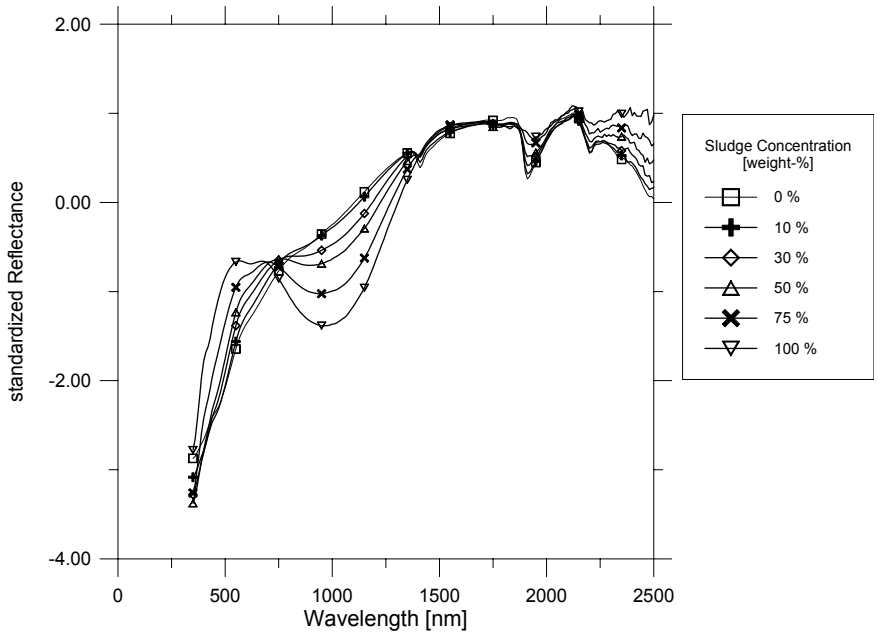

Figure 6.7. Standardised reflectance spectra of examples from mixture series (10 nm). See Figure 6.1 for original reflectance spectra

6.3.3.3 Vector normalisation

The length of a vector x = (x_1, x_2, …, x_n) is defined as the square root of the sum of the squared elements in a vector. The normalisation of a data vector to length one is achieved by division of the vector x with the length of the vector (Otto 1999):

$$x_{ik}^{*} = \frac{x_{ik}}{\|x_k\|} \qquad \text{Eq. 6.4}$$

where $\|x_k\| = \sqrt{x_{1k}^2 + x_{2k}^2 + \ldots + x_{nk}^2}$

The effects of vector normalisation are similar to those of the standardisation (Figure 6.8). The brightness differences are significantly reduced, whereas structural information is preserved or even enhanced. Only the data range is reduced and the values are all positive.

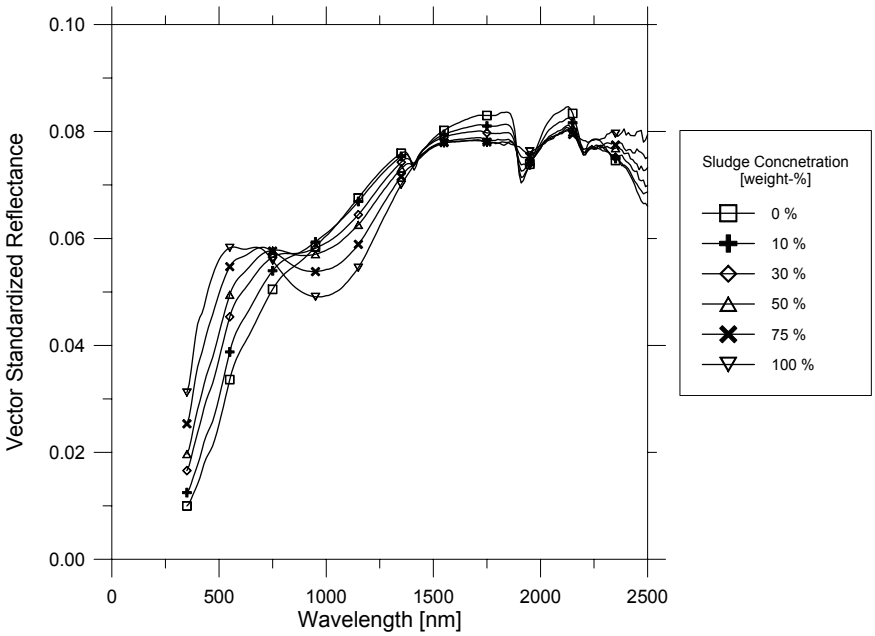

Figure 6.8. Vector standardised reflectance spectra of examples from mixture series (10 nm). See Figure 6.1 for original reflectance spectra

6.3.3.4 Derivatives

Derivatives are a well-established signal processing approach in analytical chemistry. Derivatives of VIS/NIR spectra carry predominantly chemical information of the sample, because albedo effects are reduced and overlapping spectral features are resolved. For example, the OH-absorption of a soil (Figure 6.1) at 1400 nm is shown in the second derivative of this spectrum as a distinct peak (Figure 6.10). The FWHM is smaller for the peak in the second derivative compared with the original spectrum. Consequently, the smaller FWHM of the derivatives allows overlapping absorption features that are recognised as a single broad absorption in the reflectance spectrum to be distinguished. Baseline shifts are removed because the curvature of a straight line is zero and hence, the derivative of a spectrum plus a constant offset is the same as the derivative of the pure spectrum. The first order derivative has also these effects, but to a lesser extent. It can be interpreted as the slope of a spectrum at each wavelength. Higher order derivatives have the same two basic effects and will resolve overlapping absorptions even better than lower order derivatives. However, they are more sensitive to noise and generate more artefacts than lower order derivatives. Furthermore, they do not have any easily visualised geometric interpretation and hence, have not been widely used in VIS/NIR spectroscopy (Hruschka 1987).

There are three common methods of calculating derivatives: the finite-differences, Fourier transform and Savitzky-Golay methods; each has its advantages and disadvantages. The Fourier transform is most useful, if the Fourier transform of a spectrum is already available for other purposes. The finite-difference is easiest to calculate but is more sensitive to noise than the Savitzky-Golay method, which includes a smoothing based on a polynomial function. Therefore the latter has been used for this study.

The Savitzky-Golay method fits the spectrum in a wavelength interval with a polynomial and then takes the derivative of that polynomial. Savitzky & Golay (1964) used simplified least-square-fit convolution for smoothing and computing of derivatives of a spectrum. The general equation is represented as follows:

$$Y_j^* = \frac{\sum_{i=-m}^{m} C_i Y_{j+i}}{N} \qquad \text{Eq. 6.5}$$

where Y is the original spectrum, Y^* is the resultant spectrum, C_i is the coefficient of the i-th spectral value of the filter window, and N is the number of convoluting integers. The index j is the running index for the wavelength of the original spectrum data table. The filter window consists of 2m+1 points, where m is the half width of the filter window. Savitzky & Golay (1964) provided several tables of coefficient values. Corrections to these tables were provided by Steinier et al. (1972). The use of these

tables limits the application of the method. The maximum filter window size of the tables provided by Savitzky & Golay (1964) is 25 (m=12). Furthermore, for application of several combinations of polynomials and derivatives, a general analytical form for calculation would be preferable. Tsai & Philpot (1998) have implemented in their algorithms the equations of Madden (1978) to overcome the limit of 25 points for the filter window. According to Madden, equation Eq. 6.5 can be rewritten as:

$$Y_j^* = \frac{\sum_{i=-m}^{m} P_i^{(0)} Y_{j+i}}{N} \qquad \text{Eq. 6.6}$$

where $P_i^{(0)}$ is the coefficient of the *i*-th point of the filter in the zeroth order of derivative computation. Accordingly, the smoothed *q*-th order derivative point of the midpoint is represented as:

$$\frac{d^q \overline{Y_j}}{d\ x^q} = \sum_{i=-m}^{m} P_i^{(0)} Y_{j+i} \qquad \text{Eq. 6.7}$$

Madden's equations allow calculation of the coefficients of least-square-fit convolution from zeroth order to the sixth order of smoothed derivatives.

It has to be mentioned that the derivative spectra obtained with the procedures described above are shorter than the original spectrum by the width of the filter because the procedures cannot be applied correctly at the ends of the spectrum.

The computer code for the calculation of the derivatives was kindly provided by Tsai & Philpot (1998). The different modules, collectively called HyperSpec, were developed in MATLAB (Mathworks 2000) script.

The derivatives of the respective data sets have been treated differently according to their spectral bandwidth; the broader the bandwidth the smaller the filter size (Table 5.3). All data sets were filtered with a second order polynomial.

Table 6.2. Filter sizes used for calculating first and second order derivatives

Bandwidth [nm]	1st derivative	2nd derivative
1	25	25
5	11	17
10	5	11
20	3	5
50	3	3

The first derivative produces two opposed peaks in front and behind absorption features. At the wavelength of the peak, the first derivative equals zero. For example, the H_2O absorption at 1400 nm is preceded by a local minimum and followed by a local

maximum (Figure 6.9). The disappearance of the H_2O and OH-features at 1400, 1900 and 2200 nm in the mixture series with increasing sludge content is clearly reflected. As sludge content increases, so the first derivative becomes flatter.

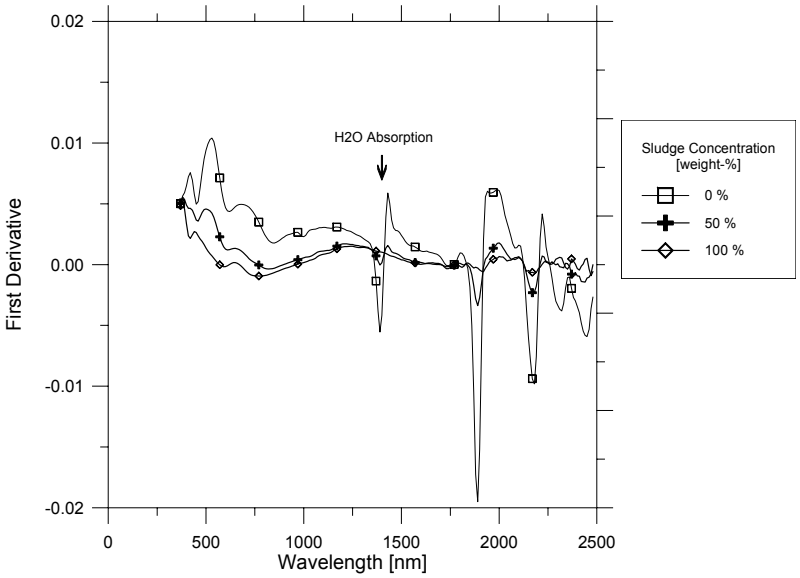

Figure 6.9. First derivatives of reflectance spectra of examples from mixture series (10 nm, Savitzky-Golay Method). See Figure 6.1 for original reflectance spectra

The second order derivative produces a positive peak at the position of an absorption feature, which is enclosed by two smaller opposed peaks. Hence, the most obvious features are again the H_2O and OH-absorptions in the soil with little or no contamination (Figure 6.10).

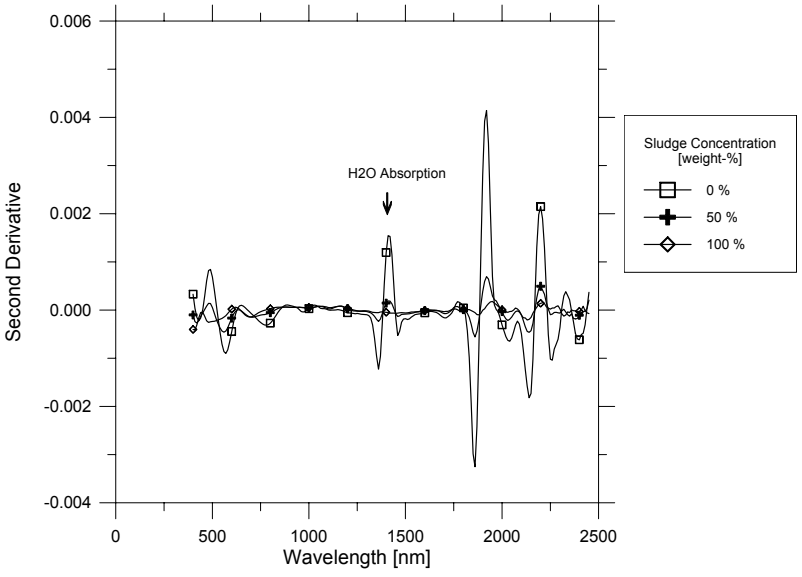

Figure 6.10. Second derivatives of reflectance spectra of examples from mixture series (10 nm, Savitzky-Golay Method). See Figure 6.1 for original reflectance spectra.

6.3.3.5 Discussion of data pre-treatment

The examples of the different spectral transformations were taken from the mixture series, but were applied to all samples. It became clear that the different data treatments changed the aspect of the spectra entirely. Whether these changes are also reflected in the correlations between the soil constituents and the spectra can be assessed by the analysis of so called 'correlograms'. In a correlogram, the correlation coefficients between soil constituents and reflectance are plotted as a function of wavelength. These 'correlation-spectra' bear a lot of information, which are also very helpful for the analysis of the predictive models. They show spectral features or regions, which may correlate highly with a soil component and hence will be important for the later modelling. Due to the amount of information (26 soil constituents), the elements were grouped into different figures according to similar correlation structure. The grouping resulted in three sets, which are almost identical with the groups identified in the correlation matrix of elements (Table 5.5): trace metals, soil matrix and soil nutrients. Figure 6.11 shows the correlograms for the three groups in relationship to the 10 nm reflectance spectra. The trace metal group is mostly negatively correlated to reflectance, only in the VIS part of the spectrum a small, positive correlation peak can be observed at 400 nm, after which the correlation becomes negative. The negative correlations are very stable and range mainly between – 0.6 and – 0.8 for all elements, except Cu and Zn that are less strongly correlated. Exactly the contrary behaviour can be observed for the soil matrix group; the only difference is that the correlations are weaker and the feature in the VIS is wider. The organic part is mostly positively, but even weaker correlated with reflectance.

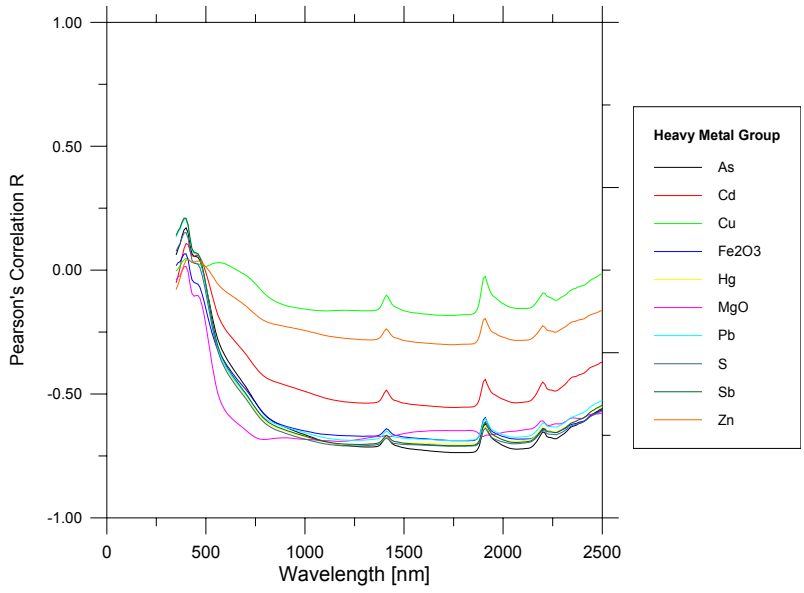

Figure 6.11. Correlograms of soil constituents and reflectance spectra (10nm). Trace metal group

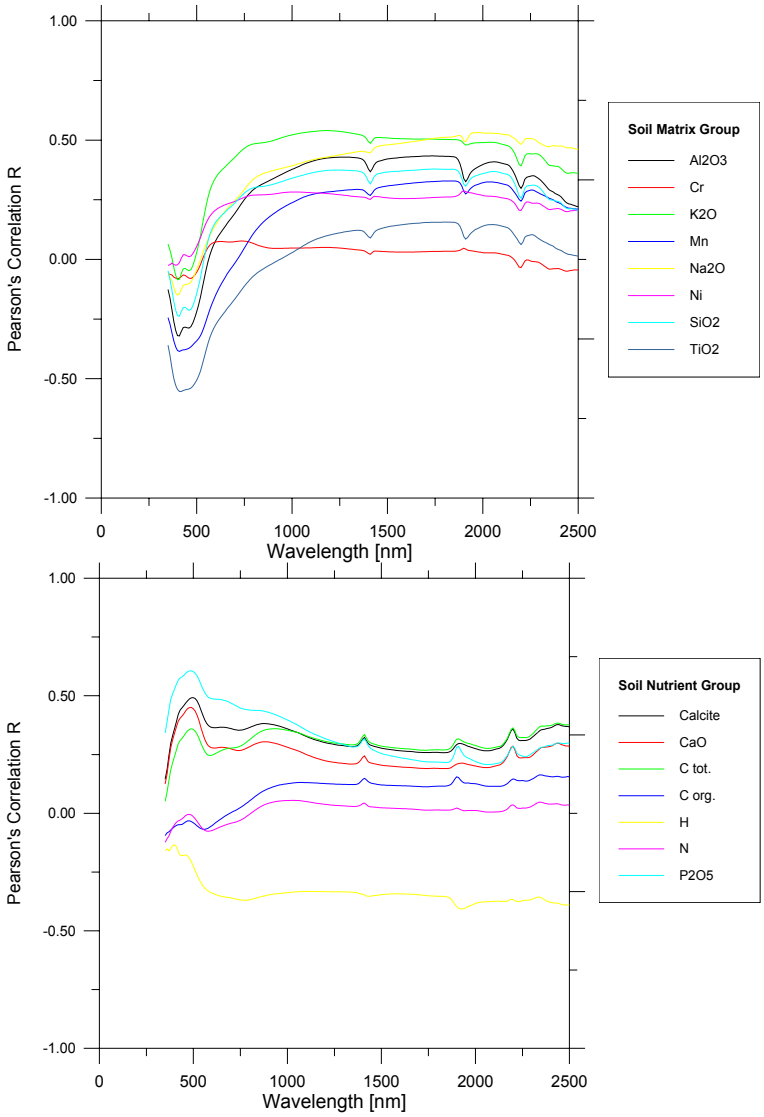

Figure 6.11. (continued) Correlograms of soil constituents and reflectance spectra (10nm). Soil matrix group (top), Organic group (bottom)

It was previously postulated that the transformation of the spectra enhances important absorption features. This should be reflected also in the correlation structure of the correlograms. The changes in the correlation structure of the trace metal group due to the standardisation are used as an example because here the differences are most obvious. The changes after standardisation are very evident (Figure 6.12). Due to the scaling, the reflectance spectra have a zero mean and have positive and negative parts, which have a strong influence on the sign of correlation. After standardisation, there are two spectral features with very strong correlations: a small positive feature at 520 nm and a wide feature with negative correlations centred at 1100 nm. Both can be attributed to iron absorptions. The three other positive peaks at 1400, 1900 and 2200 can be attributed to water and hydroxyl absorptions.

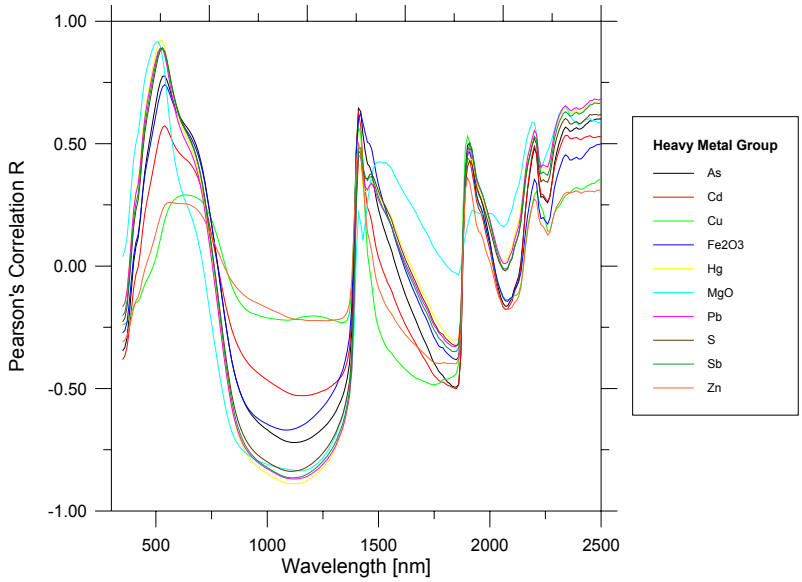

Figure 6.12. Correlograms of soil constituents and standardised reflectance spectra (10 nm). Trace metal group

The example has shown that the transformations have quite a strong influence on the correlation structure. It can be expected that this positively influences the predictive quality of the multivariate calibration models, which will be discussed in the next section.

6.4 Building models using multivariate calibration

In this section, the spectral data described above will be used for the prediction of the chemical soil components. If it is possible to model known data, the models could then be transferred to unknown spectral measurements. However, the first step in the modelling process is calibration. Calibration plays an important role in analytical chemistry. All analytical instrumentation is dependent on a calibration that uses some regression model for a set of calibration samples. This has lead to the development of a number of different calibration methods, which cannot all be treated here (more detailed discussions can be found in the standard literature for chemometrics such as Martens and Naes (1989), Massart et al. (1997, 1998) and Otto (1999).

However, a valuable classification is given by Martens and Naes (1989). The most basic distinction is between univariate and multivariate calibration. Due to the huge number of variables that are produced with today's spectrometers, we will concentrate on multivariate data.

Another basic distinction is between linear and non-linear calibration, e.g. methods that yield linear or non-linear functions for the X-variables. Most of the models focus on linear models, because theory may indicate a linear relationship, e.g. the Lambert-Beer law of the linear relationship between concentration and absorption. Even when the

linear relationship does not hold, it can be a sufficiently good local approximation (Massart et al. 1998).

An important question in multivariate calibration is whether all available X-variables should be used or only a few of them. Many methods can employ only a limited number of predicting variables for purely mathematical reasons. In contrast, the full spectrum methods use all available wavelengths of relevance.

The distinction between direct and indirect calibration is related to the amount of *a priori* information available. All model parameters are known for direct calibration and can be used to construct a predictor. This may be possible in some simple situations (e.g. linear mixtures), but in most analytical situations, such causal calibration is not possible because not all parameters are known due to unknown interferents.

The last distinction concerns two ways of thinking about the calibration modelling: causal vs. predictive modelling. The latter is referred to as forward or inverse modelling, the causal modelling as reverse or classical; this method was the original and basic approach to calibration and is therefore sometimes referred to as classical calibration. In controlled calibration experiments, the X-variables are designed. They can be set exactly at the values prescribed by the experimental design, e.g. calibration standards of known composition can be prepared. In the classical way of thinking, a spectrum can be expressed as a function of its composition. It may work well for one-constituent problems and simple mixtures, but it does not work with spectra, which are affected by unidentified constituents or whose constituents interact.

Three different methods have been selected for this study trying to cover a wide range of the above-mentioned distinctions: multiple linear regression (MLR), partial least squares regression (PLSR) and artificial neural networks (ANN). These methods are all multivariate, indirect models, which perform forward calibration from X to Y. MLR and PLSR are linear methods, with ANN non-linear modelling is possible. MLR can be used as wavelength selection method, if it is combined with appropriate selection methods, PLSR and ANN are full-spectrum methods.

6.4.1 Multiple Linear Regression (MLR)

One of the most widely used spectroscopic quantification methods is Multiple Linear Regression (MLR). It uses the information at a number of wavelengths to isolate the effect of a property of interest on the spectrum. Given a set of data with one dependent variable Y (e.g. property concentration) and i independent variables (e.g. wavelengths) X_1, X_2, …, X_i, the problem is to find the set of constants a, b_1, b_2, …, b_i so that the function:

$$Y^* = a + b_1X_1 + b_2X_2 + \ldots + b_iX_i \qquad \text{Eq. 6.8}$$

is the best to fit the data.

With MLR, it is possible to build models for complex mixtures when only some of the constituent concentrations are known. However, the MLR approach does have some drawbacks. One problem is due to the dimensionality of the matrix equations, which limits the number of selected wavelengths to be smaller than the number of calibration samples.

The reflectances in a spectrum tend to increase and decrease together as the concentrations of the constituents in the mixture change. This linear dependence, known as collinearity, causes the mathematical solution to become less stable with respect to each constituent.

Another problem with adding more wavelengths to the model is an effect known as overfitting. Generally, starting from very few wavelengths, and adding more to the model (provided they are chosen to reflect the constituents of interest) will improve the prediction accuracy. However, at some point, the predictions will start to get worse. When the number of wavelengths increases in the calibration equations, the likelihood that "unknown" samples will vary in exactly the same manner decreases. Using too much information in the spectrum for calibration, the model starts to include the spectral noise, which is unique to the training set, and the prediction accuracy for unknown samples suffers.

In MLR, wavelength selection is critically important to building an accurate model. Ideally, there is a crossover point between selecting enough wavelengths to compute an accurate least squares line and selecting few enough so that the calibration is not overly affected by the collinearity of the spectral data.

There are a number of methods to select which and how many variables to use in the final model. On one side there are the so-called forward selection methods. These start with one wavelength, incorporate further wavelengths one at a time and stop when a certain criterion is met. Another type are the backward elimination methods, which start with the full spectrum and eliminate the wavelengths one by one until a stopping criterion is reached. Finally, there are the best subset selection methods where all possible submodels are tested relative to an optimisation criterion and the best model is selected (Martens & Naes 1989). A number of selection criteria can be applied for each of the selection strategies (see Weisberg (1985) for details).

In this study, a stepwise forward selection method based on the F-test criterion was used. The F-value is calculated for each variable, which is not incorporated at an earlier step, and the variable with the most significant coefficient is included into the model. Variables in the equation whose significance drops below a certain level are removed from the model. The whole process terminates, when no variables reach the significance level. The calibration using stepwise MLR was accomplished in IDL® (Research Systems Incorporate 1999) using the *stepwise.pro* routine, which is based on an algorithm by Afifi & Azen (1971). The significance level for variables to be entered into the model was set to $\alpha = 0.05$ and $\alpha = 0.1$ to be removed.

6.4.2 Partial Least Squares Regression (PLSR)

A more complex way of calibration is the so-called bilinear modelling such as principal components regression (PCR) or PLSR. It is a powerful, flexible approach and yields informative and reliable predictors $\hat{Y} = f(X)$ by projecting the many variables X = (x_1,x_2, …, x_k) onto the few variables $\hat{T} = (\hat{t}_1, \hat{t}_2, \ldots, \hat{t}_a)$. The compressed variables are then used as regressors for y. In this way, the common structures in the X-variables are compressed into a stabilised, more easily interpretable model, leaving out much of the noise and not relevant information (Martens & Naes 1989).

The data compression applied in PCR gives substantial improvement over ordinary MLR in the modelling of collinear data. The important problem is the choice of the right number of eigenvectors. Nevertheless, sometimes improvements in PCR can be obtained by leaving out some major eigenvectors, since they correspond to phenomena in X of no relevance for modelling Y.

PLSR is an extension of classical PCR. The concept of partial least squares (PLS) was developed by H. Wold (1981) in the field of economy and social sciences and propagated to the field of chemometrics by his son S. Wold (Wold et al. 1983). PLSR differs from PCR by using the Y-variables actively during the bilinear decomposition of X. By balancing the X- and Y-information, the method reduces the impact of large, but irrelevant variations in the calibration modelling (Martens & Naes 1989).

PLSR is now dominating the practice in multivariate calibration because of the quality of calibration models and because it is implemented in many commercial software packages (Brown et al. (1996), Lavine (1998) and references therein). For more detailed discussions of the algorithm, see e.g. Haaland & Thomas (1988a, 1988b) or Massart et al. (1997, 1998). The description used here is based on the review of Wold et al. (2001).

The PLSR model is developed from a training set of N observations (soil samples in this study) with K X-variables (spectral bands) and M Y-variables (soil constituents). These training data form the matrices X and Y with dimensions (N*K) and (N*M), respectively.

The linear PLSR model finds new variables, which are estimates of the latent variables or their rotations. They are few in number and orthogonal. These new variables T are called X-scores and are linear combinations of the original variables X and with the weights (or coefficients) W:

$$T = XW \qquad \text{Eq. 6.9}$$

The X-scores T, multiplied by the loadings P, good summaries of X, so that the residuals E are small:

$$X = TP' + E \qquad \text{Eq. 6.10}$$

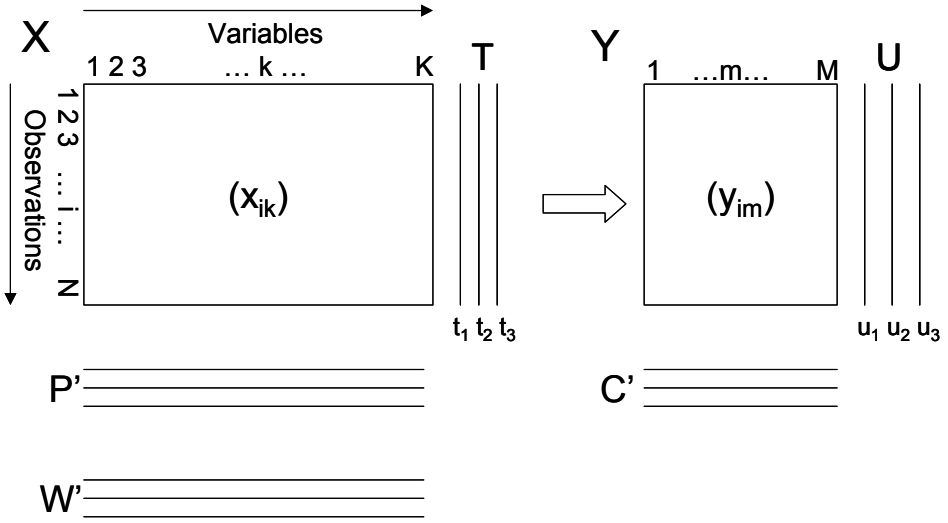

Figure 6.13: Data arrangement for PLSR (from Wold et al. 2001). The variables are described in the text.

With multivariate Y (when M > 1), the corresponding Y-scores U, multiplied by the loadings Q are good summaries of Y, so that the residuals F are small:

$$Y = UC' + G \qquad \text{Eq. 6.11}$$

The X-scores T are also good predictors of Y:

$$Y = TC' + F \qquad \text{Eq. 6.12}$$

The Y residuals G express the deviations between observed and modelled responses and comprise the elements of the Y residual matrix G.

Because of Eq. (6.9), Eq. (6.12) can be rewritten to resemble a multiple regression model:

$$Y = XW \cdot C' + F = XB + F \qquad \text{Eq. 6.13}$$

The PLS-regression coefficients can be written as:

$$B = W \cdot C' \qquad \text{Eq. 6.14}$$

The score matrices T and U contain information about the objects and their similarities/dissimilarities with respect to the given model and problem for the interpretation of the PLSR model. The weights W and C give information about how the variables combine to form a quantitative relationship between X and Y, thus providing an interpretation of the weights T and U. Therefore, the weights are important for an understanding of which X-variables are important (e.g. having large numerical weight

values) and which provide the same information (e.g. having similar profiles of weights) (Wold et al. 2001).

All parameters T, U, W, P and C are calculated by a PLSR algorithm. There are several variants developed for different types of data. The algorithms work either with (scaled and centred) original data or with variance-covariance matrices. The most common algorithm is the non-linear partial least squares (NIPALS) algorithm, which is numerically and statistically very stable (Wold et al. 1983). It is also used in this study.

The calibration with PLSR was achieved using the N-way toolbox for Matlab, which is a freely available collection of functions and algorithms for modelling multiway data sets by a range of multilinear models (Anderson & Bro 2000).

6.4.3 Artificial Neural Networks (ANN)

Artificial neural networks were first developed as a model of the human brain structure. It turned out that these simplified, computerised models are capable of handling non-linearities in problems of modelling and pattern recognition without requiring knowledge of underlying functions or distributions, which is a great advantage over classical statistical techniques (Brown et al. 1996).

Many different types of networks have been developed. They all consist of small units (neurons) that are interconnected. The local behaviour of these units determines the overall behaviour of the network. The most common is the multi-layer-feed-forward network (MLF), which was also applied in this study. A good overview of other neural networks types and learning algorithms is given by Zell (1994). The description used here is based on Massart et al. (1998), Despagne & Massart (1998) and Zupan & Gasteiger (1993).

The following gives an overview of the basic concepts of neural networks, describes the MLF and the standard back propagation to facilitate the understanding of the resilient propagation learning rule, which was used in this study.

The basic structural unit of ANN is the neuron, an abstraction of the biological neuron. A biological neuron consists of a cell body from which many branches (dendrites and axon) grow in various directions. Impulses are received through the dendrites. In the cell body, these signals are checked and integrated. When a certain threshold impulse is reached, a suitable response signal is delivered. The axon transports the response signal to other neurons through a complex branching system. The contact points between different nerve cells, through which the signals are propagated, are called synapses. The efficiency of the propagation of signals from one cell to another is influenced by various chemical and electrical factors. However, the basic processes are the same for all neurons. Hence, the overall behaviour of a neural system is determined by the neural connecting structure.

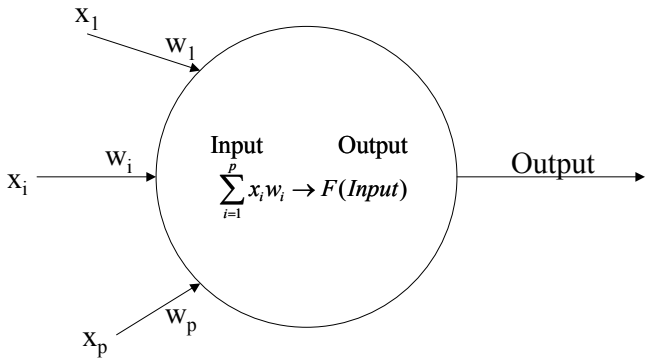

Figure 6.14. Artificial neuron. $x_1,...,x_p$ are incoming signals, $w_1,...w_p$ are the corresponding weight factors, F is the transfer function.

The artificial neurons are a strong simplification of the processes that take place in biological neurons. The basic process of information reception, integration and weighted output in ANN neurons is shown in Figure 6.14. The incoming signals are passed to the neuron body, where they are weighted and summed. Then they are transformed with the help of a transfer function into the output signal. The propagation of the signal is determined by the connections between the neurons and by their associated weights.

The different types of networks are distinguished by their different connection pattern, since this determines the information flow through the network. The weights are equally essential, because they determine, in combination with the connection pattern, the signal flow through the network. Each signal that is transported through a connection is multiplied by the associated weight. The appropriate setting of the weights is essential for their proper performance. They determine the relationship between input and eventual output of the network. Therefore, they are considered the distributed knowledge content of the network. Finding the proper weight setting is achieved in a training phase in which the weights are adapted according to a learning rule. This is the major phase of the developing process of ANN (Massart et al. 1998).

MLF networks became popular after Rumelhart et al. (1986) published the back-propagation learning rule, which allowed a training of more than one layer network. In analytical chemistry more than 90 % of applications are based on this learning algorithm (Otto 1999).

The general structure of a MLF network is shown in Figure 6.15. The network is ordered in layers: input, hidden and output layer. All neurons in a layer are connected to all neurons of the following layer. The network receives the input signals through the input layer. The number of neurons is determined by *p*, the number of variables in the (*n***p*) matrix *X*. In this study, the matrix *X* consists of the spectra, *p* refers to the number of wavelengths and n is the number of samples. The information is then passed to the hidden layer(s). There may be zero, one or more hidden layers, but in the majority of

applications only one layer is used. The number of neurons in the hidden layer(s) has to be determined empirically. Finally, information is forwarded to the output layer that produces the response of the network. The number of neurons in the output layer is determined by *q*, the number of variables in the (*n***q*) matrix *Y*. In this study, the output matrix refers to the soil constituents that are to be predicted.

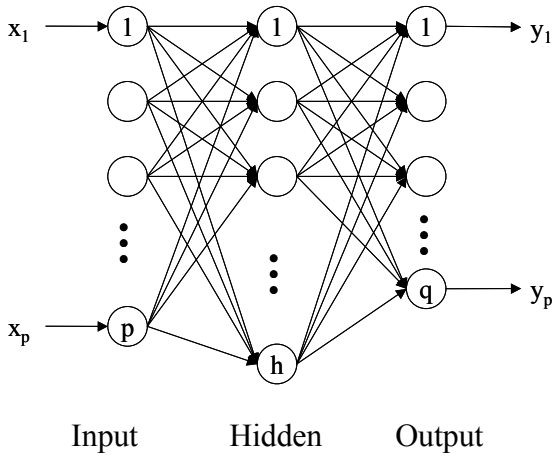

Figure 6.15. General structure of a MLF network

For each sample *n*, each unit, or neuron, in the input layer is fed with one variable of the *X* matrix, and each unit in the output layer is fed with one variable of the *Y* matrix. The values are passed unchanged to the hidden layer. Each hidden unit *h* receives the signals from the *p* neurons of the input layer. From these signals the net input is calculated:

$$NET_j(x_i) = x_i^T w_i^T \qquad \text{Eq. 6.12}$$

where $x_i^T = [x_{i1}, x_{i2}, ..., x_{ip}]$ is the input vector,

$w_j^T = [w_{j1}, w_{j2}, ..., w_{jp}]$ is the weight vector associated with the hidden unit *j*.

The net input NET_j is then passed to the transfer function that transforms it into the output signal of the unit. Different transfer functions may be used, the most common non-linear one is the sigmoidal function:

$$output_j = o_j = sf(NET_j) = \frac{1}{1 + e^{-(NET(x))}} \qquad \text{Eq. 6.13}$$

The output units receive the weighted output signals of the *h* hidden units. The weighted sums are calculated and passed through the transfer function to yield the final output of the network

$$NET_j(o_i) = o_i^T w_i^T \qquad \text{Eq. 6.14}$$

where $O_i^T = [O_{i1}, O_{i2}, \ldots, O_{ih}]$ is the input vector to the output units.

The signals are only forwarded from one layer to the next, not to the neurons within the same layer.

In MLF, supervised training optimises the proper setting of the weights. During the training the weights are adapted according to the learning rule. The original learning rule is the back-propagation rule (Verbos (1974), Rumelhart et al. (1986)). The weight updates are based on the differences between actual and desired network output of the training set.

The training is initialised with random weights. For each output unit *j*, the error E_j between output value and desired output using the current weight setting is calculated:

$$E_j = \frac{1}{2}(d_j - o_j)^2 \qquad \text{Eq. 6.15}$$

The error E_j is determined by the weights; d_j is the teaching input (e.g. a measured concentration). The factor ½ is used in order to cancel later the value 2, which forms after differentiation. For the estimation of optimal weights, it does not matter if the full or half error is optimised (Zell 1994). The weight adaptation of the output neurons is carried out as follows:

$$\Delta w_{hj} = \eta \delta_j o_h \qquad \text{Eq. 6.16}$$

w_{hj} is the weight between the *h*th hidden unit and the *j*th output unit; η is the learning rate, a positive constant between 0 and 1; o_h is the output of the *h*th hidden unit and δ is a term based on the error.

In back-propagation, the weight adaptation is made in the direction that minimizes the error; it is essentially a gradient-based optimisation method. Hence, the gradient of the error as a function of the weights must be calculated. This leads to the following equation:

$$\delta_j = (d_j - o_j)\frac{d(sf(NET_j))}{sf(NET_j)} = (d_j - o_j)sf(NET_j)[1 - sf(NET_j)] \qquad \text{Eq. 6.17}$$

$sf(NET_j)$ represents the value of the sigmoidal function NET_j.

The adaptation of the weights to the hidden layer in back-propagation is calculated from the errors of the output neurons:

$$\delta_j = \frac{d(sf(NET_j))}{d(NET_j)} \sum_{k=1}^{q} \delta_k w_{jk} = sf(NET_j)[1 - sf(NET_j)] \sum_{k=1}^{q} \delta_k w_{jk} \qquad \text{Eq. 6.18}$$

In this equation, k represents the units of the output layer.

All weights can be calculated using equations (5) and (7). Now it becomes clear that the error is back-propagated through the network. The process is repeated for all input pattern. One iteration is defined as one weight correction for all samples.

In equation (5), the learning rate η was introduced. This term is important for the training procedure. If it is small, the convergence of the weights to an optimum will be slow and there is a risk of becoming trapped in a local optimum. On the other hand, the system may start oscillating if the chosen learning rate is too high.

The slow convergence of the basic algorithm and its tendency to become trapped in one of the many local minima in the error surface triggered the need for improvements and many algorithms have been proposed to deal with the problem of appropriate weight update by parameter update during learning (Zell 1994).

In this study, the 'resilient propagation' (RPROP, Riedmiller & Braun 1993) learning algorithm was used. In several studies, it has been tested regarding the sensitivity of the learning parameters against other algorithms such as standard back-propagation, Quickprop and SuperSAB (Riedmiller & Braun 1993, Braun 1997, Udelhoven & Schütt 2000). RPROP was most insensitive for the initial learning rate and, together with Quickprop, the training rates were considerably faster, but the RPROP was more robust concerning the tuning of the parameters.

The algorithm combines ideas of different adaptive learning schemes. The basic principle of RPROP is to eliminate the harmful influence of the size of the partial derivative on the weight step. The weights are not changed according to the gradient in the error function, but according to the sign of the gradient. The size of the weight change is exclusively determined by a weight specific 'update value':

$$\Delta w_{ij}(n) = \begin{cases} -\Delta_{ij}^{(n)}, if \dfrac{\partial E^{(n)}}{\partial w_{ij}(n)} > 0 \\ +\Delta_{ij}^{(n)}, if \dfrac{\partial E^{(n)}}{\partial w_{ij}(n)} < 0 \\ 0, else \end{cases} \qquad \text{Eq. 6.19}$$

where $\dfrac{\partial E^{(n)}}{\partial w_{ij}(n)}$ denotes the summed gradient information over all patterns in the pattern set. RPROP is a 'batch learning' or 'offline' algorithm, because it adapts the weights only after presentation of all training patterns.

The second step of RPROP learning is to determine the update-value $\Delta_{ij}^{(n)}$. This is based on a sign dependent adaptation process:

$$\Delta_{ij}(n) = \begin{cases} \eta^{+} \cdot \Delta_{ij}^{(n-1)}, if \frac{\partial E^{(n-1)}}{\partial w_{ij}} \cdot \frac{\partial E^{(n)}}{\partial w_{ij}} > 0 \\ \eta^{-} \cdot \Delta_{ij}^{(n-1)}, if \frac{\partial E^{(n-1)}}{\partial w_{ij}} \cdot \frac{\partial E^{(n)}}{\partial w_{ij}} < 0 \\ \Delta_{ij}^{(n-1)}, else \end{cases} \qquad \text{Eq. 6.20}$$

where $0 < \eta^{-} < 1 < \eta^{+}$

Every time the partial derivative of the corresponding weight w_{ij} changes its sign, which indicates that the last update was too big and the algorithm has jumped over a local minimum, the update-value $\Delta_{ij}^{(n)}$ is decreased by the factor η^{-}. If the derivative retains its sign, the update-value is slightly increased to accelerate convergence in flat regions. Additionally, in the case of a change in sign, there is no adaptation in the succeeding learning step.

The building and training of the ANN was accomplished using the Stuttgart Neural Network Simulator (SNNS, version 4.2) in the following way:

1. In a test series, the optimal size of the multi-layer-feed-forward network (MLF) was defined. The test series resulted in a network with only one hidden layer and a ratio between hidden and input neurons set to 0.15.
2. In a second test series, the optimal learning parameters were determined for the resilient propagation algorithm. The initial update value Δ_0, which directly determines the size of the first weight step was set to 0.1. The maximum weight step Δ_{max}, which prevents the weights from becoming too large, was set to 50; and finally the weight decay term α, which determines the relationship between the output error and the reduction in the size of the weights, is set to 10^4.
3. Finally, the training of the different data sets was accomplished with training and monitoring sets.

6.4.4 Results and discussion of modelling

6.4.4.1 Modelling set up

Validation of the models is of fundamental importance for multivariate calibration. To achieve this, the data set was split into a calibration set and a validation set. However, only for MLR is the validation set a validation set in its' strictest sense, because both

PLSR and ANN use the validation set for the model definition (PLSR use the data to determine the number of principal components used in the model; for ANN the validation error determines the end of the training). In that case the validation set is referred to as monitoring set.

The data were sorted from lowest to highest lead concentration (lead was chosen, because it is one of the key elements of the contamination). The samples were divided into two groups by taking odd-numbered spectra for the calibration group and even-numbered samples for the validation group. In such a way, both sets represent approximately the full range of concentrations. The samples of the artificial mixture series were added to the 214 samples collected in 1999, which resulted in a data set of 238 samples. These were split into a calibration and a validation set, consisting of 119 samples each. The calibration was done twice with an exchange of the calibration and validation sets.

The analysis of correlation matrix and correlograms revealed a grouping of the elements, which was also used for multivariate calibration in order to maximize the model quality. Based on their correlation structure in the correlograms, three groups were selected, which were modelled together in PLSR and ANN (in MLR elements are modelled one at a time):

Trace Metals: As, Cd, Cu, Fe_2O_3, Hg, MgO, Pb, S, Sb, Zn

Soil Matrix: Al_2O_3, Cr, K_2O, Mn, Na_2O, Ni, SiO_2, TiO_2

Carbonatic/organic soil fraction: Calcite, CaO, C_{tot}, C_{org}, H, N, P_2O_5

The trace metal group was used to test the different methods and data preprocessing combinations. The best method was then more thoroughly checked for quality and optimised. Finally, it was used for further predictions.

The prediction quality of the models and the selection of the best model are based on the validation set. This approach gives the best estimate of the model's performance since none of the samples in the validation set were used to build the model. In general, the prediction error is calculated as predictive residuals sum of squares (PRESS) from:

$$PRESS = \sum (y_i - \hat{y}_i)^2 \qquad \text{Eq. 6.21}$$

The root mean square value of the prediction error is derived from PRESS as:

$$RMSPE = \sqrt{\frac{PRESS}{n}} \qquad \text{Eq. 6.22}$$

Correlations of measured versus predicted concentration are expressed as coefficients of determination (R^2). Due to the skewed distribution of concentration values, the

coefficient of determination would overestimate the quality of the results. Therefore, additional error measures were calculated. The standard error of prediction (SEP) was calculated as standard deviation of differences between reference values and predicted values. From the SEP, two other measures were derived for the evaluation of the model quality. The relative percent difference (RPD) is the ratio of the standard deviation of the reference chemistry to the SEP. It should be as high as possible (RPD > 3 for prediction purposes). The relative error ratio (RER) is the ratio of the range in the prediction set to the SEP. It should be greater than 10 (Malley & Williams 1997).

6.4.4.2 MLR models

The models derived with the stepwise MLR algorithm achieved good results for some elements. However, due to the limitations of the algorithm, it caused problems in calibration of models with many wavelengths (1 or 5 nm). The F-value selection criterion was not able to select a number of wavelengths smaller or equal to the number of observations for these wavelength intervals. Even a decrease of the F-value could not overcome the problem. Nevertheless, for the other wavelength intervals, reliable results could be achieved (Table 6.3).

Table 6.3. Prediction results for MLR (validation set)*

Elements	*R²*	*SEP*	*RPD*	*RER*	*PRESS*	*RMSE*	*FWHM*	*Method*
As	0.847	0.0079	3.12	17.62	0.0137	0.0107	20	vec
Cd	0.528	0.079	1.04	6.53	0.929	0.0258	hymap	std
Cu	0.54	0.0858	1.23	6.95	1.5537	0.1143	10	abs
Fe_2O_3	0.718	0.0449	2.17	10.09	0.4015	0.0581	20	abs
Hg	0.955	0.023	5.82	33.02	0.1174	0.0314	20	vec
MgO	0.941	0.0247	5.81	35.98	0.1558	0.0362	10	vec
Pb	0.944	0.0312	5.3	30	0.1858	0.0088	10	std
S	0.83	0.0439	2.4	12.8	0.2836	0.0084	50	std
Sb	0.93	0.0296	4.55	25.87	0.16	0.0084	50	std
Zn	0.213	0.0832	0.56	2.22	1.0247	0.0932	20	ref

*** FWHM denotes the wavelength interval yielding the best results; Method refers to the type of transformation (abs) absorption, der1) 1st derivative, der2) 2nd derivative, ref) reflectance, std) standardisation, vec) vector standardization)**

Very good results were achieved for Hg, Pb, Sb and MgO with coefficients of determination above 0.9. Also the RPD and RER are very high with values above 4 and 25, respectively. The results obtained for As, Fe_2O_3 and S are also significant with R^2's between 0.7 and 0.9. The RER is above 10, but the RPD drops below 3 for Fe_2O_3 and S. The prediction for Cd and Cu was not satisfactory with R^2's below 0.55. The prediction

of Zn was not possible using MLR. The best prediction results were achieved with absorption, standardisation and vector normalisation; but the latter two are more reliable, because they were selected mainly for the elements with the best predictive results (e.g. Hg, Pb). Derivatives and reflectance spectra were not useful for prediction with MLR i.e., the prediction results obtained with these spectra were generally in the lower part of the prediction quality range. The best resampling intervals are generally longer FWHM with a slight preference of 20 nm intervals. However, this selection is strongly influenced by the above-mentioned limitations of the algorithm with too many input variables. The collinearity is a problem even in the models selected. It becomes obvious when analysing the wavelengths selected by the different MLR models (Table 6.4). In many models, adjacent wavelengths have been selected, like the first three bands (360, 380, 400 nm) in the As-model or the two wavelengths 1860 and 1800 nm in the Fe_2O_3 prediction model.

Nevertheless, this table also provides valuable information for the interpretation of the models, since the wavelengths in the models represent spectral features that are directly linked to certain spectrally active constituents (e.g. Fe^{3+}, H_2O, etc.).

Table 6.4. Number of variables selected for optimal prediction (first line) and central wavelength positions [nm] of the selected variables in the order of their selection

As	Cd	Cu	Fe_2O_3	Hg	MgO	Pb	S	Sb	Zn
7	4	4	5	8	7	8	6	7	4
380	1222	1400	860	380	1160	2290	1125	1125	1720
1400	1346	460	1580	860	2140	2160	2225	775	2340
360	981	430	1880	1380	2220	1170	1225	2075	1680
400	1401	1450	1920	2060	2490	1930	2075	1875	380
2340			1860	360	1920	2300	2175	2225	
2200				400	620	350	1375	2175	
520				1860	2250	2250		1825	
				1400		1940			

6.4.4.3 ANN models

The calibration of ANN is more complex than MLR, because more decisions have to be taken concerning network architectures, size of the network, learning algorithms, learning parameters, etc. Only after these decisions have been taken can the calibration process start. Subsequently a further decision has to be made, namely when to stop training. If it is stopped too early, the prediction results will be poor. If the network ‘learns’ for too long (e.g. too many learning cycles), overfitting reduces the predictive power of the model, because it learnt exactly the relationship presented in the training set, but lost all generalisation capabilities.

Hence, in this case the training was controlled by the monitoring set. After every learning cycle, the calibration and the validation error were plotted and the training was

terminated when the rate of the improvement in the monitoring set had reached a minimum; longer learning cycles showed that the error asymptotically approaches a constant. Thus, the training was terminated after 30 to 70 cycles; the more wavelengths used, the longer the training. The initial weights were determined randomly. Therefore, the results vary each time the network is re-initialised. In order to account for these variations, the network was initialised five times and the best model was selected.

The results of the prediction for the validation set are presented in Table 6.5. Best results were achieved for Pb, Sb, Hg, MgO with R^2's above 0.9, RPD's above 3 and RER's above 20. The coefficient of determination for As is below 0.9, but the high RPD and RER indicate that also for As the models could be used for prediction purposes. Reliable results are also obtained for S and Fe_2O_3, however, the RPD drops below the threshold of 3.0. The prediction quality for Cd, Cu and Zn, in contrast, is less reliable.

The best transformations in ANN models were the derivatives, mainly the first order; only in one occasion did standardisation yield better results. A comparison with derivatives calculated using the finite difference method showed that the 'Savitzky-Golay derivatives' yield considerably better results and should be preferred. Best resampling intervals are generally longer wavelengths with an optimum at 20 nm. The prediction results achieved with the different combinations were very similar, which proves that the ANN models are very robust and provide stable results for a wide range of different inputs.

Table 6.5. Prediction results of ANN (monitoring set)*

Element	*R²*	*SEP*	*RPD*	*RER*	*PRESS*	*RMSEP*	*FWHM*	*Method*
As	0.858	0.0073	3.28	15.88	0.0125	0.0103	20	der2
Cd	0.494	0.085	0.96	4.32	1.0474	0.0942	20	der1
Cu	0.446	0.0965	0.84	4.57	1.9661	0.1291	1	der1
Fe_2O_3	0.714	0.0447	1.98	9.83	0.4057	0.0586	10	der1
Hg	0.928	0.0335	4.12	21	0.1735	0.038	20	der2
MgO	0.903	0.032	3.86	21.33	0.2827	0.0489	10	der1
Pb	0.934	0.0285	5.53	27.74	0.19	0.0401	50	der1
S	0.845	0.041	2.66	13.05	0.2658	0.047	20	std
Sb	0.932	0.0267	5	25.11	0.1538	0.0361	50	der1
Zn	0.22	0.0861	0.51	2.17	1.0736	0.0954	20	der1

*** FWHM denotes the wavelength interval yielding the best results; Method refers to the type of transformation (abs) absorption, der1) 1st derivative, der2) 2nd derivative, ref) reflectance, std) standardisation, vec) vector standardization)**

6.4.4.4 PLSR models

One of the most difficult tasks in using PLSR is determining the correct number of loading vectors to use to model the data. The first vectors in the model are most likely to be the ones related to the constituents of interest, while later vectors generally have less information that is useful for predicting concentration. In fact, if these vectors are included in the model, the predictions can actually be worse than if ignored altogether. Thus, decomposing spectra with PLSR and selecting the correct number of loading vectors is a very effective way of filtering out noise. However, if too few vectors are used to construct the model, the prediction accuracy for unknown samples will suffer since not enough terms are used to model all the spectral variations that make up the constituents of interest. Therefore, it is very important to define a model that contains enough vectors to properly model the components of interest without adding too much contribution from the noise.

To avoid building a model that is either an overfit or an underfit, the number of factors where the PRESS plot reaches a minimum would be the obvious choice for the best model. While the minimum of the PRESS may be the best choice for predicting the particular set of samples, it is however, unlikely to be the optimum choice for all unknown samples.

Since there is a finite number of samples in the set used for prediction, in many cases the number of factors that gives a minimum PRESS value can still create an overfit for predicting unknown samples. In other words, there is a statistical possibility that some of the "noise" vectors from the spectral decomposition may be present in more than one sample. These vectors can appear to improve the calibration by a small amount when, by random correlation, they are added to the model. However, if these exact same noise vectors are not present in unknown (future) samples, the predicted concentrations will have significantly larger prediction errors than if those additional vectors were left out of the model.

A solution to this problem has been suggested by Haaland & Thomas (1988a) in which the PRESS values for all previous factors are compared to the PRESS value at the minimum. The ratio between these values can be calculated and assigned a statistical significance based on the number of samples used in the calibration set:

$$Fratio_i = \frac{PRESS_i}{PRESS_{\min}} \qquad \text{Eq. 6.23}$$

This ratio is an indicator of the relative significance of each model to the model with the number of factors at the minimum of the PRESS. The number of factors where the F-ratio falls below a predefined significance level determines the optimum number of factors for a model used for predicting unknowns:

$Fratio_i < F_{\alpha;m,m}$, where $F_{\alpha;m,m}$ is the (1-α) percentile of Snedecor's F distribution with m and m degrees of freedom (m is the number of calibration samples). Haaland & Thomas (1988a) found that α = 0.25 is a good compromise in practice, and this was also adopted for this study.

The best prediction results for each element are shown in Table 6.6. As for the previous methods, the best prediction results could be obtained for As, Hg, Mg, Pb and Sb with high R^2's, RPD and RER. These are clearly above the threshold values for prediction. Fe_2O_3 and S were also predicted satisfactorily. Again, the results for Cd, Cu and particularly Zn were insufficient. The results in Table 6.6 show only the best results. However, the predictions obtained with PLSR are very similar regarding resampling intervals. The best results indicate that smaller wavelength intervals are preferred or at least yield as good results as the broader resampling intervals. Concerning transformation types, standardised and vector-normalised spectra were preferred over reflectance and derivatives.

Table 6.6. Prediction results for PLSR (monitoring set)*

Elements	*R²*	*SEP*	*RPD*	*RER*	*PRESS*	*RMSEP*	*FWHM*	*Method*	*Factors*
As	0.862	0.0266	17.39	3.68	0.0122	0.0101	1	abs	9
Cd	0.506	0.0921	1.16	5.05	1.0014	0.0917	hymap	abs	11
Cu	0.581	0.1311	1.58	7.9	1.383	0.1078	1	vec	12
Fe_2O_3	0.718	0.0969	10.57	2.1	0.4015	0.0581	5	abs	9
Hg	0.95	0.1425	30.57	5.8	0.1255	0.0325	20	std	9
MgO	0.936	0.1424	32.6	5.5	0.1667	0.0374	20	vec	10
Pb	0.945	0.164	30.16	5.65	0.1778	0.0387	1	std	9
S	0.826	0.1066	12.45	2.44	0.2863	0.049	hymap	std	9
Sb	0.934	0.1359	25.87	4.84	0.15	0.0355	1	std	9
Zn	0.3	0.0546	3.6	0.68	0.9527	0.0895	20	vec	10

*** FWHM denotes the wavelength interval yielding the best results; Method refers to the type of transformation (abs) absorption, der1) 1st derivative, der2) 2nd derivative, ref) reflectance, std) standardisation, vec) vector standardization); Factors denotes the number of factors used in the model**

The PLSR algorithm applied in this study has the ability to model and analyse several Y's simultaneously, which has the advantage of giving a simpler overall picture than having one separate model for each Y-variable. It is particularly useful, when, like in the case of the heavy metals, the Y-variables are correlated (Wold et al. 2001). This is of course only possible with a single spectral input. Hence, the spectral combination generating the smallest PRESS for all predicted elements was selected for further analysis. Best overall results were achieved with 10 nm vector-normalised spectra (Table 6.7).

Table 6.7. PLSR Prediction results for vector-normalised data with 10 nm FWHM (monitoring set)

Elements	*R^2*	*SEP*	*RPD*	*RER*	*PRESS*	*RMSEP*
As	0.849	0.0266	3.62	18.58	0.0133	0.0106
Cd	0.581	0.0948	1.29	6.11	0.7728	0.0806
Cu	0.521	0.1249	1.55	8.52	1.6394	0.1174
Fe_2O_3	0.721	0.0989	2.03	9.93	0.459	0.0621
Hg	0.935	0.1453	5.03	26.43	0.1031	0.0294
MgO	0.936	0.1419	5.48	32.62	0.1901	0.04
Pb	0.933	0.1689	5.03	27.1	0.2264	0.0436
S	0.787	0.1058	2.18	11.47	0.346	0.0539
Sb	0.918	0.1395	4.36	23.34	0.1953	0.0405
Zn	0.299	0.0538	0.67	3.48	0.9943	0.0914

6.4.4.5 Final model selection and analysis

The predictions obtained with the three different methods yield very similar results, which are summarised in Figure 6.16. Considerable differences can be observed for Cd, Cu and Zn. However, the models predictive capacities are poor; hence the predictive quality should not be used as a single criterion for the selection of the best model.

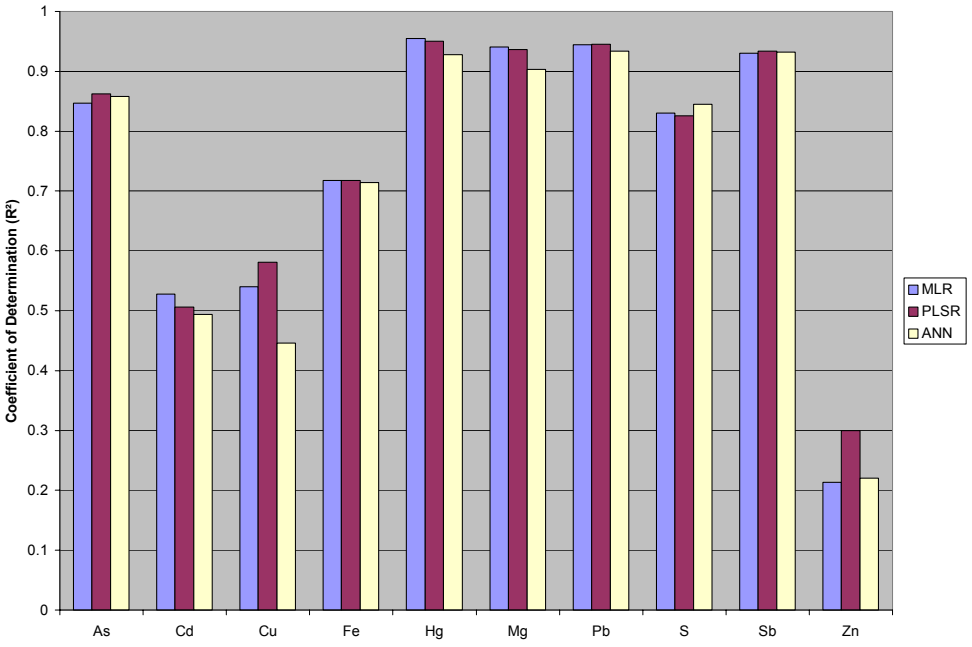

Figure 6.16. Coefficients of determination for the best results obtained with the three methods MLR, PLSR and ANN for the heavy metal group.

MLR had some problems in the wavelengths selection due to the strong collinearity in the data. Nevertheless, it proved to be a valuable tool for multivariate calibration and may be even preferable over the other methods in some cases due to its straightforward

interpretability, since the estimated parameters relate the property of interest linearly to a set of original variables; but PLSR and ANN have the ability to model and analyse several constituents together, which is considerably faster and simplifies the overall picture. Moreover, correlations between the Y-variables can be exploited. Hence, MLR was not used for further modelling.

The predictive quality is again exploited for the comparison of the two remaining methods; the results of PLSR are in nine out of ten cases slightly superior. This might be caused by a linear behaviour of the heavy metals with regard to the reflectance spectra. In such cases Despagne & Massart (1998) recommend the use of linear models. Following these recommendations, the PLSR was selected. It proved to be a very robust method being able to handle highly collinear data sets with large amounts of X variables. Also with different spectral transformations comparable results could be obtained.

6.4.4.6 Outlier detection

The presence of outliers may have a detrimental effect on the quality of the calibration model. Therefore, the identification of outliers is an important part of the modelling process. Outliers usually arise from some incorrect measurement, whether it is in the concentration data, or in the spectral data. The inclusion of outlier samples in the training set will introduce a bias to the final model. In effect, outlier samples will tend to 'pull' the model in their direction, causing the predicted concentrations of valid samples to be less accurate (or even erroneous) than if the sample was completely eliminated from the training set. A discussion of standard diagnostic tools for the detection of calibration and prediction outliers is given by Martens & Naes (1989). There are two approaches for outlier detection. The first approach is to fit the data with least squares, construct regression diagnostics and remove the outliers. The second approach is to construct estimators that fit the majority of data and examine the residuals from this fit to detect the outliers (Pell 2000).

A tool for outlier detection is the cross-validation procedure, which is often used as a validation method. The most common approach is the Leave-Out-One (LOO) procedure, where n calibration steps are calculated leaving out one sample at a time. The samples not included are then used to assess the PRESS of the cross validation (Figure 6.17). The model attempts to account for all the variations in the training data when the calibration calculations are performed, thus rendering approximately the same prediction error for most of the samples should be approximately the same. Samples that have significantly larger concentration residuals than the rest of the training set are known as concentration outliers. The samples az092 and az125 are significantly different from the rest of the training set and represent the most likely outliers. However, with the samples az126 or az146 such a decision based on visual

interpretation is more difficult and a mathematical way to accurately determine the likelihood that a sample is really an outlier is needed.

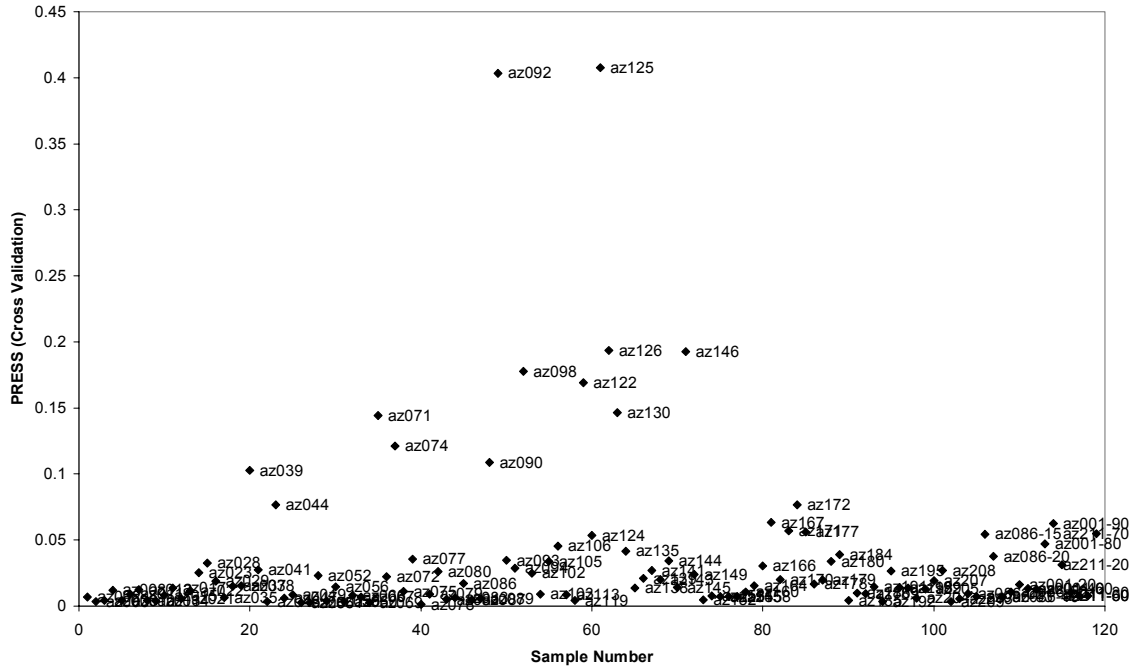

Figure 6.17. Cross Validation of vector normalised data (10 nm). High values signalise potential outliers

The F-test method for determining the optimum number of factors from PRESS analysis is also useful for determining the statistical significance of a sample's concentration residual with respect to the rest of the training set. In this case, the F-ratio value is calculated by:

$$F_{\alpha;1,n-1}(c_i) = \frac{(n-1)(e_{c_i})^2}{(\sum_{i \neq j} e_{c_j}{}^2)} \qquad \text{Eq. 6.24}$$

where i is the number of the sample being tested, n is the number of samples in the training set and e_{c_i} is the difference between measured and predicted concentration for the i-th sample left out during cross validation. Generally, samples that exhibit probabilities of 0.99 (α=0.01) are considered outliers and should be removed from the training set before calculating the final calibration model (Haaland & Thomas 1988a).

Four samples were deleted from the model for the vector-normalised data set with a FWHM of 10 nm before final calibration. However, this did not influence the prediction results significantly (Table 6.8).

Table 6.8. Final prediction results after outlier detection for vector-normalised data, 10 nm (validation) using PLSR

Elements	*R²*	*SEP*	*RPD*	*RER*	*PRESS*	*RMSEP*
As	0.843	0.0242	2.96	15	0.0139	0.0108
Cd	0.524	0.0772	0.91	4.45	1.0125	0.0922
Cu	0.568	0.1169	1.41	7.71	1.4402	0.11
Fe_2O_3	0.725	0.0894	1.8	9.39	0.4004	0.058
Hg	0.932	0.1416	4.89	26.29	0.1663	0.0374
MgO	0.935	0.1375	5.15	32.02	0.1738	0.0382
Pb	0.942	0.1632	5.24	28.25	0.1878	0.0397
S	0.796	0.1024	2.12	11.02	0.3419	0.0536
Sb	0.924	0.135	4.39	23.28	0.1745	0.0383
Zn	0.27	0.0395	0.46	2.07	1.0314	0.0931

It was possible to estimate seven elements out of ten with high precision. Coefficients of determination for Hg, Pb, Mg and Sb are above 0.9. Also RPDs > 4 and RER > 20 are indicative of very good models. The validation results for As, Fe and S gave R²s between 0.7 and 0.9, RPDs between 2 and 3 and RERs between 9 and 16, which can also be considered as satisfactory. The models didn't provide a reliable prediction for Cd, Cu and Zn. The poor prediction quality can be attributed to different geochemical behaviour. According to Blume & Brümmer (1991) and Ainsworth et al. (1991) the solubility of trace metals decreases in the following order: Cd > Zn > Cu >As > Hg ~ Pb ~ Sb. Accordingly, Simon et al. (2001) found that the larger part of the Cd, Cu and Zn penetrated the soil and precipitated from the solution phase of the spill, while the other elements were deposited by sedimentation processes as part of the pyrite dominated solid phase. Hence, a great part of the mobile Cd, Cu and Zn are distributed in the soil profile by an independent process and thus not directly linked to the pyritic sludge, which most significantly influences the spectral response of the contaminated soils. Alastuey et al. (1999) and Galán et al. (2002) found similar results in their studies of the mobility of heavy metals in sludge and soils in the study area. Figure 6.18 shows the scatterplots of predicted vs. measured concentrations. The one to one line shows a perfect relationship; deviations from this relationship occur mainly with small concentrations. Some outliers in the validation set are visible, e.g., in the scattergrams for iron or sulphur. The results would be even better if these outliers would have been deleted from the validation set.

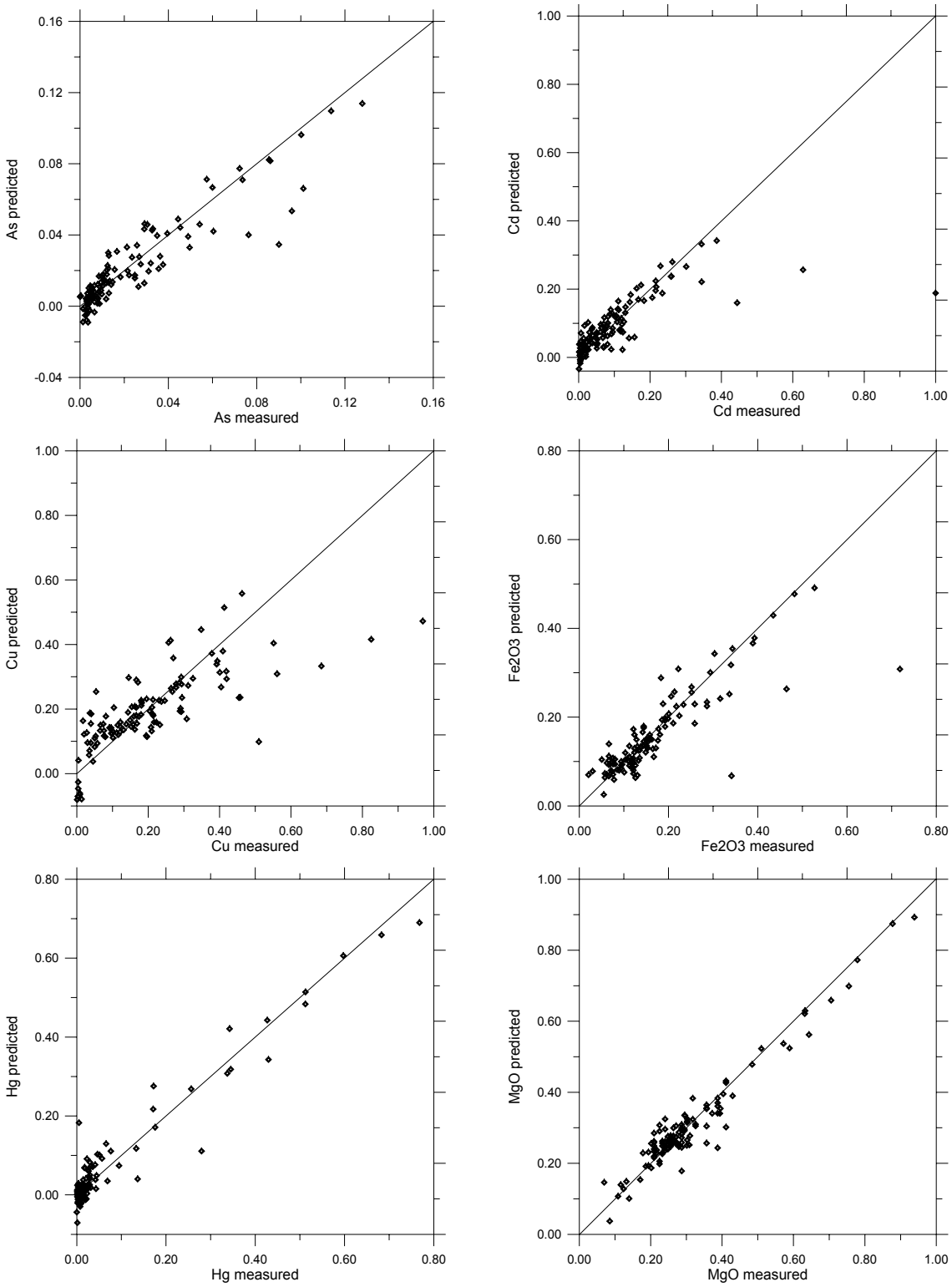

Figure 6.18. Scatterplots of predicted vs. measured concentrations. 1:1 line for perfect fit

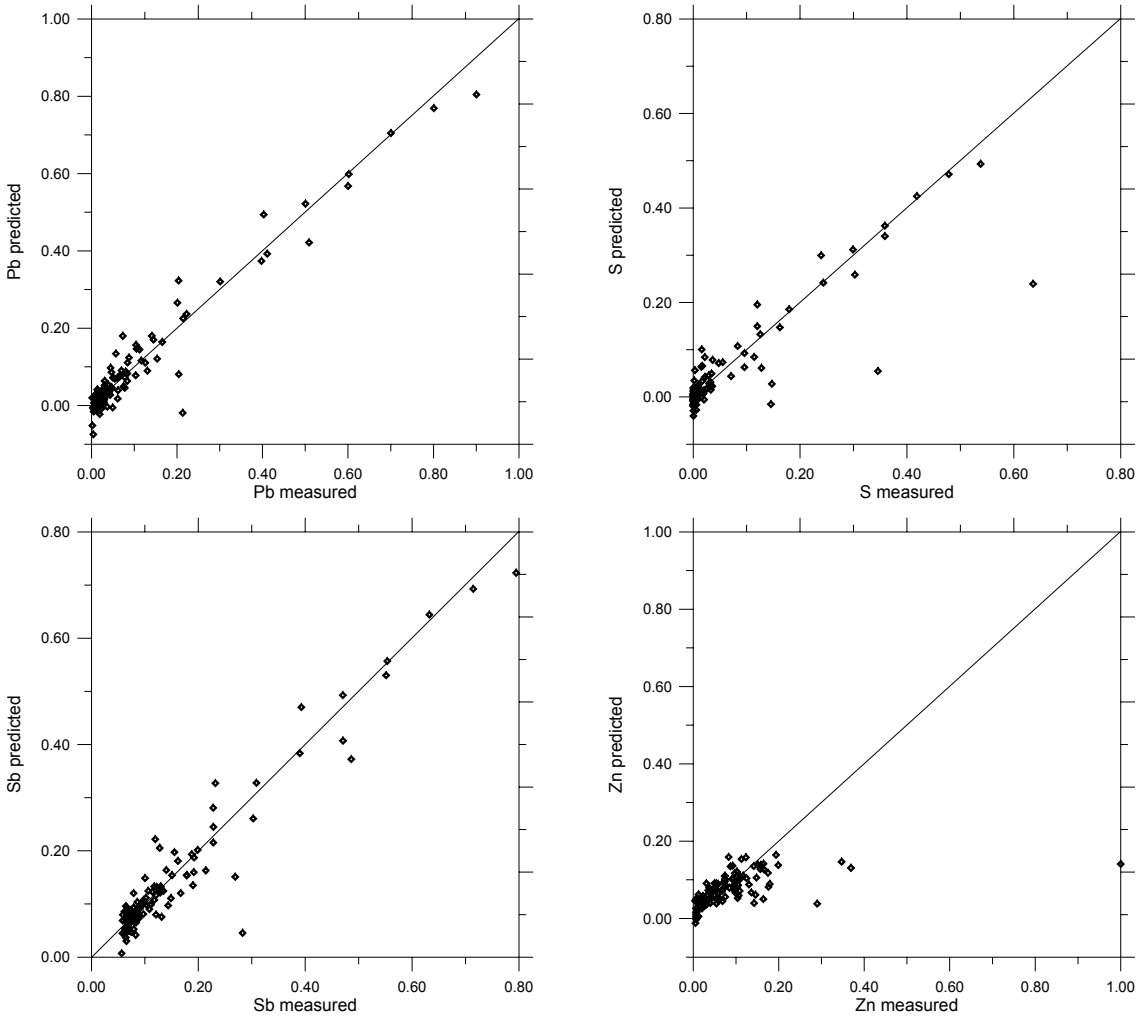

Figure 6.18. (continued) Scatterplots of predicted vs. measured concentrations. 1:1 line for perfect fit

The correlation structure of HM and spectral information was examined for a better understanding of the functioning of multivariate statistics and ANN, which are often regarded as black boxes, since both prediction methods make use of the correlation structure amongst intercorrelated variables (Table 5.5). Most heavy metals, iron and sulphur (As, Fe, Hg, Pb, S, Sb) were strongly intercorrelated ($r > 0.8$); only copper and zinc was less correlated with the other elements. Cadmium played an intermediate roll, as it was correlated significantly with As, Fe, Hg, Pb, S, and Sb and relatively high ($r = 0.83$) with Zn. The correlation structure clearly reflects the prediction results: all elements that were highly correlated were predicted more precisely.

The separation of different subgroups was even more clearly visible in the correlogram (Figure 6.19) illustrating the correlation between the reflectance at single wavelengths and respective elements. The structure is similar for all elements, but there were strong differences in the strength of the correlation. The areas of strongest correlation could be

attributed mainly to absorption features of iron and iron oxides. The high positive correlation at about 550 nm displayed the change from opaque to transparent behaviour, which was caused by an intense charge-transfer band in the UV region of the spectrum (Hunt et al. 1971). The broad area with the highest negative correlations (1000 – 1800 nm) was linked to the strong absorption band of the ferrous ion centred at about 1000 nm (Clark 1999). It was interrupted by the peaks of strong molecular water bands at 1400 and 1900 nm in combination with hydroxyl absorption, centred at 1400 and 2200 nm. In particular, secondary clay minerals show distinct absorption features at these wavelengths. In this data set, higher amounts of secondary clay minerals represented less contaminated soils.

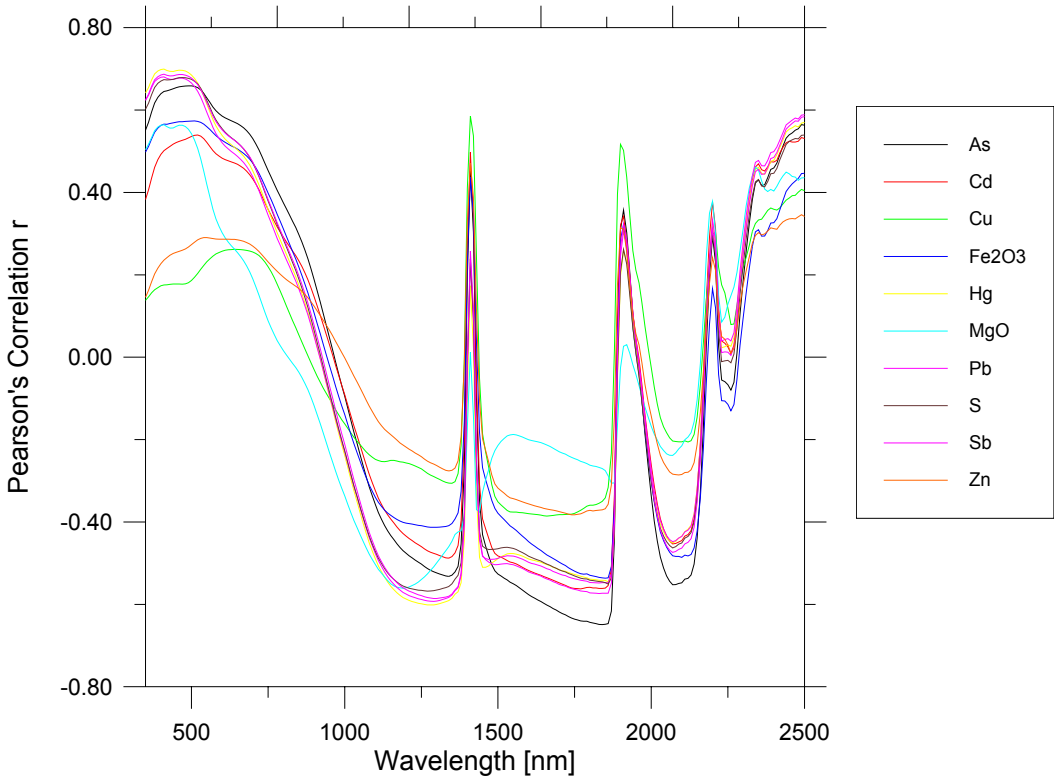

Figure 6.19. Correlogram for vector normalised spectra (10 nm) and HM

6.4.5 Modelling other element groups

New models were developed for the other two element groups using PLSR and the resampling and transformation combinations described previously.

The group of elements related to the soil matrix could be modelled best with vector-normalised spectra with a FWHM of 20 nm. After cross validation and outlier detection, the final model was built with 13 factors and with three outliers deleted. The prediction results in Table 6.9 show very similar values for Al_2O_3, K_2O, Mn, Na_2O, SiO_2 and TiO_2

with R^2's of 0.7 RPD's above two and RER's above ten. The prediction of Cr and Ni was not reliable.

Table 6.9. Final prediction results of elements related to soil matrix with vector-normalised spectra and 20 nm FWHM

Elements	*R²*	*SEP*	*RPD*	*RER*	*PRESS*	*RMSEP*
Al_2O_3	0.7	0.1149	2.08	12.1	0.8169	0.0832
Cr	0.343	0.0458	0.98	5.97	0.5236	0.0666
K_2O	0.787	0.1111	2.73	16.7	0.3957	0.0579
Mn	0.726	0.0465	2.17	11.33	0.1204	0.0319
Na_2O	0.714	0.1823	2.16	9.62	1.6504	0.1183
Ni	0.461	0.08	1.17	7.75	1.0138	0.0927
SiO_2	0.662	0.0778	2.35	13.28	0.3383	0.0535
TiO_2	0.711	0.1098	2.15	9.29	0.7075	0.0774

The final model for the group of elements related to organic soil components and plant nutrients consisted of twelve factors with five outliers removed from the calibration set. The results obtained for Calcite, CaO, $C_{tot.}$, $C_{org.}$ and H were similar, but not sufficient for predictive models (Table 6.10). No reliable results were obtained for N and P_2O_5.

Table 6.10. Final prediction results of elements related to organic soil matrix with standardised spectra and 10 nm FWHM

Elements	*R²*	*SEP*	*RPD*	*RER*	*PRESS*	*RMSEP*
Calcite	0.543	0.0773	2	8.86	0.4801	0.0635
CaO	0.562	0.0589	2.11	9.67	0.2373	0.0447
$C_{tot.}$	0.604	0.0802	2.34	10.92	0.3868	0.057
$C_{org.}$	0.599	0.0775	1.54	9.04	0.6458	0.0737
H	0.668	0.072	1.45	6.82	0.5233	0.0663
N	0.396	0.0577	0.72	4.06	0.9734	0.0904
P_2O_5	0.298	0.0356	1.58	8.25	0.1409	0.0344

The elements not directly related to the accident could not be predicted successfully, because the major changes in spectral behaviour are clearly linked to the pyritic sludge. Already the modelling of mobile elements, which originate from the mine, but which were distributed in solution, was unsuccessful.

The prediction of calcite and organic matter would have been very valuable for remediation planning, because they have the ability to buffer acidity and fixate HM. However, the sampling strategy was emphasised on HM and thus, variation in concentrations for the other elements too small (see Table 5.3).

6.4.6 Modelling heavy metal concentration for subsequent year

The data collected in 1999 were used to estimate the concentrations of samples collected one year later. The calibration model consisted of 238 samples. In the crossvalidation 11 factors were used and 8 samples were removed from the final model as outliers (Table 6.11).

Table 6.11. Prediction results for samples 2000 using vector normalised spectra (10nm) from 1999

Elements	*R²*	*SEP*	*RPD*	*RER*	*PRESS*	*RMSEP*
As	0.774	0.0275	0.15	0.7	3.401	0.1977
Cd	0.541	0.0904	1.2	6.07	0.7062	0.0901
Cu	0.279	0.201	1.51	7.52	2.7943	0.1792
Fe_2O_3	0.689	0.1174	1.18	5.16	1.293	0.1219
Hg	0.878	0.14	2.56	14.49	0.3704	0.0653
MgO	0.055	0.1301	0.64	4.76	5.5197	0.2519
Pb	0.839	0.1622	2.66	14.88	0.4703	0.0735
S	0.863	0.1031	0.8	4.36	1.7818	0.1431
Sb	0.839	0.1356	1.95	10.75	0.8231	0.0973
Zn	0.232	0.0476	0.49	2.53	1.131	0.114

Like in the models described earlier, the prediction of Cd, Cu and Zn was impossible. Additionally, Mg could not be predicted anymore. In fact, the element was added to the heavy metal group due to its similar correlogram (Figure 6.11), but in the correlation matrix of elements it did not correlate strongly with this group and in the year 2000 it did not show any correlation with other elements.

The prediction for As was not reliable. With regard to the coefficient of determination (R^2), the results for As seem to be comparable to those of the models described earlier. However, the RPD and RER are smaller, indicating a poor model performance. The geochemical conditions changed strongly between the year 1999 and the year 2000, which is clearly reflected in the samples (see paragraph 5.4.3.2). The greatest change could be observed for As, whose concentrations in the samples increased from 119 ppm to 289 ppm, while those of the other elements diminished. A model calibrated for the conditions in 1999 obviously cannot estimate concentrations, which are not reflected in the spectral behaviour.

6.4.7 Modelling with field and image spectra

Until now, the models were only applied to spectra measured in the laboratory. Whereas in the laboratory soil spectra are measured under controlled conditions, in the field uncontrolled conditions provide an environment that makes soil reflectance measurement more difficult. Nevertheless, the good prediction results obtained could also allow application to spectra measured with the ASD in the field and finally to the image spectra of the Hymap sensor. The laboratory models also revealed that with the

spectral resolution of the HyMap sensor very good results could be obtained. Hence, the field spectra were transformed to HyMap spectral resolution, which allowed a direct comparison of the models. However, the models have to be adapted, because both field and image spectra are strongly affected by noise due to atmospheric interference in the water absorption bands, in the blue part of the VIS bands and towards the end of SWIR bands (chapter 5.3). In total 18 bands were deleted, resulting in a data set with 110 bands. This reduction of bands had little impact on the predictive power of the models (Table 6.12).

Table 6.12. Comparison of R^2's of prediction results using simulated Hymap full resolution (128 bands) and HyMap reduced band set (110 bands) with laboratory data from 1999

Element	*128 bands*	*110 bands*
As	0.839	0.826
Cd	0.563	0.454
Cu	0.567	0.381
Fe	0.693	0.684
Hg	0.951	0.937
Mg	0.935	0.927
Pb	0.936	0.948
S	0.776	0.792
Sb	0.916	0.930
Zn	0.266	0.162

6.4.7.1 Field spectra

The PLSR model was calibrated using the data collected in 2000, because in this sampling campaign the field spectra were collected prior to the soil sampling allowing the measurement of the undisturbed topsoils, which was not possible during the campaign in 1999. After cross validation and outlier detection, the final model was build with four factors and three outliers deleted (Table 6.13). The results of the field spectra obtained for As, Hg, Pb, Sb and with some respect also for Fe and S are acceptable. Taking into consideration that it is a case of self-prediction (because the calibration spectra describe the same soils as measured in the laboratory), the results shown are below those to be expected.

The reasons for the inferior model performance can be assigned to the change in the geochemical behaviour, which already caused problems in the prediction of concentrations with laboratory data from 2000 using data from 1999: The residual pyrite in the soils had started oxidation and formed gypsum together with other iron-sulphate minerals and poorly crystalline iron oxy-hydroxides on the soil surface (Galán et al. 2002). The spectral behaviour of these crusts is very different from the non-oxidised pyrite and thus, the main source of error, when the models are calibrated with homogenised laboratory spectra. Furthermore, the spectral measurement is strictly

limited to the tip few millimetres of the surface, whereas the soil sample for laboratory analysis is an average of the first two centimetres, which may also represent a considerable source of error. Finally, surface roughness effects have to be taken into consideration; macro- and micro-aggregation cause changes in the albedo, which can not be removed fully by the pre-treatment of spectra (Udelhoven et al. 2000).

Table 6.13. Prediction results for field spectra with HyMap reduced band set resolution using vector normalised spectra of the year 2000

Elements	R^2	*SEP*	*RPD*	*RER*	*PRESS*	*RMSEP*
As	0.745	0.0886	2.57	8.64	0.9896	0.1274
Cd	0.347	0.1175	1.51	3.82	1.2633	0.1439
Cu	0.036	0.1335	1.28	1.94	1.7042	0.1671
Fe_2O_3	0.582	0.1	2.06	6.65	1.1103	0.1349
Hg	0.771	0.0808	2.41	8.28	0.6732	0.1051
MgO	0.112	0.1424	1.52	6.91	2.989	0.2214
Pb	0.772	0.0764	2.62	8.91	0.7191	0.1086
S	0.695	0.0912	2.56	8.4	1.1066	0.1347
Sb	0.779	0.0798	2.73	9.22	0.8341	0.1169
Zn	0.002	0.1246	1.18	0.81	1.3105	0.1466

An example from the Sobarbina site illustrates the problems caused by crusting processes. Figure 6.20 shows an area, where the residual pyrite (which was worked into the soil) oxidised and created crusts of diverse colours on the surface. Different coloured crusts were measured with the spectrometer and afterwards samples prepared for laboratory analysis. From Figure 6.21 it can be seen that the crusts are only a few millimetres thick and the underlying soil is often much darker.

Figure 6.20. Strongly oxidised surfaces at the Sobarbina site (July 2000)

Figure 6.21. Sampling point of a bright crust (AZ 426)

The shape and the albedo of the spectra measured in laboratory are very different. The albedo differences are not a major issue, because they can be reduced using the normalisation procedures described in paragraph 6.3.3, but the spectra also exhibit different spectral features (Figure 6.22). For example, the field measurement of AZ426 is most probably a gypsum crust (a more detailed identification of these spectra is given in chapter 4.3), because it exhibits the typical absorption features of water bonding in the mineral at 1.4, 1.9 and 2.2 µm. The laboratory sample in contrast, is composed mainly of the underlying contaminated soil. According to the spectral shape it is a highly contaminated sample, which corresponds well with the laboratory analysis. Sample AZ422 shows a similar shape in the field spectrum than AZ426, but both the laboratory spectrum and the chemical analysis classify it as non-contaminated.

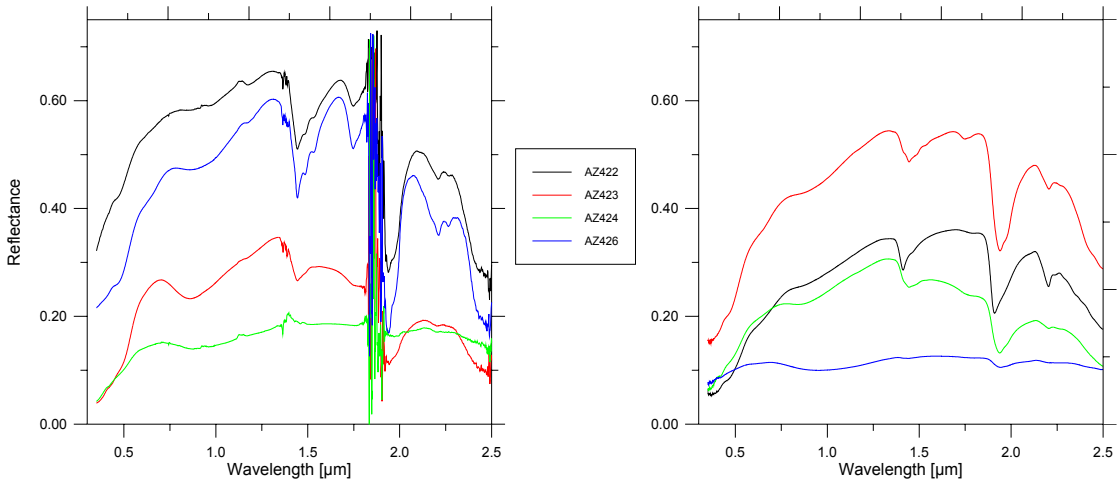

Figure 6.22. Comparison of field (left) and laboratory spectra (right)

6.4.7.2 Image spectra

The prediction of HM concentrations from the HyMap image 2000 was performed with spectra collected from the georeferenced image using the GPS coordinates taken during the sampling campaign. The spectra were selected in such a way, that they represent the corresponding soil-sampling site as well as possible. A sampling point, for example, may have fallen close to a dense vegetation patch and due to inaccuracies in the georeferencing, the vegetation patch would have been selected. In such cases the next pixel with soil reflectance characteristics was selected. Examples of image spectra corresponding to the spectra of the sampling points are shown in Figure 6.23. The shape of the spectra is very different compared to the field and laboratory spectra (Figure 6.22). The factors influencing the image spectra are manifold and complex. According to Ben-Dor et al. (1999), they can be broadly divided into biosphere, surface cover and atmospheric interference. Even for the high spatial resolution of airborne sensors such as HyMap the registered spectrum always represents a mixture of the surface

components. Vegetation is one of the mayor factors masking the soil signal. The spectral region of 0.68 to 1.3 µm of soils is the region most affected by green vegetation, as a result of the steep rise in reflectance caused by green vegetation (see Figure 4.8) (Ben-Dor et al. 1999). Furthermore, tall vegetation causes shading of soil surfaces. Dry vegetation does not change the spectral shape of soils in the VIS-NIR region, except a rise in albedo; in the SWIR spectral features related to cellulose, lignin and water content alter the soil reflectance spectrum. Surface cover interference is related to a change of natural surfaces due to human interaction, e.g. tillage, crusting processes (physical & biogenic) and surface roughness (aggregate size). The difficulties caused by atmospheric interference were discussed earlier (see chapter 4.4.2) and are apparent in the noise of the spectra. The peaks at about 1.4 µm were caused by strong water vapour absorptions and were left out from the models.

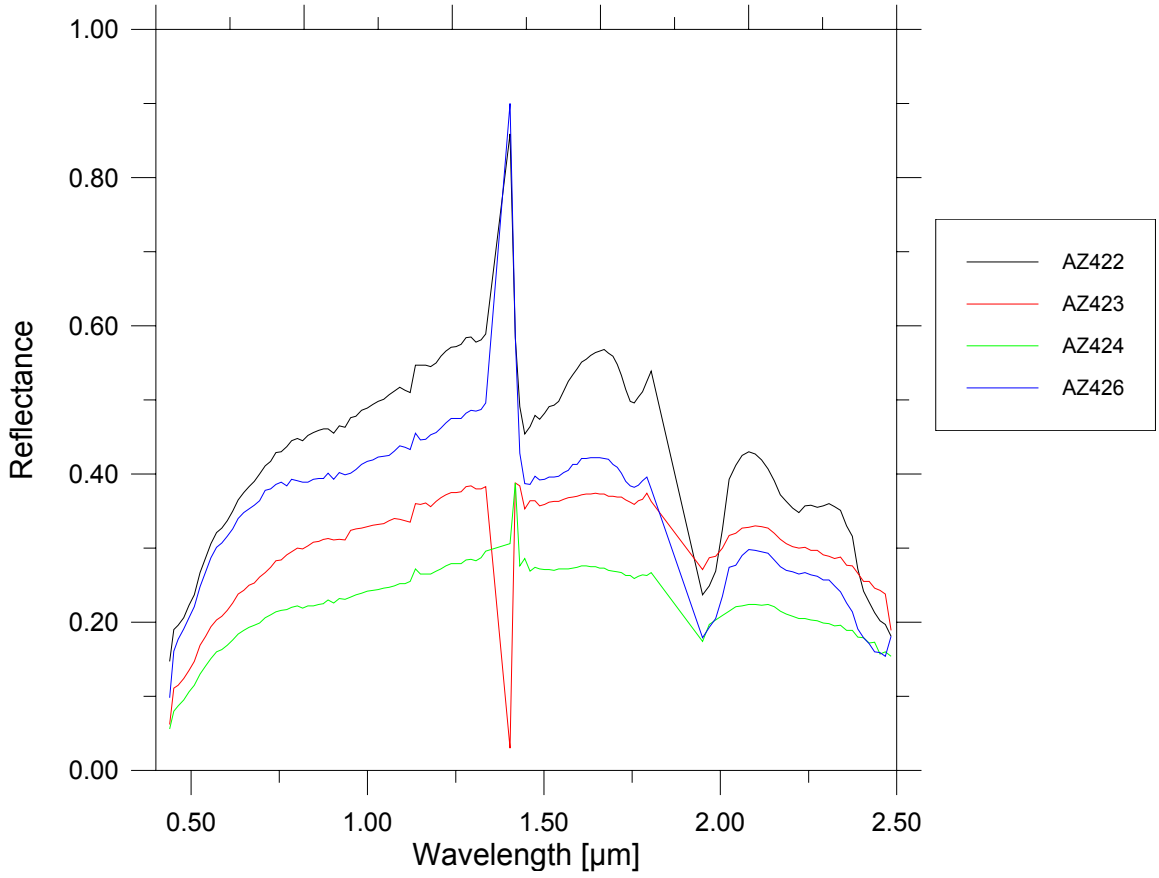

Figure 6.23. Image spectra extracted from HyMap image 2000 at the Sobarbinas site. The spectra show approximately the same surfaces as the field spectra in Figure 6.22

The influence of green and dry vegetation on the sensitivity of the models was assessed using the surface spectra of the data collected in 1999. The soil spectra were linearly mixed with reflectance spectra of green and dry vegetation in various amounts. The

influence of green vegetation is shown in Figure 6.24. The vegetation reflectance affects the original soil reflectance already at low percentages. The strong rise of reflectance between 0.68 and 1.3 µm changes the shape of the spectra drastically. The contaminated soils exhibit in this region a strong iron absorption feature, which is a key area in the modelling. This feature is masked for soil AZ021 at only 5 % vegetation coverage. The chlorophyll absorptions in the VIS also considerably alter the spectral pattern.

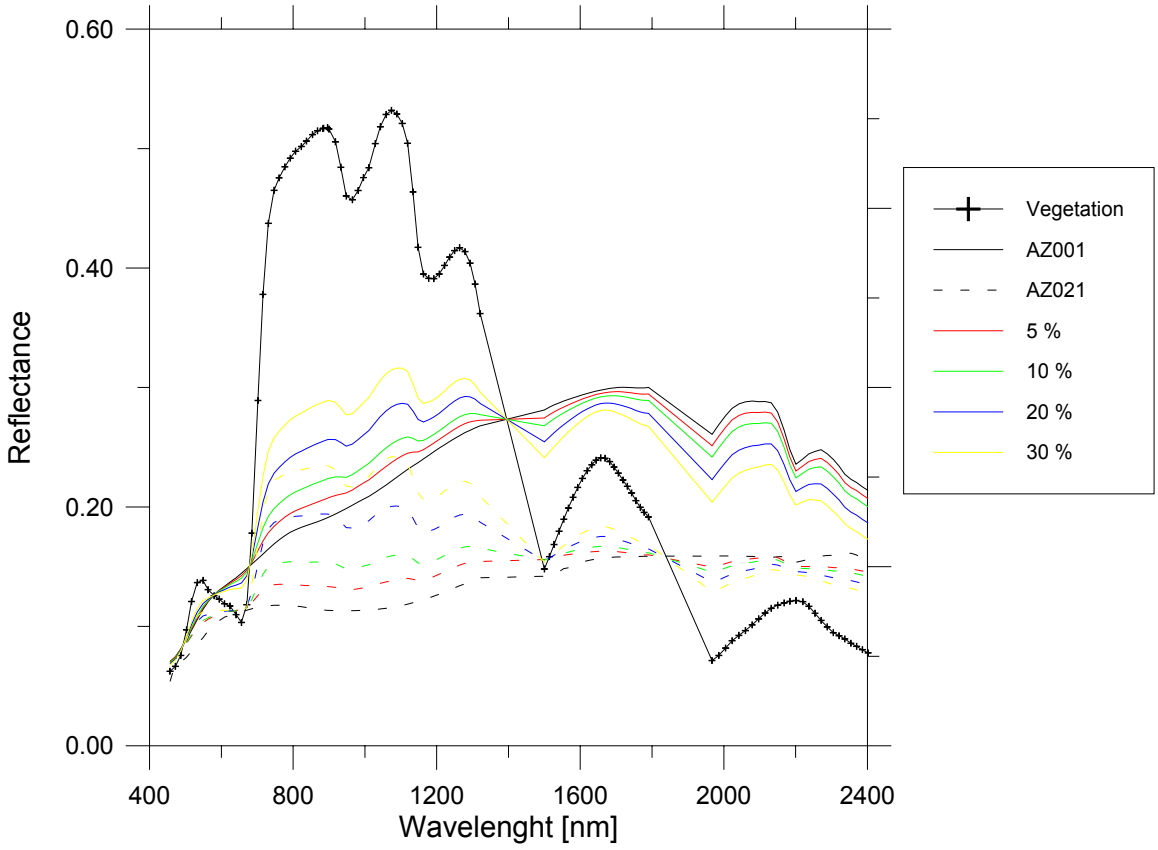

Figure 6.24. Linear mixture of two soils and green vegetation for the assessment of vegetation influence on the modelling. AZ001 uncontaminated, AZ021 contaminated

The influence of dry vegetation is smaller (Figure 6.25). In the VIS-NIR part of the spectrum it is mainly the overall albedo that increases. This affects the darker contaminated soils more than the brighter uncontaminated soils. However, the wide iron absorption is still visible with a higher percentage vegetation cover. In the SWIR, the reflectance exhibits contrary behaviour. The hydroxyl absorption soil at 2200 nm, for example, is ‘balanced’ by the dry vegetation reflectance peak.

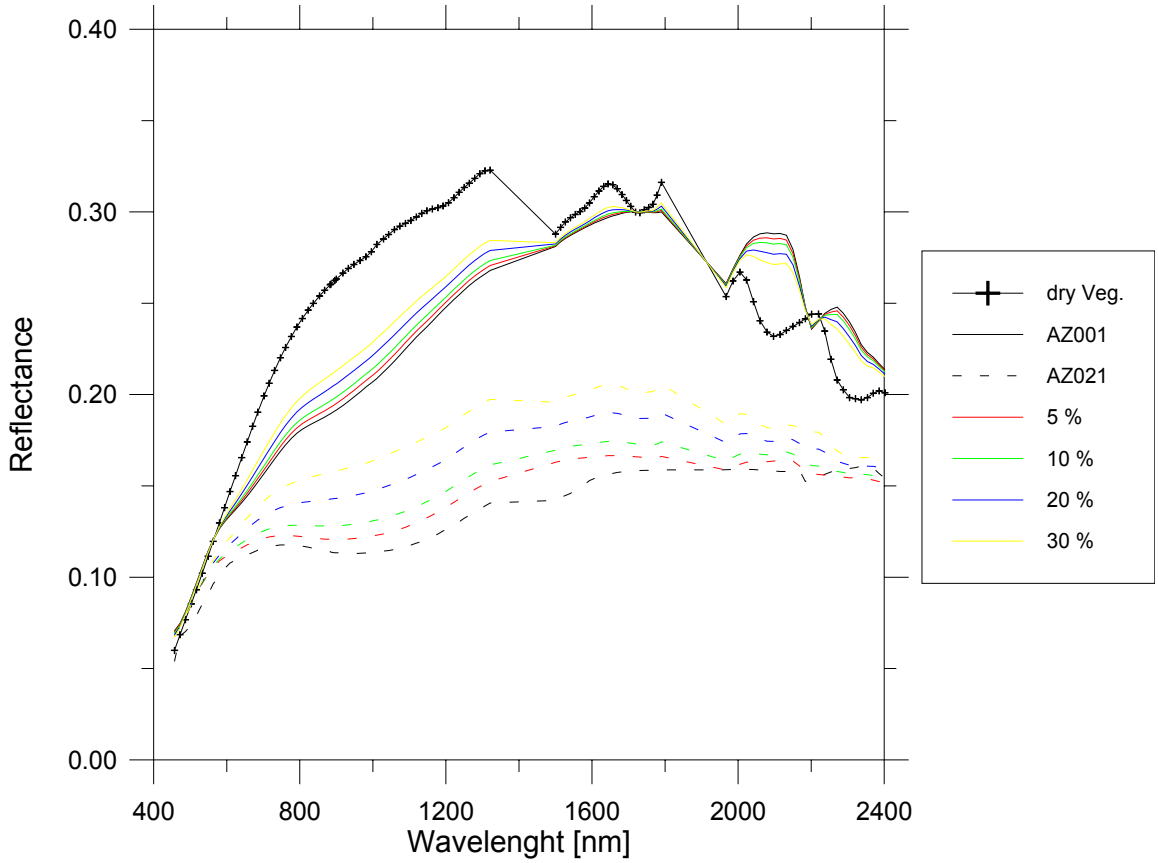

Figure 6.25. Linear mixture of two soils and dry vegetation for the assessment of vegetation influence on the modelling. AZ001 uncontminated, AZ021 contaminated

The examples presented above, show clearly the strong influence of green and dry vegetation on the spectra. This is also reflected in the predictive power of the models, when the spectra are influenced by vegetation. The influence of green vegetation is already too strong at coverages above 5%. Figure 6.26 shows the prediction results for Pb with an increasing coverage of dry vegetation. In the vegetation-free case, the trend line is more or less congruent with the 1:1 line. With increasing vegetation cover, the trend line leans over more and more. The models underestimate the measured Pb concentrations and with dry vegetation cover above 20 %, most of the concentrations are negative.

Having in mind the various factors influencing the spectra, as described above, it is not surprising that the laboratory models are not able to predict the HM concentrations of image spectra (Table 6.14). The obtained results are not significant. Several tests with field spectra as calibration or cross validation with image spectra could not improve the poor results. Calibration with image spectra could possibly provide better results, but this implies an adapted sampling strategy with homogeneous sample areas, which was not possible in the sampling campaigns.

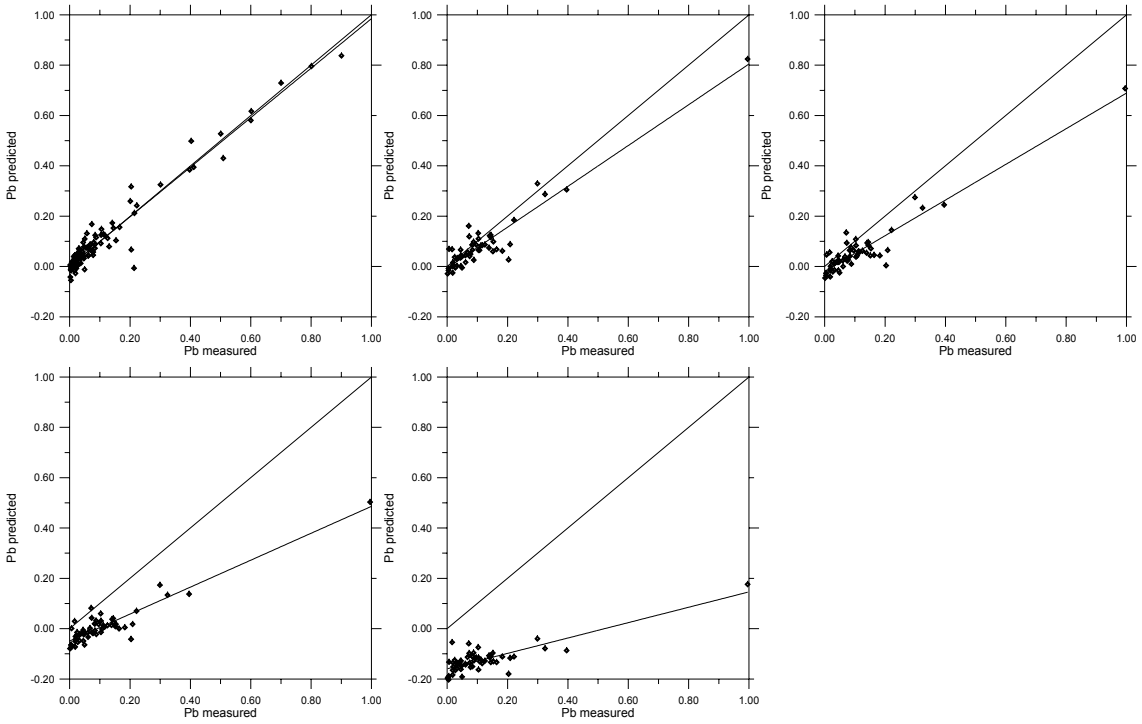

Figure 6.26. Prediction results for Pb using PLSR and vector normalised spectra with increasing influence of dry vegetation (0, 5, 10, 20, 30 % from left to right). The first line shows the 1:1 relationship, the second line is the trend line of the predicted data. The plot with 0 % vegetation shows the results of the validation

Table 6.14. Prediction Results for image spectra

Elements	R^2	*SEP*	*RER*	*RPD*	*PRESS*	*RMSEP*
As	0.028	0.2437	3.31	0.72	0.1137	0.052
Cd	0.061	0.1338	2.78	0.63	0.4163	0.0996
Cu	0.135	0.1264	3.05	0.7	0.2704	0.0802
Fe_2O_3	0.053	0.2145	3.31	0.72	0.1394	0.0576
MgO	0.016	0.1873	3	0.66	0.1191	0.0533
Pb	0.006	0.2175	4.15	0.97	0.2414	0.0758
S	0.018	0.2267	3.36	0.74	0.1921	0.0676
Sb	0.022	0.2356	3.07	0.67	0.2852	0.0824
Zn	0.028	0.2173	3.16	0.7	0.2825	0.082

6.5 Conclusions

In this chapter the chemical analysis data of the soil samples were combined with the spectral data for the prediction of chemical concentrations based on the spectral data. The models built with laboratory data were then transferred to field and image spectra.

In a mixture series of artificially contaminated soils, a strong decrease in albedo could be observed with increasing sludge content and a wide iron absorption feature became

the main absorption feature centred at about 1000 nm. The depth of this absorption was used for the estimation of heavy metals for laboratory data.

Multivariate calibration has been chosen as the method for the quantitative estimation of HM and other soil constituents, because it has the advantage that it does not have to be based on a known physical assumption, but instead on the data available. This allows for a quantitative estimation of visually featureless spectra. On the other hand, it may be hard to interpret these results. When a wavelength is selected based on a statistical relationship that cannot be related to a physically explicable absorption feature. Stepwise multiple linear regression (MLR), partial least squares regression (PLSR) and artificial neural networks have been tested for their ability to estimate HM concentrations based on their reflectance spectra. The spectra were transformed using different techniques (absorption, derivatives, standardisation and vector normalisation) in order to enhance important spectral features, and spectrally degraded (1, 5, 10, 20, 50 nm) to evaluate the effect of wavelength reduction with regard to the predictive power of the models. This is particularly important, when the models are adapted to the spectral resolution of imaging spectrometers.

All calibration methods obtained meaningful and significant results for many of the elements related to the accident (As, Fe_2O_3, Hg, Pb, S, Sb). The prediction of Cd, Cu and Zn was not possible due to the fact that these elements penetrated the soil and precipitated from the solution phase of the spill, while the other elements were deposited as part of the pyrite dominated solid phase (Simón et al. 2001). Hence, a great part of the mobile Cd, Cu and Zn are distributed in the soil profile by an independent process and thus not directly linked to the pyritic sludge, which most significantly influences the spectral response of the contaminated soils. This is underpinned by the fact that the prediction quality for As of samples collected in the year 2000 is reduced. In this year, As had shown to be very mobile and widely distributed within the soil profile and strongly accumulated in the oxidation crusts.

The estimation of other elements, which were not directly related to the mining accident, was possible for those elements related to the normal soil matrix (Al_2O_3, K_2O, Mn, Na_2O, SiO_2, TiO_2), but failed for calcite, carbon (total & organic) and phosphorous. These elements are normally concentrated in the upper soil horizons, but due to the cleaning activities, the top soils were removed (cut profiles) and the concentration range very small. The quantitative estimation of Calcite, organic matter and phosphorous would have been very helpful for the estimation of the acidification risk, because they are important agents for buffering and the retention of acidification/heavy metal.

The transfer of models from laboratory to spectra measured in the field or extracted from the image was only partially possible. The results for the field spectra were strongly influenced by the presence of surface crusts with a totally different spectral behaviour than the laboratory spectra. An estimation of the heavy metal concentration for the image spectra was not possible; also attempts to calibrate the models using field or image spectra failed. The problems caused by integration of the signal over 25 m^2

produces even on pure soil surfaces mixtures that are not represented by the laboratory models. The influence of green and dry vegetation is very strong even at surface coverages of less than 10 %. Improvements might be achieved for both, field and image spectra, with a calibration/validation with field and image spectra. However, the factors influencing the spectrum will always strongly degrade the prediction quality.

7 Imaging spectroscopy for quantification of residual contamination

As previously reported, spatial mixing of reflectance at sub-pixel scale is an inherent feature of remote sensing data sets. This causes considerable problems in their interpretation as demonstrated in the previous chapter; on the other hand such spectral mixtures can be exploited quantitatively (Mustard & Sunshine 1999). Hence, in this chapter the spectral mixing is analysed in its spatial context to derive qualitative and quantitative information about the materials making up the reflectance of each pixel.

7.1 Addressing the problems of mixed pixels

The first approaches to solve the mixture problem were proposed by Detchmendy & Pace (1972) and Horwitz et al. (1975). In the mid-eighties the spectral mixture analysis (SMA) was used for the analysis of multispectral data obtained by NASA's missions to the Moon and Mars (Singer & McCord 1979, Adams et al. 1986). Today, it is widely used to determine the sub-pixel abundance of vegetation, soils and other spectrally distinct materials that fundamentally contribute to the spectral signal of mixed pixels (e.g. Smith et al. 1990; Thomson & Salisbury 1993; Roberts et al. 1998). This is of particular importance to obtain quantitative estimates of distinct materials, which is a typical application of hyperspectral data. SMA aims to decompose the measured reflectance spectrum of each pixel into the proportional spectral contribution of so-called 'endmembers' (EM). These EMs are known reflectance spectra considered to represent the spectral characteristics of the relevant surface components. The strategy to select these EMs is one of the key issues in the successful application of SMA. It has to consider the changing spectral significance of EMs as a function of the variability of the occurring surface materials, the spatial and spectral resolution of the data and the thematic purpose of the study. Different strategies have been described in the literature; the most widely used method consists of employing the same EMs to the whole image, and using all available EMs at the same time.

Although it is mathematically possible to use one EM more than the number of spectral bands available in the decomposition, which for imaging spectrometry data would allow the use of dozens of EMs, usually a limited number of EMs is sufficient to explain the mixed spectral signature of an individual pixel in a physically meaningful way. In an absolutely noise free system it should be theoretically possible to retrieve out of a large number of distinct spectra abundance values above zero only for those EMs that really contribute to the mixed signal, while for the other spectra the abundance value would be zero. In real data sets, however, the natural variability of the EM's material reflectance,

residual errors of calibration and atmospheric correction as well as electronic noise from the detector system prevent such ideal, absolutely unambiguous solutions of the spectral unmixing. When using more EMs than really present in the pixel, there is a high risk to produce mathematically well fitting results, which are physically misleading and do not explain the real composition of the pixel.

In recent years, many authors have proposed and used a more complex model where both the number and the set of EMs vary dynamically on a per-pixel basis (e.g. Roberts et al. 1991, Lacaze et al. 1996), which has become known as 'Multiple Endmember Spectral Mixture Analysis' (MESMA). The idea consists of restricting the large set of possible EMs to a small set of appropriate EMs which can be different for each pixel, thereby allowing accurate decomposition using a virtually unlimited number of EMs. These spectra are chosen to represent the spectral variability of a larger area of interest, but would overdetermine the spectral signal of most of the single pixels. Nevertheless, MESMA in not optimal and presents some drawbacks. Estimated local EMs may be incorrect, for example, because different EM subsets may model the same areas equally well. In general, authors consider that EMs characterize the overall variance in the image as a unique condition. However, this is not sufficient since low modelling errors may coexist with relatively high fractional errors, e.g. when the spectrum of interest resembles a mixture of other materials such as the spectrum of dry grass, which resembles mixtures of shade, green foliage, and soil (Ustin et al. 1993). Thus, one additional pre-requisite is that EMs should reflect the different surface conditions in the scene. As a result, to address these limitations the entire unmixing process must be guided by a significant amount of user knowledge (Gross & Schott 1998).

This was the rationale for the development of a software tool, called 'Variable Multiple Endmember Spectral Mixture Analysis' (VMESMA) that combines, amongst other features, two complementary unmixing approaches: first, the use of standardised signatures to represent the scene materials and, second, an improved strategy for image segmentation (García-Haro & Sommer 2001).

VMESMA is used in this study to map the residual sludge on a sub pixel level and to estimate its surface concentration. This information could be used to estimate the total residual sludge amount, which in turn allows calculation of parameters important for risk assessment and remediation management, like the potential acidification risk. The application of VMESMA to the data collected in the second year is used for monitoring purposes and the identification of areas still contaminated.

7.2 The variable multiple endmember approach

The VMESMA unmixing tool is an image analysis package that extends the possibilities of multiple EM spectral unmixing. The categorisation of the scene and the variety of techniques available to model the different scene sub-areas enhance the ability to implement analysis strategies adapted to the problem under consideration. The

hierarchical analysis can incorporate *a priori* knowledge from different sources of data, including information derived from the unmixing results. Based on an iterative feedback process, the unmixing performance may be improved at each stage until an optimum level is reached (Figure 7.1). After each unmixing run, the program provides different outputs (abundances, residuals, RMS, etc.), which can be used to modify the EM combinations for subsequent unmixing runs in order to improve the results. Appropriate segmentation tools allow the identification of subunits within the image based on spectral and spatial features of interest, usually representing incorrectly modelled areas. Problematic areas can be identified not only from high modelling errors, but also from either negative proportions or solutions not matching the proportions derived from field observations, aerial photographs or other sources. From these unmodelled areas image EMs can be extracted, which may be incorporated in the unmixing library, possibly after spectrally matching them with a complete spectra database. A subsequent run will use a modified list of EM models extracted from the updated library and a hierarchical optimised strategy on the basis of the updated segmentation.

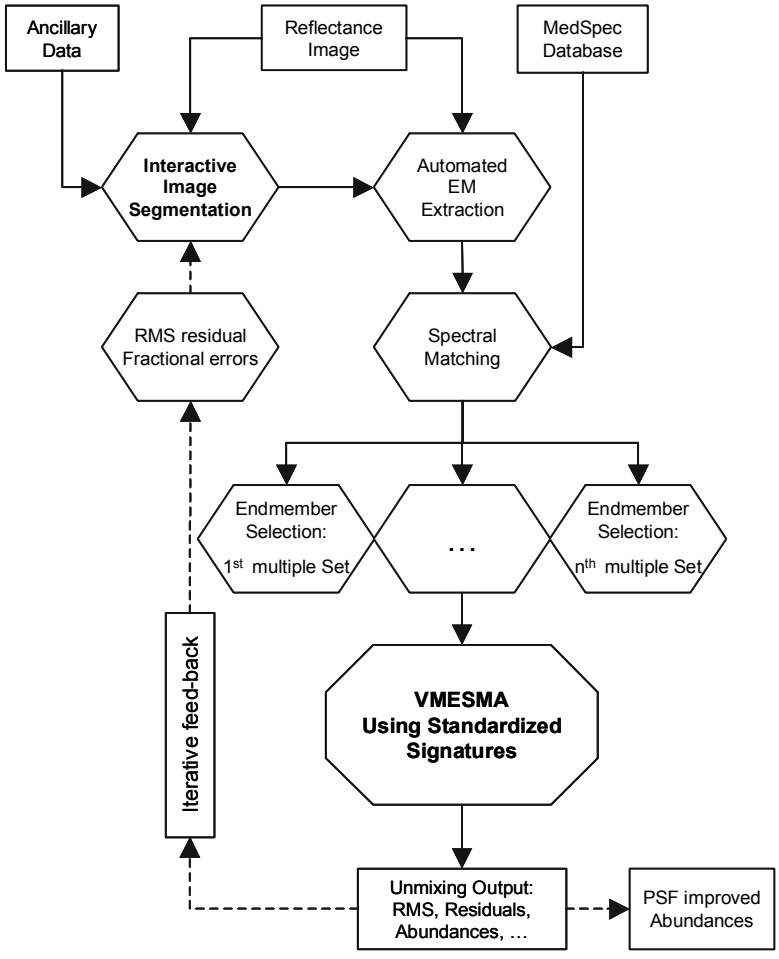

Figure 7.1. General VMESMA scheme

In this study, VMESMA was applied as outlined in Figure 7.2. Based on GIS information about the maximum extent of the sludge a first separation of areas affected by the mining accident was possible. A simple EM set was selected for both units consisting of the main landscape elements (green, dry vegetation and the main soil types of the area). The RMS and residuals of the first unmixing were used to separate pixels in the affected area with small errors. The small errors indicate that these areas were already cleaned and no residual sludge could be detected.

In areas where the modelling error was higher sludge EMs were added to the multiple EM set and more complex EM subsets were used for unmixing. In the third run a water EM was added to the multiple EM set to separate out the water surfaces.

The EMs for the mixture analysis were taken from the spectral library acquired during the fieldwork campaigns. However, for the mapping of residual sludge and its oxidation products, it is important to know the mineral composition of the spectral EM. Therefore the selected spectra of sludge and crusts were compared to spectra from the USGS spectral library (Clark et al. 1993) using spectral feature fitting for identification of minerals based on diagnostic absorption features.

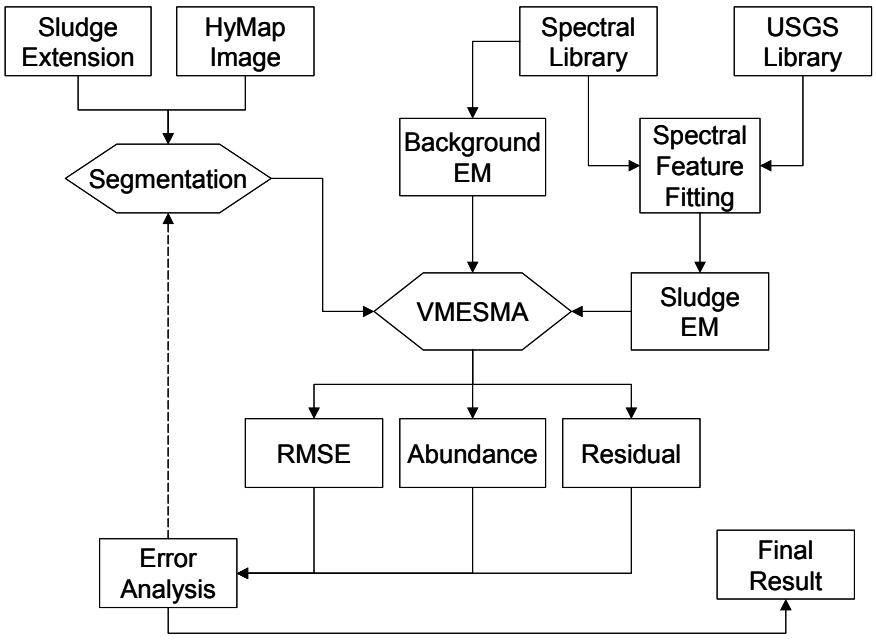

Figure 7.2. Application scheme of VMESMA in the present study

7.3 Linear spectral mixture analysis with standardised variables

In the previous chapter it was demonstrated that the standardisation of spectra enhances the spectral contrast of spectral features of interest for this study. Therefore, also the SMA is also based on standardised signatures rather than reflectance values.

Standardised SMA is based on the same principles as conventional SMA, simply solving the problem using standardised coordinates, which introduces some differences in the equations. The formulation of standardised SMA is expressed as follows:

$$\mathbf{r} = \sum_{i=1}^{c} \mathbf{E}_i f_i + \varepsilon \qquad \text{Eq. 7.2}$$

where $\mathbf{r}$ is the standardised pixel vector, $\mathbf{E}_i$ represents the *i*-th standardised endmember, f_i is the proportion of such an endmember in the standardised coordinates, *c* is the number of components in the pixel and ε is the residual vector (expressed in standardised units). Standardised SMA consists of unmixing the pixel vector $\mathbf{r}$ using standardised EMs $\mathbf{E}_i$ (i =1,…c) in order to obtain the proportions f_i. A constrained analytical estimator is used according to which the sum-to-one condition in standardised SMA is expressed as follows (García-Haro et al., 1999):

$$\sum_{i=1}^{c} \frac{f_i}{\sigma_{E_i}} = \frac{1}{\sigma_r} \qquad \text{Eq. 7.3}$$

where σ_{E_i} and σ_r represent the standard deviation of the vectors $\mathbf{E}_i$ and $\mathbf{r}$, respectively. Finally, the proportions in the original system, f_i, are obtained using the expression:

$$f_i = \sum_{i=1}^{c} \frac{\sigma_r}{\sigma_{E_i}} \hat{f}_i \qquad \text{Eq. 7.4}$$

This transformation ensures the sum-to-one condition and also preserves the positive proportions.

Unlike conventional SMA, standardised SMA accounts for differences in shadow or shade, because the standardisation eliminates such brightness variations. Hence it is possible to add a new EM to better represent complex mixture pixels or, alternatively, apply the SMA with less EMs thus increasing the reliability of estimated abundances. Conventional and standardised SMA focus on different information, and hence both strategies can be used in a complementary manner to find the proportions of mixed pixels, each one isolating contrasting features. For example, conventional SMA is rather insensitive to spectral absorptions of minor constituents because the analysis predicts the best-fit least square regression over the full spectrum. However, standardised SMA provides increased enhancement of these absorption features.

For this study, standardised SMA is ideal, because it enhances the features of the sludge related materials and drastically reduces the variability of vegetation features, which are not of interest in this study. This is demonstrated with the following figure (Figure 7.3). The differences in the architecture of the various plant canopies cause different shade

proportions, particularly in the NIR. However, after standardisation only one green vegetation spectrum may be sufficient to represent the spectral variability of all green vegetation components in the scene, because the intra-class variability/separability has been significantly reduced. The effect of standardisation on soil and sludge reflectance spectra was discussed in the previous chapter; the standardisation removes most of the spectral differences associated with soil texture (e.g. aggregation) while spectrally interesting features (e.g. iron absorption of sludge) are enhanced (Figure 6.7).

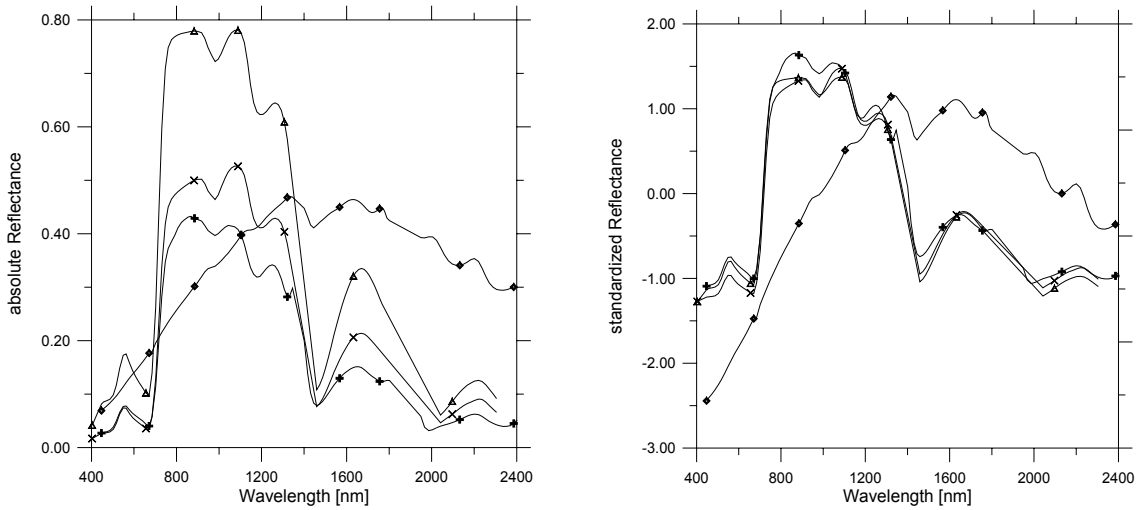

Figure 7.3. Example of four different types of vegetation (taken from Medspec database (Preissler et al. 1998)): herbaceous (*Asphodelus albus,*△), shrub with some shade (*Euphorbia characias*, ✕), dense coniferous forest canopy (*Pinus brutia*, ✚) and dry shrub (Arbutus unedo, ◇). Reflectance (left) and standardised reflectance (right)

7.4 Identification of endmembers

The accuracy of the SMA results is highly influenced by the selected EMs. Thus, the strategy to select the EMs is one of the key issues in the successful application of SMA. It has to consider the changing spectral significance of EMs as a function of the variability of the occurring surface materials, the spatial and spectral resolution of the data and the thematic purpose of the study. The correct EMs have to fulfil the physically based and statistically determined requirement of purity, which means that the selected EMs have to represent the relevant feature space. This is achieved with materials that represent the endpoints of the vectors enclosing the feature space (Figure 7.4). In an ideal case all possible mixtures of EMs lie within the spanned feature space; pixels outside the feature space produce physically erroneous abundance (<0 or >1), or high errors.

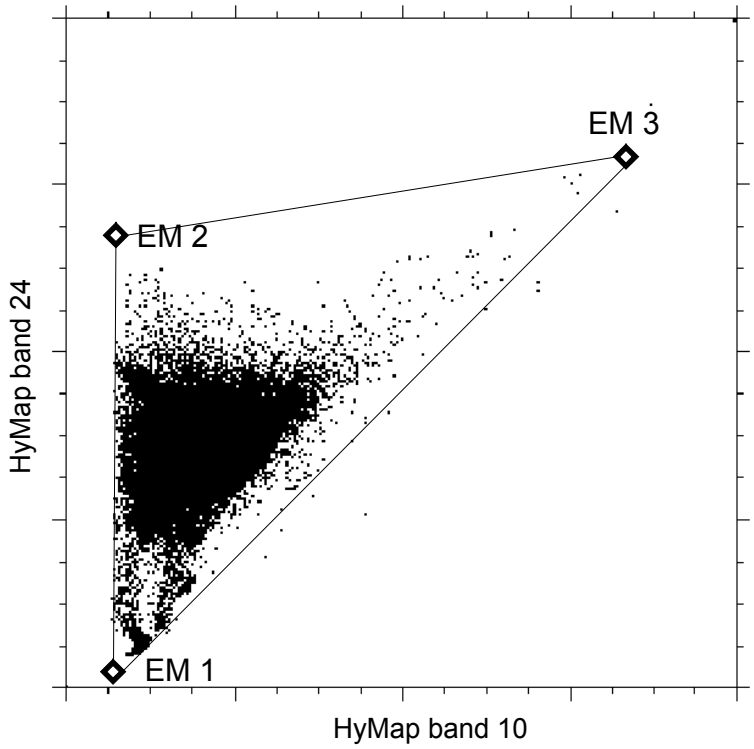

Figure 7.4. 2D-scatterplot of data representative of a scene with EMs, which define the mixture space

The EMs may be selected objectively using methods based on mathematic/statistical models, which can be divided into image EM extraction and spectral library search algorithms. On the other hand, EM selection can be based on criteria such as field knowledge and a trial-and-error approach. According to Tompkins et al. (1997) an ideal approach is an objective pre-selection of possible EMs followed by user control and optimisation. There are a number of methods for the detection of extremes within the image which are considered potential EMs, ranging from automatic methods based on the exploration of abstract factor space of principal components (Bateson and Curtiss 1996; García-Haro et al. 1999) and artificial neural networks (García-Haro et al. 1999) to the use of spectral libraries (Boardman 1989) and the Pixel Purity Index (PPI), an empirical measure for the purity of a pixel (Boardman et al. 1995).

In this study, it was necessary to separate sludge related spectral information from other 'background' information for the extraction of the residual sludge signal. The corresponding background spectra were selected based on an principal components analysis (García-Haro et al. 1999). The proposed candidate EMs were then compared to spectra of the spectral data base and finally typical spectra of green and dry vegetation and two different soils were selected as background information (Figure 7.5). The green vegetation spectrum is a spectrum of stacked sugar beet leaves; the dry vegetation spectrum was measured over a stack of dry grass. The brighter soil had a fine texture and a yellowish red colour (Munsell value 5YR 5/6), the absorption at about 1.0 µm is

indicative of certain amounts of iron oxides and the absorption at 2.2 µm is typical for clay minerals. The darker soil has an intermediate structure and a brown colour (Munsell value 7.5YR 5/3). This soil does not exhibit strong iron absorption, but has a distinct absorption caused by clay minerals.

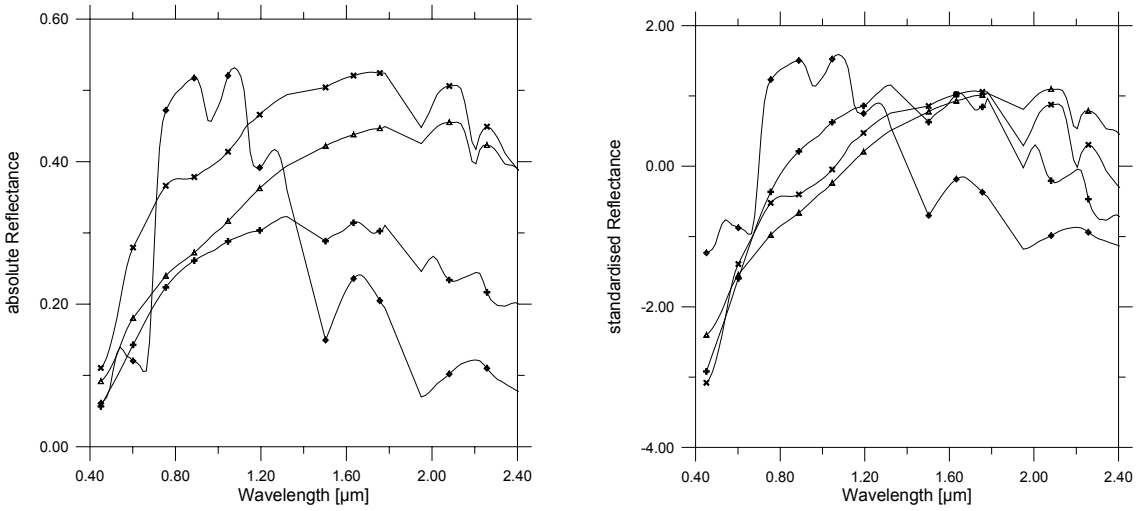

Figure 7.5. Background EM: green vegetation (◇), dry vegetation (△), soil 1 (✖), soil 2 (✚). Absolute reflectance (left), standardised reflectance (right)

The identification of specific minerals, which is one of the great strengths of imaging spectroscopy, is of particular importance for the sludge related EM. As described in chapter 3.2, pyrite oxidation produces a number of secondary minerals, which can be used as indicators for the location of potential acid producing areas. The identification of minerals with hyperspectral data is physically based, which distinguishes it from simple ratios or statistical classifications, and takes advantage of the diagnostic absorption features of these minerals, whose formation was described in chapter 4.

The easiest approach simply characterizes position, strength and symmetry of an absorption feature using the continuum removal as described in chapter 6.2 (Clark & Roush 1984). This approach can be quite effective, but it is very sensitive to noise. Furthermore, the method reduces the spectral information of many spectral bands into four parameters (position of the absorption (lowest point), starting point, end point and depth). This information reduction can lead to ambiguity in the identification of minerals, particularly for absorption features with a greater width like ferric or ferrous absorptions, which are of special interest for this study (Mustard & Sunshine 1999). The full information is preserved and used by an approach developed by Clark et al. (1990), Clark et al. (1991) and Clark & Swayze (1995). The algorithm computes the degree of similarity between the spectrum of interest and spectra from a spectral library. After the continuum removal using a predefined spectral subset, the contrast is adjusted in such a way that the continuum removed library spectrum best fits the continuum removed observed spectrum. This adjustment is rearranged to a standard least squares equation

and results in a superposition of the library spectrum by a linear gain and offset into the same reference frame as the observed spectrum (Figure 7.6). From this, the relative strength of the absorption and the RMS can be calculated, where the RMS serves as a goodness-of-fit measure and the strength is related to the abundance of the mineral. In this study, the algorithm was used as implemented in the ENVI software and the USGS library of minerals, which is one of the most complete mineral libraries available, was used as reference database (Clark et al. 1993).

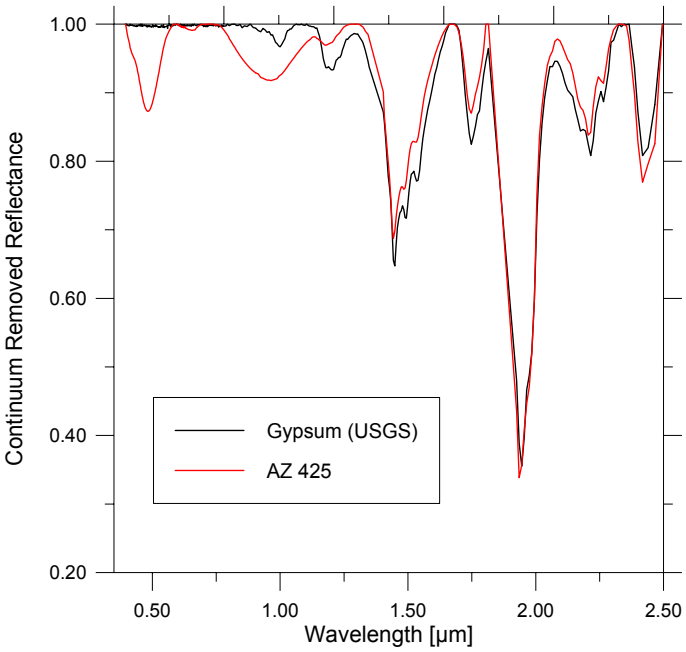

Figure 7.6. Example of Spectral Feature Fitting (SFF). Reference spectrum of gypsum (black) is fitted to the field measurement AZ425 (red) using least squares. The SFF score can be calculated from this fit. See Table 7.1 for results.

The selection of sludge EM had to consider the potential secondary minerals of pyrite, like jarosite, copiapite, ferrihydrite and goethite (see chapters 3.2 and 4.3.1 for details). However, for the images for 1999, the oxidation was limited to areas with a constant water supply and for the major part of the contaminated area no considerable oxidation took place. Thus, a single spectrum of pure sludge was sufficient to represent the sludge fraction.

In the year 2000 images other sludge related spectra had to be taken into consideration, because field and image assessment confirmed that the oxidation processes had produced various crusts on the soil surface. During the second field campaign, spectral measurements of the most abundant crusts were recorded. Due to the fact that no qualitative mineralogy of these crusts could be obtained, the spectral feature-fitting algorithm was used to identify some minerals based on diagnostic absorption features.

The spectra of surface crusts were matched to the spectra of the USGS spectral library. First, the algorithm was applied to spectra resampled to the 5nm spectral resolution of the USGS library, and then the HyMap reduced band set of 110 bands was used to obtain an insight into the possibilities to map these minerals in the HyMap images.

The crusts are most probably not pure minerals but mixtures of different components with different absorption features. Due to these mixtures the SFF scores for the full spectrum may be not be very high. Therefore, SFF was carried out in three steps covering different spectral regions: the full spectrum, the VIS-NIR (0.4 – 1.35 μm) and NIR-SWIR parts (1.35 – 2.4 μm. The VIS-NIR region was analysed for minerals having diagnostic electronic transitions of ferrous and ferric ions, like hematite, goethite, ferrihydrite, copiapite, jarosite and others. The NIR-SWIR part was analysed for minerals having diagnostic vibrational features mainly in the 2.2 and 2.3-μm region.

The results of the SFF are displayed in Table 7.1. Sample AZ423 shows features of jarosite, copiapite and ferrihydrite. In fact, the score matches for the full spectrum are not very high, indicating that it is a mixture of different minerals. In the SWIR, the diagnostic absorption of jarosite at 2.27 μm is absent, but the higher values of the VIS-NIR spectral range suggest that it is dominantly composed of jarosite with minor parts of ferrihydrite and copiapite. In any case, the minerals are closely related to each other in the oxidation process, so that the spectrum can be used as indicator of pyrite oxidation.

Sample AZ424 matches highly with jarosite, pyrite and copiapite. By taking into account the overall albedo, the sample is composed mainly of the opaque pyrite.

The bright spectrum AZ425 matches very well with pure gypsum spectrum showing exactly the same absorption features (1.45 and 1.55, 1.75, 1.9 2.2 and 2.27 μm). The absorptions in the VIS-NIR (0.65 and 0.9 μm and strong absorptions < 0.6 μm) match with goethite, with which it is mixed in some minor parts. Gypsum ($CaSO_4 \cdot 2H_2O$) is not a secondary mineral of pyrite weathering. It is the product of chemical treatment using limestone-derived alkali for neutralisation of sulphuric acid, which is produced by pyrite oxidation.

Table 7.1. Results of the spectral feature fitting for full range spectra, VIS-NIR and NIR-SWIR

Sample	*Full Range*	*Mineral*	*VIS-NIR*	*Mineral*	*SWIR*	*Mineral*
AZ423	0.222	Jarosite	0.713	Jarosite	0.661	Ferrihydrite
	0.209	Copiapite				
AZ424	0.680	Pyrite	0.860	Jarosite	0.827	Copiapite
			0.802	Pyrite		
AZ425	0.567	Gypsum	0.878	Goethite	0.744	Gypsum

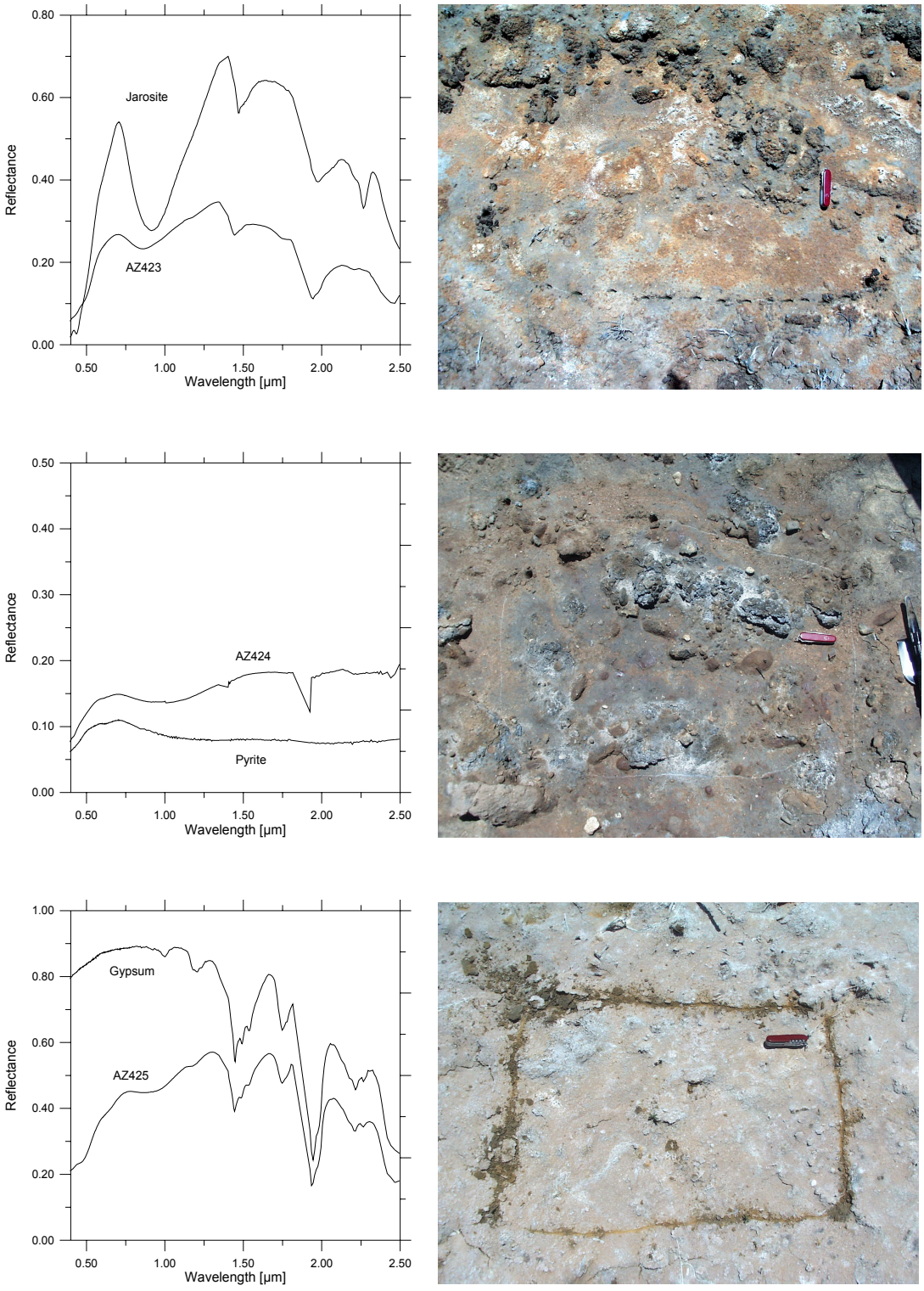

Figure 7.7. Comparison of field measurement and best fitting reference spectrum. The photos on the right show the crusts from which the field spectra were derived.

7.5 Results

7.5.1 Derivation of residual sludge distribution for the year 1999

The SMA results are demonstrated with a subset of the HyMap images in order to allow a sufficient level of detail. However, the entire affected area was analysed in the same way (see Annex F). The site 'Sobarbina' is located in the northern part of the affected area, just in the South of the confluent of the Agrio and Guadiamar rivers. The area is mainly built up of point bar deposits, formed by gravels and medium to coarse sand textures, and by finer grained overbank deposits. The gravel and sand deposits are mined in open pits. The zone exhibited an elevated contamination level in both years (see chapter 5.4.3).

In the first unmixing step, the four background spectra (Figure 7.5) were used to unmix the entire scene. Although a maximum of four EMs per pixel was allowed, only in less than 0.5 % of the cases as many EMs were used. In the majority (75 %) two EMs were sufficient to model the scene. The RMS error after the first unmixing clearly separated the sludge-affected areas with a high RMSE from the non contaminated areas (Figure 7.8).

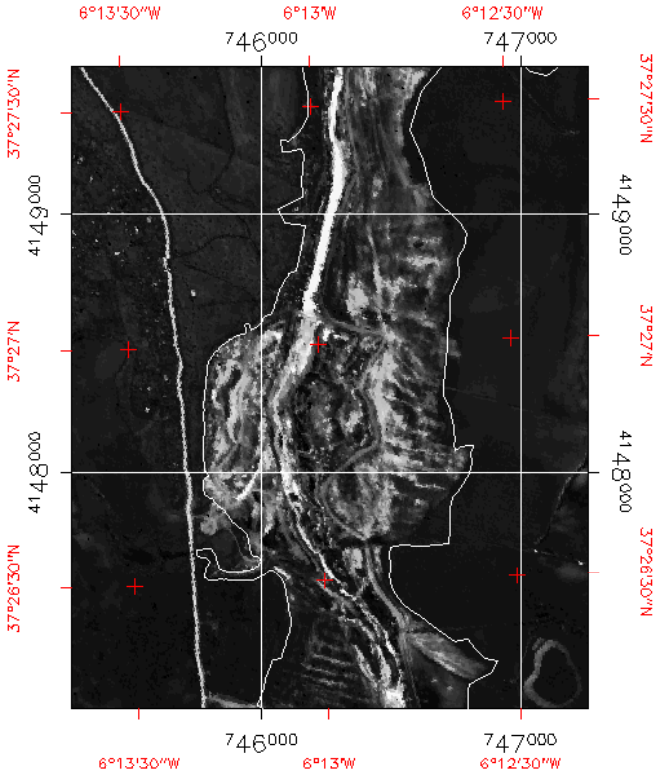

Figure 7.8. RMS error after the first unmixing. Border of the green corridor for delineation of maximum sludge extension

Some areas with an equally high error (other than the sludge-contaminated areas) are open waters like the Guadiamar River or paved roads, which still have to be separated from the sludge affected area. In areas with a higher RMSE the residuals also clearly reflect the lack of another EM. On the other hand, in most of the non affected areas, the proposed EMs were sufficient, which is shown by low RMS and featureless residuals (Figure 7.9).

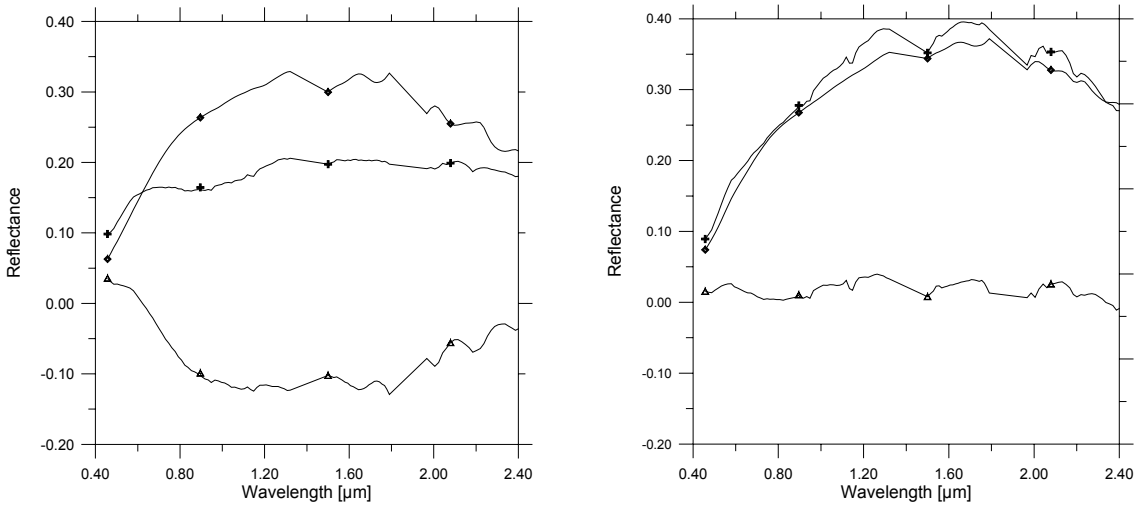

Figure 7.9. Comparison of original (✚) and modelled (◇)spectra and residuals (△). Pixel in sludge affected area (left) and pixel in non affected area (right)

The next unmixing step was performed on a segmented image. Areas outside the green corridor were neglected, and in the affected area, a RMSE threshold was used to separate areas that were already sufficiently modelled from areas, which were most probably sludge affected.

The sludge abundance map for June 1999 (Figure 7.10) shows that the sludge abundances were still very high with an average abundance of 0.51 (calculated for areas with sludge abundances > 0). The results were obtained with only one sludge EM. In fact, tests with additional sludge EMs were not successful. This is a clear indicator that at this point in time, 13 months after the accident, oxidation of pyrite did not yet reach a high intensity and consequently it was possible to map the sludge using only the pyrite sludge EM.

The retrieved sludge distribution corresponds well with the field observations and reflects the discontinuous distribution pattern caused by the mechanical clean up. However, a quantitative validation of the sludge abundances is difficult, because the corresponding sludge concentration (amount of residual sludge) cannot be measured directly. On the other hand, it is possible to estimate the concentrations of sludge constituents. These constituents were derived from the sludge abundance in the following chapter. They were validated against the results of the chemical analysis.

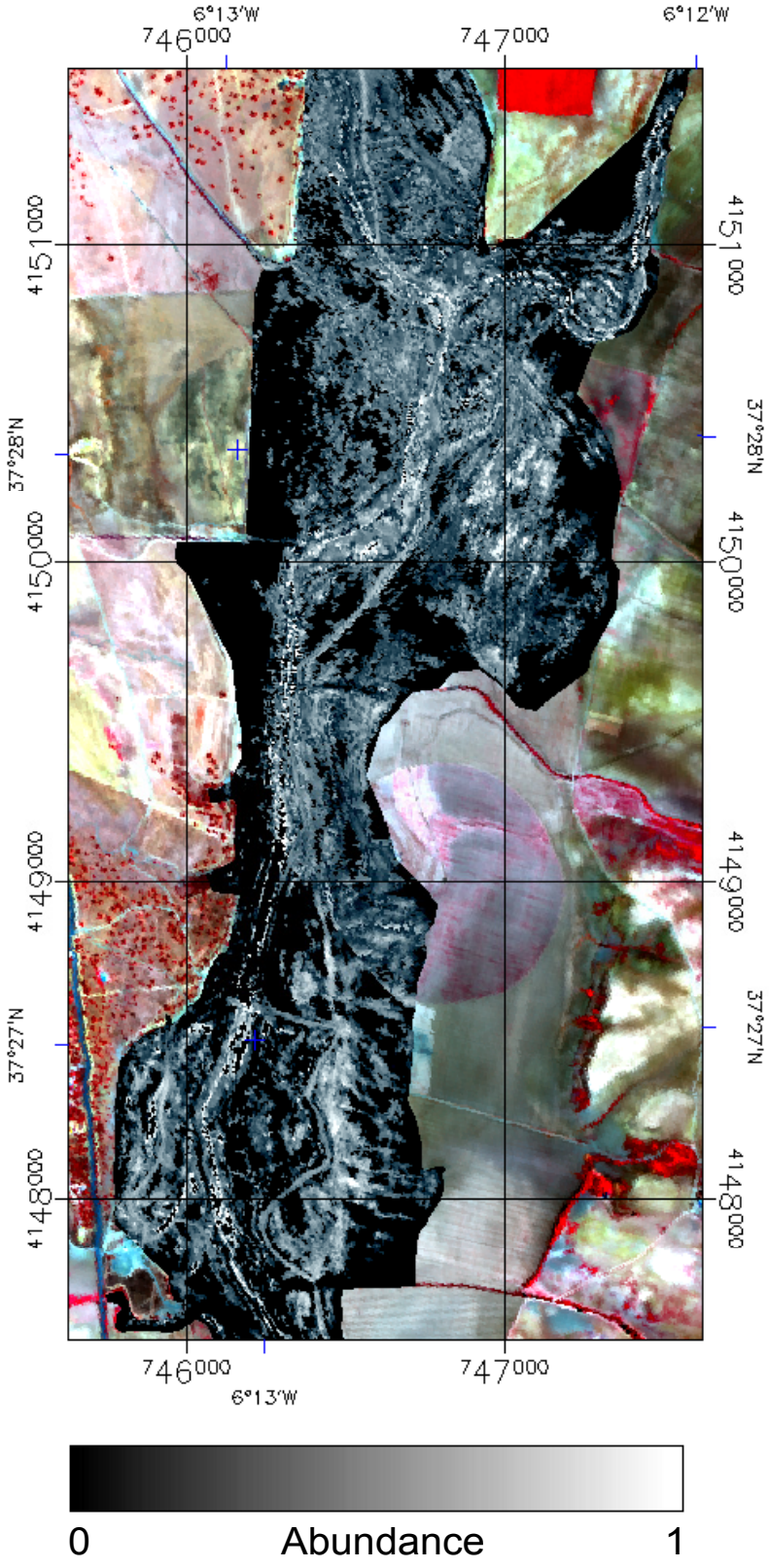

Figure 7.10. Sludge abundance map 1999. The affected area (black) superimposed on the HyMap false colour image for better orientation. Sludge abundance within the affected area is scaled from zero (black) to one (white).

7.5.2 Derivation of residual sludge abundance and pyrite oxidation products for the year 2000

The same unmixing strategy was applied for the data collected in 2000. However, the situation had changed significantly. The Consejería de Medio Ambiente proceeded with the remediation of the area. The remediation process included a second cleaning phase in combination with fixation of the trace metals. This was achieved by augmentation of the pH-level of the soil through addition of lime-rich material as described in chapter 3.5. At the time of the second field and flight campaign the work was still ongoing. In many areas, particularly in the northern part, efflorescent crusting could be observed. According to Nordstrom (1982), these crusts are most commonly formed during dry periods when evaporation promotes the rise of subsurface water to the uppermost soil surfaces by capillary action. As the water reaches the surface it becomes progressively more concentrated and finally precipitates various salts in efflorescence. The formation of these iron sulphate salts is an intermediate step, which precedes the precipitation of more common insoluble iron minerals such as goethite and jarosite. In order to account for this change in surface composition two new EMs (the jarosite and the gypsum spectra, see Figure 7.7) representing these efflorescent crusts were included in the SMA modelling.

The abundance map for July 2000 shows a considerable reduction of areas with sludge EM abundances compared to the abundances obtained for June 2000 (Figure 7.11, see also Annexes F and G). This reduction was achieved by the second remediation process initiated by of the Consejería de Medio Ambiente. As explained in chapter 3.5, they re-cleaned some areas, distributed Ca-rich products for buffering and covered the area with non-contaminated topsoils. In those covered areas, sludge or its secondary products cannot be detected anymore, even if it is still present in deeper layer of the profile.

However, in areas where the remediation was not finished, higher abundances of secondary minerals were found. This is demonstrated for a subset from the confluent of the Agrio and Guadiamar rivers, where the sludge wave contaminated the wide floodplains (see zoom window, Figure 7.11). In this area, jarosite was found to be abundant. It was widely distributed in the area. It is formed under dryer conditions according to the reaction sequence explained in chapter 3.2 (see Figure 3.4), which explains its wider distribution. The patches of gypsum, which were found, are restricted to shallow depressions, in which more water gathered after rainfalls and the humidity was sufficient for the formation of gypsum when the water evaporates (Figure 7.12). However, these few millimetres thin crusts are only on the surface and below them secondary minerals are found (see chapter 6.4.7.1 Figure 6.21 and Figure 6.22). This pattern was also observed at the gravel pits close to the *Sobarbinas* site in the south of Figure 7.11. The gravel pits are in the same level as the riverbed and hence the water supply was sufficient to form gypsum. The gypsum is distributed more widely, because the groundwater provided a more constant source of humidity than do the shallow depressions.

Hence, the presence of gypsum is on the one hand an indicator for buffering of acidity by the distributed material Ca-rich material; on the other hand it shows that there is still residual sludge in the soil, which produces acidity.

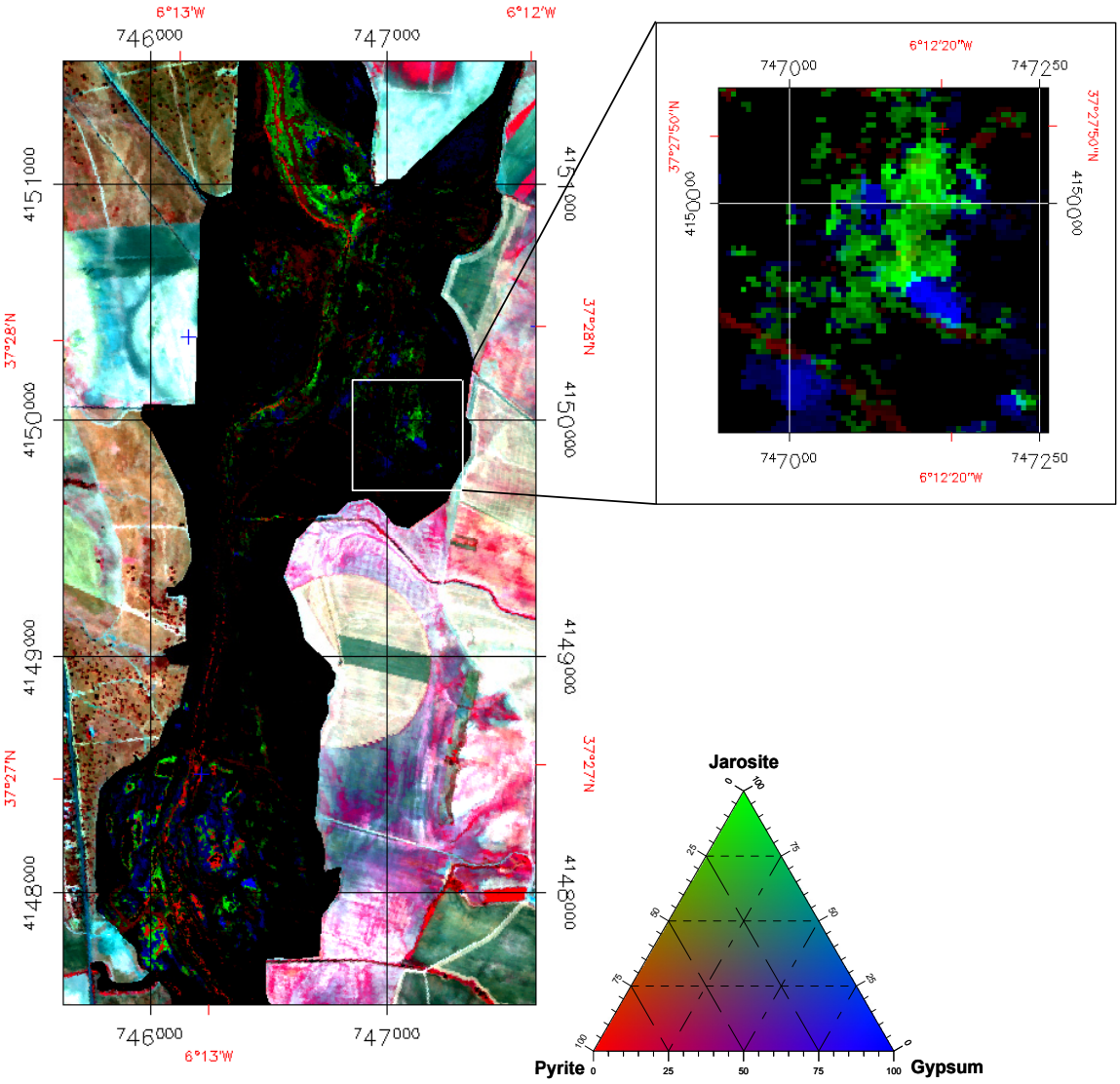

Figure 7.11. Mineral abundance map 2000. The mixtures of the different EMs can be derived from the colour coded ternary diagram. Red is the pyrite EM, green is the jarosite EM, blue the gypsum EM.

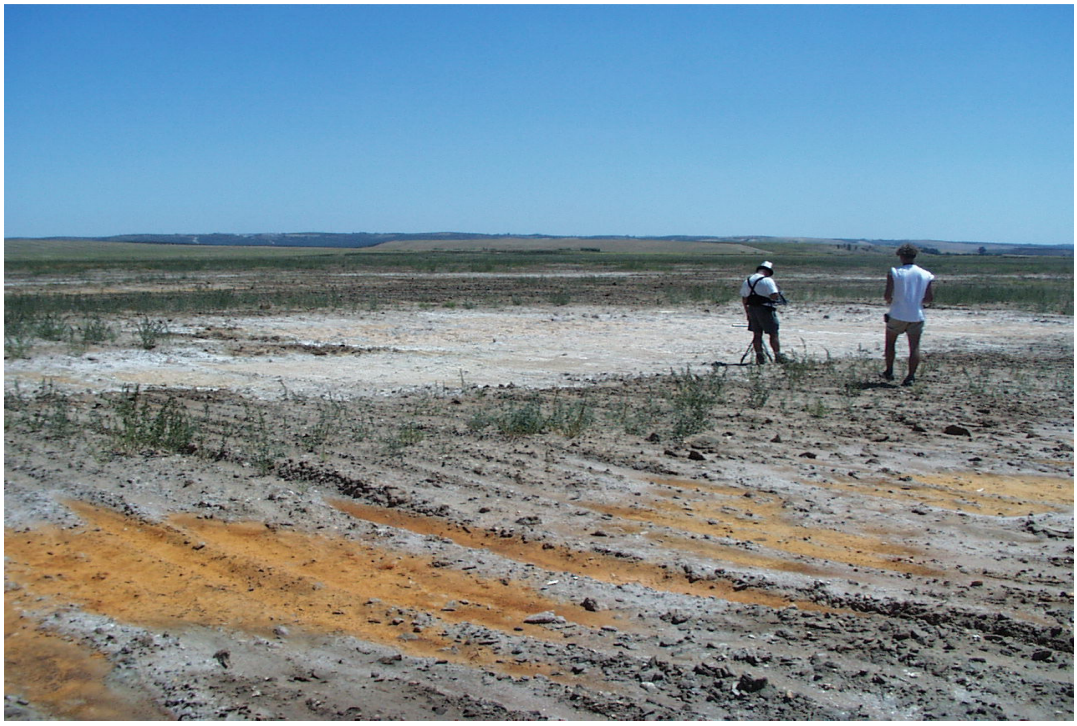

Figure 7.12. Field measurements on a typical gypsum patch (bright) in the area. In the foreground some yellow-red patches of jarosite

7.6 Conclusions

In this chapter SMA was used for mapping residual sludge and sludge derivatives. This was achieved with a variable multiple endmember SMA system (VMESMA), which offers greater flexibility and new possibilities to get improved performances and more accurate interpretation of the unmixing results.

The iterative approach of VMESMA starting with a simple endmember (EM) set of background material worked very successful; the delineation of the affected area using the RMS error after the first unmixing was almost congruent with the GIS layers of the affected area.

The standardisation of spectra was very helpful for the detection of sludge, which is a very dark and almost spectral featureless material. First, it was possible to use EM models without shade, which could have caused problems in separation of shade and sludge. Second, the standardisation enhanced the wide absorption features of sludge and it lets different types of green vegetation appear so similar that a single vegetation EM is sufficient to cover their variability.

The multiple EM approach enhanced the stability of the models in combination with the standardisation due to the fact that in most of the cases two or three EM were sufficient to model the reflectance of a pixel.

In 1999 the sludge could be characterised using a pure sludge EM, because the oxidation did not start yet. The obtained sludge abundances are in good agreement with the field observations and the results obtained by the Consejería de Medio Ambiente (2000). As mentioned before the conditions changed drastically between 1999 and 2000. The remediation efforts of the CMA resulted in a drastic reduction of the surface contamination, which is clearly reflected in the unmixing results. However in areas, where the remediation was not concluded yet the oxidation of the residual sludge had started. The complex weathering leads to an efflorescence of easily dissolved salt crusts and more stable secondary minerals. Using the spectral feature fitting algorithm and field measurements, it was possible to detect indicators like jarosite, copiapite and ferrihydrite and separate them from still not oxidised pyrite and gypsum, which points to the remediation efforts by buffering of acidity. Using these spectra as EM the spatial distribution of the oxidation becomes evident. Mayor problematic areas are found in the riverbed of the Agrio River at the confluent of the Agrio and Guadiamar rivers and in the gravel pits at Sobarbinas.

The comparison between the sludge abundance obtained in 1999 and the oxidation products obtained in 1999 shows that imaging spectroscopy is able to follow the full process of pyrite oxidation: the initial pyrite could be identified in 1999 mapping the oxidation potential. In 2000, the minerals, identified by SFF and SMA, give qualitative evidence of oxidation processes.

8 Transformation of abundances into quantitative information for remediation management

The results obtained through SMA show clearly a very heterogeneous distribution of the residual sludge. Such abundance maps are already very useful information, which could be used for remediation planning. However, a transformation into maps comparable to the results obtained by conventional approaches would facilitate their application in remediation management.

In the following section such a transformation is implemented based on the knowledge and results obtained so far. This transformation is only possible for the data of the year 1999, because it is linked directly to the close relationship between pyritic sludge matrix and associated heavy metals. The conditions changed drastically within one year. The oxidation processes and the crusting have altered the close relationship between sludge, associated heavy metals and sludge reflectance.

8.1 The artificial mixture series as a link between abundances and contamination

The artificial mixture series of soils and sludge, described in section 6.2, was initially prepared for a better understanding of the influence of sludge on reflectance, and eventually the mixture series was used to stabilize the calibration of the chemometric models. However, it is also possible to regard these samples as a spectral mixture and apply SMA as described previously. By comparison of sludge abundance and known sludge concentration of the artificial mixture series a direct link can be established, which can be exploited further for the estimation of weight-percentages and eventually transformed into concentrations of elements related to the mining accident.

The artificial mixture series was prepared with three different soils and pure sludge. The spectra of the non-contaminated soils and the pure sludge were used as EM in the unmixing. The SMA was set up as a multiple EM model in such a way that the sludge EM could mix only with one of the three soil EM. The unmixing was performed with standardised variables, thus a shade EM was neglected. Figure 8.1 shows the obtained abundances with respect to the weight percentage of the sludge in the mixture. The clearly non-linear behaviour can be explained by the fact that the soil – sludge mixture is an intimate mixture, where the darker pyrite dominates because photons are absorbed when they encounter a dark grain (Clark 1999).

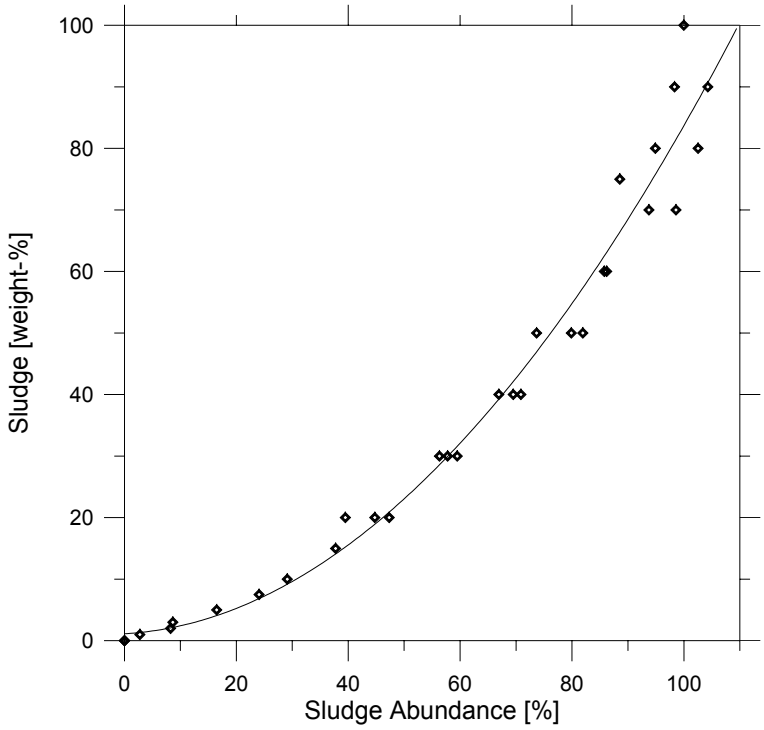

Figure 8.1. Comparison of sludge abundance derived from SMA of the mixture series and sludge weight percentage. A second order polynomial is fitted to the data ($R^2 = 0.973$).

8.2 Quantification of residual contamination and assessment of acidification risk

Knowing the relationship between sludge abundance and weight percentage offers the possibility for a quantitative assessment of the residual sludge and the related heavy metal contamination. The quantification is based on the sulphur content. Sulphur plays a key role in the assessment, because it is one of the two elements forming pyrite (FeS_2), which is the main component of the sludge, and it is the main source for acidity when pyrite oxidizes. The sulphur content is also used in conventional mining waste analysis for prediction of the geochemical behaviour of mining waste in order to identify wastes that are likely to be acid generating, potentially acid generating or otherwise susceptible to heavy metal leaching (Tremblay & Hogan 2001). A commonly applied method is Acid-Base Accounting (ABA), which is a two part analytical procedure for determination of the Acid Potential (AP) and the Neutralisation Potential (NP) of the waste (Miller 1991).

The Acid-Base Accounting process has been adapted to the Aznalcóllar accident to determine parameters that provide important information for remediation planning and can be derived in a spatial context from the unmixing results. The Acid Potential refers to the maximum potential acidity, which can be obtained by complete oxidation of residual sludge. The Neutralisation Potential is presumed to measure carbonate

minerals, exchangeable bases and weatherable silicate minerals (Sobek et al. 1978). Instead of neutralisation potential, in this study the neutralisation requirements are calculated based on the maximum potential acidity.

The calculations necessary to derive the wanted information are based on the following assumptions:

- The relationship between sludge abundance and weight-percent derived with the artificial mixture is applicable for the whole area: the mixture series was build using three different soils from different parts of the riverbed (Sobarbinas, Puente Nuevo and Vado de Quemas), which are representative for the affected area. This should reflect sufficiently the soil variability.
- The abundances obtained from the HyMap images are representative for the first twenty centimetres: in reality, the penetration depth of the radiation, and consequently the abundances obtained, is limited to less than a millimetre. The sludge contaminated the soil superficially and residual sludge was worked into the soil by ploughing, which allows the assumption that the sludge is distributed more or less homogeneously in this ploughing layer. This is also supported by the soil profiles (see Figure 5.8), which show clearly that the contamination is limited to the upper centimetres of the soil.
- The geochemical/mineralogical composition of the sludge solid phase is fundamentally stable in the entire area, although a certain grain size differentiation as function of transport length along the river course occurred.
- Sulphur is present predominantly in connection to pyrite: other secondary minerals such as jarosite or metal sulphate salts are intermediate products of starting pyrite oxidation after the accident.

Bearing in mind these assumptions, the following calculations were made. In the first step the weight percentage of sulphur was extracted from the relationship sludge abundance and sulphur content. This relationship can be expressed as a second order polynomial:

$$\text{Sulphur} = 13.98 \times (\text{Abundance})^2 + 0.8465 \times (\text{Abundance}) + 0.3751 \qquad \text{Eq. 8.1}$$

The second step implies the transfer from weight percentage to effective weight. In order to achieve such a transfer, the bulk density of the soil has to be taken into consideration, which can be approximated with 1.3 t/m³ (Brady 1984). Based on that value the amount of sulphur in the ploughing layer of the soil was calculated for each pixel:

$$\text{Sulphur [tons]} = \text{Sulphur [weight-\%]} \times 1.3\ \text{t/m}^3 \times 0.2\ \text{m} \times 5\ \text{m} \times 5\ \text{m} \qquad \text{Eq. 8.2}$$

The total amount of pyrite in this soil layer was derived from the amount of sulphur, based on the molecular composition of pyrite, which consists of 53.45 % sulphur and 46.55 % iron. Finally, the amount of residual sludge after the remediation was calculated. According to Galán et al. (2002), the pyrite concentration of the sludge ranges between 75 and 80 weight-%. With this information it is possible to roughly estimate on a pixel basis the amount of residual sludge at the time of the first sampling campaign. The overall quantity in the first 20 centimetres totalled 148976 to 186220 tons (depending on the pyrite content). Compared to the amount of tailings that was spilled (according to Eriksson & Adamek (2000) between 1.3 and 1.9 million tons), this means that after the first remediation campaign between 9.4 and 14.3 % of the released tailings remained in the area.

The amount of residual sludge is an indicator for the quality of the first clean up. This information is very valuable for remediation planning, because it allows the estimation of the maximum potential acidity and the neutralisation requirements. The calculations of the maximum potential acidity are based on the overall reaction for pyrite oxidation (Puura 1998), which is a simplified summary of the reactions described in chapter 3.2:

$$FeS_2 + 3.75\ O_2 + 3.5\ H_2O \rightarrow Fe(OH)_3 + 2\ SO_4^{2-} + 4\ H^+ \qquad \text{Eq. 8.3}$$

This means that each gram of sulphur in pyrite produces 3.06 grams of acidity (in the form of H^+ and SO_4^{2-}). The two additional cations H^+ were derived from the hydrolysis of ferric iron with water to form solid ferric hydroxide.

The calculations of the neutralisation requirements are based on the following assumed stoichiometry (Cravotta et al. 1990):

$$FeS_2 + 2CaCO_3 + 3.75O_2 + 1.5H_2O \rightarrow 2SO_4^{2-} + Fe(OH)_3 + 2Ca^{2+} + 2CO_2 \qquad \text{Eq. 8.4}$$

For each mole of pyrite that is oxidised, two moles of calcite are required for acid neutralisation, or on a mass ratio basis, for each gram of sulphur present, 3.125 grams of calcite are required for acid neutralisation.

An estimation of heavy metals is also possible. The good fit that was obtained with the second order polynomial for the estimation of the weight percentage also allows an estimation of the heavy metals, because their concentration in the samples of the mixture series can be calculated from the known concentrations of sludge and soils, and substitution of the weight percentage values. An example is given for lead (Pb) as one of the key contaminants. The second order polynomial function that was obtained from the unmixing of the mixture series has the following form:

$$Pb = 2541.1 \times (Abundance)^2 + 148.24 \times (Abundance) + 100.66 \qquad \text{Eq. 8.5}$$

These functions can be directly applied to the sludge abundance image derived from unmixing of the HyMap images from 1999 (Figure 8.2, see Annex H for the full flightline). The results show the heterogeneous spatial distribution caused by the clean up activities.

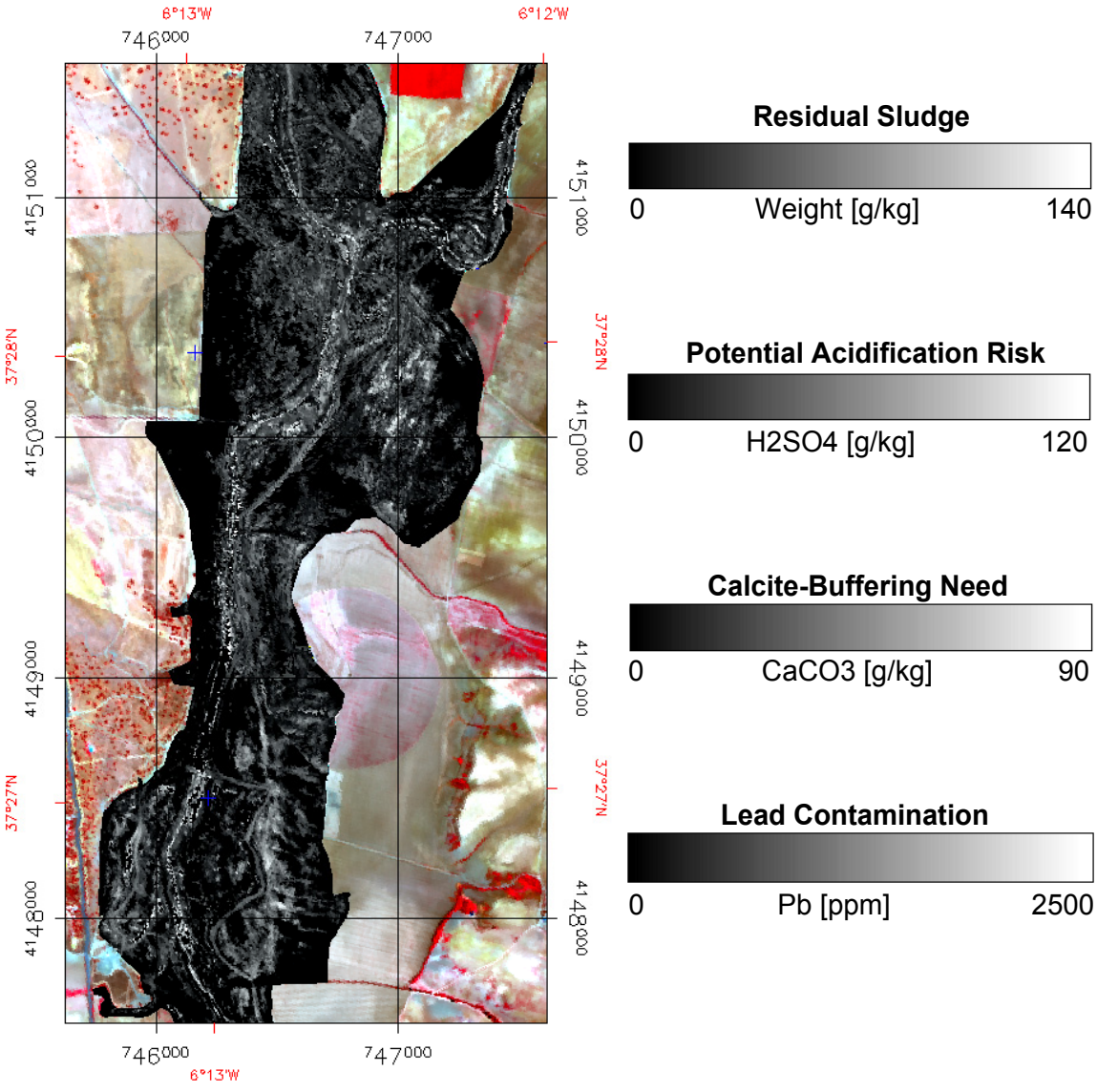

Figure 8.2. Contamination parameters derived from the sludge abundance image for June 1999: residual sludge in g/kg, maximum potential acidification after full oxidation of pyrite in g/kg, neutralisation requirements for full oxidation of pyrite in g/kg and lead contamination in ppm

8.3 Validation SMA maps against conventional methods

The transformation of abundance information into heavy metal concentrations allows validating the obtained results with the results of the geochemical analysis of soil samples collected in the field in a quantitative way.

The validation is based on the 56 surface soil samples collected during the field work, and the results of the soil sampling and analysis accomplished by the Consejeria de Mediomabiente in parallel to our field work (see chapter 5.1). For the validation, 180 points sampled from the mine downstream to the bridge of road A472 (Sanlúcar La Mayor – Castilleja del Campo) were taken into account. The direct comparison of the laboratory derived concentration with the corresponding pixel values was not possible due to inaccuracies in both the georeferenced image and the measured GPS location of the sampling point. Therefore, the best fitting pixel within a 15 m search radius around the sampling location was selected. Lead (Pb) and Arsenic (As) were selected for validation, because they were still present in high concentrations and represent different mobile heavy metals (see chapter 5.1). A total of 236 sampling points was available for Pb, but 128 samples were excluded, either because no sludge could be detected in the vicinity or the concentrations measured in the laboratory were below 100.66 ppm. This value is the detection limit in the remote sensing maps, which was imposed by the offset in equation (Eq. 8.5). Figure 8.3 shows the comparison between laboratory and image derived lead concentration. After excluding 5 outliers, a coefficient of determination of 0.729 was obtained. However, the data are strongly controlled by the skewed distribution of the data. Generally, the model works better for medium and high concentrations; e.g., when considering only concentrations above 300 ppm, the coefficient of determination improves ($R^2 = 0.852$).

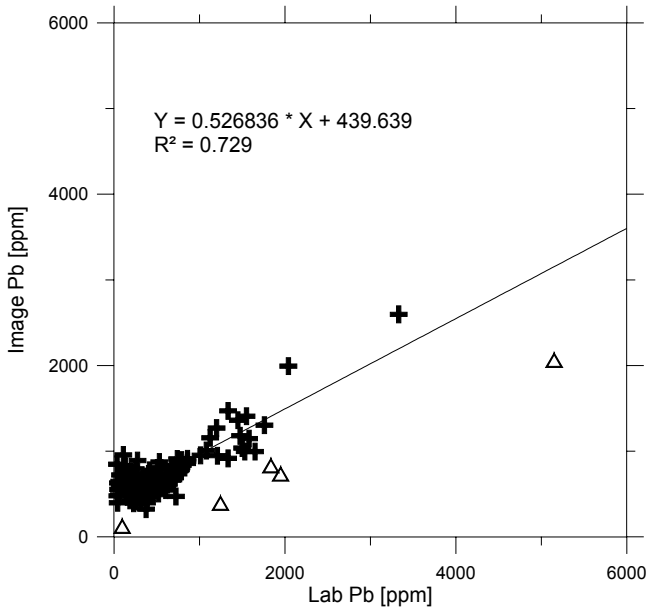

Figure 8.3: Comparison of Pb concentrations for samples analysed in laboratory with concentrations derived from HyMap data. Outliers (△) were not included into the regression.

The relationship between As and sludge abundance was derived from the SMA of the artificial mixture series in the same way as described for lead and sulphur using a second order polynomial:

$$As = 328.18 \times (Abundance)^2 + 18.345 \times (Abundance) + 24.809 \qquad \text{Eq. 8.6}$$

For As, 122 samples could be used after removing samples without sludge abundances in the vicinity or with concentrations measured in the laboratory below the detection limit of 24.8 ppm for As. The range of arsenic concentrations in the laboratory is much wider than in the image-derived data (Figure 8.4). The concentration maximum reaches 282 ppm for the image data and 2649 ppm for the laboratory data (this value has been left out in Figure 8.4 for illustration reasons; there the highest value is 1204). Therefore, the match of high laboratory data with image data is very poor. In the low and medium range the match is much better; if laboratory concentrations above 400 ppm are left out, a strong coefficient of determination ($R^2 = 0.732$) can be obtained.

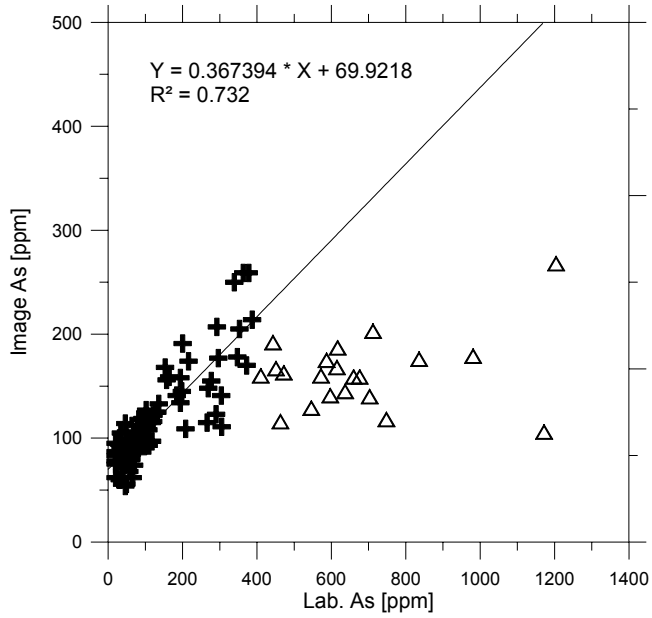

Figure 8.4. Comparison of As concentrations for samples analysed in laboratory with concentrations derived from the HyMap data. Outliers (△) were not included into the regression. Note that the scales of the axes are chosen differently for illustration purposes.

Both examples show that there is a strong correlation between laboratory samples and field data particularly for the medium concentration ranges. They also show that the image data generally underestimate the laboratory data. On the one hand, this can be attributed to the fact that the image data are averaged over the area of one pixel. That means that locally high concentrations are reduced due to the averaging with less high

concentrations within one pixel. On the other hand, the image concentrations are derived with the artificial mixture series, which do not reflect extreme high situations. In fact, the maxima in the data set provided by the Consejería de Medioambiente are higher than the maxima found in our sludge samples, which were used in the artificial mixture series.

However, the spatial information derived here is not meant to substitute conventional geochemical analysis methods, but to provide area-wide spatial information on a per-pixel basis, which is one of the major advantages of remote sensing data. Given a sufficient spatial resolution, remote sensing can provide information on heterogeneous environments, where an *in situ* sampling would need an enormous number of samples to cover the variability of the entire area. This is particularly true for the monitoring of residual contamination after the Aznalcóllar mining accident.

In the context of remediation planning it is more important to know a threshold for contamination above which an intervention is necessary rather than the exact contamination range. Consequently, for each heavy metal the Consejería de Medioambiente defined thresholds for intervention for sensitive and less sensitive areas, which are based on Andalusian law (Table 7.1). The law considers areas to be less sensitive areas, if they are closed for public use after establishment of the green corridor. Consequently, sensitive areas are considered public areas with a recreational aspect (Consejería de Medio Ambiente 1998).

Table 8.1. Intervention limits for sensitive and less sensitive areas applied in the green corridor (from Consejería de Medio Ambiente 1998)

	Less sensitive	Sensitive
As	100 ppm	52 ppm
Cd	10 ppm	5 ppm
Cu	500 ppm	250 ppm
Pb	500 ppm	350 ppm
Zn	1200 ppm	700 ppm

The differences between spatial information based on conventional soil sampling and remote sensing derived contamination maps will be shown with maps classified according to the thresholds mentioned in Table 8.1.

The data set of 676 samples provided by the Consejeria de Medioambiente was used to interpolate a raster-map of As concentration with a standard interpolation algorithms implemented in ArcView Spatial Analyst (ESRI 1997). The inverse distance weighted (IDW) interpolation was used, which uses a linearly weighted combination of a set of

neighbouring points, where the weight is a function of inverse distance (e.g. the smaller the distance, the higher the weight) (e.g. Davis 1986, Cressie 1993). There are a number of (more sophisticated) methods for spatial interpolation, e.g. kriging; however it is out of the scope of this study to compare different interpolation approaches. More detailed information can be found in the above-mentioned literature. In this study the IDW interpolation with a weight of 2 and 4 nearest neighbours obtained the best results.

Figure 8.5 shows the comparison of the two different maps and the sampling points with the symbol size attributed to the contamination level. The portions of the contamination levels are very similar for the soil samples, the remote sensing and the interpolated map, respectively (Table 8.2). Both maps show generally similar patterns of contamination, e.g. the high contamination in the northern part, which is the lower part of the Rio Agrio and its confluent with the Rio Guadiamar. However, the level of detail is much higher in the remote sensing derived map due to the ability to estimate the contamination based on the abundance rather than interpolating between neighbouring points.

There are also areas with differences between remote sensing data and soil analysis/interpolation. For example, in the southern part of Figure 8.5 the concentration in the remote sensing image is generally higher than in the interpolated one. In this area the Sobarbina site is located. According to our analyses, the As concentration is still high with an average of 172 ppm for the surface samples (Table 5.4). In view of that, it can be assumed that the results obtained by remote sensing reflect the contamination situation in this area better than the interpolation. The soil sampling in this area has possibly taken less contaminated samples by chance or the contamination situation has changed significantly between the different sampling dates due to clean-up activities.

Table 8.2. Comparison of relative amounts of contamination levels for different data sets

As [ppm]	Geochemistry (soil samples)	Remote sensing (area)	Interpolation (area)
As < 52	69.53 %	66.97 %	68.23 %
52 < As < 100	16.27 %	16.28 %	13.85 %
As > 100	14.20 %	16.75 %	17.92 %

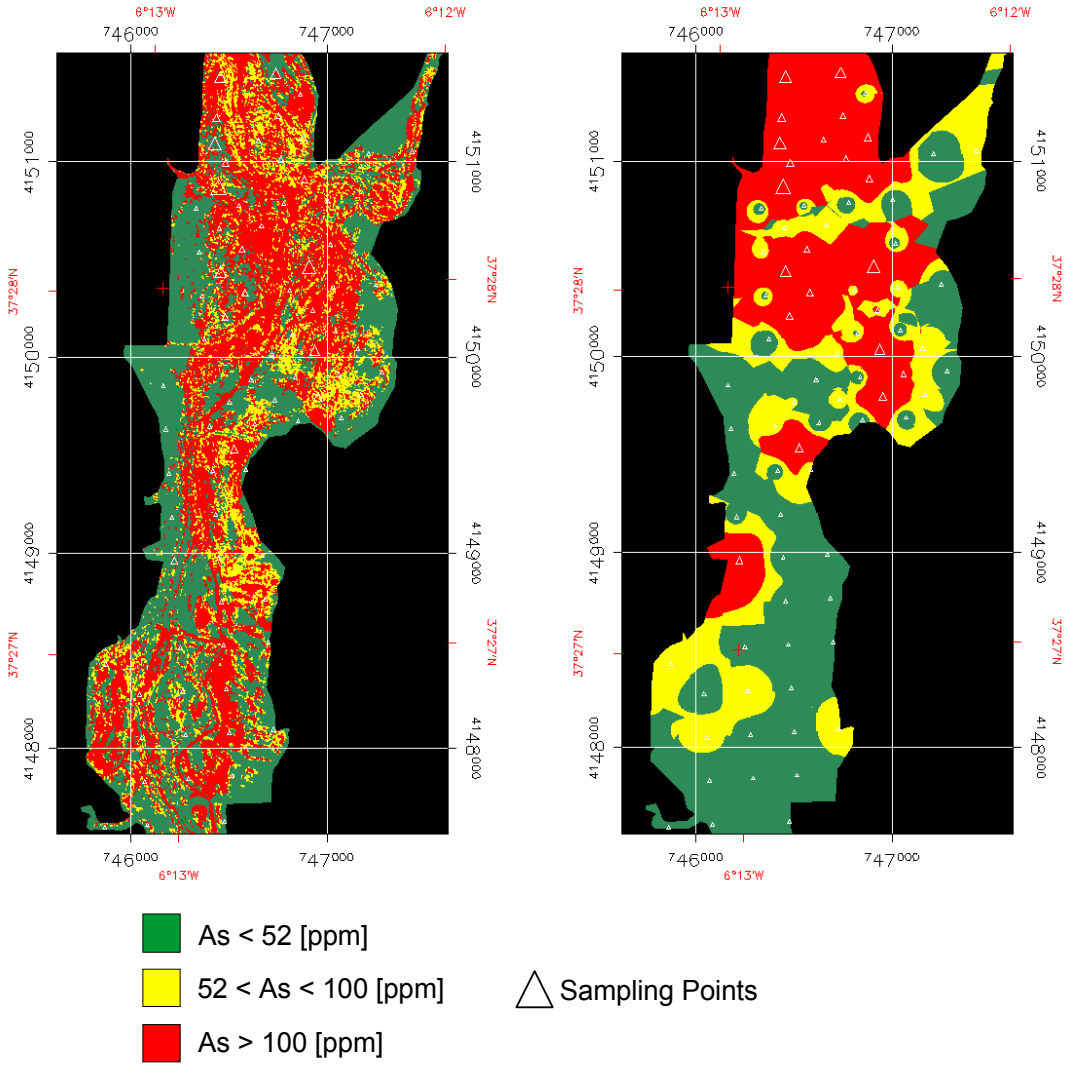

Figure 8.5. Comparison of classified As maps based on remote sensing (left) and based on interpolated point measurements (right). The size of the sampling points is related to the measured As concentration.

8.4 Conclusion

The unmixing of the artificial mixture series allowed linking the sludge abundances and the sludge weight. Through this link also the heavy metal concentrations could be linked to the abundances and maps of heavy metals, oxidification risk and neutralisation needs, which can be very valuable products for remediation, were produced. The comparison with a fully independent data set acquired at the same time showed that the results obtained with remote sensing data are very precise and that they are superior to the interpolation example carried out.

However, this approach was only possible as long as the sludge in the field was not considerably altered and the samples of the mixture in the lab are comparable to the intimate mixture in the field, which was caused by the ploughing after the first clean up. Already the data of the year 2000 are so different that this relationship has to be handled with care.

Nevertheless, it demonstrates the potential of unmixing of imaging spectroscopy for fast screening of residual contamination. The produced maps could have helped much better in coordination of the remediation by providing detailed information about location and approximate amount of residual tailings and leading to more efficient distribution of neutralizing material.

9 Conclusions and recommendations

Laboratory, field and imaging spectroscopy have been tested and applied to develop a concept for identification, quantification and monitoring of metal mining related contamination addressing particularly the situation in the Guadiamar floodplain after the Aznalcóllar accident in 1998. The conclusions related to the methodology and the results obtained are listed below:

The levels of contamination found in June 1999 after the first cleaning campaign were in many areas still very high, making a second clean-up campaign necessary. The clean-up with heavy machinery left considerable amounts of tailings sludge on the grounds and favoured a mixing up of pyritic material and soil, which led to a discontinuous distribution of the contamination. In July 2000, the remediation efforts of the Consejería de Medio Ambiente had reduced the level and extent of contamination significantly. However, in some areas oxidation processes were detected and for several toxic elements the concentrations in deeper soil layers increased indicating a mobilisation of these elements. Particularly, the increasing concentrations of arsenic give rise to concern. This underpins the necessity for a continuous monitoring of the entire area and new remediation actions in cases of detection of oxidation processes. Despite the huge dimension of the accident, the Aznalcóllar case is a positive example for the remediation of an affected area. There are many examples of mining areas, which are sources of contaminant emission without major attempts to solve the problems. Only 30 km East of the Guadiamar basin, for example, the Rio Tinto every year releases high amounts of heavy metals into the Gulf of Cadiz (Van Geen et al. 1997, Davis et al. 2000).

Based on the experiences made in the Aznalcóllar case, a concept to apply combined laboratory, field and imaging spectroscopy is proposed, which includes the following steps:

1. Soil sampling, geochemical analysis and spectral measurements in the laboratory
2. Building predictive chemometric models with the laboratory data
3. Determination of the relationship between sludge concentration and reflectance of the mixture
4. SMA of mixture series and hyperspectral images and application of the empirical relationship of the mixture series to the hyperspectral data
5. Assessment of spatial distribution of residual sludge and potential acidification risk
6. Monitoring of oxidation processes

The above-described working steps are based on the following methodological implications:

- The pre-processing of spectra has a strong influence on the prediction quality of the chemometric models. Depending on the model used, best results were obtained with standardised, vector-normalised spectra or first order derivatives, because these methods best enhance the features of interest. In most cases, spectra with 10 or 20 nm FWHM produced the best results, because they are the best compromise between ability to resolve spectral features, the number of variables and noise.
- The three different chemometric methods produced comparable results for the laboratory data set, because the link between reflection decrease and sludge content increase was very strong and linear and the heavy metals were clearly associated with the pyritic sludge matrix.
- A careful model calibration and validation is crucial for the modelling process. The application of the models always has to consider the data, which were used for calibration. If the conditions change, the model has to be recalibrated. This became obvious when applying the laboratory models to field spectra, whose spectral characteristics changed drastically compared to the laboratory spectra. After recalibration with field spectra, the models were able to predict also the concentrations of crusted surfaces. Furthermore, the models should be validated from time to time with new data for quality control.
- The construction of an artificial mixture series of sludge and non-contaminated soils improved considerably the understanding of the relationship between sludge content and sludge reflectance of the mixtures. It highlighted the strong correlation between sludge content and spectral reflectance with a strong decrease in albedo with increasing sludge content and a wide iron absorption at about 1.0 µm becoming the main feature.
- In order to understand chemometric models, a deeper understanding of the underlying chemistry and physics is as important as a set of statistical parameters describing the models. This means for spectral data that a basic understanding of spectra and their errors is useful and that spectral representation should be included in the usefulness of the data treatment (Geladi & Martens 1996a). In this context the mixture series was very helpful. In this data set, the best results were obtained for elements linked to the mining accident such as heavy metals, iron and sulphur. However, also within this group big differences could be observed which were related to the mobility of the heavy metals: the less mobile the elements, the better their prediction.
- Spectral mixture analysis (SMA) is a method to solve successfully the problems of scale-induced mixtures. The use of multiple EM sets and an iterative approach proved to be superior to conventional methods allowing a very site-

specific mixture strategy, which is necessary to separate sludge and non-sludge reflectance. In that respect also the use of standardised reflectance improved strongly the unmixing results.

- With SMA it was possible to identify clearly the residual sludge in the year 1999. Moreover, with the data of the year 2000 it was possible to detect hot spots, where the oxidation of the residual sludge had started. This opens the possibilities to use hyperspectral remote sensing as a monitoring tool. Since pyrite and also the secondary minerals can be identified, it is possible to use hyperspectral data and SMA as screening tool for metal mining related contamination.
- The abundance of residual sludge and its oxidation products are already valuable products for semi quantitative estimation, which can be used to locate areas in which further remediation efforts are necessary. However, this semi quantitative information could be turned into quantitative maps through incorporation of the artificial mixture series. By unmixing the spectra of the artificial mixture series, a non-linear relationship between sludge abundance and sludge weight was established, which we consider applicable to describe also the intimate mixture of non-oxidised sludge and soil as represented in the imaging spectroscopy data.
- Based on this relationship the amount of residual sludge in the area was estimated for the year 1999. To our knowledge such information was not available so far. According to these estimates between 9.4 and 14.3 % of the released tailings remained in the area after the first clean up. With simple geochemical models, this information could be turned into maps of potential acidification risk, calcite buffering needs and heavy metals.
- A comparison of the obtained results with an independent conventional data set, which was acquired at the same time by the Consejería de Medio Ambiente, showed a good correlation between image derived concentrations and laboratory measurements. Remote sensing data usually underestimate the concentrations, because of the bigger areal integral compared to point sampling, which however, may be strongly influenced by nugget effects. The level of detail provided by remote sensing data overcomes that of standard interpolation methods.

The applied method proved to be able to provide quantitative information for identification and characterisation of environmental contamination related to metal mining. For example, in the case of the remediation of the Leadville mining area (Colorado, USA), the use of mineral maps derived from imaging spectroscopy data accelerated the remediation efforts by two years, saving over 2 million US$ in investigation costs (Swayze et al. 2000). The U.S. Bureau of Reclamation and the Environmental Protection Agency used the produced maps to prioritise field sampling of mine waste sites.

On the basis of this study an integrated mapping and monitoring approach for similar tailings pond accidents and the inventory of related contamination is proposed, which is discussed using the Aznalcóllar example. Assuming the availability of the necessary equipment (field spectrometer, airborne imaging spectrometer), the remediation of the contaminated area could have been alleviated according to the following scenario (Figure 9.1):

Few days after the accident, the extent of the contamination is mapped using an airborne sensor. The derived map is a direct input for the planning of the clean-up activities. In parallel a soil sampling campaign is carried out to describe the contamination level using geochemical analysis. The data are also used for calibration of chemometric models.

The first clean up is controlled with imaging spectroscopy data. The derived sludge abundance map is used to locate areas with high sludge abundances and HM concentrations, where a re-cleaning is necessary. The maps of potential acidification risk and acidity buffering needs are used to determine precisely the amount of calcite necessary to buffer fully the oxidation of pyrite.

After the remediation, imaging spectroscopy is proposed for monitoring purposes based on the hypothesis that the occurrence of secondary minerals on the soil surface is an indicator for pyrite oxidation, which could mobilise HM. The presence of these minerals on the surface is also a strong indicator for sub-surface oxidation processes going on, which must be verified by a closer examination *in situ*.

However, the described scenario requires an *ad hoc* availability of hyperspectral sensors. Today, there are only few airborne hyperspectral sensors for scientific purposes available in Europe. This limits a fast disaster monitoring in the case of accidents in some way due to the long preparation times for the flight campaigns.

The proposed methodology has to be adapted to the local geological environment, if applied to similar accidents. However, it can be expected that it can be transferred to other VMS or porphyric copper deposits. For every accident a new calibration data set is necessary, due to the changing composition of the ores and different soil background. However, the calibration methodology can be applied in the same standardised way. Moreover, the identification of indicator minerals is rather robust, because the key minerals of the sulphate oxidation (e.g. jarosite, copiapite) always exhibit the same spectral features.

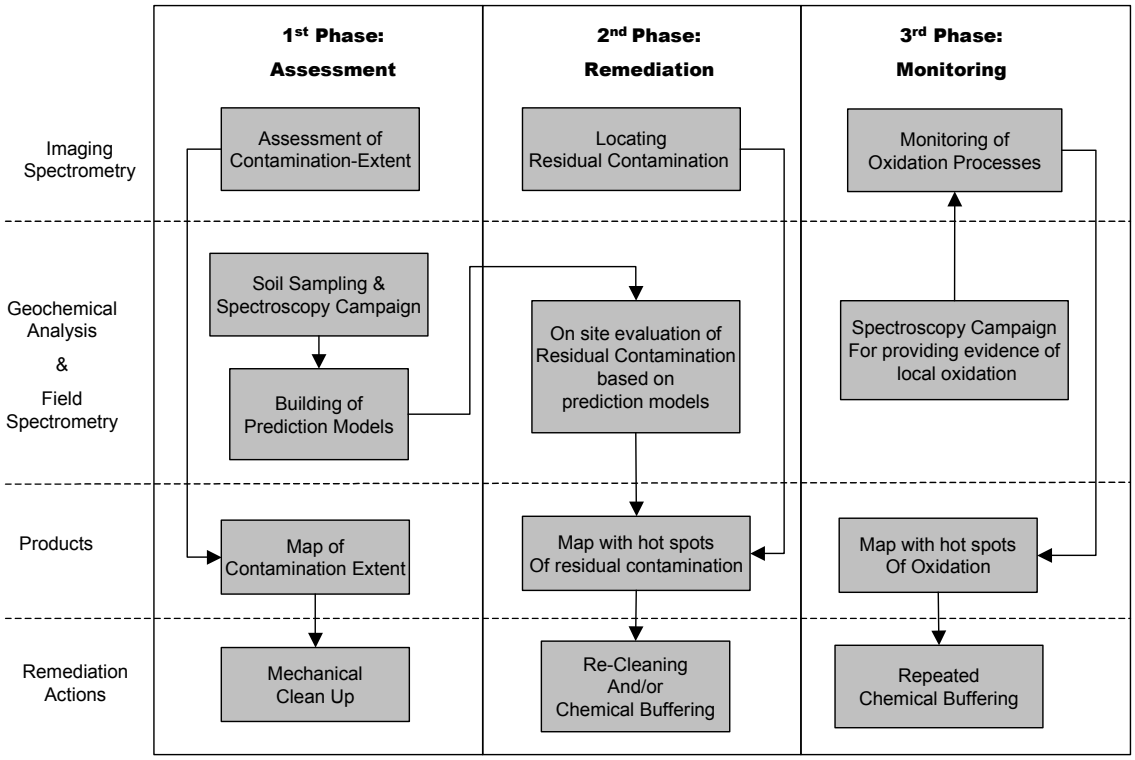

Figure 9.1. Proposed scheme for an integrated assessment and spatial monitoring of metal mining related contamination

10 Literature

Adams, J.B., Sabol, B., Kapos, V., Filho, R.A., Roberts, D.A., Smith, M.O., and Gillespie, A.R. (1995): Classification of multispectral images based on fractions of endmembers: application to land-cover change in the Brazilian Amazon. *Remote Sensing of Environment,* **52**, 137-154

Adams, J.B., Smith, M.O., Johnson, P.E. (1986): Spectral mixture modelling: A new analysis of rock and soil types at the Viking Lander 1 Site, *Journal of Geophysical Research*, **91,** B8, 8098-8112

Adams, J.B., Smith, M.O., Gillespie, A.R. (1993): Imaging spectroscopy: interpretation based on spectral mixture analysis. In: *Remote geochemical analysis: Elemental and mineralogical composition*, edited by C.M. Pieters & P.A.J. Englert, *Cambridge University Press, Cambridge*, 145-166

Afifi, A.A. & Azen, S.P. (1971): Statistical Analysis, a computer aided approach. *Academic Press, London*

Aguilar, J., Dorronsoro, C., Fernández, E., Fernández, J., García, I., Martín, F., Ortiz, I., Simón, M. (2000): El desastre ecológico de Aznalcóllar. http://edafologia.ugr.es/donana/aznal.htm, assessed 31.10.2002

Ainsworth, N., Cooke, J.A., Johnson, M.S. (1991): Biological significance of antimony in contaminated grassland. *Water, Air and Soil Pollution*, **57-58**, 193-199

Alastuey, A., García-Sánchez, A., López, F., Querol, X. (1999): Evolution of pyrite mud weathering and mobility of heavy metals in the Guadiamar valley after the Aznalcóllar spill, southwest Spain. *Science of the Total Environment*, **242**, vol. 1-3, 41-55

Alba, F.O, (1991): El medio físico. In: *Geografía de España. Anadalucía, Canarias. Volumen 8,* edited by Bosque Maurel, J. & Vilá Valentí, J., *Editorial Planeta, Barcelona*, 33-109

Alexander, S.S., Dein, J., Gold, D.P. (1973): The use of ERTS-1 MSS data for mapping strip mines and acid mine drainage in Pennsylvania. *Proceedings of the Symposium on Significant Results Obtained from Earth Resources Satellite-1*, edited by Freden, S.C. & Mercanti, E.P., *Greenbelt, MD; NASA Goddard Space Flight Center X-650-73-155*, Vol. 1, 569-575

Alloway, B.J. (1999): Schwermetalle in Böden, Analytik, Konzentrationen, Wechselwirkungen. *Springer, Berlin, Heidelberg, New York*

Almodóvar, G.R., Sáez, R., Pons, J.M., Maestre, A., Toscano, M., Pascual, E. (1998): Geology and Genesis of the Aznalcóllar massive sulphide deposits, Iberian Pyrite Belt, Spain. *Mineralium Deposita*, **33**, 111-136

Alpers, C.N. & Bowles, D.W. (eds.) (1994): Environmental Geochemistry of Sulfide Oxidation. *American Chemical Society Symposium Series 550, Washington, D.C.*

Analytical Spectral Devices, Inc. (1999): ASD Technical Guide. *3rd ed., Boulder*

Anderson, C.A. & Bro, R. (2000): The N-way toolbox for Matlab. *Chemometrics and intelligent Laboratory Systems*, **52**, 1-4, http://www.models.kvl.dk/source/nwaytoolbox/, assessed 31.10.2002

Anderson, J.E., & Robbins, E.I. (1998): Spectral reflectance and detection of iron-oxide precipitates associated with acid mine drainage. *Photogrammetric Engineering & Remote Sensing*, **64**, 12, 1201-1208

Arambarri, P., Cabrera, F., González-Quesada, R. (1996): Quality evaluation of the surface waters entering the Doñana National Park (SW Spain). *Science of the Total Environment*, **191**, 185-196

Bateson, A., & Curtiss, B. (1996): A method for manual endmember selection and spectral unmixing. *Remote Sensing of Environment*, **55**, 229-243

Baumgardner, M.F., Silva, L.F., Biehl, L.L., Stoner, E.R. (1985): Reflectance properties of soils. *Advances in Agronomy*, **38**, 1-44

Ben-Dor, E. & Banin, A. (1990): Near-infrared reflectance analyses of carbonate concentrations in soils. *Applied Spectroscopy*, **44**, 1064-1069

Ben-Dor, E. & Banin, A. (1994): Visible and near-infrared (0.4-1.1μm) analysis of arid and semiarid soils. *Remote Sensing of Environment*, **48**, 261-274

Ben-Dor, E., Irons, J.R., Epema, G.F. (1999): Soil Reflectance. In: *Remote sensing for the earth sciences; manual of remote sensing, 3rd ed., vol. 3,* edited by Rencz, A.N., *Wiley & Sons, New York,* 111-188

Berk, A., Bernstein, L.S., Robertson, D.C. (1989): MODTRAN – a moderate resolution model for LOWTRAN7. *Report GL-TR-89-0122, Geophysics Laboratory, Bedford, MA, USA*

Bigham, J.M., Schwertmann, U., Carlson, L. (1992): Mineralogy of precipitates formed by biochemical oxidation of Fe(II) in mine drainage. In: *Biomineralisation processes of iron and manganese: Modern and ancient environments,* edited by Skinner, H.C.W. & Fitzpatrick, *Catena supplement 21, Catena Verlag, Cremlingen-Destedt, Germany*, 219-232

Blume, H.P. & Brümmer, G. (1991): Prediction of heavy metal behaviour by means of simple field tests. *Ecotoxicology, Environmental Safety*, **22**, 164-174

Boardman, J. W., and Goetz, A. F. H. (1991): Sedimentary facies analysis using imaging spectrometry: A geophysical inverse problem. *Proceedings of the 3rd AVIRIS Airborne Geoscience Workshop,* http://popo.jpl.nasa.gov/docs/workshops/91_docs/3.PDF, assessed 31.10.2002

Boardman, J. W., Kruse, F. A., Green, R.O. (1995): Mapping target signatures via partial unmixing of AVIRIS data. *Proceedins of the 5th AVIRIS Airborne Geoscience Workshop,* http://popo.jpl.nasa.gov/docs/workshops/95_docs/7.PDF, assessed 31.10.2002

Boardman, J.W. (1989): Inversion of Imaging Spectrometer Data using Singular Value Decomposition. In: *Proceedings of the 1989 International Geoscience and Remote Sensing Symposium (IGARRS '89) and Twelfth Canadian Symposium on Remote Sensing, Vancouver, British Columbia,* vol. 4, 2069-2072

Bowen, H.J.M. (1979): Environmental Chemistry of Elements. *Academic Press, London*

Brady, N.L. (1984): The nature and properties of soils. *9th ed., Macmillan, New York*

Braun, H. (1997): Optimierung durch Lernen und Evolution. *Springer, Berlin*

Brown, S.D., Sum, S.T., Despagne, F., Lavine, B.K. (1996): *Chemometrics. Analytical Chemistry*, **68**, 21R-61R

Burns, R. (1993): Mineralogical applications of crystal field theory. *2nd ed., Cambridge University Press, Cambridge*

Cabrera, F., Clemente, L., Diaz Barrientos, E., López, R., Murillo, J.M., (1999): Heavy metal pollution of soils affected by the Guadiamar toxic flood. *Science of the Total Environment,* **242(1-3)**, 117-130

Cabrera, F., Soldevilla, M., Cordón, R., Arambarri, P. (1987): Heavy metal pollution in the Guadiamar river and the Guadalquivir estuary (south west Spain). *Chemosphere*, **16**, 463-468

Cabrera, F., Toca, C.G., Diaz, E., de Arambarri, P. (1984): Acid mine-water and agricultural pollution in a river skirting the Doñana national park (Guadiamar river, SW Spain). *Water Research*, **18**, 1469-1482

Castellan, G.W. (1983): Physical chemistry. *3rd ed., Addison-Wesley, Reading, Mass.*

Chase, P.J. & Pettyjohn, W. (1973): ERTS-1 investigation of ecological effects of strip mining in Eastern Ohio. *Proceedings of the Symposium on Significant Results Obtained from Earth Resources Satellite-1*, edited by Freden, S.C. & Mercanti, E.P., *Greenbelt, MD; NASA Goddard Space Flight Center X-650-73-155*, Vol. 1, 561-568

Chiu, H.Y. & Collins, W.E. (1978): A spectroradiometer for airborne remote sensing. *Photogrametric Engineering & Remote Sensing*, **44**, 507-517

Clark, R.N. & Swayze, G.A. (1995): Mapping Minerals, Amorphous Materials, Environmental Materials, Vegetation, Water, Ice and Snow, and Other Materials: The USGS Tricorder Algorithm. *Proceedings of the 5th AVIRIS Airborne Geoscience Workshop*, http://popo.jpl.nasa.gov/docs/workshops/95_docs/12.PDF, assessed 31.10.2002

Clark, R.N. & T.L. Roush (1984): Reflectance Spectroscopy: Quantitative Analysis Techniques for Remote Sensing Applications, *Journal of Geophysical Research*, **89**, B7, 6329-6340

Clark, R.N. (1999): Spectroscopy of rocks, minerals, and principles of spectroscopy. In: Remote sensing for the earth sciences: *Manual of remote sensing, 3rd ed., vol. 3, edited by Rencz, A.N., Wiley & Sons, New York*, 3-58

Clark, R.N., A.J. Gallagher, G.A. Swayze (1990): Material absorption band depth mapping of imaging spectrometer data using a complete band shape least-squares fit with library reference spectra. *Proceedings of the 2nd AVIRIS Airborne Geoscience Workshop*, http://popo.jpl.nasa.gov/docs/workshops/90_docs/17.PDF, assessed 31.10.2002

Clark, R.N., G.A. Swayze, A. Gallagher, N. Gorelick, F. Kruse (1991): Mapping with Imaging Spectrometer Data Using the Complete Band Shape Least-Squares Algorithm Simultaneously Fit to Multiple Spectral Features from Multiple Materials. *Proceedings of the 3rd AVIRIS Airborne Geoscience Workshop*, http://popo.jpl.nasa.gov/docs/workshops/91_docs/2.PDF, assessed 31.10.2002

Clark, R.N., Swayze, G.A., Gallagher, A.J., King, T.V.V., Calvin, W.M. (1993): The U.S. Geological Survey Digital Spectral Library, Version 1, 0.2 to 3.0 microns. *U.S. Geological Survey Open File Report 93-592*

Clark, R.N., Vance S., Green R.O. (1998) Mineral Mapping with Imaging spectroscopy: the Ray Mine, AZ. *Proceedings of the 7th AVIRIS Airborne Geoscience Workshop*, http://popo.jpl.nasa.gov/docs/workshops/98_docs/10.pdf, assessed 31.10.2002

Cocks, T., Jenssen, R., Stewart, A., Wilson, I., Shields, T. (1998): The HyMap ™ airborne hyperspectral sensor: the system, calibration and performance. *Proceedings of the 1st EARSeL Workshop on Imaging Spectroscopy, 6-8 October 1998, Zurich*, 37-42

Collins, W., Chang, S.H., Raines, F., Canney, F., Ashley, R.F. (1983): Airborne geophysical mapping of hidden mineral deposits. *Economic Geology*, **76**, 737-749

Consejería de Medio Ambiente (1998): Orden de 18 de Diciembre de 1998 (Orden por la que se fijan las concentraciones límites en los suelos afectados por el accidente minero de Aznalcóllar). *Junta de Andalucia, Sevilla*, http://www.cma.junta-andalucia.es/guadiamar/normativa/orden13.html, assessed 31.10.2002

Consejería de Medio Ambiente (1999): Marco geográfico de la cuenca del Guadiamar. *Junta de Andalucia, Sevilla*

Consejería de Medio Ambiente (2000): The strategy for the green corridor of the Guadiamar river, fundamentals of the strategy. *Junta de Andalucia, Sevilla*

Consejería de Medio Ambiente (2001): El estado de la contaminación dos años después del vertido minero de Aznalcóllar. Seguimento de la contaminación residual en suelos. http://www.cma.junta-andalucia.es/guadiamar/situacion2a/suelo1.html, assessed 31.10.2002

Coopers & Lybrand (1998): Información sobre el seguimento del accidente de Aznalcóllar. *Junta de Andalucia, Sevilla*

Cravotta, C.A., Brady, K.B.C., Smith, M.W., Beam, R.L. (1990): Effectiveness of alkaline addition at surface mines in preventing or abating acid mine drainage: part1, geochemical considerations. *Proc. 1990 Mining and Reclamation Conference and Exhibition, West Virginia University, Charleston, West Virginia*, 221-226

Cressie, N.A.C. (1993): Statistics for spatial data. *Revised edition, Wiley & Sons, New York*

CSIC (1998): Grupo de expertos del Consejo Superior de Investigaciones Cientificas y otros organismos colaboradores sobre la emergencia ecologica del Rio Guadiamar, Informe 9, 26 de noviembre de 1998. http://www.csic.es/hispano/coto/infor9/infor9.htm, assesed 31.10.2002

Davis, J.C. (1986): Statistics and data analysis in geology. *2nd edition, Wiley & Sons, New York*

Davis, R.A., Welty, A.T., Borrego, J., Morales, J.A., Pendon, J.G., Ryan, J.G. (2000): Rio Tinto estuary (Spain) - 5000 years of pollution. *Environmental Geology*, **39(10)**, 1107-1116

Despagne, F. & Massart, D.L. (1998): Neural networks in multivariate calibration. *The Analyst*, **123**, 157R-178R

Detchmendy, D.M. & Pace, W.H. (1972): A model for spectral signature variability for mixtures. *Proceedings of the Earth Resources Observations and Information Analysis Conference, Tullahoma, Tennesee*, 596-620

Elachi, C. (1987): Introduction to the physics and techniques of remote sensing. *Wiley & Sons, New York*

Elvidge, C.D. (1990): Visible and near-infrared reflectance characteristics of dry plant materials. *International Journal of Remote Sensing*, **12**, 1775-1795

Eriksson, N. & Adamek, P. (2000): The tailings pond failure at the Aznalcóllar mine, Spain. *Proceedings of the 6th International Symposium in Environmental Issues and Waste Management in Energy and Mineral Production, Calgary, Alberta, Canada, 30 May – 2 June 2000*, http://www.mineralresourcesforum.org/workshops/regulators/2000/docs/LosFrailes.pdf, assessed 31.10.2002

ESRI (1997): Using ArcView Spatial Analyst. *Environmental Systems Research Institute Inc., Redlands, Ca, USA*

European Commission (2000): Safe operation of mining activities: a follow-up to recent mining accidents. *Communication from the Commission, Comm (2000) 664 final, 23.10.2000*, http://europa.eu.int/eur-lex/en/com/cnc/2000/com2000_0664en01.pdf, assessed 31.10.2002

Farrand, W.H. (1997): Identification and mapping of ferric oxide and oxyhydroxide minerals in imaging spectrometer data of Summitville, Colorado, USA and the surrounding San Juan Mountains. *International Journal of Remote Sensing*, **18**, 1543-1552

Farrand, W.H., Singer, R.B., Merenyi, E. (1994): Retrieval of apparent surface reflectance from AVIRIS data: a comparison of empirical line, radiative transfer and spectral mixture models. *Remote Sensing of Environment*, **47**, 311-321

Farrand, W.H. & Harsanyi, J.C. (1997): Mapping the distribution of mine tailings in the Coeur d'Alene River Valley, Idaho, through the use of a constrained energy minimisation technique. *Remote Sensing of Environment*, **59**, 64-76

Fenstermaker, L.K. & Miller, J.R. (1994): Identification of fluvially redistributed mill tailings using high spectral resolution aircraft data. *Photogrammetric Engineering & Remote Sensing*, **60**, 989-995

Ferrier, G. (1999): Application of imaging spectrometer data in identifying environmental pollution caused by mining at Rodaquilar, Spain. *Remote Sensing of Environment*, **68**, 125-137

Gaffey, S.J., L.A. McFadden, D. Nash, C.M. Pieters (1993): Ultraviolet, visible, and near-infrared reflectance spectroscopy: laboratory spectra of geologic materials. In: *Remote Geochemical Analysis: Elemental and Mineralogical Composition edited by Pieters, C. M. & Englert, P.A.J., Cambridge University Press, Cambridge*, 43-78

Galán, E., González, I., Fernández-Caliani, J.C. (2002): Residual pollution load of soils impacted by the Aznalcóllar (Spain) mining spill after clean-up operations. *Science of the Total Environment*, **286**, 167-179

Gallart, F., Benito, G., Martín-Vide, J.P., Benito, A., Prió, J.M., Regüés, D. (1999): Fluvial geomorphology and hydrology in the dispersal and fate of pyrite mud particles released by the Aznalcóllar mine tailings spill. *Science of the Total Environment*, **242(1-3)**, 13-26

García Novo, F. (1981): Ecosistemas del Coto de Doñana. *Mundo Cientifico*, **1(4)**, 440-451

García, I., Simón, C., Dorronsoro, C., Aguilar, J., Martín, F., Ortiz, I. (2000): Contaminación por oxidación de lodos piríticos. *Edafología*, **7-3**, 159-168

García-Haro, F. J., Gilabert, M. A., Meliá, J. (1999): Estimation of endmembers from spectral mixtures. *Remote Sensing of Environment*, **68**, 237-253

García-Haro, F.J. & Sommer, S. (2001): Un entorno integrado, operativo y eficiente para el análisis y estimación de parámetros en teledetección. Teledetección, Medio Ambiente y Cambio Global. Proceedings IX Congreso Nacional de Teledetección, Universidad de Lleida, Editorial Milenio, 495-499

Gates, D.M., Keegan, H.J., Schleter, J.C., Weidner, V.R. (1965): Spectral properties of plants. *Applied Optics*, **4**, 11-20

Geerken, R. (1991): Informationspotential von spektral hochaufösenden Fernerkundungsdaten für die Identifizierung von Mineralen und Gesteinen: Laborversuche und Anwendungsbeispiele in der Geologie. *Dissertation, Karlsruhe*

Geladi, P. & Martens, H. (1996a): A calibration tutorial for spectral data. Part 1, data pre-treatment and principal component regression using Matlab. *Journal of Near Infrared Spectroscopy*, **4**, 225-242

Geladi, P. & Martens, H. (1996b): A calibration tutorial for spectral data. Part 2, partial least squares regression using Matlab and some neural network results. *Journal of Near Infrared Spectroscopy*, **4**, 243-255

Geophysical & Environmental Research Corp. (1993): Single Field of View Infrared Intelligent Spectroradiometer (SIRIS) User Manual, Version 1.3. *GER, One Bennett Common, Milbrook, New York*

Goetz, A.F.H. (1989): Spectral remote sensing in geology. In: *Theory and applications of optical remote sensing, edited by Asrar, G., Wiley, New York*, 491-526

Goetz, A.F.H. (1992a): Imaging spectrometry for earth remote sensing. *In: Imaging Spectroscopy: Fundamentals and future prospective, edited by Toselli, F. & Bodechtel, J., Kluwer Academic Publishers, Dordrecht, The Netherlands*, 1-19

Goetz, A.F.H. (1992b): Principles of narrow band spectrometry in the visible and IR: instruments and data analysis. *In: Imaging Spectroscopy: Fundamentals and future prospectives, edited by Toselli, F. & Bodechtel, J., Kluwer Academic Publishers, Dordrecht, The Netherlands*, 21-32

Goetz, A.F.H., Vane, G., Solomon, J.E., Rock, B.N. (1985): Imaging Spectrometry for Earth Remote Sensing. *Science*, **228(4704)**, 1147-1153

Goguen, J.D. (1981): A theoretical and experimental investigation of the photometric functions of particulate surfaces. *PhD thesis, Cornell University, Ithaca, New York*

Green, R.O., Eastwood, M.L., Sarture, C.M., Chrien, T.G., Aronsson, M., Chippendale, B.J., Faust, J.A., Pavri, P.E., Chovit, C.J., Solis, M., Olah, M.R., Williams, O. (1998): Imaging Spectroscopy and the Airborne Visible/Infrared Imaging Spectrometer (AVIRIS). *Remote Sensing of Environment*, **65**, 227-248

Grimalt, J.O. & Macpherson, E. (1999): Editorial. Special issue of Science of the Total Environment "The environmental impact of the mine tailing accident in Aznalcóllar, SW Spain", *Science of the Total Environment*, **242(1-3)**, 1-2

Grimalt, J.O., Ferrer, M., Macpherson, E. (1999): The mine tailing accident in Aznalcóllar. *Science of the Total Environment*, **242(1-3)**, 3-11

Gross, H. N., and Schott, J. R. (1998): Application of spectral mixture analysis and image fusion techniques for image sharpening. *Remote Sensing of Environment* **63**, 85-94

Haaland, D.M. & Thomas E.V. (1988a): Partial least squares methods for spectral analyses. 1. Relation to other quantitative calibration methods and the extraction of qualitative information. *Analytical Chemistry*, **60**, 1193-1202

Haaland, D.M. & Thomas E.V. (1988b): Partial least squares methods for spectral analyses. 2. Application to simulated and glass spectral data. *Analytical Chemistry*, **60**, 1202-1208

Hapke, B. (1981): Bidirectional reflectance spectroscopy: 1. Theory. *Journal of Geophysical Research*, **86**, 3039-3054

Hapke, B. (1993): Introduction to the theory of reflectance and emittance spectroscopy. *Cambridge University Press, New York*

Harries, J. (1997): Acid mine drainage in Australia: Its extent and potential future liability. *Supervising Scientist Report 125, Supervising Scientist, Canberra*

Hildrum, K.I., Isaksson, T., Naes, T., Tandberg, A. (1992): Near infrared spectroscopy, bridging the gap between data analysis and NIR applications. *Ellis Horwood, New York*

Hill, J. (1993): High precision land cover mapping and inventory with multi-temporal earth observation satellite data: the Ardeche Experiment. *European Commission, EUR 15271 EN, Brussels, Luxembourg*

Hill, J. & Megier, J. (eds.) (1994): Imaging spectroscopy – a tool for environmental observations. *Kluwer, Dordrecht, The Netherlands*

Hill, J., Mehl, W., Sommer, S., Smith, M.O., Lacaze, B. (1995): The use of high spectral resolution imaging systems for mapping land degradation patterns in mediterranean ecosystems. *Proceedings of MAC Europe'91 Final Results Workshop, 4-6 October 1994, Lengries, Germany, European Space Agency, ESTEC, WPP-88, Noordwijk, The Netherlands*

Horwitz, H.M., Lewis, J.T., Pentland, A.P. (1975): Estimating proportions of objects from multispectral scanner data. *Final Report, NASA Contract NAS9-14123, NASA-CR-141862, Environmental Research Institute, Michigan*

Hruschka, W.R. (1987): Data analysis: wavelength selection methods. In: *Near-infrared technology in the agriculture and food industries, edited by Williams P.C. & Noris, K., American Association of Cereal Chemists, St. Paul, Minnesota*

Hudson, B.D. (1995): Reassessment of Polynov's ion mobility series. *Soil Science Society of America Journal*, **59**, 1101-1103

Huete, A.R. (1984): Separation of soil-plant mixtures by factor analysis. *Remote Sensing of Environment*, **19**, 237-251

Hunt, G.H., Salisbury, J.W., Lenhoff, C.J. (1971): Visible and near-infrared spectra of minerals and rocks: III. Oxides and Hydroxides. *Modern Geology*, **2**, 195-205

Hunt, G.R. (1980): Electromagnetic radiation: The communication link in remote sensing. In: *Remote Sensing in Geology, edited by Siegal, B.S. & Gillespie, A.R., John Wiley, New York*, 5-45

ICOLD (2001): Tailings dams risk of dangerous occurrences – lessons learnt from practical experiences. *International Committee on Large Dams, Bulletin 121, Paris*, http://www.mineralresourcesforum.org/docs/pdfs/tailingsdams.pdf, assessed 31.10.2002

Irons, J.R., Weismiller, R.A., Petersen, G.W. (1989): Soil Reflectance. In: *Theory and application of optical remote sensing, edited by Asrar, G., Wiley Ser. Remote Sensing, Wiley, New York*, 66-106

Johnson, P.E, Smith, M.O., Adams, J.B. (1992): Simple algorithms for remote sensing determination of mineral abundances and particle sizes from reflectance spectra. *Journal of Geophysical Research*, **97**, 2649-2657

Kabata-Pendias, A. & Pendias, H. (1984): Trace elements in soils and plants. *CRC press, Boca Raton, Florida*

Knipling, E.B. (1970): Physical and physiological basis for reflectance of visible and near-infrared radiation from vegetation. *Remote Sensing Environment*, **1**, 155-159

Kooistra, L., Wehrens, R., Leuven, R.S.E.W., Buydens, L.M.C. (2001): Possibilities of visible-near-infrared spectroscopy for the assessment of soil contamination in river floodplains. *Analitica Chimica Acta*, **446**, 97-105

Kramer, H.J. (1994): Observation of the earth and its environment; survey of missions and sensors. *2nd ed., Springer, Berlin*

Lacaze, B., Caselles, V., Coll, C., Hill, J., Hoff, C., De Jong, S., Mehl, W., Negendank, J. F. W., Riezebos, H., Rubio E., Sommer, S., Teixeira Filho, J., Valor, E. (1996): Integrated approaches to desertification mapping and monitoring in the Mediterranean basin, DEMON-I Project Final report. *EUR 16448 EN (Office for Official Publication of the European Communities: Luxembourg)*

Lavine, B.K. (1998): Chemometrics. *Analytical Chemistry*, **70**, 209R-228R

Leistel, J.M., Marcoux, E., Thiéblemont, D., Quesada, C., Sánchez, A., Almodóvar, G.R., Pascual, E., Sáez, R. (1998): The volcanic-hosted massive sulphide deposits of the Iberian Pyrite Belt: Review and preface to the thematic issue. *Mineralium Deposita*, **33**, 2-30

Lide, D.R. (ed.)(2000): CRC handbook of chemistry and physics: A ready –reference book of chemical and physical data. *81st edition 2000-2001, CRC press, Boca Raton*

Lillesand, T.M., Kiefer R.W. (1994) Remote sensing and image interpretation. *3rd edition, Wiley & Sons, New York*

Lumme, K., Bowell, E. (1981): Radiative transfer in the surfaces of atmosphere-less bodies: 1. Theory. *Astronomical Journal*, **86**, 1694-1704

Lydon, J.W. (1988): Volcanogenic Massive Sulphide Deposits. Part 1: A Descriptive Model. In *Ore Deposit Models, edited by Roberts R.G. & Sheahan P.A., Geoscience Canada, Reprint Series 3, 1994*, 145-153.

Mackin, S, Settle, J, Drake, N. and Briggs, S (1991): Curve shape matching, end-member selection and mixture modeling of AVIRIS and GER data for mapping surface mineralogy and vegetation communities. *Proceedings of the 3rd AVIRIS Airborne Geoscience Workshop*, http://popo.jpl.nasa.gov/docs/workshops/91_docs/20.PDF, assessed 31.10.2002

Madden, H. (1978): Comments on the Savitzky-Golay convolution method for least square fit smoothing and differentiation of digital data. *Analytical Chemistry*, **50(9)**, 1383-1386

Malley, D.F. & Williams, P.C. (1997): Use of near-infrared reflectance spectroscopy in prediction of heavy metals in freshwater sediment by their association with organic matter. *Environmental Science and Technology*, **31**, 3461-3467

Marcoux, E., Moelo, Y., Leistel, J.M. (1996): Compared ore mineralogy and geochemistry of the massive sulphide and stringers ore deposits of Southern Spain. *Mineralium Deposita*, **31**, 1-26

Martens, H., Naes, T. (1989): Multivariate Calibration. *Wiley & Sons, Chichester*

Massart, D.L., Vandeginste, B.G.M., Deming, S.N., Buydens, L.M.C., De Jong, S., Lewi, P.J., Smeyers-Verebeke, J. (1997): Handbook of chemometrics and qualimetrics, part A. *Elsevier, Amsterdam*

Massart, D.L., Vandeginste, B.G.M., Deming, S.N., Buydens, L.M.C., De Jong, S., Lewi, P.J., Smeyers-Verebeke, J. (1998): Handbook of chemometrics and qualimetrics, part B. *Elsevier, Amsterdam*

Mathworks (2000): MATLAB, the language of technical computing. *The Mathworks, Natrick, MA, USA*

Merton, R. N. (1999): Multi-temporal analysis of community scale vegetation stress with imaging spectroscopy. *Ph.D. Thesis, Geography Department, University of Auckland, New Zealand.*

Miller, S.D., Jeffery, J.J., Wong, J.W.C. (1991): Use and misuse of the acid base account for "AMD" prediction. *Proceedings of the 2nd International Conference on the Abatement of Acidic Drainage, Vol. 3, CANMET, Ottawa, Ontario*, 489-506

Mustard, J.F. & Pieters, C.M. (1987a): Quantitative abundance estimates from bidirectional reflectance measurements. *Proceedings of the 17th Lunar and Planetary Science Conference, Journal of Geophysical Research*, **92**, E617-E626

Mustard, J.F. & Pieters, C.M. (1987b): Abundance and distribution of serpentinized ultramafic microbreccia in Moses Rock dike: quantitative application of mapping spectrometer data. *Journal of Geophysical Research*, **92**, 10376-10390

Mustard, F.M. & Sunshine, J.M. (1999): Spectral analysis for earth science: investigations using remote sensing data. In: *Remote sensing for the earth sciences: Manual of remote sensing, 3rd edition, vol. 3, edited by Rencz, A.N., Wiley & Sons*, 251-306

Nash, D.B. & Conel, J.E. (1974): Spectral reflectance systematics for mixtures of powdered hyperstene, labradorite and ilmenite. *Journal of Geophysical Research*, **79**, 1615-1621

Nordstrom, D K. 1982. Aqueous pyrite oxidation and the consequent formation of secondary iron minerals. In: *Acid Sulfate Weathering, edited by Kittrick J A, Fanning D S, and Hossner L R, Soil Science Society of America Special Publication No. 10, Madison, Wisconsin*, 37-56

Otto, M. (1999): Chemometrics – statistics and computer application in analytical chemistry. *Wiley-VCH, Weinheim*

Peddle, D. R., Forrest, G. H., Ledrew, E. F. (1999): Spectral mixture analysis and geometric-optical reflectance modeling of boreal forest biophysical structure. *Remote Sensing of Environment*, **67**, 288-297

Pell, R.J. (2000): Multiple outlier detection for multivariate calibration using robust statistical techniques. *Chemometrics and Intelligent Laboratory Systems*, **52**, 87-104

Peters, D. (1983): Use of airborne multispectral scanner data to map alteration related to roll-front uranium migration. *Economic Geology*, **78**, 641-653

Peters, D.C., Hauff, P.L., Livo, E.K. (1995): Remote sensing for mine waste discrimination and characterisation. In: *RSS'95 – Remote sensing in Action*, edited by Curran, P.J. & Robertson, Y.C., *11-9-1995, University of Southampton*, 866-877

Plumlee, G.S., & Logsdon, M.J. (1999): The Environmental Geochemistry of Mineral Deposits, Part A. Processes, methods, and health issues. *Reviews in Economic Geology, Vol. 6, Society of Economic Geology, Littleton, Colorado, 1999*

Preissler, H., Bohbot, H., Mehl, W., Sommer, S. (1998): MEDSPEC – a spectral database to support the use of imaging spectroscopy data for environmental monitoring. Proceedings of the 1st EARSeL Workshop on Imaging Spectroscopy, Zürich, Switzerland, 6-8 October, 455-462

Press, W.H, Teukolsky, S.A., Vetterling, W.T., Flannery, B.P. (1992): Numerical recipes in C – The art of scientific computing. *2nd edition, Cambridge University Press, New York*

Puura, E. (1998): Weathering of mining rock waste containing alum shale and limestone: a case study of the Maardu dumps, Estonia. *Dissertation, Department of Chemical Engineering and Technology, Royal Institute of Technology, Stockholm, Sweden*

Ramos, L., Hernández, M., Gonzalez, M.J. (1994): Sequential fractionation of copper, lead, cadmium and zinc in soils from or near Doñana National Park. J. Environmental Quality, 23, 50-57

Rast, M. (1991): Imaging spectroscopy and its application in spaceborne systems. European Space Agency, ESTEC, ESA SP-1144, Noordwijk, The Netherlands

Reinhäckel, G. & Krüger, G. (1998): Combined use of laboratory and airborne spectrometry from the reflective to thermal wavelength range for a quantitative analysis of lignite overburden dumps. *Proceedings 27th International Symposium on Remote Sensing of the Environment, Tromsø, Norway*, 507-512

Research Systems Incorporate (RSI) (1999): The Interactive Data Language (IDL), version 5.2.1. *RSI, Boulder*

Richter, R. & Schlaepfer, D. (2001): Geo-atmospheric processing of airborne imaging spectrometry data. Part 2: atmospheric/topographic correction. Accepted by *International Journal of Remote Sensing*, ftp://ftp.geo.unizh.ch/pub/rsl2/paper/2001/ijrs01_atcor.pdf, assessed 31.10.2002

Riedmiller, M. & Braun, H. (1993): A direct adaptive method for faster backpropagation learning: The Rprop algorithm. *Proceedings of ICNN'93, IEEE Int. Conf. On Neural Networks, San Francisco, CA*, 586-591

Roberts, D. A., Gardner, M., Church, R., Ustin, S., Scheer, G., Green, R. O. (1998): Mapping chaparral in the Santa Monica Mountains using multiple endmember spectral mixture models. *Remote Sensing of Environment*, **65**, 267-279

Roberts, D., Smith, M.O., Adams, J.B., Ustin, S.L. (1992): Mapping the spectral variability in photosynthetic and non-photosynthetic vegetation, soils and shade using AVIRIS. *Proceedings of the Third Annual Airborne Geoscience Workshop*, http://popo.jpl.nasa.gov/docs/workshops/92_docs/14.pdf, assessed 31.10.2002

Roberts, D.A., Smith, M.O., Adams, J.B., Gillespie, A.R. (1991): Leaf Spectral Types, Residuals, and Canopy Shade in an AVIRIS Image. Proceedings of the 3rd AVIRIS Airborne Geoscience Workshop, http://popo.jpl.nasa.gov/docs/workshops/91_docs/7.PDF, assessed 31.10.2002

Roberts, D.A., Yamaguchi, Y., Lyon R.J.P. (1985): Calibration of airborne imaging spectrometer data to percent reflectance using field spectral measurements. *Proceedings of the 19th International Conference of Remote Sensing of the Environment, Ann Arbor, Michigan, 21-25 Oct.*

Rumelhart, D.E., Hinton, G.E., Williams, R.J. (1986): Learning internal representations by error propagation. In: *Parallel distributing processing, explorations in the microstructure of cognition, Vol. 1, Foundations, edited by Rumelhart, D.E., & McLelland, J.L., MIT Press, Cambridge*, 318-362

Savitzky, A. & Golay, M.J.E. (1964): Smoothing and differentiation of data by simplified least squares procedures. *Analytical Chemistry*, **36(8)**, 1627-1639

Schermerhorn, L.J.G. (1982): Framework and evolution of hercynian mineralisation in the Iberian Meseta. Comunicaçao Serviços Geolólgicos de Portugal, **68**, 91-140

Schlaepfer, D. & Richter, R. (2001): Geo-atmospheric processing of airborne imaging spectrometry data. Part 1: parametric orthorectification. *Accepted by International Journal of Remote Sensing*, ftp://ftp.geo.unizh.ch/pub/rsl2/paper/2001/IJRS_2000_parge.pdf, assessed 31.10.2002

Schlaepfer, D., Schaepman, M.E. , Itten, K.I. (1998): Parge: parametric geocoding based on GCP-calibrated auxiliary data. *Proceedings of SPIE International Symposium on Optical Science, Engeneering and Instrumentation, Imaging Spectrometry IV, San Diego, SPIE 3438*, 334-344, ftp://ftp.geo.unizh.ch/pub/rsl2/paper/1998/SPIE_98_parge.pdf, assessed 31.10.2002

Schubert, J.S. & MacLeod, N.H. (1973): Digital analysis of Potomac River basin ERTS imagery: Sedimentation levels at the Potomac-Anacostia confluence and strip mining in Alleghany County, Maryland. *Proceedings of the Symposium on Significant Results Obtained from Earth Resources Satellite-1*, edited by Freden, S.C. & Mercanti, E.P., *Greenbelt, MD; NASA Goddard Space Flight Center X-650-73-155*, Vol. 1, 659-664

Shimabukuro, Y. E., Batista, G. T., Mello, E. M. K., Moreira, J. C., Duarte, V. (1998): Using shade fraction image segmentation to evaluate deforestation in Landsat Thematic Mapper images of the Amazon region. *International Journal of Remote Sensing,* **19**, 535-541

Simón, M., Martin, F., Ortiz, I., García, I., Fernández, E., Fernández, J., Dorronsoro, C., Aguilar, J. (2001): Soil pollution by oxidation of tailings from toxic spill of a pyrite mine. *Science of the Total Environment*, **279(1-3)**, 63-74

Simón, M., Ortiz, I., García, I., Fernández, E., Fernández, J., Dorronsoro, C., Aguilar, J. (1998): El desastre ecológico de Doñana. *Edafología*, **5**, 153-161

Simón, M., Ortiz, I., García, I., Fernández, E., Fernández, J., Dorronsoro, C., Aguilar, J. (1999): Pollution of soils by the toxic spill of a pyrite mine. *Science of the Total Environment*, **242(1-3)**, 105-116

Singer, P.C., and Stumm, W. (1970): Acidic mine drainage-The rate-determining step. *Science*, **167**, 1121-1123

Singer, R.B. & McCord, T.B. (1979): Mars: Large scale mixing of light and dark surface materials and implications for the analysis of spectral reflectance. *Proc. 10th Lunar Planetary Science Conference, Journal of Geophysical Research Supplement*, 1835-1848

Smith, M. O., Susan, L. U., Adams, J. B., and Gillespie, A. R. (1990): Vegetation in deserts: I. A regional measure of abundance from multispectral images. *Remote Sensing of Environment*, **31**, 1-26

Sobek, A., Schuller, W., Freeman., J.R., Smith, R.M. (1978): Field and laboratory methods applicable to overburdens and minesoils. *Prepared for US Environmental Protection Agency, Cincinnati, Ohio, EPA-600/2-78-054*

Sol, V.M., Peters, S.W.M., Aiking, H. (1999): Toxic waste storage sites in EU countries, a preliminary risk inventory. *IVM Report number E-99/02, Feb. 1999, WWF Freshwater Programme, Copenhagen, Denmark*

Staenz, K. & Williams, D.J. (1997): Retrieval of surface reflectance from hyperspectral data using a look-up-table approach. *Canadian Journal of Remote Sensing*, **23**, 354-368

Steinier, J., Termonia, Y., Deltour, J. (1972): Comments on smoothing and differentiation of data by simplified least squares procedure. *Analytical Chemistry*, **44(11)**, 1906-1909

Steinnes, E. (1999): Quecksilber. In: *Schwermetalle in Böden edited by Alloway, B.J., Springer, Berlin*, 265-281

Stoner, E.R. & Baumgardner, M.F. (1981): Characteristic variations in reflectance of surface soils. *Soil Science Society of America Journal*, **45**, 1161-1165

Strauss, G.K. (1965): Zur Geologie der SW-iberischen Kiesprovinzund ihrer Lagerstätten, mit besonderer Berücksichtigung der Pyritgrube Lousal/Portugal. *Dissertation, Universität München*

Sturm, B. (1992): Atmospheric and radiometric corrections for imaging spectroscopy. In: *Imaging Spectroscopy: Fundamentals and Prospective applications, edited by Toselli, F. & Bodechtel, J., Kluwer Academic Publishers, London*, 47-60

Suits, G.H. (1983): The nature of electromagnetic radiation. In: *Manual of remote sensing edited by Simonett, D.S. & Ullaby, F.T., 2nd edition, Vol. 1, American Society of Remote Sensing, Falls Church, Va*, 37-60

Swayze, G.A., Clark, R.N., Pearson, R.M., Livo, K.E. (1996): Mapping Acid-Generating Minerals at the California Gulch Superfund Site in Leadville, Colorado Using Imaging Spectroscopy. *Proceedings of the 6th AVIRIS Airborne Geoscience Workshop*, http://popo.jpl.nasa.gov/docs/workshops/96_docs/34.PDF, assessed 31.10.2002

Swayze, G.A., Smith K.S., Clark R.N., Sutley S.J., Pearson R.M., Vance J.S., Hageman P.L., Briggs P.H., Meier A.L., Singleton M.J., Roth S. (2000) Using imaging spectroscopy to map acid mine waste. *Environmental Science and Technology*, **34**, 47-54

Tanré, E., Deroo, C., Duhaut, P., Herman, M., Morcette, J.J., Perbos, J., Deschamps, P.Y. (1990): Description of a computer code to simulate the signal in the solar spectrum: the 5S code. *International Journal of Remote Sensing*, **11**, 659-668

Thomson L. J., and Salisbury, J. W. (1993): The Mid-Infrared reflectance of mineral mixtures (7-14 μm). *Remote Sensing of Environment*, **17**, 37-53

Tompkins, S., Mustard, J. F., Pieters, C. M., Donald, W. F. (1997): Optimisation of endmembers for spectral mixture analysis. *Remote Sensing of Environment*, **59**, 472-489

Tremblay, G.A. & Hogan, C.M. (2001): MEND manual: volume 1, summary. *Ottawa, Ontario, Canada*

Tsai, F. & Philpot, W. (1998): Derivative analysis of hyperspectral data. *Remote Sensing of Environment*, **66**, 41-51

U.S. Bureau of Mines (1994): Proceedings of the International Land Reclamation and Mine Drainage Conference and 3rd International Conference on the Abatement of Acidic Drainage: *U.S. Bureau of Mines Special Publication SP 06D-94, 1-4, 1994*

U.S. Environmental Protection Agency (1985): Wastes from extraction and benefication of metallic ores, phosphate rock, asbestos, overburden from uranium mining, and oil shale. *U.S. EPA report to the congress, EPA/530-SW-85-033, Washington*

Udelhoven, T. & Schütt, B. (2000): Capability of feed-forward neural networks for a chemical evaluation of sediments with diffuse reflectance spectroscopy. *Chemometrics and intelligent Laboratory Systems*, **51**, 9-22

Udelhoven, T., Jarmer, T., Hill, J. (2000): The acquisition of spectral reflectance measurements under field and laboratory conditions as support for hyperspectral applications in precision farming. *Proceedings of the 2nd EARSeL Workshop on Imaging Spectroscopy, July 11-13, Enschede, The Netherlands*, CD-Rom

UNEP/OCHA (2000): Cyanide Spill at Baia Mare, Romania: UNEP/OCHA Assessment mission. United Nations Environment Programme & UN Office for the Coordination of Humanitarian Affairs, Joint UNEP/OCHA Environment Unit, Geneve, http://www.mineralresourcesforum.org/incidents/BaiaMare/docs/final_report.pdf , assessed 31.10.2002

UNESCO (1972): Convention concerning the protection of the world cultural and natural heritage. *UNESCO, Paris*

UNESCO (1994): Convention on wetlands of international importance especially as waterfowl habitat. *UNESCO, Paris*

USDA Forest Service (1993): Acid Mine Drainage From Mines on the National Forests, A Management Challenge. *Program Aid 1505, Washington, D.C.*

Ustin, S. L., Smith, M. O., and Adams, J. B. (1993): Remote sensing of ecological processes: a strategy for developing and testing ecological models using spectral mixture analysis. In: *Scaling Physiological Processes: Leaf to Globe, edited by Ehlringer, J. & Field, C., Academic Press, New York*, 339-357

Van Geen A., Adkins, J. F., Boyle, E. A., Nelson, C. H., Palanques A. (1997): A 120-yr record of widespread contamination from mining of the Iberian pyrite belt. *Geology*, **25**, 291–294

Vermote, E., Tanré, E., Deuzé, J.L., Herman, M., Morcette, J.J. (1997): Second simulation of the satellite signal in the solar spectrum. An overview. *IEEE Tansactions on Geoscience and Remote Sensing*, **35**, 675-686

Verbos, P. (1974): Beyond regression: new tools for prediction and analysis in the behavioural sciences. *PhD thesis, Harward, Cambridge*

Weisberg, S. (1985): Applied linear regression. *John Wiley & Sons, New York*

Weyer, L.G. (1985): Near-infrared spectroscopy of organic substances. *Applied Spectroscopy Reviews*, **21**, 1-43

Williams, P.C. & Norris, K. (eds)(1987): Near-infrared analysis in agriculture and food industries. *American Association of Food Chemists Inc., St. Paul, Minnesota*

Wold, H. (1981): Soft modelling: The basic design and some extensions. In: *Systems under indirect observation, causality-structure-prediction edited by Jöreskog, K.G. & Wold, H., North Holland, Amsterdam*

Wold, S., Martens, H., Wold, H. (1983): The multivariate calibration problem in chemistry solved by the PLS method. *Proceedings of the Conference of Matrix Pencils, edited by Ruhe, A., Kagström, B., Lecture Notes in Mathematics, Springer, Heidelberg*, 286-289

Wold, S., Sjöström, M., Eriksson, L. (2001): PLS-regression: a basic tool for chemometrics. *Chemometrics and intelligent Laboratory Systems*, **58(2)**, 109-130

World Bank (1998): Environmental Assessment of Mining Projects. In: *Environmental Sourcebook Update. World Bank, Washington*

WWF Spain (2002): Mining in Doñana, learned lessons. *WWF Spain, Madrid, Spain*

Zell, A. (1994): Simulation neuronaler Netze. *Addison Wesley Longman, Bonn*

Zupan, J. & Gasteiger, J. (1993): Neural networks for chemists. An introduction. *VCH Verlagsgesellschaft, Weinheim*

Annex

A. Description of sampling sites

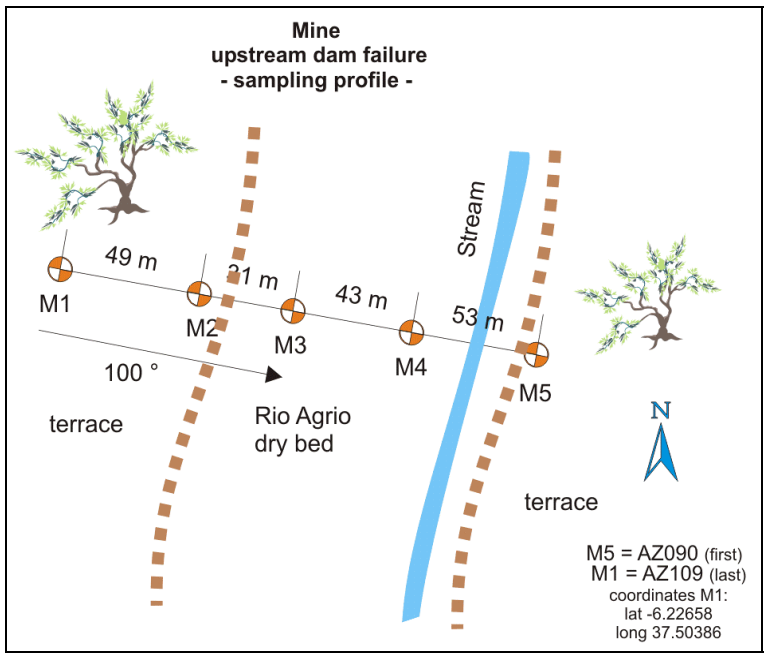

Figure A.1. Sketch of Sampling Site 'Mine North'

Table A.1. Sampling points, coordinates [decimal degrees, WGS84], corresponding soil samples and sampling depth [cm] for 'Mine North' site (non-contaminated samples in blue)

Point	Latitude	Longitude	Id	Depth
M 1	37.50386	6.22658	AZ106	0 - 2
			AZ107	2 - 20
			AZ108	20 - 40
			AZ109	40 - 60
M 2	37.50383	6.22600	AZ102	0 - 2
			AZ103	2 - 20
			AZ104	20 - 40
			AZ105	40 - 60
M 3	37.50375	6.22569	AZ098	0 - 2
			AZ099	2 - 20
			AZ100	20 - 40
M 3	37.50375	6.22569	AZ101	40 - 60
M 4	37.50377	6.22521	AZ094	0 - 2
			AZ095	2 - 20
			AZ096	20 - 40
			AZ097	40 - 60
M 5	37.5037	6.22462	AZ090	0 - 2
			AZ091	2 - 20
			AZ092	20 - 40
			AZ093	40 - 60

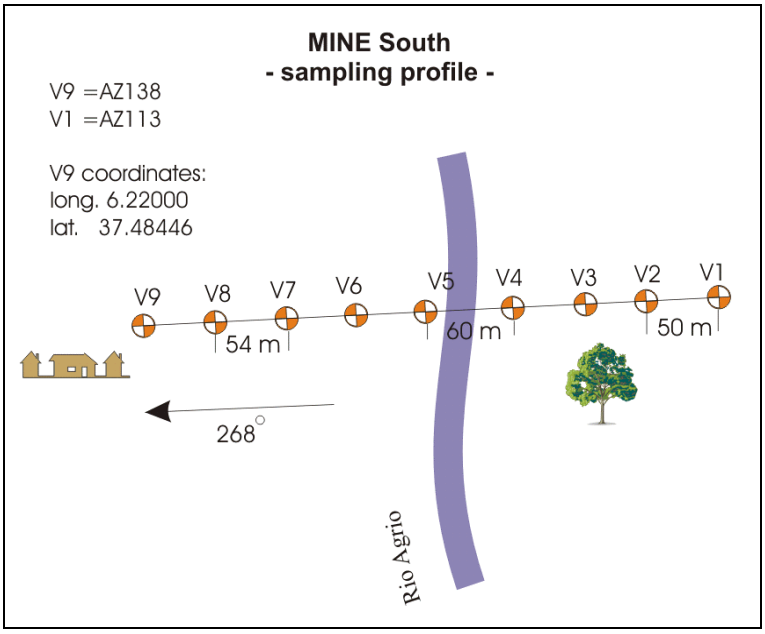

Figure A.2. Sketch of Sampling Site 'Mine South'

Table A.2. Sampling points, coordinates [decimal degrees, WGS84], corresponding soil samples and sampling depth [cm] for 'Mine South' site

Point	Latitude	Longitude	Id	Depth
V 1	37.48481	6.21537	AZ137	0 - 2
			AZ138	2 - 20
			AZ139	20 - 40
			AZ140	40 - 60
V 2	37.48481	6.21588	AZ133	0 - 2
			AZ134	2 - 20
			AZ135	20 - 40
			AZ136	40 - 60
V 3	37.48471	6.21646	AZ131	0 - 2
			AZ132	2 - 20
				20 - 40
				40 - 60
V 4	37.48472	6.21702	AZ127	0 - 2
			AZ128	2 - 20
			AZ129	20 - 40
			AZ130	40 - 60
V 5	37.48460	6.21774	AZ124	0 - 2
			AZ125	2 - 20
			AZ126	20 - 30
V 5	37.48460	6.21774		40 - 60
V 6	37.48459	6.21825	AZ121	0 - 2
			AZ122	2 - 20
			AZ123	20 - 30
				40 - 60
V 7	37.48457	6.21882	AZ118	0 - 2
			AZ119	2 - 20
			AZ120	20 - 40
				40 - 60
V 8	37.48450	6.21946	AZ114	0 - 2
			AZ115	2 - 20
			AZ116	20 - 40
			AZ117	40 - 60
V 9	37.48446	6.22000	AZ110	0 - 2
			AZ111	2 - 20
			AZ112	20 - 40
			AZ113	40 - 60

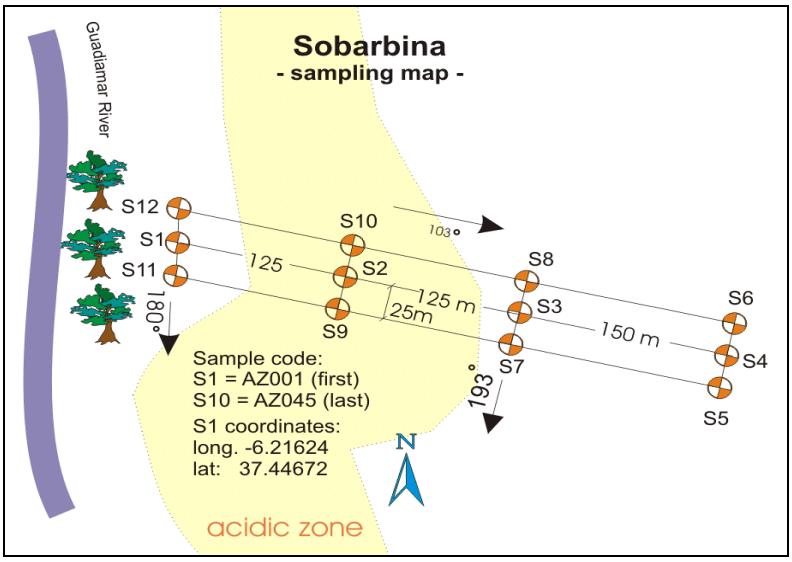

Figure A.3. Sketch of Sampling Site 'Sobarbina'

Table A.3. Sampling points, coordinates [decimal degrees, WGS84], corresponding soil samples and sampling depth [cm] for 'Sobarbina' site. (non-contaminated samples in blue)

Point	Latitude	Longitude	Id	depth
S 12	37.44695	6.21632	AZ033	0 - 2
			AZ034	2 - 20
			AZ035	20 - 40
			AZ036	40 - 60
S 1	37.44672	6.21624	AZ029	0 - 2
			AZ030	2 - 20
			AZ031	20 - 40
			AZ032	40 - 60
S 11	37.44653	6.21624	AZ025	0 - 2
			AZ026	2 - 20
			AZ027	20 - 40
			AZ028	40 - 60
S 10	37.44676	6.2148	AZ045	0 - 2
			AZ046	2 - 20
			AZ047	20 - 40
			AZ048	40 - 60
S 2	37.44659	6.21485	AZ041	0 - 2
			AZ042	2 - 20
			AZ043	20 - 40
			AZ044	40 - 60
S 9	37.44627	6.21482	AZ037	0 - 2
			AZ038	2 - 20
			AZ039	20 - 40
			AZ040	40 - 60

Point	Latitude	Longitude	Id	depth
S 8	37.44663	6.21341	AZ013	0 - 2
			AZ014	2 - 20
			AZ015	20 - 40
			AZ016	40 - 60
S 3	37.44636	6.21348	AZ017	0 - 2
			AZ018	2 - 20
			AZ019	20 - 40
			AZ020	40 - 60
S 7	37.44616	6.21351	AZ021	0 - 2
			AZ022	2 - 20
			AZ023	20 - 40
			AZ024	40 - 60
S 6	37.44662	6.21174	AZ005	0 - 2
			AZ006	2 - 20
			AZ007	20 - 40
			AZ008	40 - 60
S 4	37.44616	6.21181	AZ001	0 - 2
			AZ002	2 - 20
			AZ003	20 - 40
			AZ004	40 - 60
S 5	37.44592	6.21182	AZ009	0 - 2
			AZ010	2 - 20
			AZ011	20 - 40
			AZ012	40 - 60

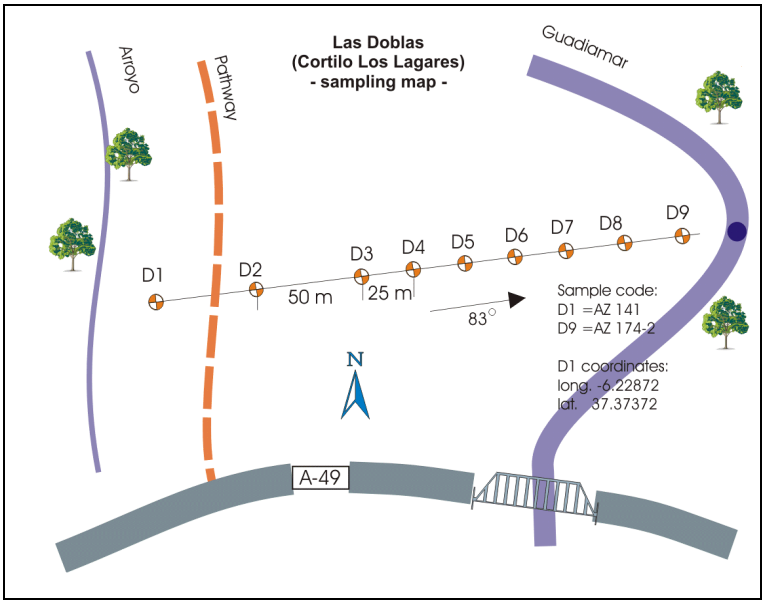

Figure A.4. Sketch of Sampling Site 'Las Doblas'

Table A.4. Sampling points, coordinates [decimal degrees, WGS84], corresponding soil samples and sampling depth [cm] for 'Las Doblas' site

Point	Latitude	Longitude	Id	Depth
D 1	37.37372	6.22872	AZ141	0 - 2
			AZ142	2 - 20
			AZ143	20 - 40
			AZ144	40 - 60
D 2	37.37383	6.28815	AZ145	0 - 2
			AZ146	2 - 20
			AZ147	20 - 40
			AZ148	40 - 60
D 3	37.37388	6.22759	AZ149	0 - 2
			AZ150	2 - 20
			AZ151	20 - 40
			AZ152	40 - 60
D 4	37.37401	6.22704	AZ153	0 - 2
			AZ154	2 - 20
			AZ155	20 - 40
			AZ156	40 - 60
D 5	37.37404	6.22678	AZ157	0 - 2
			AZ158	2 - 20
			AZ159	20 - 40

Point	Latitude	Longitude	Id	Depth
D 5	37.37404	6.22678	AZ160	40 - 60
D 6	37.37406	6.22648	AZ161	0 - 2
			AZ162	2 - 20
			AZ163	20 - 40
			AZ164	40 - 60
D 7	37.37413	6.2262	AZ165	0 - 2
			AZ166	2 - 20
			AZ167	20 - 40
			AZ168	40 - 60
D 8	37.37415	6.22593	AZ169	0 - 2
			AZ170	2 - 20
			AZ171	20 - 40
			AZ172	40 - 60
D 9	37.37418	6.22568	AZ173	0 - 2
			AZ174	2 - 20
				20 - 40
				40 - 60

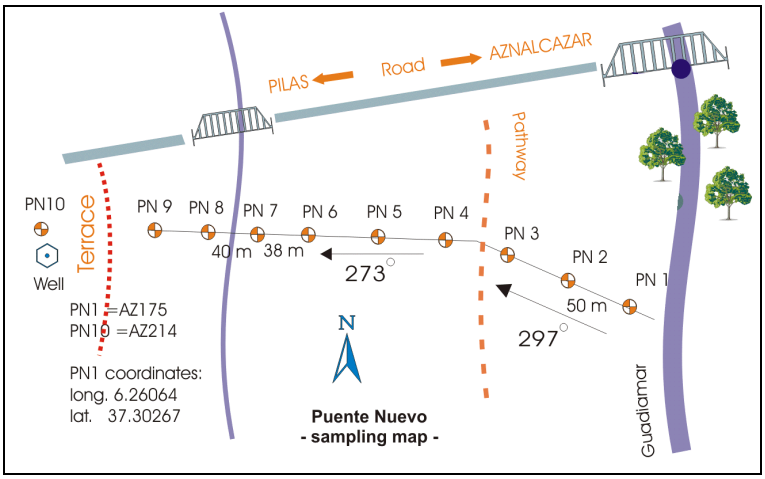

Figure A.5. Sketch of Sampling Site 'Puente Nuevo'

Table A.5. Sampling points, coordinates [decimal degrees, WGS84], corresponding soil samples and sampling depth [cm] for 'Puente Nuevo' site. (non-contaminated samples in blue)

Point	Latitude	Longitude	Id	Depth
PN 1	37.30267	6.26064	AZ175	0 - 2
			AZ176	2 - 20
			AZ177	20 - 40
			AZ178	40 - 60
PN 2	37.30282	6.26113	AZ179	0 - 2
			AZ180	2 - 20
			AZ181	20 - 40
			AZ182	40 - 60
PN 3	37.30303	6.2616	AZ183	0 - 2
			AZ184	2 - 20
			AZ185	20 - 40
			AZ186	40 - 60
PN 4	37.30301	6.26222	AZ187	0 - 2
			AZ188	2 - 20
			AZ189	20 - 40
			AZ190	40 - 60
PN 5	37.30303	6.26280	AZ191	0 - 2
			AZ192	2 - 20
			AZ193	20 - 40
			AZ194	40 - 60

Point	Latitude	Longitude	Id	Depth
PN 6	37.30302	6.26335	AZ195	0 - 2
			AZ196	2 - 20
			AZ197	20 - 40
			AZ198	40 - 60
PN 7	37.30303	6.26380	AZ199	0 - 2
			AZ200	2 - 20
			AZ201	20 - 40
			AZ202	40 - 60
PN 8	37.30306	6.26428	AZ203	0 - 2
			AZ204	2 - 20
			AZ205	20 - 40
			AZ206	40 - 60
PN 9	37.30303	6.26482	AZ207	0 - 2
			AZ208	2 - 20
			AZ209	20 - 40
			AZ210	40 - 60
PN 10	37.30307	6.26537	AZ211	0 - 2
			AZ212	2 - 20
			AZ213	20 - 40
			AZ214	40 - 60

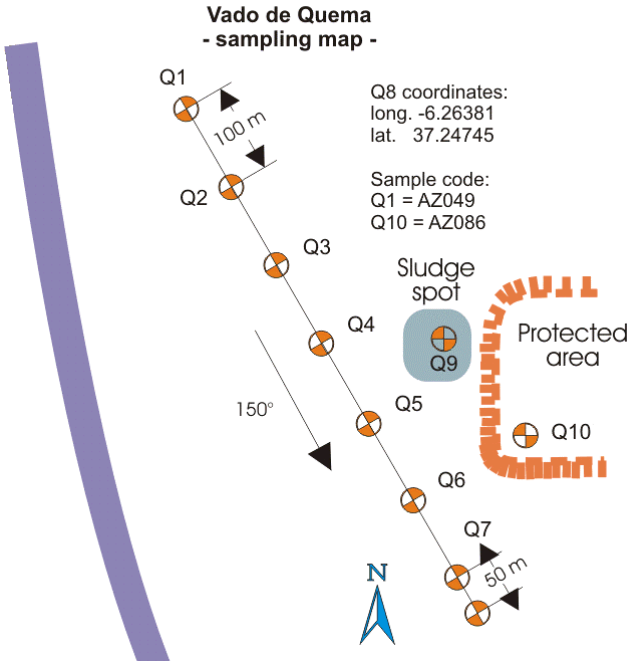

Figure A.6. Vado de Quema

Table A.6. Sampling points, coordinates [decimal degrees, WGS84], corresponding soil samples and sampling depth [cm] for 'Vado de Quema' site. (non-contaminated in blue, sludge sample in red)

Point	Latitude	Longitude	Id	Depth
Q 1	37.25232	6.26786	AZ049	0 - 2
			AZ050	2 - 20
			AZ051	20 - 40
			AZ052	40 - 60
Q 2	37.25157	6.26724	AZ053	0 - 2
			AZ054	2 - 20
			AZ055	20 - 40
			AZ056	40 - 60
Q 3	37.25084	6.26668	AZ057	0 - 2
			AZ058	2 - 20
			AZ059	20 - 40
			AZ060	40 - 60
Q 4	37.25008	6.26598	AZ061	0 - 2
			AZ062	2 - 20
			AZ063	20 - 40
			AZ064	40 - 60
Q 5	37.24929	6.26536	AZ065	0 - 2
			AZ066	2 - 20
			AZ067	20 - 40
			AZ068	40 - 60

Point	Latitude	Longitude	Id	Depth
Q 6	37.24857	6.26473	AZ069	0 - 2
			AZ070	2 - 20
			AZ071	20 - 40
			AZ072	40 - 60
Q 7	37.2478	6.26417	AZ073	0 - 2
			AZ074	2 - 20
			AZ075	20 - 40
			AZ076	40 - 60
Q 8	37.24745	6.26381	AZ077	0 - 2
			AZ078	2 - 20
			AZ079	20 - 40
			AZ080	40 - 60
Q 9	37.25039	6.26456	AZ085	sludge
Q 9	37.25039	6.26456	AZ081	0 - 2
			AZ082	2 - 20
			AZ083	20 - 40
			AZ084	40 - 60
Q 10	37.25028	6.26415	AZ086	0 - 2
			AZ087	2 - 20
			AZ088	20 - 40
			AZ089	40 - 60

Table A.7. Sampling points, coordinates [decimal degrees, WGS84], corresponding soil samples and sampling depth [cm] for sampling campaign 2000. (non-contaminated in blue, sludge sample in red)

Point	Latitude	Longitude	Id	Depth
EC 0	37.178625	6.204499	Az300	0 - 2
EC 1	37.179048	6.205497	Az301	0 - 2
EC 2	37.179217	6.206062	Az302	0 - 2
EC 3	37.178479	6.205201	Az303	0 - 2
EC 4	37.178830	6.204993	Az304	0 - 2
			Az311	2 - 20
			Az312	20 - 40
			Az313	40 - 60
EC 5			Az305	0 - 2
EC 6			Az306	0 - 2
EC 7			Az307	0 - 2
EC 8			Az308	0 - 2
EC 9			Az309	0 - 2
EC 10			Az310	0 - 2
EL 0	37.178640	6.206206	Az314	0 - 2
EL 1	37.179641	6.206478	Az315	0 - 2
EL 2	37.178752	6.206731	Az316	0 - 2
EL 3	37.179732	6.207059	Az317	0 - 2
EL 4			Az318	0 - 2
EL 5			Az319	0 - 2
EL 6			Az320	0 - 2
EL 7	37.179191	6.206611	Az324	0 - 2
			Az325	2 - 20
			Az326	20 - 40
			Az327	40 - 60
EL 8			Az321	0 - 2
EL 9			Az322	0 - 2
EL 10			Az323	0 - 2
Q 0	37.242736	6.264359	Az328	0 - 2
Q 1	37.242692	6.264834	Az329	0 - 2
Q 2			Az330	0 - 2
Q 3	37.240946	6.264048	Az331	0 - 2
Q 4	37.237651	6.260042	Az332	0 - 2
Q 5	37.240845	6.264596	Az333	0 - 2
Q 6			Az334	0 - 2
Q 8			Az335	0 - 2
Q 9			Az336	0 - 2
Q 10			Az337	0 - 2
Q 7	37.241854	6.264450	Az338	0 - 2
			Az339	2 - 20
			Az340	20 - 40
			Az341	40 - 60
Q 11	37.242846	6.264704	Az342	sludge
			Az343	2 - 20
			Az344	20 - 40
			Az345	40 - 60
Q 12	37.243027	6.264561	Az346	sludge
			Az347	2 - 20
			Az348	20 - 40
			Az349	40 - 60
Q 13	37.237741	6.259770	Az350	sludge
			Az351	2 - 20
			Az352	20 - 40
			Az353	40 - 60
Q 14	37.237651	6.260042	Az354	sludge
			Az355	2 - 20
S 12	37.446950	6.216320	Az355-1	0 - 2
			Az356	20 - 40
			Az356-1	2 - 20
			Az357	40 - 60
			Az357-1	20 - 40
			Az358	40 - 60
S 1	37.446720	6.216240	Az359	0 - 2
			Az360	2 - 20
			Az361	20 - 40
			Az362	40 - 60
S 11	37.446530	6.216240	Az363	0 - 2
			Az364	2 - 20
			Az365	20 - 40
			Az366	40 - 60
S 9	37.446270	6.214820	Az367	0 - 2
			Az368	2 - 20
			Az369	20 - 40
			Az370	40 - 60
S 2	37.446590	6.214850	Az371	0 - 2
			Az372	2 - 20
			Az373	20 - 40
S 2	37.446590	6.214850	Az374	40 - 60
S 10	37.446760	6.214800	Az375	0 - 2

Point	Latitude	Longitude	Id	Depth
			Az376	2 - 20
			Az377	20 - 40
			Az378	40 - 60
S 8	37.446630	6.213410	Az379	0 - 2
			Az380	2 - 20
			Az381	20 - 40
			Az382	40 - 60
S 3	37.446360	6.213480	Az383	0 - 2
			Az384	2 - 20
			Az385	20 - 40
			Az386	40 - 60
S 7	37.446160	6.213510	Az387	0 - 2
			Az388	2 - 20
			Az389	20 - 40
			Az390	40 - 60
V 1	37.484810	6.215370	Az391	0 - 2
V 1	37.484810	6.215370	Az392	2 - 20
V 1	37.484810	6.215370	Az393	20 - 40
V 1	37.484810	6.215370	Az394	40 - 60
V 2	37.484810	6.215880	Az395	0 - 2
V 3	37.484710	6.216460	Az396	0 - 2
V 4	37.484720	6.217020	Az397	0 - 2
V 5	37.484600	6.217740	Az398	0 - 2
V 6	37.484590	6.218250	Az399	0 - 2
V 7	37.484570	6.218820	Az400	0 - 2
V 8	37.484500	6.219460	Az401	0 - 2
V 9	37.484460	6.220000	Az402	0 - 2
M 1	37.503860	6.226570	Az403	0 - 2

Point	Latitude	Longitude	Id	Depth
			Az404	2 - 20
			Az405	20 - 40
			Az406	40 - 60
M 2	37.503870	6.226000	Az407	0 - 2
M 3	37.503750	6.225690	Az408	0 - 2
M 4	37.503770	6.225210	Az409	0 - 2
M 5	37.503700	6.224620	Az410	0 - 2
PN 2	37.302820	6.261130	Az411	0 - 2
PN 3	37.303030	6.261600	Az412	0 - 2
PN 4	37.303010	6.262220	Az413	0 - 2
PN 5	37.303030	6.262800	Az414	0 - 2
PN 6	37.303020	6.263350	Az415	0 - 2
PN 7	37.303030	6.263800	Az416	0 - 2
PN 8	37.303060	6.264280	Az417	0 - 2
PN 9	37.303030	6.264820	Az418	0 - 2
			Az419	2 - 20
			Az420	20 - 40
			Az421	40 - 60
PN 10	37.306556	6.265458	Az422	0 - 2
S 20	37.444730	6.216320	Az423	0 - 2
S 21	37.444470	6.216180	Az424	0 - 2
S 22	37.444490	6.216090	Az425	0 - 2
S 23	37.444410	6.215850	Az426	0 - 2
S 24	37.444500	6.215990	Az427	0 - 2
S 25	37.444840	6.216210	Az428	0 - 2

B. HyMap sensor setup

Table B.1. HyMap band positions 1999 (WL = centre wavelength [nm]; FWHM = Full width at half maximum [nm])

Band	WL	FWHM
1	0.403	0.013
2	0.447	0.014
3	0.457	0.0147
4	0.472	0.0159
5	0.487	0.018
6	0.503	0.016
7	0.517	0.0163
8	0.533	0.017
9	0.549	0.0159
10	0.563	0.014
11	0.58	0.0146
12	0.594	0.0152
13	0.609	0.0163
14	0.624	0.0186
15	0.641	0.0152
16	0.656	0.0156
17	0.671	0.0156
18	0.685	0.01471
19	0.702	0.0172
20	0.716	0.0162
21	0.731	0.0155
22	0.747	0.0155
23	0.761	0.0156
24	0.777	0.0164
25	0.792	0.016
26	0.807	0.0161
27	0.823	0.0167
28	0.837	0.01541
29	0.854	0.019
30	0.868	0.0164
31	0.883	0.0166
32	0.885	0.0192
33	0.896	0.0137
34	0.9	0.021
35	0.918	0.0158
36	0.933	0.0184
37	0.948	0.0164
38	0.965	0.025
39	0.981	0.01651
40	0.996	0.01639
41	1.011	0.01619
42	1.029	0.0218
43	1.043	0.01599
44	1.059	0.01701
45	1.074	0.017
46	1.089	0.0179
47	1.104	0.01659
48	1.119	0.0172
49	1.134	0.017
50	1.148	0.0166
51	1.163	0.01659
52	1.178	0.0164
53	1.192	0.016
54	1.207	0.0164
55	1.222	0.01659
56	1.236	0.016
57	1.25	0.016
58	1.264	0.0165
59	1.279	0.017
60	1.293	0.0158
61	1.307	0.016
62	1.321	0.0158
63	1.334	0.0163
64	1.346	0.0152
65	1.401	0.0164
66	1.417	0.0157
67	1.431	0.01621
68	1.445	0.01599
69	1.459	0.01561
70	1.473	0.017
71	1.487	0.0165
72	1.5	0.01621
73	1.514	0.0163
74	1.527	0.0163
75	1.541	0.01701
76	1.554	0.0163
77	1.567	0.0165
78	1.58	0.016
79	1.593	0.0164
80	1.606	0.0164
81	1.619	0.0164
82	1.632	0.01679
83	1.644	0.0165
84	1.657	0.01619
85	1.669	0.0165
86	1.682	0.0161
87	1.694	0.01621
88	1.706	0.01631
89	1.719	0.0165
90	1.731	0.016
91	1.743	0.0158
92	1.755	0.0158
93	1.767	0.0156
94	1.778	0.01551
95	1.79	0.016
96	1.802	0.01599
97	1.949	0.0204
98	1.967	0.02131
99	1.986	0.0215
1	2.5	0.021199
101	2.023	0.02099
102	2.042	0.02049
103	2.06	0.02049
104	2.079	0.02099
105	2.097	0.02101
106	2.115	0.02059
107	2.132	0.0204
108	2.15	0.0202
109	2.168	0.0202
110	2.184	0.01941
111	2.201	0.02049
112	2.22	0.02011
113	2.237	0.0195
114	2.254	0.0202
115	2.271	0.01971
116	2.288	0.01979
117	2.305	0.01962
118	2.321	0.02
119	2.337	0.0202
120	2.354	0.02101
121	2.37	0.022
122	2.386	0.02
123	2.402	0.0195
124	2.418	0.02999
125	2.434	0.01959
126	2.449	0.02011
127	2.465	0.0195
128	2.48	0.01939

TableB.2. HyMap band positions 2000 (WL = centre wavelength [nm]; FWHM = Full width at half maximum [nm])

Band	*WL*	*FWHM*
1	0.439	0.015
2	0.451	0.012
3	0.463	0.016
4	0.479	0.015
5	0.494	0.015
6	0.509	0.016
7	0.525	0.016
8	0.541	0.016
9	0.556	0.015
10	0.572	0.015
11	0.587	0.015
12	0.602	0.016
13	0.618	0.016
14	0.633	0.016
15	0.649	0.015
16	0.664	0.015
17	0.679	0.016
18	0.694	0.016
19	0.71	0.015
20	0.725	0.016
21	0.74	0.016
22	0.755	0.015
23	0.771	0.015
24	0.785	0.015
25	0.801	0.016
26	0.816	0.016
27	0.831	0.016
28	0.846	0.016
29	0.862	0.016
30	0.875	0.019
31	0.877	0.016
32	0.888	0.02
33	0.904	0.019
34	0.92	0.019
35	0.936	0.018
36	0.952	0.019
37	0.967	0.019
38	0.983	0.019
39	0.999	0.019
40	1.015	0.019
41	1.03	0.019
42	1.046	0.019
43	1.061	0.018
44	1.076	0.019
45	1.091	0.019
46	1.106	0.018
47	1.121	0.019
48	1.136	0.018
49	1.15	0.018
50	1.165	0.018
51	1.179	0.019
52	1.194	0.018
53	1.208	0.017
54	1.222	0.018
55	1.237	0.018
56	1.251	0.018
57	1.265	0.017
58	1.279	0.017
59	1.293	0.017
60	1.307	0.018
61	1.322	0.017
62	1.335	0.017
63	1.404	0.017
64	1.419	0.016
65	1.432	0.017
66	1.446	0.017
67	1.461	0.016
68	1.475	0.016
69	1.488	0.016
70	1.502	0.016
71	1.515	0.016
72	1.529	0.016
73	1.542	0.017
74	1.556	0.017
75	1.569	0.016
76	1.582	0.017
77	1.594	0.017
78	1.607	0.017
79	1.62	0.016
80	1.633	0.016
81	1.646	0.016
82	1.658	0.016
83	1.671	0.015
84	1.683	0.016
85	1.696	0.016
86	1.708	0.016
87	1.72	0.015
88	1.732	0.015
89	1.745	0.015
90	1.756	0.015
91	1.768	0.014
92	1.78	0.014
93	1.792	0.014
94	1.804	0.014
95	1.95	0.021
96	1.969	0.021
97	1.987	0.021
98	2.006	0.021
99	2.025	0.021
100	2.044	0.021
101	2.062	0.021
102	2.081	0.021
103	2.099	0.02
104	2.117	0.021
105	2.135	0.021
106	2.153	0.021
107	2.17	0.02
108	2.187	0.019
109	2.205	0.021
110	2.223	0.019
111	2.24	0.019
112	2.257	0.019
113	2.275	0.019
114	2.292	0.018
115	2.308	0.018
116	2.324	0.018
117	2.341	0.018
118	2.358	0.018
119	2.374	0.018
120	2.39	0.018
121	2.406	0.017
122	2.422	0.017
123	2.437	0.016
124	2.453	0.017
125	2.468	0.017
126	2.484	0.016

C. Geochemical analysis 1999

Table C.1. Geochemical laboratory analysis for 1999. Part I

ID	Depth [cm]	Al_2O_3 [%]	As [ppm]	CaO [%]	$CaCO_3$ [%]	$C_{tot.}$ [%]	$C_{org.}$ [%]	Cd [ppm]	Cl [%]	Cr [ppm]	Cu [ppm]	Fe_2O_3 [%]	H [%]	Hg [ppm]
AZ 001	0 - 2	15.1	10	2.05	0.5	0.9	0.89	0.13	0.02	124	22	5.45	0.75	0.04
AZ 002	2 - 20	15.05	16	2	1.3	0.93	0.77	0.12	0.02	123	19	5.4	0.76	0.03
AZ 003	20 - 40	15.1	16	2.1	0.5	0.83	0.77	0.12	0.02	118	22	5.4	0.68	0.03
AZ 004	40 - 60	14.65	16	3.3	3.3	0.71	0.31	0.1	0.02	124	17.5	5.3	0.65	0.02
AZ 005	0 - 2	15.15	15	2.05	0.7	0.96	0.87	0.13	0.02	120	19.5	5.45	0.73	0.02
AZ 006	2 - 20	15.15	16	2.05	0.5	0.88	0.82	0.12	0.02	119	18	5.35	0.71	0.03
AZ 007	20 - 40	15.1	9	2.05	0.6	0.9	0.83	0.13	0.02	115	21	5.4	0.84	0.03
AZ 008	40 - 60	14.9	15	2.8	1.1	0.72	0.59	0.1	0.02	110	19.5	5.35	0.66	0.03
AZ 009	0 - 2	15.35	19	2.4	0.5	0.91	0.86	0.13	0.02	118.5	20.5	5.65	0.7	0.03
AZ 010	2 - 20	15.45	18	2.3	0.8	0.9	0.8	0.12	0.02	114.5	19.5	5.6	0.74	0.04
AZ 011	20 - 40	15.3	11	2.25	0.9	0.89	0.78	0.12	0.02	111.5	22	5.5	0.8	0.03
AZ 012	40 - 60	14.9	8	3.8	2.1	0.84	0.59	0.11	0.02	112	20	5.6	0.58	0.02
AZ 013	0 - 2	10.7	114	2.05	0.5	0.67	0.64	2.17	0.03	132.5	119	8.4	0.5	1.08
AZ 014	2 - 20	12.15	46	2.15	0.5	0.67	0.67	1.08	0.02	123.5	71.5	6.7	0.51	0.47
AZ 015	20 - 40	13.75	16	2.1	0.5	0.5	0.47	0.17	0.02	126	41	5.65	0.47	0.08
AZ 016	40 - 60	12.85	25	2.5	0.5	0.39	0.33	0.38	0.02	130	40	5.85	0.52	0.11
AZ 017	0 - 2	9.3	173	2.35	0.5	0.75	0.73	3.51	0.06	103.5	170.5	10.1	0.62	0.09
AZ 018	2 - 20	11.6	29	2.4	0.7	0.83	0.77	0.46	0.03	111.5	60	6.15	0.7	0.25
AZ 019	20 - 40	12.4	10	3.55	2.8	0.86	0.52	0.12	0.02	106	42.5	5.65	0.69	0.11
AZ 020	40 - 60	12.35	11	4.5	3.7	0.82	0.37	0.07	0.02	116	28	5.65	0.59	0.1
AZ 021	0 - 2	3.3	317	5.25	2.7	0.97	0.65	9.33	0.13	79	309	18.45	0.76	5.5
AZ 022	2 - 20	10.95	83	4	4.6	1.37	0.82	0.49	0.03	103.5	59	6.6	0.74	0.3
AZ 023	20 - 40	12.45	43	3.1	3	1	0.64	0.15	0.02	109.5	57	5.7	0.71	0.08
AZ 024	40 - 60	12.45	50	3.45	3.8	1.1	0.64	0.15	0.02	103	63.5	5.7	0.68	0.12
AZ 025	0 - 2	10.45	175	3.65	3.9	1.82	1.35	1.56	0.04	152	109.5	6.8	0.6	0.58
AZ 026	2 - 20	12	43	2.3	0.5	0.69	0.65	0.1	0.02	120.5	51.5	5.45	0.4	0.05
AZ 027	20 - 40	12.95	41	2.2	1.2	0.66	0.52	0.89	0.02	109	52	5.6	0.52	0.07
AZ 028	40 - 60	15.25	47	2.5	0.8	0.65	0.56	0.1	0.02	114.5	67.5	5.75	0.55	0.11
AZ 029	0 - 2	11.65	192	3.2	1.3	0.59	0.43	1.69	0.02	143.5	106.5	6.85	0.39	0.76
AZ 030	2 - 20	12	174	3.2	0.5	0.5	0.45	1.11	0.02	95	90	6.6	0.37	0.54
AZ 033	0 - 2	11.1	131	3.5	1.7	0.78	0.58	2.5	0.02	123.5	138.5	7.7	0.37	1.18
AZ 034	2 - 20	13.6	22	4.95	4.5	1.22	0.68	0.2	0.02	117	52	5.35	0.43	0.11
AZ 035	20 - 40	13.6	19	3.3	1	0.64	0.52	0.12	0.02	95.5	56	5.5	0.35	0.07
AZ 036	40 - 60	13.7	15	3.05	1.8	0.65	0.44	0.1	0.02	134	64.5	5.35	0.47	0.1
AZ 037	0 - 2	11.95	45	2.85	0.7	0.68	0.59	0.44	0.02	138	45.5	5.9	0.41	0.3
AZ 038	2 - 20	12.7	21	2.85	0.7	0.61	0.53	0.13	0.02	88	38.5	5	0.35	0.05
AZ 039	20 - 40	13.2	18	2.6	0.8	0.59	0.49	0.07	0.02	123.5	26.5	5.35	0.43	0.03
AZ 040	40 - 60	13.5	18	2.75	0.7	0.63	0.54	0.08	0.02	123.5	30.5	5.2	0.49	0.03
AZ 041	0 - 2	10.75	157	2.65	1.3	0.75	0.59	2.52	0.02	143.5	104	7.5	0.43	0.93

ID	Depth [cm]	Al_2O_3 [%]	As [ppm]	CaO [%]	$CaCO_3$ [%]	$C_{tot.}$ [%]	$C_{org.}$ [%]	Cd [ppm]	Cl [%]	Cr [ppm]	Cu [ppm]	Fe_2O_3 [%]	H [%]	Hg [ppm]
AZ 042	2 - 20	12.1	49	2.7	0.5	0.57	0.58	0.66	0.02	109	54.5	6.1	0.36	0.35
AZ 043	20 - 40	13.35	23	2.7	0.6	0.58	0.5	0.21	0.02	123	36.5	5.4	0.42	0.09
AZ 044	40 - 60	13.95	19	2.65	0.5	0.57	0.52	0.12	0.02	130	68.5	5.55	0.45	0.06
AZ 045	0 - 2	5.6	280	2.35	0.5	0.57	0.53	4.58	0.09	83	203.5	14.7	0.36	3.85
AZ 046	2 - 20	14.05	19	2.95	0.5	0.65	0.59	0.28	0.05	163	29	5.25	0.4	0.07
AZ 047	20 - 40	11.7	17	2.55	0.9	0.61	0.5	0.17	0.02	126	38	6.4	0.5	0.06
AZ 048	40 - 60	13.3	16	2.45	0.5	0.58	0.51	0.1	0.02	130	45	5.75	0.5	0.07
AZ 049	0 - 2	9.65	118	8.8	13	2.29	0.73	1.67	0.02	78.5	97.5	5.9	0.55	0.49
AZ 050	2 - 20	11.15	21	6.5	9.2	1.66	0.55	0.38	0.02	81	43.5	4.8	0.56	0.11
AZ 051	20 - 40	12.15	23	5.65	8	1.56	0.6	0.23	0.02	89.5	36	5.15	0.5	0.07
AZ 052	40 - 60	12.85	20	5	7.1	1.46	0.6	0.12	0.02	92.5	38	5.2	0.56	0.07
AZ 053	0 - 2	7	36	13	18.9	3.04	0.77	2.25	0.03	124.5	105.5	5.05	0.43	0.43
AZ 054	2 - 20	9.5	20	7.4	11.5	1.95	0.57	1.24	0.02	79	67.5	4.05	0.41	0.12
AZ 055	20 - 40	10.3	11	6	7	1.26	0.41	0.4	0.02	90	47.5	4	0.33	0.05
AZ 056	40 - 60	10.6	7	6.25	9.7	1.6	0.44	0.08	0.02	83.5	28	4.4	0.44	0.04
AZ 057	0 - 2	7.85	36	7.4	10.4	1.87	0.62	2.47	0.04	95	123.5	5.7	0.39	0.63
AZ 058	2 - 20	9.2	39	7.05	10.4	1.83	0.58	1.31	0.02	103.5	88	4.65	0.44	0.18
AZ 059	20 - 40	9.8	26	6.25	8.8	1.64	0.58	0.93	0.02	86	77	4.65	0.42	0.13
AZ 060	40 - 60	10.75	16	5.6	9.3	1.67	0.55	0.36	0.02	82.5	51.5	4.85	0.48	0.36
AZ 061	0 - 2	8.15	26	8.65	13.3	2.31	0.71	1.36	0.02	72.5	71.5	3.75	0.41	0.13
AZ 062	2 - 20	9.4	17	7.25	11.1	1.95	0.61	1.02	0.02	77	72.5	4.2	0.44	0.07
AZ 063	20 - 40	10.3	18	5.85	8.1	1.56	0.58	0.45	0.02	82.5	67.5	4.65	0.4	0.07
AZ 064	40 - 60	12.35	26	5.85	7.7	1.57	0.65	0.75	0.02	96.5	118.5	4.75	0.44	0.12
AZ 065	0 - 2	10.5	115	7.35	9.7	1.83	0.67	2.67	0.02	64	162	5.6	0.45	0.51
AZ 066	2 - 20	11.7	34	5	5.6	1.22	0.55	1.4	0.02	70.5	167.5	4.7	0.38	0.13
AZ 067	20 - 40	11.9	34	4.85	6.1	1.28	0.55	1.24	0.02	93.5	168.5	4.8	0.4	0.14
AZ 068	40 - 60	11.25	19	4.85	4.1	0.83	0.34	0.31	0.02	65	81.5	3.95	0.26	0.06
AZ 069	0 - 2	9.8	38	9.1	13.8	2.35	0.69	1.25	0.02	77	80.5	3.85	0.42	0.15
AZ 070	2 - 20	11.2	34	6.25	8.3	1.57	0.57	0.93	0.02	68	105	4.45	0.42	0.1
AZ 071	20 - 40	11.25	27	4.95	5.6	1.07	0.4	0.45	0.02	84.5	78	4.3	0.37	0.06
AZ 072	40 - 60	6.45	20	7.7	5.6	0.95	0.27	0.1	0.06	98.5	282.5	10.2	0.25	0.04
AZ 073	0 - 2	10.3	244	5.65	5.5	1.25	0.58	4.97	0.02	102	30	3.85	0.79	1.39
AZ 074	2 - 20	9.35	75	7.25	8.3	1.57	0.57	1.84	0.02	89	102	5.75	0.4	0.42
AZ 075	20 - 40	9.1	63	7.4	10.3	1.77	0.53	1.46	0.02	85	104	5.65	0.44	0.44
AZ 076	40 - 60	9.55	20	6.9	9.8	1.55	0.37	0.29	0.02	93	104	5.3	0.36	0.11
AZ 077	0 - 2	9.6	37	6.95	10.8	2.03	0.74	1.92	0.02	93	104	4.2	0.48	0.35
AZ 078	2 - 20	9.9	24	6.3	8	1.58	0.61	0.57	0.02	65	80.5	4.6	0.38	0.1
AZ 079	20 - 40	10.45	20	5.7	7.5	1.42	0.52	0.33	0.02	100.5	70	4.45	0.38	0.08
AZ 080	40 - 60	10.2	17	6.55	9.4	1.49	0.36	0.09	0.02	89.5	32	4	0.34	0.05
AZ 081	0 - 2	7.45	241	4.15	2.6	0.81	0.5	14.8	0.07	79	521	9	0.74	0.59
AZ 082	2 - 20	10.4	28	4.95	5.6	1.22	0.54	2.41	0.02	104	160	5.35	0.42	0.13
AZ 083	20 - 40	10.7	18	5.75	7.7	1.43	0.5	0.8	0.02	112.5	75.5	4.8	0.42	0.07
AZ 084	40 - 60	10.1	22	6.3	8	1.39	0.43	0.27	0.02	92	34.5	4.55	0.39	0.05

ID	Depth [cm]	Al_2O_3 [%]	As [ppm]	CaO [%]	$CaCO_3$ [%]	$C_{tot.}$ [%]	$C_{org.}$ [%]	Cd [ppm]	Cl [%]	Cr [ppm]	Cu [ppm]	Fe_2O_3 [%]	H [%]	Hg [ppm]
AZ 085	sludge	0.5	442	2.9	0.5	0.11	0.1	6.38	0.1	59.5	197	15.25	0.65	13.9
AZ 086	0 - 2	9.75	23	6.7	10.8	2.34	1.04	1.46	0.02	91.5	126.5	5.1	0.58	0.11
AZ 087	2 - 20	10.1	24	6.55	11.2	2.29	0.94	1.41	0.02	90	125.5	4.95	0.53	0.1
AZ 088	20 - 40	11.95	21	6.55	10	2.07	0.86	1.06	0.02	102	130	4.85	0.48	0.11
AZ 089	40 - 60	11.25	14	5.7	6.5	1.19	0.41	0.22	0.02	141	45	4.1	0.38	0.05
AZ 090	0 - 2	13.75	27	2.15	2.9	2.1	1.75	1.88	0.02	190.5	177.5	5.45	0.59	0.29
AZ 091	2 - 20	13.25	15	1.55	0.5	0.9	0.8	0.55	0.02	164	65.5	4.8	0.33	0.08
AZ 092	20 - 40	13.5	24	2.15	1.7	1.49	1.29	1.09	0.02	169	105	5.2	0.5	0.17
AZ 093	40 - 60	13.35	22	1.95	1.5	1.53	1.35	0.78	0.02	135.5	100.5	5.2	0.47	0.17
AZ 094	0 - 2	12.2	43	1.85	1.8	1.61	1.4	1.74	0.02	128.5	111.5	6.35	0.57	0.29
AZ 095	2 - 20	13	24	1	0.5	0.58	0.54	0.71	0.02	215.5	75.5	5.55	0.34	0.11
AZ 096	20 - 40	13	30	1	0.8	0.51	0.45	0.37	0.02	219	68.5	5.6	0.36	0.1
AZ 097	40 - 60	12.75	29	0.7	0.5	0.26	0.23	0.18	0.02	225.5	60.5	5.65	0.29	0.08
AZ 098	0 - 2	11.6	46	1.8	1.5	1.65	1.46	1.99	0.02	124	169.5	6.95	0.59	0.48
AZ 099	2 - 20	12.65	30	1	1.4	1.24	1.11	0.86	0.02	159	83.5	5.8	0.48	0.23
AZ 100	20 - 40	12.55	64	1.65	0.6	0.77	0.7	0.35	0.02	117.5	99	6.2	0.45	0.13
AZ 101	40 - 60	12.55	16	0.6	0.5	0.22	0.22	0.11	0.02	141	82.5	5.5	0.29	0.05
AZ 102	0 - 2	11.7	88	0.5	0.5	0.31	0.26	0.82	0.03	216	99.5	6.5	0.36	0.32
AZ 103	2 - 20	10.95	50	1.1	0.6	0.39	0.32	1.86	0.04	128	138.5	6.2	0.38	0.33
AZ 104	20 - 40	11.5	21	0.45	0.5	0.12	0.1	0.2	0.06	151.5	130.5	6.85	0.36	0.04
AZ 105	40 - 60	10.65	24	0.4	0.5	0.11	0.1	0.23	0.06	322.5	93	6.05	0.33	0.03
AZ 106	0 - 2	13.2	301	1.1	4.2	2.43	1.92	5.13	0.02	117.5	158	6.75	1.6	4.56
AZ 107	2 - 20	10.85	51	1.05	0.5	1.44	1.37	1.46	0.09	134.5	315	11.7	0.78	0.53
AZ 108	20 - 40	14.9	30	1.15	0.5	1.12	1.08	1.15	0.02	116.5	110.5	6.05	0.52	0.18
AZ 109	40 - 60	14.4	16	0.7	0.5	0.32	0.31	0.34	0.02	139	52	5.4	0.35	0.06
AZ 110	0 - 2	10.95	125	3.3	2.9	1.13	0.78	6.41	0.03	111.5	238.5	9.45	0.52	1.85
AZ 111	2 - 20	12.95	106	1.5	1.9	0.78	0.55	1.77	0.02	88	161.5	8.05	0.47	0.8
AZ 112	20 - 40	14.75	75	0.9	0.5	0.76	0.76	0.82	0.02	112.5	190	6.9	0.42	0.38
AZ 113	40 - 60	15.2	79	0.85	1	1.74	1.61	1.23	0.02	148.5	373.5	6.8	0.57	0.71
AZ 114	0 - 2	10.35	152	3.75	3.7	0.74	0.3	2.05	0.05	135.5	200	7.95	0.38	0.98
AZ 115	2 - 20	11.55	85	0.9	1.5	0.31	0.12	0.35	0.03	88	135	5.8	0.6	0.31
AZ 116	20 - 40	11.65	71	0.65	0.5	0.13	0.12	0.32	0.02	189	123.5	5.65	0.28	0.21
AZ 117	40 - 60	12.55	80	0.65	0.5	0.22	0.2	0.37	0.02	93.5	150	5.9	0.35	0.22
AZ 118	0 - 2	4.35	46	32.8	42.4	6.69	1.6	0.33	0.02	41	62	2.75	0.53	0.17
AZ 119	2 - 20	12.6	48	1.25	0.8	0.21	0.12	0.34	0.02	83	169.5	6	0.3	0.23
AZ 120	20 - 40	12.55	74	0.9	0.5	0.25	0.18	0.5	0.03	98	223	6.2	0.34	0.32
AZ 121	0 - 2	11.75	109	5.6	9.4	1.87	0.74	6.13	0.07	83.5	419	10.5	0.98	1.36
AZ 122	2 - 20	9.95	96	0.7	0.5	0.22	1.07	0.29	0.11	93	258	7.6	0.41	0.38
AZ 123	20 - 30	10.55	99	0.55	0.7	0.22	0.14	0.29	0.15	129	239.5	7.1	0.41	0.77
AZ 124	0 - 2	7.05	128	1.85	0.5	0.43	0.4	6.6	0.13	135	446	12.9	0.72	2.23
AZ 125	2 - 20	10.8	72	0.8	0.5	0.27	0.21	0.63	0.14	85.5	198.5	8.25	0.54	0.73
AZ 126	20 - 30	11.25	91	0.7	0.5	0.18	0.15	0.8	0.09	132	151	7.65	0.44	0.47
AZ 127	0 - 2	10.85	211	4.3	1.5	1.89	1.71	5.53	0.05	98	202	9.45	0.7	1.66

ID	Depth [cm]	Al_2O_3 [%]	As [ppm]	CaO [%]	$CaCO_3$ [%]	$C_{tot.}$ [%]	$C_{org.}$ [%]	Cd [ppm]	Cl [%]	Cr [ppm]	Cu [ppm]	Fe_2O_3 [%]	H [%]	Hg [ppm]
AZ 128	2 - 20	11.85	116	1.65	1.6	1.67	1.48	2.28	0.04	106.5	124	8.55	0.88	0.98
AZ 129	20 - 40	14.5	98	1.5	0.5	1.38	1.35	1.4	0.02	92	140.5	7.75	0.69	0.94
AZ 130	40 - 60	16.95	39	1.3	0.5	1.68	1.63	0.26	0.02	104.5	81	6.95	0.68	0.21
AZ 131	0 - 2	10	196	13.6	18.9	3.86	1.59	3.22	0.02	90.5	139	7.55	0.61	1.5
AZ 132	2 - 20	15.75	55	0.95	2	1.49	1.25	0.23	0.02	101.5	101.5	6.25	0.57	0.21
AZ 133	0 - 2	13.05	76	4.75	7.3	1.86	0.99	0.85	0.02	77.5	116.5	6.05	0.47	0.4
AZ 134	2 - 20	15.3	52	0.85	0.6	0.72	0.64	0.11	0.02	86.5	96.5	5.95	0.57	0.14
AZ 135	20 - 40	14.85	46	0.65	0.5	0.46	0.42	0.09	0.02	85.5	119.5	5.9	0.38	0.18
AZ 136	40 - 60	14.4	75	0.6	0.5	0.37	0.31	0.09	0.02	146.5	118.5	5.8	0.4	0.17
AZ 137	0 - 2	9.45	393	1.25	1.5	3.47	3.28	7.1	0.08	99.5	258	12.7	1	3.58
AZ 138	2 - 20	13.25	159	1.3	0.9	1.76	1.65	1.11	0.02	113.5	89.5	7.85	0.89	0.84
AZ 139	20 - 40	13.8	116	1.25	1.3	1.37	1.21	0.78	0.02	98.5	85.5	7.35	0.74	0.53
AZ 140	40 - 60	15.3	44	1.05	1.1	0.96	0.82	0.18	0.02	108.5	71.5	6.15	0.65	0.18
AZ 141	0 - 2	10.65	96	8.35	13.8	2.4	0.74	0.96	0.02	62.5	102	5	0.58	0.37
AZ 142	2 - 20	11.45	62	7.65	12	2.32	0.87	0.5	0.02	74.5	106	4.9	0.56	0.27
AZ 143	20 - 40	12.75	73	4.35	5.6	1.79	1.11	0.62	0.02	81.5	166.5	6.05	0.64	0.31
AZ 144	40 - 60	13.7	83	2.8	2.2	1.69	1.42	0.95	0.02	109	235.5	6.2	0.68	0.28
AZ 145	0 - 2	10.15	102	6.95	2.8	1.18	0.85	1.81	0.02	71	130	5.9	0.69	0.69
AZ 146	2 - 20	11.85	122	6.4	9.8	2.26	1.08	1.27	0.02	81.5	156.5	6.2	0.63	0.49
AZ 147	20 - 40	11.35	106	5.65	8.8	2.16	1.1	1.3	0.03	78.5	161.5	6.25	0.65	0.51
AZ 148	40 - 60	12.8	99	2.85	2.8	1.74	1.4	1.12	0.03	98.5	189.5	6.3	0.66	0.38
AZ 149	0 - 2	7.5	283	6.65	8.8	1.72	0.66	3.09	0.07	79	170	8.4	0.42	1.55
AZ 150	2 - 20	8.9	55	7.25	10.6	1.9	0.63	0.97	0.02	64.5	83	4.45	0.48	0.29
AZ 151	20 - 40	11	51	4.95	7.4	1.78	0.89	1.28	0.03	91.5	158	5.65	0.57	0.26
AZ 152	40 - 60	12.4	52	2.75	0.6	1.46	1.39	1.05	0.03	109	227.5	6.05	0.67	0.26
AZ 153	0 - 2	8.6	146	3.3	2.6	1.21	0.89	3.23	0.08	131.5	230	9	0.57	1.25
AZ 154	2 - 20	7.8	108	3.5	2.2	1.29	1.02	3.26	0.1	96	232	9.65	0.7	1.13
AZ 155	20 - 40	10.85	47	3.1	2.2	1.39	1.12	1.44	0.07	120.5	214	6.95	0.55	0.49
AZ 156	40 - 60	11.6	42	2.8	2.2	1.4	1.13	1.04	0.03	112.5	207.5	6.3	0.56	0.33
AZ 157	0 - 2	9.9	77	4.25	3.9	1.29	0.82	2.17	0.07	144	223	7.25	0.46	0.71
AZ 158	2 - 20	11.5	33	3.45	4.5	1.5	0.96	0.8	0.03	125.5	186.5	5.8	0.55	0.24
AZ 159	20 - 40	11.85	25	3.1	2.2	1.47	1.21	0.71	0.03	89	228	5.9	0.54	0.25
AZ 160	40 - 60	12	21	3.25	2.8	1.36	1.02	0.55	0.02	120	255.5	5.7	0.54	0.18
AZ 161	0 - 2	11.1	71	4.1	2.3	1.32	1.04	2.99	0.02	90.5	248	7.75	0.62	0.63
AZ 162	2 - 20	13.75	41	3.5	10	2.28	1.08	0.94	0.02	135	205.5	6.05	0.99	0.29
AZ 163	20 - 40	14.1	29	3.35	2	1.42	1.17	0.69	0.02	101	244.5	6	0.64	0.32
AZ 164	40 - 60	13.4	23	4.45	3.9	1.37	0.9	0.47	0.02	96	253.5	5.45	0.55	0.13
AZ 165	0 - 2	10.3	193	4.35	1.8	1.39	1.17	2.83	0.06	93.5	261	9	0.67	1.1
AZ 166	2 - 20	12.85	58	3.05	0.9	1.54	1.43	1.71	0.02	90	304	7.1	0.74	0.43
AZ 167	20 - 40	12.8	44	3.5	1.8	1.32	1.1	1.26	0.02	93.5	222	6.3	0.58	0.24
AZ 168	40 - 60	13.1	41	3.4	2.5	1.42	1.12	1.4	0.02	113	237.5	6.1	0.62	0.25
AZ 169	0 - 2	12.3	43	6.95	8.8	2.48	1.43	1.19	0.02	113	189.5	6.65	0.7	0.36
AZ 170	2 - 20	13.35	40	2.95	1.3	1.4	1.24	1.15	0.02	84.5	225.5	6.1	0.53	0.27

ID	Depth [cm]	Al_2O_3 [%]	As [ppm]	CaO [%]	$CaCO_3$ [%]	$C_{tot.}$ [%]	$C_{org.}$ [%]	Cd [ppm]	Cl [%]	Cr [ppm]	Cu [ppm]	Fe_2O_3 [%]	H [%]	Hg [ppm]
AZ 171	20 - 40	12.95	41	3.2	1.4	1.4	1.23	1.14	0.02	114.5	221	6.05	0.59	0.27
AZ 172	40 - 60	12.4	44	3.9	2.4	1.44	1.15	0.99	0.02	95	235	6.1	0.67	0.23
AZ 173	0 - 2	10.45	107	4.5	3.4	1.05	0.64	2.18	0.03	106.5	243	6.65	0.39	0.57
AZ 174	2 - 20	11.55	87	2.8	1.2	1.07	0.92	1.37	0.05	99.5	244.5	6.6	0.46	0.43
AZ 175	0 - 2	7.55	105	9.55	14.8	2.53	0.76	3.87	0.03	104	169.5	5.55	0.38	0.66
AZ 176	2 - 20	6.45	137	6.55	6.8	1.39	0.57	4.24	0.05	92.5	199.5	7	0.47	0.83
AZ 177	20 - 40	7.2	89	6.65	8.6	1.49	0.46	2.75	0.03	72.5	154	5.45	0.39	0.43
AZ 178	40 - 60	7	31	7.3	10.8	1.76	0.47	2.36	0.02	64	67.5	3.2	0.34	0.12
AZ 179	0 - 2	8.1	37	8.2	12.9	2.14	0.59	1.79	0.02	119.5	96.5	4.1	0.36	0.17
AZ 180	2 - 20	7.45	27	7	9.9	1.49	0.3	1.07	0.02	88	118.5	3.95	0.24	0.07
AZ 181	20 - 40	7.65	32	6.4	8.6	1.6	0.57	1.53	0.03	69	125	4.2	0.39	0.13
AZ 182	40 - 60	8.25	34	5.2	7.4	1.58	0.69	1.48	0.03	79.5	146	4.65	0.39	0.15
AZ 183	0 - 2	7.7	43	7.65	8.8	2.32	1.26	2.03	0.03	89.5	114	4.45	0.47	0.21
AZ 184	2 - 20	7.55	27	7.6	11.8	2.18	0.77	1.64	0.03	93.5	112	4.25	0.41	0.15
AZ 185	20 - 40	7.75	26	4.6	6.8	1.14	0.32	1.08	0.03	157	111.5	4.35	0.29	0.09
AZ 186	40 - 60	8.45	19	4.8	5.5	1.12	0.46	0.32	0.03	126.5	52	4.35	0.35	0.05
AZ 187	0 - 2	8.05	41	3.9	7.8	1.19	0.25	1.39	0.03	127	134.5	4.65	0.29	0.2
AZ 188	2 - 20	7.9	30	3.5	1.3	0.79	0.64	0.88	0.03	114	103.5	4.4	0.25	0.12
AZ 189	20 - 40	8	18	4.25	2.4	0.73	0.44	0.35	0.03	66.5	67.5	4.2	0.26	0.08
AZ 190	40 - 60	8.15	17	5	5.3	1.13	0.5	0.11	0.03	85	32.5	4.2	0.29	0.04
AZ 191	0 - 2	7	34	5.85	12.4	1.8	0.31	1.79	0.03	100.5	111	4.2	0.27	0.17
AZ 192	2 - 20	7.25	32	6.45	10.3	1.89	0.65	2.13	0.04	68	133.5	4.4	0.35	0.19
AZ 193	20 - 40	11.85	59	7.25	9.8	2.02	0.84	2	0.02	81	160.5	4.9	0.53	0.19
AZ 194	40 - 60	12.25	57	6.6	12	2.28	0.84	1.38	0.02	79	191.5	5.5	0.6	0.27
AZ 195	0 - 2	9.7	31	7.45	4.9	1.38	0.79	1.24	0.02	117.5	70	3.4	0.3	0.12
AZ 196	2 - 20	11.05	23	6.8	7.5	1.29	0.38	1.06	0.02	124	73	3.95	0.35	0.07
AZ 197	20 - 40	11.1	27	6.5	7.3	1.22	0.35	0.87	0.02	101	73	3.85	0.31	0.08
AZ 198	40 - 60	11.95	15	6.05	5.8	0.94	0.24	0.22	0.02	110.5	33	4.2	0.33	0.05
AZ 199	0 - 2	12.65	55	6.6	10	1.95	0.75	0.6	0.02	98.5	65	5.4	0.7	0.29
AZ 200	2 - 20	13.65	25	5.55	6	1.31	0.58	0.18	0.02	94.5	44	5.05	0.59	0.1
AZ 201	20 - 40	13.15	22	5.5	5.6	1.19	0.51	0.25	0.02	88.5	47.5	4.85	0.53	0.13
AZ 202	40 - 60	13.7	20	5	5	1.09	0.49	0.11	0.02	92	52.5	5	0.57	0.1
AZ 203	0 - 2	12.2	50	4.55	3.6	0.97	0.53	0.96	0.02	135	124	4.6	0.35	0.14
AZ 204	2 - 20	12.25	33	4.25	3.4	0.83	0.42	0.83	0.02	96.5	123.5	4.5	0.41	0.1
AZ 205	20 - 40	12	23	4.65	5.1	1.02	0.4	0.62	0.02	88	108	4.2	0.27	0.07
AZ 206	40 - 60	11.8	19	4.7	4.7	0.91	0.34	0.41	0.02	91	85.5	4.2	0.3	0.08
AZ 207	0 - 2	10.35	105	5.6	5.9	1.41	0.7	1.68	0.02	89	95	5.85	0.56	0.68
AZ 208	2 - 20	12.2	36	4.45	4.7	1.15	0.58	0.47	0.02	90	43.5	4.5	0.55	0.14
AZ 209	20 - 40	12.35	25	4.1	4.5	1.04	0.5	0.36	0.02	79.5	35.5	4.4	0.53	0.11
AZ 210	40 - 60	13.35	16	3.4	2.3	0.7	0.43	0.16	0.02	93.5	36.5	4.85	0.63	0.07
AZ 211	0 - 2	14.6	15	3.25	3.2	1.16	0.78	0.09	0.02	100	25.5	5.25	0.75	0.02
AZ 212	2 - 20	14.75	14	2.9	1.7	0.77	0.57	0.18	0.02	99	25	5.25	0.62	0.02
AZ 213	20 - 40	14.75	14	2.8	1.8	0.73	0.51	0.06	0.02	100.5	24.5	5.3	0.71	0.01

ID	Depth [cm]	Al_2O_3 [%]	As [ppm]	CaO [%]	$CaCO_3$ [%]	$C_{tot.}$ [%]	$C_{org.}$ [%]	Cd [ppm]	Cl [%]	Cr [ppm]	Cu [ppm]	Fe_2O_3 [%]	H [%]	Hg [ppm]
AZ 214	40 - 60	15	20	2.7	1.8	0.66	0.44	0.05	0.02	100.5	24.5	5.5	0.69	0.01

Table C.2. Geochemical laboratory analysis for 1999. Part II

ID	Depth [cm]	K_2O [%]	MgO [%]	Mn [ppm]	N [%]	Na_2O [%]	Ni [ppm]	P_2O_5 [%]	Pb [ppm]	S [%]	Sb [ppm]	SiO_2 [%]	TiO_2 [%]	Zn [ppm]
AZ 001	0 - 2	2.20	2.70	776.5	0.11	1.35	38.5	0.115	33.0	0.020	282	56.30	0.930	106.0
AZ 002	2 - 20	2.20	2.70	761.0	0.11	1.45	40.0	0.105	36.0	0.020	257	56.45	0.925	105.5
AZ 003	20 - 40	2.20	2.70	769.5	0.10	1.55	32.0	0.105	33.0	0.020	232	56.85	0.955	107.5
AZ 004	40 - 60	2.05	2.65	778.5	0.07	2.05	36.5	0.095	25.0	0.020	229	54.65	0.965	105.0
AZ 005	0 - 2	2.20	2.70	750.5	0.13	1.35	39.5	0.115	33.5	0.020	270	56.75	0.915	105.0
AZ 006	2 - 20	2.20	2.70	746.5	0.11	1.35	38.5	0.105	34.5	0.020	257	57.00	0.920	104.0
AZ 007	20 - 40	2.20	2.65	747.0	0.12	1.50	40.0	0.110	34.0	0.020	279	57.10	0.910	107.5
AZ 008	40 - 60	2.10	2.70	755.5	0.08	1.80	36.5	0.100	29.0	0.020	273	55.85	0.945	101.0
AZ 009	0 - 2	2.25	2.70	790.0	0.11	1.40	39.5	0.120	34.5	0.020	273	56.25	0.930	106.5
AZ 010	2 - 20	2.20	2.75	805.5	0.11	1.40	36.5	0.110	34.5	0.020	255	56.10	0.965	105.0
AZ 011	20 - 40	2.15	2.50	795.5	0.11	1.40	37.0	0.105	33.5	0.020	249	56.10	0.955	104.0
AZ 012	40 - 60	1.90	2.60	917.5	0.08	2.00	39.5	0.075	23.0	0.020	291	53.20	1.030	103.5
AZ 013	0 - 2	1.85	2.50	527.0	0.41	0.70	37.0	0.100	485.0	2.535	883	53.05	1.005	523.0
AZ 014	2 - 20	2.00	2.50	821.5	0.10	1.65	41.5	0.110	236.0	0.995	502	54.20	0.990	357.5
AZ 015	20 - 40	2.20	2.25	885.5	0.07	2.65	41.5	0.095	65.5	0.090	262	55.35	0.985	125.0
AZ 016	40 - 60	2.00	2.35	910.5	0.06	3.05	49.0	0.085	70.0	0.255	259	53.15	0.995	181.5
AZ 017	0 - 2	1.60	2.85	553.0	0.10	0.05	27.0	0.105	754.0	4.940	1169	49.00	1.020	744.5
AZ 018	2 - 20	1.95	2.55	790.5	0.13	1.75	35.0	0.125	140.0	0.685	399	51.80	0.940	208.0
AZ 019	20 - 40	1.90	2.40	850.5	0.08	2.25	39.5	0.105	70.5	0.075	253	50.10	0.940	125.0
AZ 020	40 - 60	1.80	2.40	847.0	0.07	2.30	35.0	0.105	55.0	0.020	308	48.20	0.940	102.0
AZ 021	0 - 2	0.90	4.00	353.0	0.09	0.05	11.0	0.100	1334.5	19.340	1872	39.15	0.865	1399.5
AZ 022	2 - 20	1.90	2.80	698.5	0.12	1.20	30.5	0.130	172.5	1.055	417	49.50	0.895	235.5
AZ 023	20 - 40	2.05	2.50	779.5	0.09	1.95	36.0	0.115	81.0	0.165	258	51.65	0.925	124.5
AZ 024	40 - 60	2.00	2.50	790.0	0.09	1.85	34.5	0.110	91.0	0.115	302	51.05	0.910	118.0
AZ 025	0 - 2	1.85	2.30	840.5	0.13	2.45	53.0	0.120	296.5	1.075	608	49.35	0.955	436.5
AZ 026	2 - 20	2.00	1.95	915.0	0.07	4.85	40.5	0.095	77.5	0.035	293	52.40	1.035	260.5
AZ 027	20 - 40	2.00	2.20	1004.5	0.07	3.30	30.0	0.095	94.0	0.020	314	52.00	1.070	145.5
AZ 028	40 - 60	2.15	2.05	1082.0	0.05	3.25	41.0	0.080	125.0	0.020	341	56.20	1.145	116.0
AZ 029	0 - 2	1.80	2.10	811.5	0.06	3.65	47.0	0.080	362.5	0.670	604	54.75	1.120	467.5
AZ 030	2 - 20	1.85	2.25	828.0	0.05	3.65	23.0	0.085	270.0	0.510	489	54.90	1.115	385.5
AZ 033	0 - 2	1.75	2.10	760.0	0.07	2.30	38.5	0.085	497.5	1.315	776	53.75	1.050	613.5
AZ 034	2 - 20	2.05	2.10	806.0	0.09	3.45	31.0	0.110	99.5	0.020	317	54.95	0.985	144.5
AZ 035	20 - 40	2.00	2.05	890.5	0.05	4.25	32.0	0.090	91.0	0.045	350	55.60	1.090	122.5
AZ 036	40 - 60	2.10	1.90	852.0	0.05	5.05	48.5	0.090	119.0	0.020	318	56.25	1.040	107.5

ID	Depth [cm]	K_2O [%]	MgO [%]	Mn [ppm]	N [%]	Na_2O [%]	Ni [ppm]	P_2O_5 [%]	Pb [ppm]	S [%]	Sb [ppm]	SiO_2 [%]	TiO_2 [%]	Zn [ppm]
AZ 037	0 - 2	1.85	2.15	868.0	0.08	5.05	47.5	0.090	169.0	0.325	383	54.25	1.150	195.5
AZ 038	2 - 20	1.90	1.95	882.5	0.07	5.95	31.5	0.085	45.5	0.020	260	55.00	1.120	295.0
AZ 039	20 - 40	1.95	2.05	907.5	0.06	5.50	38.5	0.085	52.0	0.020	233	54.60	1.125	102.5
AZ 040	40 - 60	2.00	1.85	913.5	0.06	6.20	43.0	0.080	59.0	0.020	326	57.75	1.135	162.0
AZ 041	0 - 2	1.70	2.30	1062.5	0.11	4.10	49.0	0.085	389.5	1.110	745	54.00	1.195	709.0
AZ 042	2 - 20	1.85	1.95	757.5	0.07	5.05	35.5	0.080	184.5	0.310	416	55.10	1.180	222.5
AZ 043	20 - 40	1.95	2.00	860.5	0.07	5.85	43.0	0.080	70.0	0.030	302	56.00	1.155	130.0
AZ 044	40 - 60	1.95	2.11	904.0	0.06	4.85	43.5	0.080	68.0	0.025	256	55.60	1.160	113.5
AZ 045	0 - 2	1.15	2.85	472.0	0.06	0.05	13.5	0.080	1012.5	10.920	1499	46.80	1.225	852.5
AZ 046	2 - 20	2.05	2.25	941.5	0.07	5.50	49.0	0.110	60.5	0.020	299	57.05	1.160	158.5
AZ 047	20 - 40	1.80	2.30	883.0	0.06	4.00	48.5	0.085	77.0	0.565	263	53.55	1.155	155.0
AZ 048	40 - 60	1.90	2.20	933.5	0.06	4.20	47.5	0.075	66.5	0.125	287	53.75	1.125	215.5
AZ 049	0 - 2	1.65	2.15	591.0	0.09	1.90	31.5	0.145	308.5	0.525	546	48.55	0.775	499.0
AZ 050	2 - 20	1.85	1.95	672.0	0.07	2.65	32.0	0.115	78.5	0.080	283	52.00	0.820	173.5
AZ 051	20 - 40	1.95	2.05	752.5	0.07	2.20	38.5	0.110	62.0	0.060	266	52.25	0.860	133.5
AZ 052	40 - 60	2.05	2.10	768.5	0.07	2.20	41.0	0.115	61.0	0.020	246	52.80	0.870	135.0
AZ 053	0 - 2	1.40	1.95	469.0	0.11	1.50	41.0	0.230	255.0	0.370	479	43.25	0.625	610.0
AZ 054	2 - 20	1.70	1.80	557.5	0.08	2.50	30.5	0.130	80.0	0.055	298	50.85	0.720	352.0
AZ 055	20 - 40	1.80	1.80	588.0	0.05	3.65	37.5	0.110	46.0	0.020	254	52.45	0.795	160.0
AZ 056	40 - 60	1.80	1.85	662.0	0.05	2.95	33.0	0.105	41.5	0.020	234	51.20	0.805	94.0
AZ 057	0 - 2	1.60	2.00	532.0	0.07	1.85	37.5	0.135	338.0	0.965	576	48.50	0.705	621.5
AZ 058	2 - 20	1.75	1.90	594.0	0.09	2.45	47.5	0.140	112.0	0.215	332	49.65	0.740	364.0
AZ 059	20 - 40	1.80	1.80	631.5	0.07	2.80	37.0	0.125	88.5	0.105	277	50.60	0.785	264.5
AZ 060	40 - 60	1.85	1.95	711.5	0.07	2.55	35.0	0.120	66.5	0.040	286	50.65	0.825	150.5
AZ 061	0 - 2	1.65	1.65	536.0	0.10	2.40	32.0	0.150	81.0	0.070	273	49.40	0.665	369.5
AZ 062	2 - 20	1.75	1.75	610.5	0.08	2.70	32.5	0.130	61.0	0.030	296	50.35	0.750	407.5
AZ 063	20 - 40	1.80	1.90	661.0	0.07	2.65	36.5	0.125	67.0	0.025	269	50.50	0.795	177.5
AZ 064	40 - 60	1.90	1.70	671.0	0.08	2.90	33.5	0.105	75.5	0.020	279	55.30	0.850	218.0
AZ 065	0 - 2	1.65	1.90	626.5	0.09	1.85	23.0	0.105	295.5	0.380	571	52.50	0.790	714.5
AZ 066	2 - 20	1.85	1.55	644.5	0.06	3.85	25.0	0.100	81.5	0.025	327	56.15	0.810	339.0
AZ 067	20 - 40	1.90	1.55	661.0	0.06	3.95	36.0	0.095	79.5	0.010	318	55.85	0.840	298.0
AZ 068	40 - 60	1.85	1.45	578.5	0.04	4.95	26.0	0.090	45.5	0.020	255	57.45	0.810	141.5
AZ 069	0 - 2	1.70	1.55	516.0	0.08	2.70	33.5	0.120	99.5	0.020	312	52.65	0.695	349.0
AZ 070	2 - 20	1.85	1.60	613.0	0.07	3.05	24.5	0.110	69.5	0.020	275	54.15	0.785	263.0
AZ 071	20 - 40	1.90	1.50	602.0	0.05	4.50	32.0	0.100	55.0	0.020	290	56.05	0.775	172.0
AZ 072	40 - 60	1.25	2.70	517.5	0.03	0.05	31.0	0.105	724.0	4.430	1093	45.05	0.815	1182.5
AZ 073	0 - 2	1.85	1.45	556.5	0.07	4.85	43.5	0.090	37.5	0.020	261	55.30	0.725	97.0
AZ 074	2 - 20	1.70	2.05	589.0	0.07	2.00	34.5	0.120	282.5	0.675	507	50.05	0.775	447.5

ID	Depth [cm]	K_2O [%]	MgO [%]	Mn [ppm]	N [%]	Na_2O [%]	Ni [ppm]	P_2O_5 [%]	Pb [ppm]	S [%]	Sb [ppm]	SiO_2 [%]	TiO_2 [%]	Zn [ppm]
AZ 075	20 - 40	1.65	1.95	577.5	0.07	1.95	34.5	0.115	295.5	0.640	498	49.95	0.760	448.0
AZ 076	40 - 60	1.75	1.95	709.0	0.05	2.45	38.0	0.130	218.0	0.435	462	50.35	0.755	759.5
AZ 077	0 - 2	1.75	1.75	709.0	0.12	3.45	38.0	0.105	218.0	0.070	312	51.50	0.760	759.5
AZ 078	2 - 20	1.80	1.85	635.5	0.08	2.90	24.5	0.125	72.5	0.100	286	50.85	0.775	227.5
AZ 079	20 - 40	1.85	1.80	633.0	0.06	3.05	40.0	0.110	59.5	0.025	276	51.95	0.775	166.0
AZ 080	40 - 60	1.75	1.80	598.5	0.05	3.60	39.0	0.100	37.0	0.020	257	51.75	0.765	101.0
AZ 081	0 - 2	1.45	2.85	548.0	0.07	0.85	33.0	0.110	403.5	3.890	743	45.25	0.865	3887.0
AZ 082	2 - 20	1.85	2.10	932.0	0.06	2.80	44.5	0.115	92.5	0.325	320	50.30	0.820	1246.0
AZ 083	20 - 40	1.85	2.05	961.0	0.06	2.70	49.0	0.105	57.5	0.085	267	50.30	0.805	620.0
AZ 084	40 - 60	1.80	1.90	813.0	0.05	3.05	39.5	0.110	46.0	0.045	234	50.40	0.770	236.5
AZ 085	sludge	0.30	6.65	203.5	0.02	0.05	2.0	0.070	3331.5	18.175	3362	34.85	0.550	744.5
AZ 086	0 - 2	1.80	2.05	627.0	0.11	1.90	41.0	0.145	77.5	0.230	264	48.40	0.745	349.5
AZ 087	2 - 20	1.85	2.00	626.0	0.10	2.25	36.0	0.145	81.0	0.105	309	49.05	0.755	332.0
AZ 088	20 - 40	1.90	1.80	650.5	0.10	2.60	42.5	0.120	77.5	0.015	285	53.20	0.800	353.0
AZ 089	40 - 60	1.90	1.60	577.0	0.05	4.10	55.5	0.095	47.5	0.020	278	55.55	0.755	122.5
AZ 090	0 - 2	2.50	1.55	826.5	0.16	4.00	86.5	0.115	220.5	0.050	382	57.05	0.905	748.5
AZ 091	2 - 20	2.50	1.30	786.5	0.06	6.40	76.5	0.090	57.5	0.020	346	59.55	0.865	219.5
AZ 092	20 - 40	2.50	1.45	851.0	0.10	4.20	79.0	0.105	118.5	0.015	343	56.70	0.905	317.0
AZ 093	40 - 60	2.45	1.40	856.0	0.11	4.30	66.5	0.105	114.0	0.015	325	56.40	0.925	491.5
AZ 094	0 - 2	2.35	1.65	1061.5	0.13	2.80	59.0	0.120	162.0	0.625	425	54.50	0.910	575.0
AZ 095	2 - 20	2.60	1.25	888.5	0.05	3.90	92.5	0.100	62.0	0.140	324	59.30	0.780	786.0
AZ 096	20 - 40	2.55	1.20	768.5	0.05	3.60	92.5	0.100	60.0	0.135	256	59.00	0.770	246.5
AZ 097	40 - 60	2.60	1.10	681.5	0.03	3.70	96.5	0.095	50.5	0.115	301	59.90	0.740	156.5
AZ 098	0 - 2	2.30	1.70	1177.0	0.14	2.55	59.0	0.130	241.5	1.015	477	53.15	0.905	676.5
AZ 099	2 - 20	2.50	1.35	861.0	0.12	3.20	69.0	0.110	73.5	0.195	337	56.25	0.855	216.0
AZ 100	20 - 40	2.45	1.45	1021.0	0.08	3.00	55.0	0.130	125.0	0.335	401	54.40	0.885	341.5
AZ 101	40 - 60	2.60	1.15	645.0	0.04	3.65	60.0	0.100	35.5	0.060	327	58.45	0.730	125.0
AZ 102	0 - 2	2.40	1.05	520.5	0.05	2.75	84.5	0.105	181.5	0.530	513	57.75	0.755	286.0
AZ 103	2 - 20	2.25	1.00	509.0	0.04	2.85	54.0	0.120	139.0	0.490	472	56.50	0.750	702.5
AZ 104	20 - 40	2.30	0.75	367.5	0.03	2.05	51.0	0.105	31.5	0.250	281	55.45	0.810	153.0
AZ 105	40 - 60	2.15	0.75	407.0	0.02	2.65	123.5	0.145	31.5	0.180	260	57.55	0.670	164.5
AZ 106	0 - 2	2.40	1.65	1039.0	0.24	2.05	48.0	0.110	260.5	0.495	467	52.40	1.015	393.5
AZ 107	2 - 20	2.10	1.70	833.5	0.13	0.05	45.0	0.140	1753.5	5.735	1421	46.20	0.995	1029.5
AZ 108	20 - 40	2.70	1.60	1171.0	0.08	2.65	56.0	0.100	91.5	0.075	337	59.20	1.015	422.5
AZ 109	40 - 60	2.75	1.10	812.0	0.04	3.80	60.0	0.080	36.5	0.015	278	64.15	0.845	238.5
AZ 110	0 - 2	2.05	1.75	1145.5	0.09	0.45	39.0	0.150	562.0	2.945	369	53.70	0.840	1461.5
AZ 111	2 - 20	2.45	1.50	776.5	0.06	1.30	32.5	0.125	304.5	1.395	697	57.00	0.895	604.5
AZ 112	20 - 40	2.60	1.35	813.0	0.06	2.40	42.5	0.110	200.5	0.270	499	58.45	0.930	259.0

ID	Depth [cm]	K_2O [%]	MgO [%]	Mn [ppm]	N [%]	Na_2O [%]	Ni [ppm]	P_2O_5 [%]	Pb [ppm]	S [%]	Sb [ppm]	SiO_2 [%]	TiO_2 [%]	Zn [ppm]
AZ 113	40 - 60	2.40	1.50	978.0	0.09	2.30	56.5	0.110	294.5	0.135	525	55.55	1.065	299.0
AZ 114	0 - 2	2.05	1.25	566.5	0.04	1.15	48.0	0.160	374.5	1.990	699	54.60	0.740	592.0
AZ 115	2 - 20	2.25	0.90	557.5	0.05	2.30	35.5	0.100	172.5	0.475	483	61.90	0.655	224.5
AZ 116	20 - 40	2.30	0.85	569.5	0.02	2.40	75.5	0.095	139.0	0.270	447	61.85	0.660	190.0
AZ 117	40 - 60	2.45	1.00	612.0	0.03	2.85	36.5	0.100	147.5	0.165	486	61.00	0.765	193.5
AZ 118	0 - 2	0.95	1.50	282.0	0.15	1.35	8.0	0.605	72.0	0.020	322	25.35	0.315	121.5
AZ 119	2 - 20	2.55	1.10	598.5	0.03	2.70	32.0	0.125	153.0	0.110	460	58.95	0.740	229.5
AZ 120	20 - 40	2.45	1.05	689.0	0.04	2.55	37.5	0.110	235.5	0.070	634	57.75	0.910	166.0
AZ 121	0 - 2	2.10	2.00	662.5	0.11	0.05	27.0	0.175	625.5	3.120	734	44.75	0.810	1712.0
AZ 122	2 - 20	2.05	0.65	235.5	0.02	0.90	17.5	0.105	206.0	1.685	499	51.40	0.785	211.5
AZ 123	20 - 30	2.10	0.60	241.5	0.03	1.20	28.5	0.100	178.0	0.890	573	52.50	0.785	196.0
AZ 124	0 - 2	1.40	2.05	475.0	0.04	0.05	30.5	0.120	694.0	10.515	1040	43.30	0.850	1483.5
AZ 125	2 - 20	2.05	0.95	366.0	0.04	0.95	19.5	0.115	359.5	2.165	693	51.00	0.890	483.0
AZ 126	20 - 30	2.20	0.90	345.0	0.03	1.20	36.0	0.115	223.0	1.095	649	52.60	0.840	303.0
AZ 127	0 - 2	2.00	2.25	901.0	0.15	0.20	40.5	0.175	711.5	2.835	818	46.35	0.920	1059.5
AZ 128	2 - 20	2.20	2.15	737.0	0.15	0.45	40.0	0.130	425.0	2.160	630	49.90	1.020	424.5
AZ 129	20 - 40	2.45	1.90	1039.0	0.11	0.75	39.0	0.100	435.5	0.735	655	55.95	1.095	386.5
AZ 130	40 - 60	2.80	1.85	1175.5	0.12	1.15	50.0	0.110	183.0	0.045	506	57.50	1.105	363.0
AZ 131	0 - 2	1.80	1.70	769.5	0.19	1.05	35.5	0.290	521.0	0.545	816	43.25	0.745	723.5
AZ 132	2 - 20	2.70	1.55	1080.5	0.14	2.15	45.0	0.110	276.5	0.035	559	59.25	1.105	183.0
AZ 133	0 - 2	2.35	1.45	880.5	0.13	2.20	29.5	0.155	311.0	0.200	566	55.10	0.910	530.5
AZ 134	2 - 20	2.75	1.55	872.5	0.08	2.20	34.0	0.115	245.5	0.030	513	59.50	0.990	178.0
AZ 135	20 - 40	2.75	1.30	796.0	0.05	2.85	36.5	0.100	275.0	0.020	579	60.75	0.955	285.5
AZ 136	40 - 60	2.70	1.20	768.0	0.04	2.95	60.5	0.095	275.0	0.020	569	60.80	0.885	118.5
AZ 137	0 - 2	1.65	2.55	839.5	0.30	0.05	26.5	0.125	1096.5	8.185	1466	49.15	1.085	1346.0
AZ 138	2 - 20	2.20	2.25	920.0	0.18	0.60	44.5	0.110	366.5	1.455	629	54.25	1.060	400.5
AZ 139	20 - 40	2.30	2.10	866.0	0.14	0.85	41.0	0.100	297.5	0.895	587	56.15	1.035	299.5
AZ 140	40 - 60	2.55	1.85	999.5	0.09	1.60	48.5	0.090	181.5	0.095	478	58.00	1.005	147.0
AZ 141	0 - 2	1.70	1.70	503.5	0.11	1.90	29.5	0.130	173.5	0.110	435	51.30	0.765	267.5
AZ 142	2 - 20	1.80	1.75	533.5	0.10	1.75	26.5	0.120	118.5	0.035	301	51.55	0.800	259.0
AZ 143	20 - 40	1.90	1.70	746.0	0.11	2.25	28.0	0.115	147.5	0.085	338	51.80	0.935	270.5
AZ 144	40 - 60	1.95	1.75	971.5	0.11	3.15	41.0	0.105	132.5	0.055	405	52.20	1.045	284.0
AZ 145	0 - 2	1.70	1.80	538.5	0.09	1.55	28.5	0.125	275.0	0.525	505	50.25	0.785	452.5
AZ 146	2 - 20	1.85	1.90	659.5	0.11	1.55	31.0	0.140	238.0	0.305	446	49.60	0.850	359.0
AZ 147	20 - 40	1.85	1.80	689.0	0.11	1.75	30.0	0.140	237.5	0.360	442	49.90	0.855	357.0
AZ 148	40 - 60	1.90	1.75	908.5	0.11	2.35	34.5	0.120	159.0	0.075	421	50.20	0.980	297.5
AZ 149	0 - 2	1.40	2.20	537.5	0.09	0.85	26.0	0.145	526.5	2.920	829	46.85	0.840	835.0
AZ 150	2 - 20	1.60	1.90	482.5	0.07	1.95	23.0	0.135	148.0	0.245	390	50.45	0.730	316.0

ID	Depth [cm]	K_2O [%]	MgO [%]	Mn [ppm]	N [%]	Na_2O [%]	Ni [ppm]	P_2O_5 [%]	Pb [ppm]	S [%]	Sb [ppm]	SiO_2 [%]	TiO_2 [%]	Zn [ppm]
AZ 151	20 - 40	1.85	1.80	726.5	0.09	2.20	38.0	0.130	168.5	0.150	356	50.00	0.870	333.5
AZ 152	40 - 60	1.90	1.85	927.0	0.10	3.35	45.0	0.115	129.5	0.070	359	50.45	1.020	270.5
AZ 153	0 - 2	1.55	2.15	678.5	0.09	1.05	44.5	0.120	497.5	3.475	771	47.05	0.975	704.0
AZ 154	2 - 20	1.50	2.50	756.0	0.10	0.55	30.0	0.130	451.0	4.480	737	45.90	0.995	815.5
AZ 155	20 - 40	1.80	2.00	859.0	0.09	2.70	45.5	0.120	250.0	0.910	459	49.15	0.990	641.5
AZ 156	40 - 60	1.85	1.95	902.0	0.09	3.40	39.0	0.115	174.5	0.385	394	50.20	1.005	284.5
AZ 157	0 - 2	1.70	2.10	833.0	0.08	2.40	53.5	0.125	362.5	1.375	575	48.45	0.885	647.5
AZ 158	2 - 20	1.85	1.85	908.5	0.09	4.55	51.0	0.110	119.0	0.160	400	50.65	0.980	219.5
AZ 159	20 - 40	1.85	1.80	964.0	0.09	3.80	31.5	0.110	128.5	0.115	367	50.30	1.000	220.0
AZ 160	40 - 60	1.90	1.85	948.5	0.08	4.00	45.0	0.110	92.5	0.095	289	51.25	0.990	202.0
AZ 161	0 - 2	1.65	2.40	975.0	0.10	2.10	34.0	0.105	264.5	1.245	580	51.00	1.050	611.5
AZ 162	2 - 20	1.90	1.95	969.0	0.16	3.20	45.0	0.095	138.5	0.120	400	53.90	1.085	255.5
AZ 163	20 - 40	1.95	1.85	1026.0	0.09	3.60	41.5	0.090	132.0	0.055	358	54.25	1.070	223.0
AZ 164	40 - 60	1.95	1.80	923.5	0.07	3.85	38.5	0.090	71.0	0.015	268	54.95	1.000	632.5
AZ 165	0 - 2	1.60	2.10	819.5	0.10	0.90	25.5	0.115	478.5	2.525	784	48.45	1.010	620.5
AZ 166	2 - 20	1.90	1.90	1058.0	0.11	2.45	32.0	0.105	197.5	0.625	473	51.75	1.070	448.5
AZ 167	20 - 40	1.90	1.85	939.0	0.08	3.75	39.5	0.100	118.5	0.280	387	52.95	1.040	284.5
AZ 168	40 - 60	1.85	1.90	935.5	0.09	3.40	43.0	0.095	114.0	0.185	329	52.65	1.055	329.5
AZ 169	0 - 2	1.80	1.95	857.5	0.15	2.45	38.0	0.165	169.0	0.285	423	47.95	0.940	302.5
AZ 170	2 - 20	1.95	1.75	977.0	0.10	3.80	29.0	0.105	130.0	0.080	433	52.55	1.035	262.5
AZ 171	20 - 40	1.90	1.75	953.0	0.09	4.60	44.0	0.100	139.5	0.110	339	52.30	1.050	370.5
AZ 172	40 - 60	1.80	1.90	969.5	0.09	3.60	40.0	0.095	98.0	0.215	344	51.25	1.015	219.5
AZ 173	0 - 2	1.75	1.80	732.5	0.07	3.60	37.5	0.120	294.0	0.800	499	50.85	0.945	578.5
AZ 174	2 - 20	1.90	1.60	773.0	0.08	3.60	31.5	0.105	221.0	0.545	408	51.60	0.945	432.0
AZ 175	0 - 2	1.50	1.65	499.0	0.08	2.60	41.0	0.175	359.5	0.640	585	46.95	0.640	792.0
AZ 176	2 - 20	1.40	2.05	527.0	0.06	1.65	32.5	0.125	449.0	2.255	694	47.75	0.705	915.0
AZ 177	20 - 40	1.50	1.85	522.0	0.05	2.50	30.0	0.115	264.5	1.010	559	49.15	0.695	654.0
AZ 178	40 - 60	1.50	1.35	450.5	0.05	4.05	29.5	0.105	69.5	0.030	294	51.35	0.665	273.5
AZ 179	0 - 2	1.60	1.80	560.5	0.06	2.15	39.0	0.155	107.0	0.100	303	47.75	0.695	464.0
AZ 180	2 - 20	1.60	1.65	527.5	0.03	3.20	40.5	0.130	92.0	0.190	276	48.95	0.655	473.0
AZ 181	20 - 40	1.60	1.55	529.0	0.06	3.35	24.0	0.130	102.5	0.080	259	48.75	0.705	380.5
AZ 182	40 - 60	1.75	1.60	583.0	0.08	3.75	29.5	0.135	100.5	0.065	317	49.00	0.725	394.0
AZ 183	0 - 2	1.65	1.80	516.5	0.08	2.40	36.5	0.150	122.5	0.140	343	46.50	0.675	470.0
AZ 184	2 - 20	1.65	1.80	505.5	0.08	2.70	36.0	0.155	101.5	0.115	313	46.50	0.670	426.5
AZ 185	20 - 40	1.75	1.55	568.5	0.05	4.40	67.0	0.130	88.5	0.060	263	49.45	0.745	340.0
AZ 186	40 - 60	1.80	1.75	618.5	0.05	4.30	54.5	0.120	60.0	0.030	248	49.65	0.775	150.0
AZ 187	0 - 2	1.75	1.55	632.0	0.06	4.85	50.5	0.155	129.5	0.180	368	49.90	0.710	423.0
AZ 188	2 - 20	1.75	1.60	606.0	0.05	4.80	45.5	0.130	81.0	0.095	281	49.70	0.770	277.0

ID	Depth [cm]	K_2O [%]	MgO [%]	Mn [ppm]	N [%]	Na_2O [%]	Ni [ppm]	P_2O_5 [%]	Pb [ppm]	S [%]	Sb [ppm]	SiO_2 [%]	TiO_2 [%]	Zn [ppm]
AZ 189	20 - 40	1.75	1.75	610.5	0.04	4.75	27.0	0.120	57.0	0.045	270	49.05	0.800	155.5
AZ 190	40 - 60	1.75	1.75	617.0	0.03	4.65	33.5	0.110	43.0	0.010	265	48.55	0.780	111.0
AZ 191	0 - 2	1.70	1.60	540.0	0.08	3.60	39.5	0.150	125.0	0.120	326	48.30	0.695	436.0
AZ 192	2 - 20	1.70	1.70	564.0	0.07	3.05	23.5	0.155	111.5	0.060	318	47.05	0.695	454.0
AZ 193	20 - 40	1.85	1.70	636.5	0.09	2.40	28.5	0.135	162.0	0.020	294	52.70	0.785	428.0
AZ 194	40 - 60	1.80	1.60	645.5	0.11	2.30	26.5	0.115	220.0	0.035	346	52.45	0.810	334.5
AZ 195	0 - 2	1.70	1.45	486.0	0.05	3.80	48.0	0.105	83.5	0.020	327	55.90	0.690	334.0
AZ 196	2 - 20	1.80	1.55	588.5	0.05	3.70	45.0	0.080	71.0	0.020	253	56.00	0.785	267.0
AZ 197	20 - 40	1.80	1.55	578.5	0.05	3.80	38.0	0.140	57.0	0.020	302	55.60	0.795	572.5
AZ 198	40 - 60	1.90	1.70	622.5	0.03	4.10	39.5	0.080	50.0	0.020	266	55.80	0.870	129.0
AZ 199	0 - 2	1.95	2.15	713.5	0.11	2.00	31.0	0.130	165.5	0.105	394	53.05	0.855	595.5
AZ 200	2 - 20	2.00	2.10	794.5	0.05	2.10	36.5	0.100	83.0	0.020	288	54.95	0.920	124.5
AZ 201	20 - 40	1.95	2.10	758.5	0.05	2.30	33.5	0.110	101.0	0.020	298	55.10	0.895	161.0
AZ 202	40 - 60	2.00	2.05	817.0	0.05	2.30	31.0	0.090	94.5	0.020	332	55.45	0.950	149.0
AZ 203	0 - 2	1.85	1.60	704.0	0.05	3.95	48.0	0.085	78.5	0.020	303	56.40	0.865	216.0
AZ 204	2 - 20	1.90	1.55	676.5	0.05	4.40	32.0	0.105	71.0	0.020	292	57.15	0.865	212.0
AZ 205	20 - 40	1.85	1.55	688.5	0.04	4.90	26.5	0.080	57.5	0.020	329	57.35	0.905	181.0
AZ 206	40 - 60	1.85	1.50	659.5	0.03	4.35	27.0	0.085	55.5	0.020	258	56.65	0.945	145.0
AZ 207	0 - 2	1.70	1.75	627.5	0.08	1.70	31.0	0.110	434.0	0.470	693	54.35	0.870	478.5
AZ 208	2 - 20	1.90	1.65	677.0	0.08	2.20	29.0	0.100	94.0	0.020	321	57.45	0.905	197.0
AZ 209	20 - 40	1.85	1.55	715.5	0.06	2.10	26.5	0.090	74.0	0.020	301	57.80	0.925	162.0
AZ 210	40 - 60	1.95	1.65	833.5	0.05	2.25	30.5	0.055	49.5	0.020	242	57.70	0.985	144.0
AZ 211	0 - 2	2.15	1.90	889.0	0.10	1.70	38.0	0.115	21.5	0.020	262	57.20	0.960	104.5
AZ 212	2 - 20	2.15	1.95	905.0	0.07	1.65	38.5	0.125	17.5	0.020	243	57.00	0.990	101.0
AZ 213	20 - 40	2.10	1.90	942.0	0.06	1.70	37.0	0.090	24.5	0.020	226	57.10	1.010	98.0
AZ 214	40 - 60	2.15	1.90	1071.5	0.04	1.80	40.5	0.090	20.5	0.020	196	56.90	1.050	103.0

D. Geochemical analysis 2000

Table D.1. Geochemical laboratory analysis for 2000. Part I

ID	Depth [cm]	Al_2O_3 [%]	As [ppm]	Bi [%]	CaO [%]	Cd [ppm]	Cl [%]	Cr [ppm]	Cu [ppm]	Fe_2O_3 [%]	Hg [ppm]	K_2O [%]	MgO [%]
Az300	0 - 2	11.9	125.5	1.6	9.75	2.62	0.06	79	127	5.30	0.34	1.85	1.90
Az301	0 - 2	12.3	117.5	1.3	10.40	2.44	0.08	81	115	5.50	0.34	1.85	1.80
Az302	0 - 2	10.1	110.1	1.3	10.40	2.54	0.03	68	115	4.60	0.32	1.60	1.50
Az303	0 - 2	12.5	47.7	0.7	10.30	2.54	0.06	78	126	5.30	0.15	1.95	1.95
Az304	0 - 2	10.7	83.3	1.1	9.85	2.32	0.03	70	106	4.35	0.23	1.70	1.60
Az305	0 - 2	10.9	162.5	1.9	9.80	2.58	0.02	77	121	5.15	0.39	1.75	1.60
Az306	0 - 2	10.8	54.7	1.0	9.40	2.45	0.08	71	112	4.10	0.14	1.95	1.55
Az307	0 - 2	11.8	46.2	0.7	9.70	2.22	0.03	76	102	4.50	0.13	1.85	1.80
Az308	0 - 2	8.1	82.9	0.9	17.50	1.76	0.03	64	82	4.05	0.22	1.40	1.60
Az309	0 - 2	11.1	51.5	0.7	9.55	2.46	0.03	81	111	4.25	0.18	1.75	1.60
Az310	0 - 2	12.9	127.3	1.6	9.80	2.90	0.04	85	139	5.95	0.33	1.85	1.95
Az311	2 - 20	12.7	78.6	1.2	9.70	3.82	0.02	83	181	5.75	0.26	1.95	2.00
Az312	20 - 40	16.7	64.4	2.1	5.65	1.66	0.04	99	160	7.55	0.16	2.60	3.10
Az313	40 - 60	18.8	28.3	0.6	5.15	0.23	0.05	101	51	7.05	0.04	3.30	4.70
Az314	0 - 2	17	35.1	0.6	7.2	0.48	0.15	90	56	6.35	0.08	3.1	4.8
Az315	0 - 2	17.6	37.6	0.7	6.65	0.44	0.08	97	56	6.5	0.13	3	4.95
Az316	0 - 2	17.9	41	0.9	5.75	0.45	0.05	97	60	6.9	0.11	3.1	4.35
Az317	0 - 2	17.7	37	0.7	5.45	0.4	0.09	100	60	6.9	0.12	3.05	4.15
Az318	0 - 2	18.7	32.4	0.6	6	0.36	0.06	95	93	6.8	0.13	3.2	5.65
Az319	0 - 2	17.9	38.3	0.7	5.4	0.43	0.07	102	60	6.95	0.11	3.1	4
Az320	0 - 2	18.2	34.2	0.6	5.8	0.37	0.07	99	56	6.85	0.11	3.15	4.85
Az321	0 - 2	17.5	34	0.6	5.9	0.45	0.1	97	59	6.85	0.11	3.15	4.15
Az322	0 - 2	17.8	33.2	0.6	5.6	0.39	0.1	96	59	6.95	0.11	3.1	4.2
Az323	0 - 2	18.1	34.5	0.6	5.95	0.42	0.01	100	54	6.85	0.11	3.25	4.9
Az324	0 - 2	17.6	33.9	0.6	5.9	0.4	0.09	97	58	6.8	0.11	3.15	4.2
Az325	2 - 20	17.2	32.8	0.6	6.75	0.38	0.05	95	57	6.6	0.11	3	4.25
Az326	20 - 40	18.7	12.3	0.3	5.5	0.25	0.06	97	53	7	0.06	3.2	4.9
Az327	40 - 60	17.1	-	-	9.1	0.15	0.09	87	38	6.25	0.06	3.15	4.9
Az328	0 - 2	11.4	259.1	2.7	6.00	2.16	0.02	108	140	5.80	0.54	1.70	1.50
Az329	0 - 2	12.4	139.1	1.7	6.60	1.45	0.02	122	108	5.00	0.33	1.85	1.75
Az330	0 - 2	9.9	422.5	5.4	6.95	2.42	0.02	96	138	6.30	1.04	1.50	1.35
Az331	0 - 2	12.4	17.8	0.3	6.60	0.63	0.02	102	55	3.75	0.05	1.95	1.60
Az332	0 - 2	12.4	51.1	0.8	6.45	0.88	0.02	99	84	4.25	0.14	1.90	1.75
Az333	0 - 2	14.1	17.5	0.3	4.55	0.24	0.02	92	49	4.45	0.04	2.25	1.75
Az334	0 - 2	12.3	83.2	1.2	6.00	0.97	0.02	92	73	4.50	0.89	1.90	1.60
Az335	0 - 2	12.1	195.8	2.3	6.70	1.91	0.02	96	116	4.75	0.34	1.85	1.55
Az336	0 - 2	13.0	31.5	0.5	5.45	0.55	0.02	107	73	4.40	0.07	1.95	1.70
Az337	0 - 2	11.5	98.4	1.2	6.50	1.14	0.02	102	94	4.25	0.23	1.80	1.60
Az338	0 - 2	10.8	210.1	2.5	7.25	2.13	0.02	90	126	4.95	0.44	1.75	1.50
Az339	2 - 20	13.1	42.3	0.7	5.75	0.72	0.02	105	90	4.55	0.11	1.90	1.80

ID	Depth [cm]	Al_2O_3 [%]	As [ppm]	Bi [%]	CaO [%]	Cd [ppm]	Cl [%]	Cr [ppm]	Cu [ppm]	Fe_2O_3 [%]	Hg [ppm]	K_2O [%]	MgO [%]
Az340	20 - 40	12.6	55.0	0.8	5.90	0.84	0.02	100	90	4.45	0.14	1.85	1.65
Az341	40 - 60	12.9	47.2	0.8	5.70	0.67	0.02	101	84	4.45	0.11	1.85	1.70
Az342	sludge	3.7	2857.9	49.5	1.55	5.70	0.02	62	200	23.00	12.83	0.30	0.40
Az343	2 - 20	12.2	105.0	0.8	5.95	1.49	0.02	112	113	4.46	0.14	1.75	1.75
Az344	20 - 40	12.8	73.9	0.8	5.95	1.04	0.02	104	120	4.80	0.14	1.80	1.70
Az345	40 - 60	13.3	60.0	0.9	5.75	1.10	0.02	107	143	5.05	0.13	1.75	1.75
Az346	sludge	4.0	3070.9	44.7	1.10	7.38	0.02	91	262	24.60	11.84	0.23	0.43
Az347	2 - 20	10.0	601.9	11.0	4.55	4.65	0.02	92	201	9.75	2.68	1.30	1.30
Az348	20 - 40	12.5	84.4	1.5	5.90	0.82	0.02	98	102	4.95	0.34	1.70	1.60
Az349	40 - 60	12.8	72.9	1.3	6.05	0.66	0.02	127	87	4.80	0.24	1.75	1.65
Az350	sludge	4.8	2413.6	44.2	2.15	6.02	0.02	64	250	20.10	10.37	0.48	0.60
Az351	2 - 20	11.5	196.6	0.9	6.35	1.81	0.02	86	113	4.70	0.17	1.65	1.60
Az352	20 - 40	12.7	149.0	0.8	6.00	2.00	0.02	107	123	4.95	0.14	1.75	1.70
Az353	40 - 60	12.9	-	-	5.40	-	0.02	125	40	4.15	0.04	1.80	1.60
Az354	sludge	3.0	-	-	1.60	-	0.02	65	171	23.30	16.29	0.25	0.20
Az355	2 - 20	9.7	178.3	1.0	14.50	2.66	0.02	90	130	6.55	0.16	1.35	1.65
Az355-1	0 - 2	9.7	264.7	2.9	14.60	2.10	0.02	193	128	6.65	0.76	1.35	1.70
Az356	20 - 40	15.8	64.7	0.6	3.50	0.80	0.02	128	52	5.70	0.09	1.95	1.90
Az356-1	2 - 20	16.1	33.3	0.6	3.50	0.14	0.02	186	67	5.70	0.12	1.95	2.00
Az357	40 - 60	13.1	20.5	0.3	5.60	0.22	0.02	134	40	4.15	0.04	1.80	1.65
Az357-1	20 - 40	16.4	26.9	1.0	2.85	0.11	0.02	142	51	5.65	0.09	1.95	1.85
Az358	40 - 60	17.4	32.0	0.8	2.70	0.11	0.02	146	71	6.15	0.09	1.95	2.05
Az359	0 - 2	13.7	259.1	2.7	6.40	2.48	0.02	122	123	7.05	0.77	1.65	1.70
Az360	2 - 20	16.4	61.7	1.0	3.55	0.43	0.02	132	66	6.30	0.19	2.05	1.90
Az361	20 - 40	17.3	31.2	0.8	2.55	0.13	0.02	150	57	6.10	0.08	2.10	1.95
Az362	40 - 60	-	-	-	-	-	-	-	-	-	-	-	
Az363	0 - 2	16.2	43.5	0.7	4.15	0.23	0.02	155	67	6.35	0.14	2.00	2.00
Az364	2 - 20	16.1	31.5	0.7	3.85	0.17	0.02	168	65	6.20	0.09	2.05	1.95
Az365	20 - 40	16.8	37.0	0.7	2.90	0.18	0.02	139	64	6.30	0.10	2.10	2.00
Az366	40 - 60	16.8	30.4	0.8	2.55	0.08	0.02	169	67	5.65	0.54	2.00	1.85
Az367	0 - 2	15.1	64.2	0.8	3.30	0.55	0.02	129	48	5.95	0.20	1.80	1.95
Az368	2 - 20	16.1	24.0	0.4	2.55	0.14	0.02	130	33	5.90	0.06	1.90	2.00
Az369	20 - 40	16.7	21.8	0.4	2.45	0.08	0.02	116	31	5.95	0.04	1.85	2.10
Az370	40 - 60	17.8	22.9	0.4	2.35	0.06	0.02	149	36	6.40	0.03	1.90	2.30
Az371	0 - 2	13.7	186.0	1.8	4.15	1.56	0.02	130	90	7.00	0.66	1.65	1.75
Az372	2 - 20	15.1	151.5	2.2	2.80	0.62	0.02	135	67	7.30	0.55	1.80	1.80
Az373	20 - 40	16.6	69.2	0.7	2.40	0.42	0.02	125	52	6.65	0.19	1.85	2.05
Az374	40 - 60	16.8	53.1	0.7	2.45	0.36	0.02	114	51	6.55	0.16	1.85	2.05
Az375	0 - 2	11.4	417.1	3.6	6.65	2.44	0.02	118	141	8.60	1.22	1.35	1.50
Az376	2 - 20	15.5	90.5	1.5	2.45	0.39	0.02	136	65	6.50	0.35	2.00	1.85
Az377	20 - 40	16.9	37.7	0.6	2.30	0.15	0.02	148	48	6.25	0.13	2.05	2.00
Az378	40 - 60	17.9	35.1	0.7	1.95	0.08	0.02	144	60	6.10	0.11	2.25	1.95
Az379	0 - 2	12.3	330.8	2.8	3.80	1.61	0.02	118	122	8.45	0.99	1.70	1.45
Az380	2 - 20	13.8	251.8	3.1	3.25	0.72	0.02	121	95	8.00	0.99	1.95	1.50

ID	Depth [cm]	Al_2O_3 [%]	As [ppm]	Bi [%]	CaO [%]	Cd [ppm]	Cl [%]	Cr [ppm]	Cu [ppm]	Fe_2O_3 [%]	Hg [ppm]	K_2O [%]	MgO [%]
Az381	20 - 40	16.1	64.8	0.7	2.30	0.20	0.02	143	78	7.45	0.47	2.20	1.85
Az382	40 - 60	18.5	58.0	0.8	2.15	0.29	0.02	136	53	7.00	0.15	2.50	1.80
Az383	0 - 2	11.6	792.5	6.5	5.30	2.78	0.02	117	152	9.60	1.29	1.50	1.45
Az384	2 - 20	15.6	180.8	2.4	3.10	1.61	0.02	135	90	6.90	0.44	2.00	2.25
Az385	20 - 40	14.1	417.6	6.5	3.80	1.50	0.02	124	117	7.95	1.25	1.85	1.85
Az386	40 - 60	17.0	61.5	1.6	4.15	0.19	0.02	129	113	6.70	0.23	2.05	2.30
Az387	0 - 2	14.9	200.6	2.5	3.90	0.80	0.02	115	72	6.95	0.40	2.05	2.00
Az388	2 - 20	15.5	150.6	2.0	3.60	0.45	0.02	122	65	6.80	0.36	2.05	2.15
Az389	20 - 40	15.8	154.9	2.1	3.55	0.55	0.02	127	63	6.75	0.30	2.10	2.25
Az390	40 - 60	17.1	84.3	1.4	3.20	0.28	0.02	127	59	6.75	0.17	2.10	2.40
Az391	0 - 2	16.4	254.5	3.3	3.60	1.49	0.02	124	105	7.45	0.51	2.35	1.50
Az392	2 - 20	17.1	153.3	2.1	3.10	0.85	0.02	113	81	7.25	0.40	2.40	1.60
Az393	20 - 40	18.3	108.4	1.7	2.30	0.75	0.02	122	76	7.10	0.26	2.60	1.70
Az394	40 - 60	19.4	69.6	1.5	1.30	0.21	0.02	124	75	6.50	0.15	2.85	1.50
Az395	0 - 2	16.3	112.0	2.3	5.25	0.74	0.02	111	97	5.70	0.23	2.70	1.20
Az396	0 - 2	14.5	243.9	3.9	9.90	0.92	0.02	100	139	5.85	0.45	2.25	1.30
Az397	0 - 2	17.6	274.3	3.5	3.65	2.11	0.02	112	127	7.75	0.58	2.40	1.75
Az398	0 - 2	16.1	807.8	5.5	4.00	4.63	0.02	103	447	12.20	1.37	2.15	1.50
Az399	0 - 2	16.3	779.9	7.1	7.35	12.29	0.02	82	537	9.85	1.54	2.25	1.80
Az400	0 - 2	8.7	88.3	1.2	19.70	0.63	0.02	113	106	4.65	0.31	1.65	1.20
Az401	0 - 2	10.3	785.2	8.9	8.45	4.97	0.02	147	320	11.20	1.81	1.45	0.95
Az402	0 - 2	13.7	373.8	3.9	4.95	1.75	0.02	146	173	8.05	0.62	2.30	0.95
Az403	0 - 2	17.0	216.7	2.5	2.35	0.75	0.02	99	104	6.25	0.48	2.45	1.15
Az404	2 - 20	18.9	23.4	0.5	1.85	0.13	0.02	103	74	5.65	0.07	2.75	1.25
Az405	20 - 40	19.2	19.0	0.4	1.30	0.08	0.02	107	88	5.50	0.07	2.90	1.20
Az406	40 - 60	18.4	20.6	0.4	1.10	0.06	0.02	133	73	5.40	0.06	2.90	1.00
Az407	0 - 2	15.0	46.8	0.4	0.50	1.86	0.02	439	104	5.80	0.17	2.45	0.75
Az408	0 - 2	15.9	94.5	2.2	0.80	0.96	0.02	152	131	6.45	0.28	2.30	0.85
Az409	0 - 2	13.4	438.7	2.5	2.20	1.17	0.02	184	134	8.90	0.91	2.10	0.80
Az410	0 - 2	16.8	65.3	0.8	2.40	1.79	0.02	105	189	5.20	0.29	2.45	1.05
Az411	0 - 2	11.4	42.5	0.8	6.35	1.74	0.02	97	114	3.95	0.15	1.65	1.40
Az412	0 - 2	12.1	128.0	1.8	7.40	2.21	0.02	101	140	4.95	0.34	1.70	1.60
Az413	0 - 2	13.4	83.1	1.2	5.50	1.45	0.02	106	129	5.00	0.21	1.85	1.50
Az414	0 - 2	10.1	128.5	1.5	7.15	2.27	0.02	91	150	4.70	0.23	1.55	1.40
Az415	0 - 2	9.3	197.2	2.1	5.95	2.05	0.02	123	130	4.85	0.41	1.35	1.15
Az416	0 - 2	13.8	74.4	1.1	13.40	1.91	0.02	91	90	6.50	0.32	2.35	2.40
Az417	0 - 2	12.4	120.8	2.0	6.50	1.91	0.02	94	166	6.20	0.48	1.70	1.65
Az418	0 - 2	14.4	33.2	0.5	4.30	0.93	0.02	103	44	5.05	0.80	1.95	1.50
Az419	2 - 20	15.6	20.2	0.4	3.45	0.38	0.02	110	36	5.20	0.05	2.00	1.50
Az420	20 - 40	15.0	35.2	0.6	3.80	0.60	0.02	106	36	5.10	0.06	1.95	1.50
Az421	40 - 60	15.8	26.2	0.5	3.20	0.37	0.02	114	39	5.35	0.06	2.00	1.50
Az422	0 - 2	16.6	19.9	0.35	3.05	0.08	0.02	134	31	5.65	0.01	2.15	1.80
Az423	0 - 2	9.9	277.9	2.7	7.35	3.95	0.08	96	162	7.50	0.59	0.95	6.35
Az424	0 - 2	8.7	398.9	2.4	3.80	4.76	0.06	289	243	10.00	0.60	0.80	2.20

ID	Depth [cm]	Al_2O_3 [%]	As [ppm]	Bi [%]	CaO [%]	Cd [ppm]	Cl [%]	Cr [ppm]	Cu [ppm]	Fe_2O_3 [%]	Hg [ppm]	K_2O [%]	MgO [%]
Az425	0 - 2	6.8	1060.2	2.5	1.50	17.03	0.04	323	614	14.60	0.86	0.30	1.95
Az426	0 - 2	3.7	2324.4	30.7	1.55	4.85	0.02	86	207	23.40	9.45	0.25	0.40
Az427	0 - 2	10.8	204.1	2.0	8.00	2.17	0.08	100	122	7.40	0.05	1.10	2.75
Az428	0 - 2	14.7	497.3	5.3	4.40	4.04	0.02	120	256	10.90	1.27	1.65	1.95

Table D.2. Geochemical laboratory analysis for 2000. Part II

Sample ID	Depth [(cm]	Mn [ppm]	Na_2O [%]	Ni [ppm]	P_2O_5 [%]	Pb [ppm]	S [%]	Sb [ppm]	SiO2 [%]	TiO2 [%]	Tl [ppm]	Zn [ppm]
Az300	0 - 2	583	0.90	32	0.19	198	0.85	183	51.8	0.67	1.8	690
Az301	0 - 2	618	0.75	33	0.20	174	0.87	173	50.0	0.64	1.7	540
Az302	0 - 2	489	0.95	28	0.20	189	0.87	226	53.2	0.65	1.5	548
Az303	0 - 2	644	0.95	35	0.21	82	0.30	91	51.0	0.69	1.0	617
Az304	0 - 2	514	0.95	31	0.19	142	0.50	143	54.3	0.66	1.3	528
Az305	0 - 2	529	0.85	31	0.21	240	0.92	207	52.8	0.66	2.1	600
Az306	0 - 2	501	1.20	32	0.19	76	0.26	89	55.8	0.66	1.7	534
Az307	0 - 2	546	0.90	32	0.19	70	0.22	94	53.7	0.66	1.1	489
Az308	0 - 2	480	0.50	27	0.41	114	0.95	156	39.6	0.49	1.5	373
Az309	0 - 2	515	0.95	31	0.18	84	0.35	128	54.3	0.66	4.4	526
Az310	0 - 2	643	0.75	36	0.21	176	0.58	192	50.3	0.69	2.0	748
Az311	2 - 20	637	0.85	36	0.20	157	0.42	158	51.1	0.70	1.5	906
Az312	20 - 40	969	1.30	43	0.16	100	0.16	65	51.9	0.85	0.9	381
Az313	40 - 60	905	1.35	47	0.15	77	0.09	10	52.2	0.85	0.5	100
Az314	0 - 2	993	1.4	45	0.22	67	0.14	52	50.4	0.765	0.58	144
Az315	0 - 2	866	1.25	44	0.24	72	0.855	10	49.6	0.77	2.51	126
Az316	0 - 2	929	1.1	45	0.23	72	0.185	106	51.9	0.825	1.94	138
Az317	0 - 2	901	1.3	45	0.235	70	0.375	83	52.1	0.83	0.87	125
Az318	0 - 2	845	1.15	45	0.22	69	0.21	102	50.4	0.795	0.64	122
Az319	0 - 2	915	1.3	45	0.215	70	0.22	97	52.3	0.84	0.77	130
Az320	0 - 2	955	1.25	45	0.22	71	0.135	70	51.5	0.82	2.85	121
Az321	0 - 2	910	1.35	45	0.235	73	0.38	10	51.5	0.81	0.56	128
Az322	0 - 2	898	1.3	45	0.22	70	0.115	10	52	0.835	0.72	126
Az323	0 - 2	948	1.3	47	0.225	67	0.125	48	51.2	0.81	0.63	118
Az324	0 - 2	896	1.35	46	0.22	70	0.14	10	52.2	0.825	0.6	126
Az325	2 - 20	809	1.25	44	0.22	66	1.16	10	49.9	0.77	2.3	119
Az326	20 - 40	774	1.25	46	0.17	63	0.145	10	51.5	0.82	0.33	111
Az327	40 - 60	869	1.05	43	0.165	44	0.165	-	47.9	0.7	-	84
Az328	0 - 2	559	1.30	27	0.19	370	2.73	472	53.0	0.67	2.5	587
Az329	0 - 2	596	1.35	30	0.22	206	0.86	235	55.2	0.71	1.2	421
Az330	0 - 2	507	1.05	26	0.17	628	3.44	791	52.3	0.63	4.4	662
Az331	0 - 2	553	1.25	31	0.41	57	0.06	81	58.0	0.68	0.3	210
Az332	0 - 2	578	1.55	29	0.21	96	0.21	153	57.4	0.71	0.5	257
Az333	0 - 2	734	1.55	34	0.61	77	0.02	86	58.6	0.74	0.3	122
Az334	0 - 2	612	1.50	31	0.28	150	0.38	154	57.4	0.72	0.9	332
Az335	0 - 2	561	1.40	27	0.21	230	0.96	304	55.3	0.68	2.0	554

Sample ID	Depth [(cm]	Mn [ppm]	Na_2O [%]	Ni [ppm]	P_2O_5 [%]	Pb [ppm]	S [%]	Sb [ppm]	SiO2 [%]	TiO2 [%]	Tl [ppm]	Zn [ppm]
Az336	0 - 2	620	1.65	30	0.24	66	0.19	10	57.9	0.75	0.3	189
Az337	0 - 2	541	1.45	29	0.20	158	0.54	182	57.4	0.69	0.9	349
Az338	0 - 2	545	1.20	28	0.19	294	1.52	384	55.0	0.66	1.8	635
Az339	2 - 20	606	1.60	31	0.20	80	0.18	125	57.2	0.74	0.4	206
Az340	20 - 40	595	1.60	30	0.19	102	0.44	152	57.1	0.73	0.5	241
Az341	40 - 60	607	1.70	30	0.19	84	0.32	152	57.4	0.74	0.5	202
Az342	sludge	188	0.10	6	0.06	2870	28.00	3470	21.9	0.24	46.8	678
Az343	2 - 20	561	1.40	28	0.20	92	0.69	101	56.6	0.69	0.6	452
Az344	20 - 40	620	1.65	30	0.17	88	0.40	116	56.5	0.74	0.4	294
Az345	40 - 60	627	1.70	30	0.16	86	0.18	117	56.0	0.76	0.4	279
Az346	sludge	205	0.10	8	0.07	2680	28.40	3270	19.7	0.20	43	861
Az347	2 - 20	582	0.95	22	0.14	1370	7.75	1610	46.7	0.62	9.4	1140
Az348	20 - 40	570	1.70	27	0.15	206	0.88	234	56.1	0.72	1.0	229
Az349	40 - 60	575	1.65	29	0.15	159	0.79	165	55.7	0.74	0.9	192
Az350	sludge	227	0.30	10	0.06	2470	24.20	3360	27.4	0.34	42.1	816
Az351	2 - 20	551	1.45	29	0.16	107	1.20	148	55.8	0.72	0.7	547
Az352	20 - 40	615	1.65	31	0.15	91	0.86	130	55.6	0.73	0.6	526
Az353	40 - 60	555	2.30	30	0.13	49	0.52	10	57.7	0.71	-	105
Az354	sludge	136	0.05	9	0.06	3130	30.40	3840	21.1	0.22	-	443
Az355	2 - 20	615	1.10	25	0.44	334	1.01	202	38.6	0.62	0.7	539
Az355-1	0 - 2	628	1.00	42	0.45	329	0.95	447	37.5	0.63	2.8	531
Az356	20 - 40	880	3.15	34	0.14	89	1.90	66	55.7	0.95	0.3	98
Az356-1	2 - 20	881	3.05	48	0.15	86	0.19	143	55.4	0.93	0.3	101
Az357	40 - 60	575	2.25	31	0.13	43	0.26	68	57.9	0.75	0.2	102
Az357-1	20 - 40	896	3.40	35	0.13	89	0.11	132	56.5	0.96	0.2	76
Az358	40 - 60	941	3.00	35	0.13	99	0.10	120	55.0	0.99	0.2	80
Az359	0 - 2	1020	2.40	30	0.26	352	1.50	479	48.8	0.79	2.8	652
Az360	2 - 20	892	2.70	44	0.16	138	0.50	202	54.5	0.94	0.6	179
Az361	20 - 40	915	2.90	38	0.15	98	0.13	101	55.8	0.99	0.3	86
Az362	40 - 60	-	-	-	-	-	-	-	-	-	-	-
Az363	0 - 2	928	2.50	36	0.22	105	0.31	107	52.6	0.95	0.4	118
Az364	2 - 20	953	2.60	38	0.20	94	0.23	131	53.6	0.95	0.3	103
Az365	20 - 40	957	2.90	37	0.16	97	0.17	127	54.8	0.98	0.3	100
Az366	40 - 60	809	3.50	34	0.13	117	0.12	160	56.2	0.89	0.2	71
Az367	0 - 2	892	3.30	34	0.16	113	3.31	146	54.1	1.01	0.6	222
Az368	2 - 20	950	3.50	41	0.13	55	1.16	87	56.0	1.02	0.2	92
Az369	20 - 40	920	3.45	37	0.12	49	0.40	63	55.8	1.05	0.2	68
Az370	40 - 60	999	2.95	38	0.12	52	0.21	63	54.7	1.03	0.2	72
Az371	0 - 2	904	2.85	32	0.20	261	2.14	393	50.8	1.02	1.9	450
Az372	2 - 20	791	2.70	32	0.14	293	2.10	390	51.9	1.02	1.8	233
Az373	20 - 40	946	3.05	35	0.13	105	0.85	138	54.4	1.05	0.6	176
Az374	40 - 60	966	3.00	36	0.14	94	0.74	154	53.9	1.04	0.5	167
Az375	0 - 2	805	2.10	27	0.29	448	0.82	661	43.9	0.82	4.0	681
Az376	2 - 20	859	3.05	34	0.15	174	0.28	292	55.4	1.02	1.1	170

Sample ID	Depth [(cm]	Mn [ppm]	Na_2O [%]	Ni [ppm]	P_2O_5 [%]	Pb [ppm]	S [%]	Sb [ppm]	SiO2 [%]	TiO2 [%]	Tl [ppm]	Zn [ppm]
Az377	20 - 40	935	3.05	37	0.15	87	0.09	104	55.9	1.09	0.4	94
Az378	40 - 60	841	3.00	35	0.13	121	0.07	155	55.8	0.98	0.3	77
Az379	0 - 2	648	1.75	30	0.17	384	5.02	510	48.1	0.77	3.0	477
Az380	2 - 20	578	1.70	30	0.14	419	3.69	480	50.8	0.87	3.0	287
Az381	20 - 40	668	1.95	33	0.14	240	1.74	300	54.3	0.92	0.6	243
Az382	40 - 60	1060	2.00	42	0.14	91	0.71	128	55.0	0.89	0.6	148
Az383	0 - 2	581	1.20	28	0.18	471	6.99	624	41.2	0.69	6.0	714
Az384	2 - 20	875	1.70	38	0.15	201	2.15	252	53.2	0.86	2.2	520
Az385	20 - 40	718	1.50	32	0.13	496	3.95	585	50.0	0.80	6.1	498
Az386	40 - 60	866	1.65	41	0.14	134	0.41	206	53.4	0.89	0.7	100
Az387	0 - 2	771	1.75	36	0.18	195	1.55	247	53.1	0.84	2.1	294
Az388	2 - 20	740	1.70	37	0.15	167	1.66	269	53.8	0.88	2.7	201
Az389	20 - 40	765	1.70	37	0.16	157	1.21	136	54.2	0.87	1.7	217
Az390	40 - 60	826	1.85	40	0.14	110	0.56	114	54.7	0.90	1.0	144
Az391	0 - 2	938	1.10	45	0.20	250	1.53	349	53.3	0.89	2.8	491
Az392	2 - 20	997	1.20	45	0.18	188	1.29	230	54.1	0.92	1.9	323
Az393	20 - 40	1060	1.30	48	0.17	152	0.82	214	55.1	0.95	1.4	280
Az394	40 - 60	953	1.75	43	0.14	158	0.25	219	57.4	0.92	0.7	138
Az395	0 - 2	1070	2.00	37	0.25	238	0.33	249	54.5	0.90	1.0	288
Az396	0 - 2	912	1.45	32	0.37	388	0.40	506	46.1	0.83	2.2	329
Az397	0 - 2	1120	1.20	42	0.20	280	1.41	298	51.5	0.87	3.1	653
Az398	0 - 2	599	1.00	33	0.20	475	2.15	649	45.5	0.76	7.9	1940
Az399	0 - 2	1260	1.10	42	0.35	621	0.95	806	43.7	0.73	7.1	3820
Az400	0 - 2	533	0.70	24	0.70	108	0.03	181	35.4	0.46	0.8	202
Az401	0 - 2	948	0.85	26	0.31	523	4.64	695	36.4	0.52	7.3	1620
Az402	0 - 2	706	1.70	29	0.28	256	2.03	352	49.2	0.77	3.0	543
Az403	0 - 2	1200	2.70	37	0.13	219	1.55	260	55.5	0.91	2.5	361
Az404	2 - 20	1430	2.65	41	0.16	50	0.14	119	56.9	0.96	0.6	119
Az405	20 - 40	1220	2.60	41	0.15	44	0.14	119	56.2	0.93	0.4	90
Az406	40 - 60	1080	2.85	38	0.14	40	0.18	52	59.2	0.85	0.4	77
Az407	0 - 2	887	2.50	43	0.11	70	0.26	232	64.9	0.58	0.8	604
Az408	0 - 2	738	3.40	30	0.13	224	0.78	254	59.0	0.83	1.1	338
Az409	0 - 2	450	1.95	29	0.16	343	3.99	506	50.5	0.68	3.0	375
Az410	0 - 2	933	3.00	37	0.15	189	0.26	264	57.5	0.83	1.0	541
Az411	0 - 2	566	2.05	27	0.16	96	0.20	118	57.3	0.59	0.6	445
Az412	0 - 2	607	1.45	29	0.19	180	0.70	240	53.8	0.66	1.7	575
Az413	0 - 2	646	1.90	28	0.22	123	0.49	166	54.9	0.72	0.9	407
Az414	0 - 2	579	1.50	27	0.20	149	0.85	203	54.8	0.72	1.2	650
Az415	0 - 2	521	1.65	25	0.15	225	2.01	277	56.2	0.68	1.9	597
Az416	0 - 2	548	0.35	39	0.20	121	0.65	186	42.3	0.64	1.3	405
Az417	0 - 2	661	1.25	31	0.18	269	0.75	252	53.4	0.71	1.4	481
Az418	0 - 2	703	1.40	38	0.19	67	0.20	76	58.1	0.80	0.7	465
Az419	2 - 20	753	1.50	37	0.18	42	0.11	70	58.8	0.83	0.4	207
Az420	20 - 40	731	1.40	35	0.17	51	0.21	10	58.4	0.82	0.7	301

Sample ID	Depth [(cm]	Mn [ppm]	Na_2O [%]	Ni [ppm]	P_2O_5 [%]	Pb [ppm]	S [%]	Sb [ppm]	SiO2 [%]	TiO2 [%]	Tl [ppm]	Zn [ppm]
Az421	40 - 60	864	1.65	40	0.15	47	0.12	55	58.7	0.85	0.5	209
Az422	0 - 2	795	1.35	39	0.18	25	0.07	10	58.5	0.85	0.35	78
Az423	0 - 2	3440	1.60	33	0.16	307	12.90	439	26.8	0.47	2.8	1200
Az424	0 - 2	1660	1.55	41	0.14	211	13.50	350	30.4	0.57	2.7	1380
Az425	0 - 2	2400	1.20	48	0.15	228	18.10	535	17.0	0.23	3.2	5600
Az426	0 - 2	314	0.20	14	0.07	2010	30.30	2770	15.2	0.23	40.1	636
Az427	0 - 2	1350	1.70	29	0.14	206	10.50	234	34.7	0.60	1.8	510
Az428	0 - 2	1100	1.50	37	0.16	707	5.73	786	42.1	0.74	4.7	1120

E. Soil profiles

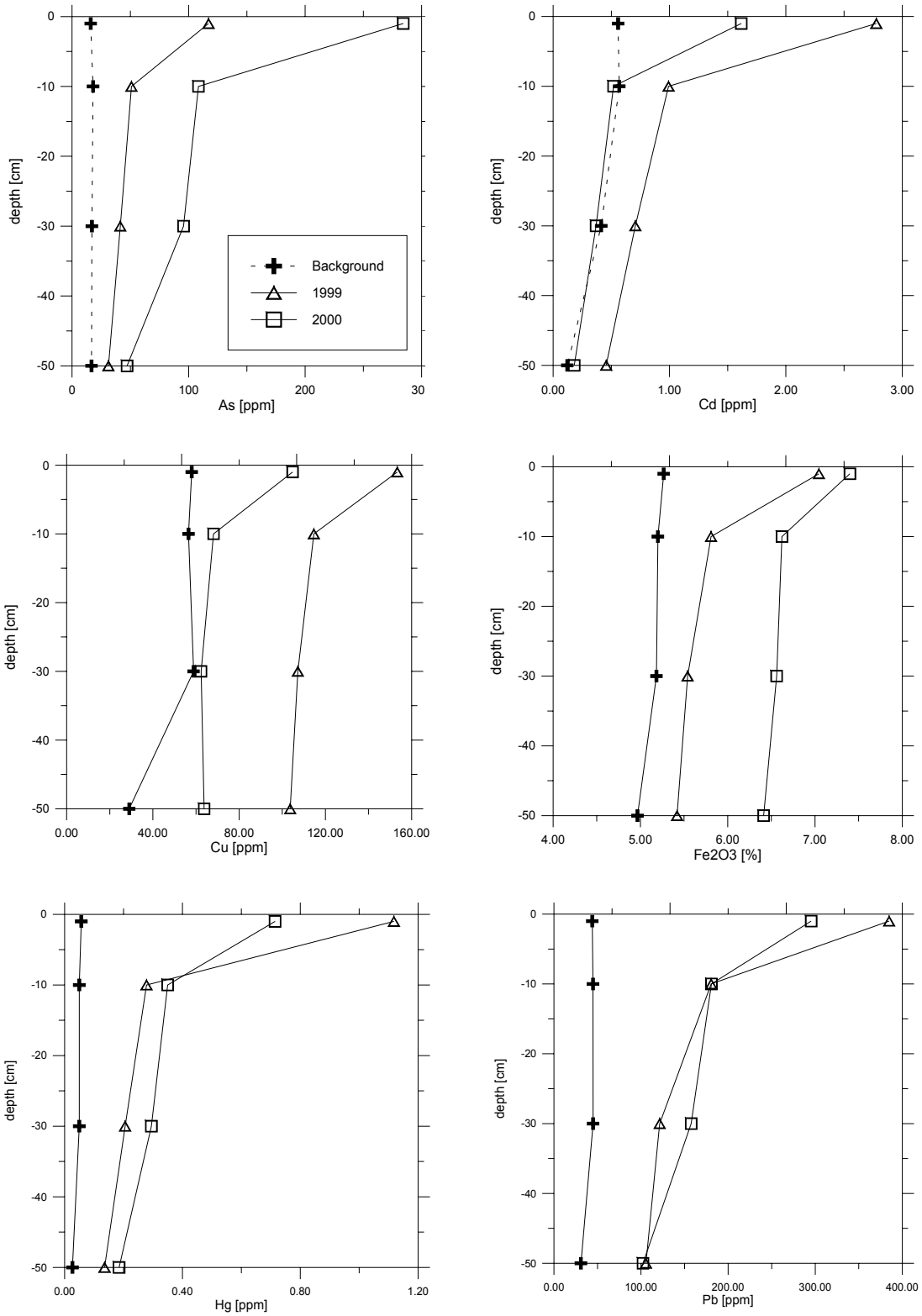

Figure E.1. Comparison of soil depth profiles 1999 (triangle) and 2000 (square) and background (cross) from Sobarbina. Part I.

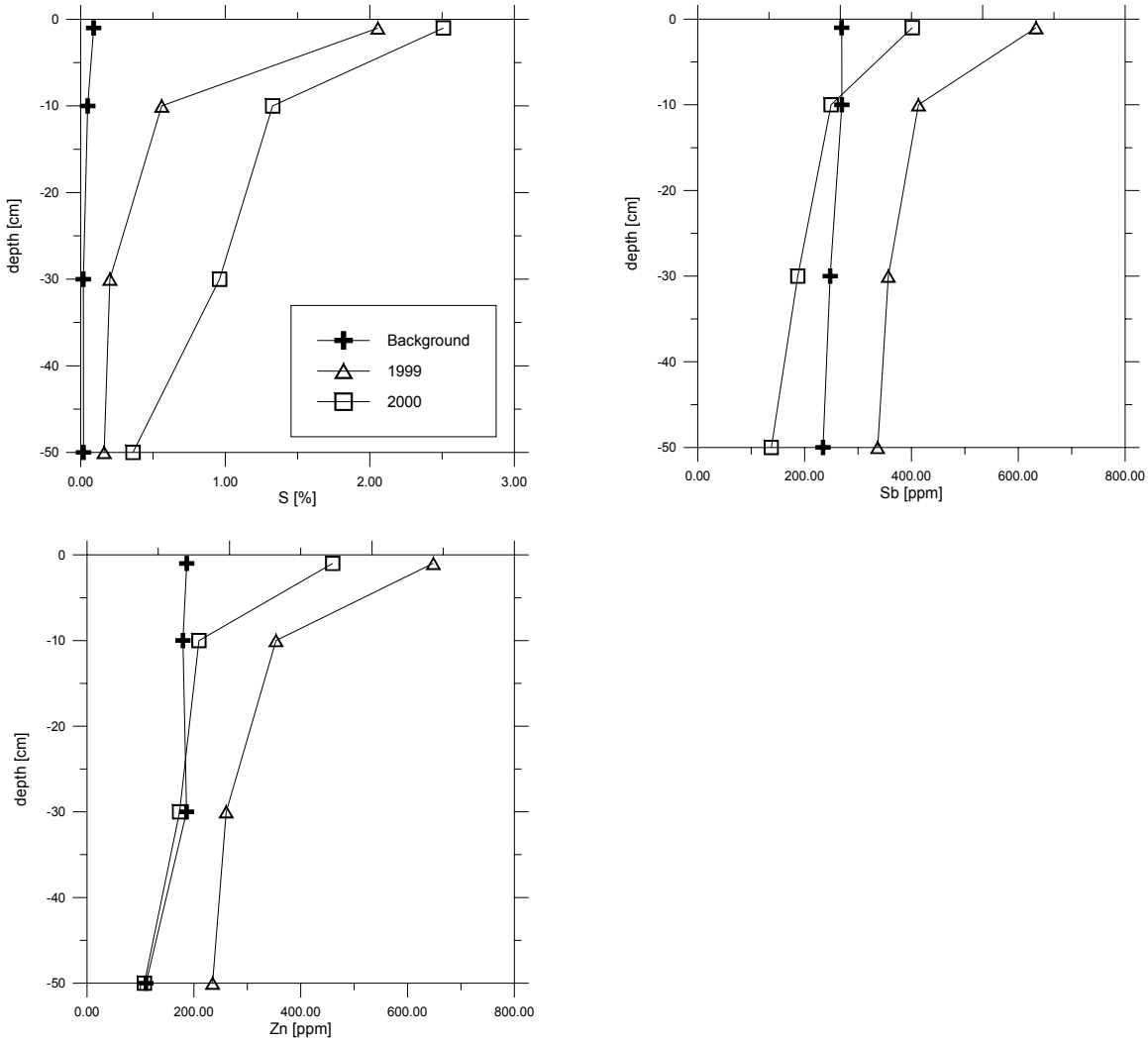

Figure E.2. Comparison of soil depth profiles 1999 (triangle) and 2000 (square) and background (cross) from Sobarbina. Part II

F. Sludge abundance 1999

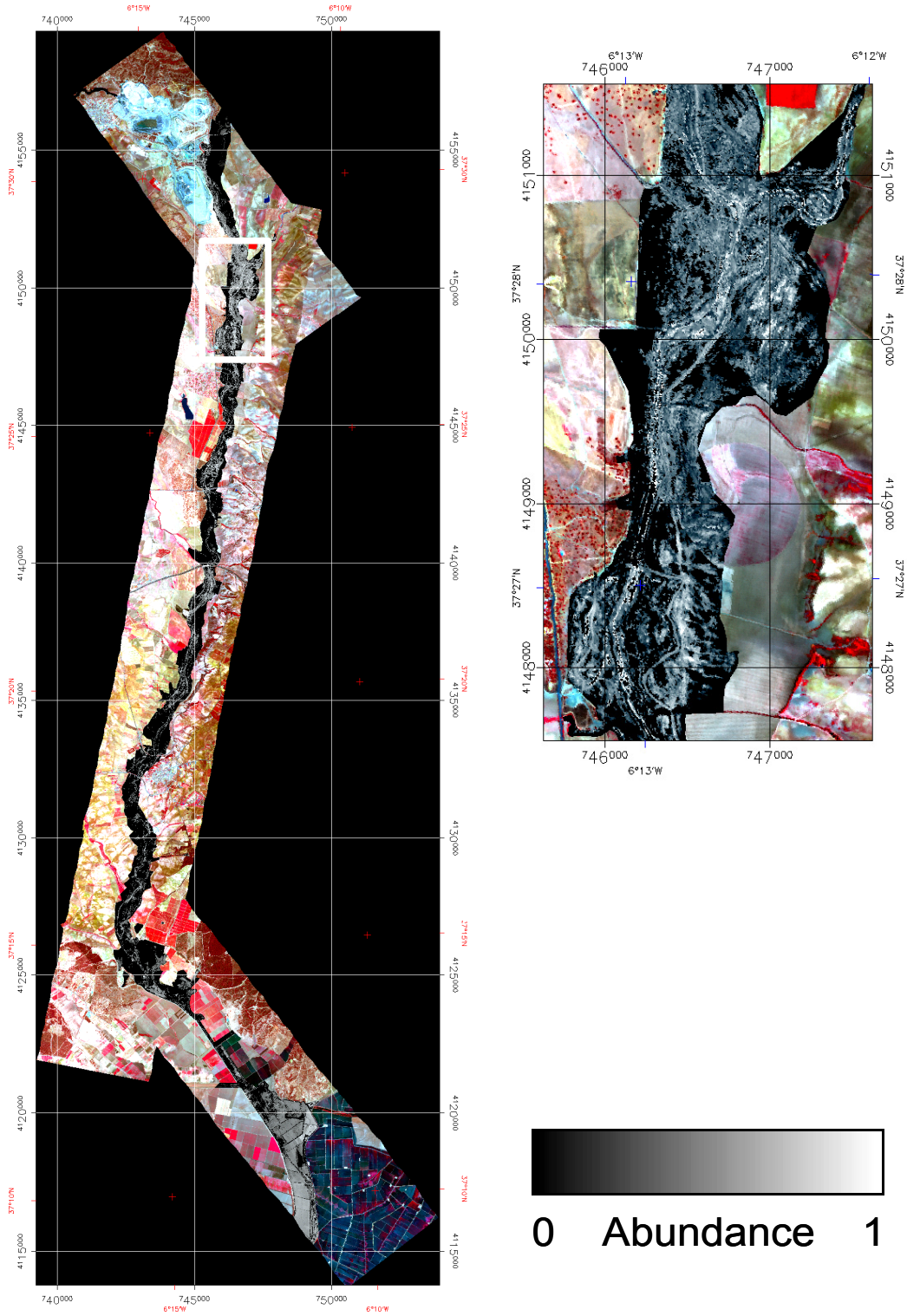

Figure F.1. Sludge abundance map 1999 for the entire flightstrip. The affected area (black) superimposed on the HyMap false colour image for better orientation. The white rectangle indicates the location of the enlargement.

G. Mineral abundance 2000

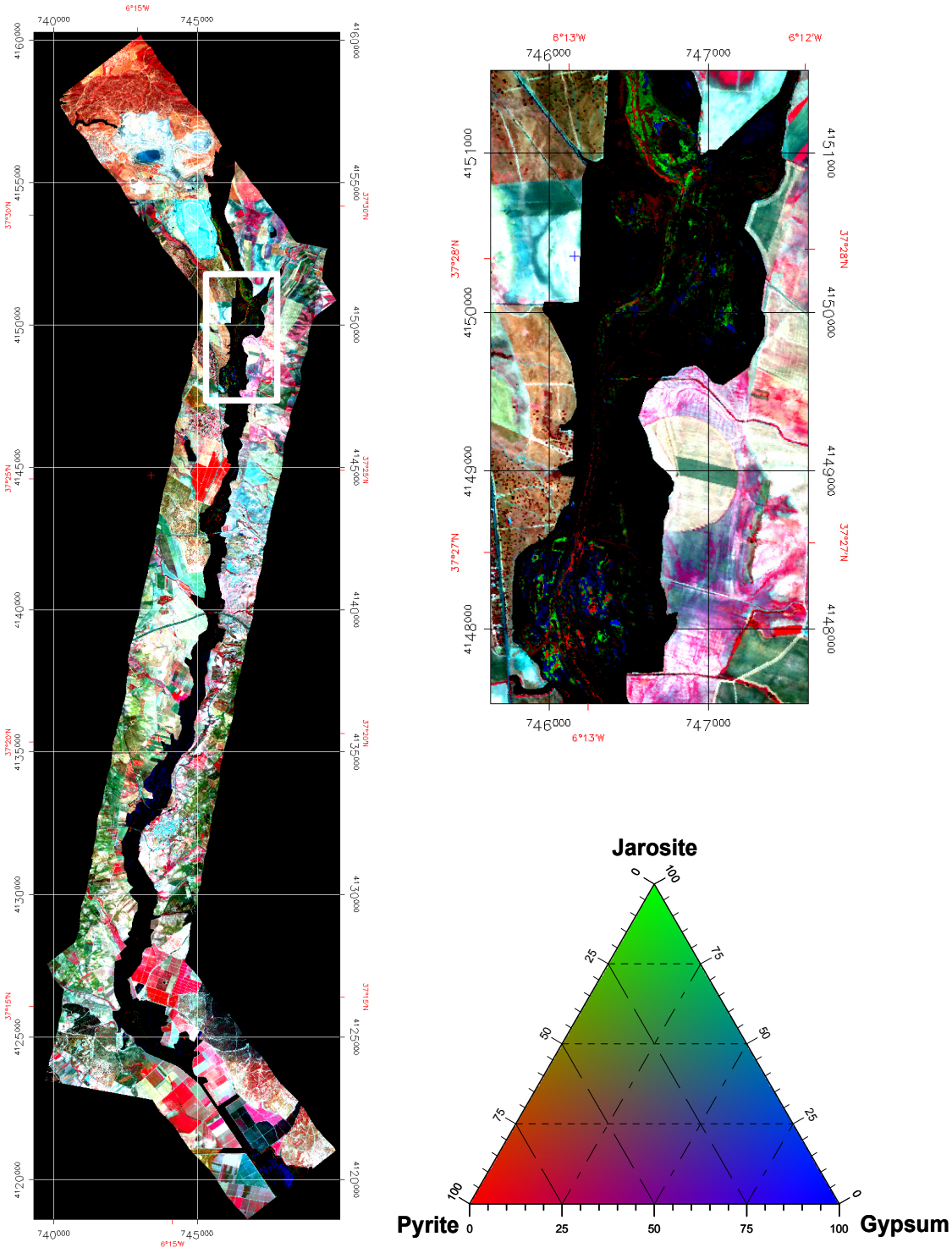

Figure G.1. Mineral abundance map 2000 for the entire flightstrip. The mixtures of the different EMs can be derived from the colour coded ternary diagram. Red is the pyrite EM, green is the jarosite EM, blue the gypsum EM. The white rectangle indicates the location of the enlargement.

H. Sludge derivatives 1999

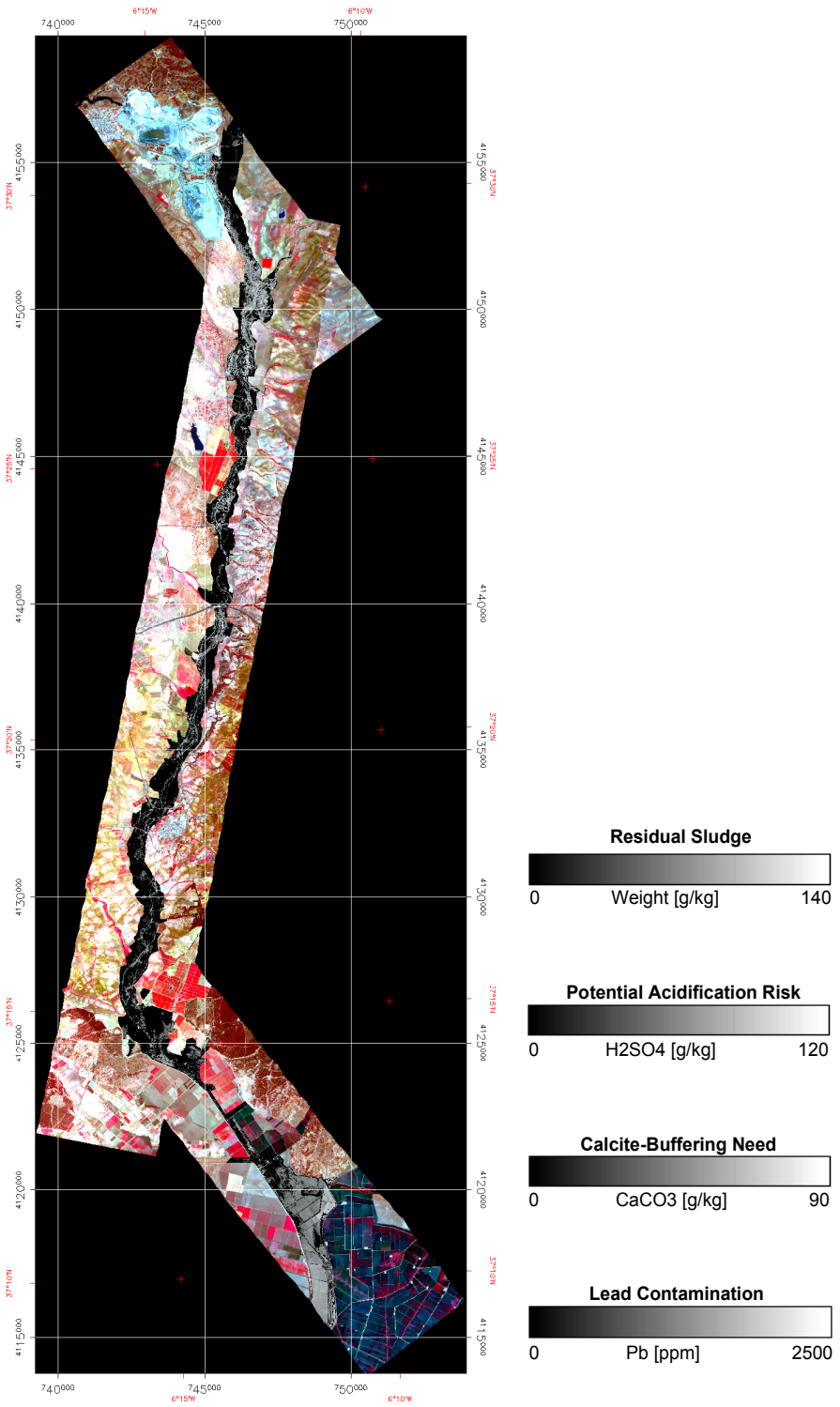

Figure H.1. Contamination parameters derived from the sludge abundance image for June 1999: residual sludge in g/kg, maximum potential acidification after full oxidation of pyrite in g/kg, neutralisation requirements for full oxidation of pyrite in g/kg

List of figures

Figure 1.1. Acid Mine Drainage at Rio Agrio, Spain 4

Figure 2.1. Flowchart of fundamental work steps and products of the thesis 8

Figure 3.1. Sketch of the study area..... 11

Figure 3.2. Major structural units and tectonostratigraphic domains in the South Portuguese Zone and location of the major volcanogenic massive sulphide deposits of the Iberian Pyrite Belt (from Leistel et al. 1998)..... 13

Figure 3.3. Geological Map of the Aznalcóllar mining district (from Almodóvar et al. 1998) 14

Figure 3.4. Overall sequence of mineral reactions for pyrite oxidation showing relationships between oxidising agents, catalysts and mineral products (from Nordstrom 1982)..... 17

Figure 3.5. Breach of the broken tailings pond dam (from Aguilar et al. 2000) 20

Figure 3.6. Aerial view of Rio Agrio floodplain after the accident. View to NW (from Aguilar et al. 2000) 20

Figure 3.7. Sludge layer at Vado de Quemas, approx. 30 km downstream (from Aguilar et al. 2000). Note the bright efflorescent crusts on top of the sludge, which are the first oxidation indicators. 22

Figure 3.8. Area affected by the toxic spill (from WWF 2002) 22

Figure 3.9. Climate diagram of Sanlucar la Mayor (Consejería de Medio Ambiente 1999) 23

Figure 3.10. Soil map of the study area (derived from 'Mapa de suelos de Andalucía 1:400 000) 27

Figure 4.1. Reflectance spectra of the iron oxide hematite (Fe_2O_3) and iron hydroxide goethite (FeOOH) (from Clark et al. 1993). The wing of an intense charge transfer band in the UV is partly visible at wavelengths < 0.5 µm. The Fe^{3+}-absorption at about 1 µm is caused by variable energy splitting within the crystal structure. 35

Figure 4.2. Reflectance spectra of sulphur (S) and Cinnabar (HgS) with a conduction band in the visible. The arrows indicate the level of the conduction and the valence band for cinnabar (from Clark et al. 1993). 35

Figure 4.3. Fundamental vibrational modes of the water molecule (from Elachi 1987).36

Figure 4.4. Reflectance spectra of calcite, gysum and jarosite, showing vibrational bands due to H_2O, OH, CO_3 (overtones) and FeOH (combination bands) (from Clark et al. 1993) 37

Figure 4.5. Wave interaction at an interface between two materials (from Elachi 1987) 38

Figure 4.6. Spectra of iron oxide, iron hydroxide, iron sulphate and sulphide minerals related to pyrite oxidation (from Clark et al. 1993) 40

Figure 4.7. Reflectance spectra of mineral soils representing different soil characteristics: organic dominated (A), minimally altered (B), iron affected (C), organic affected (D) and iron dominated (E) (from Stoner & Baumgardner 1981)41

Figure 4.8. Typical spectra of photosynthetic active vegetation (×) and non-photosynthetic dry vegetation (◊).....42

Figure 4.9. HyMap image data cube. Spatial data (x and y axes) represented as a three-band colour composite (R= band 25, G= band 17, B= band 9). The spectral data is represented by the z-axis in pseudocolour (rainbow) showing the first 64 out of 128 bands. Spectra on the right show extracted spectra from the data cube.....43

Figure 4.10. Solar radiation at top of atmosphere and on earth surface after selective absorption and scattering (from Elachi 1987) 45

Figure 4.11. Transmission windows of the atmosphere (from Elachi 1987) 45

Figure 4.12. Interactions of incoming solar radiation with the atmosphere and contamination of radiance measured at the sensor (from Tanré et al. 1995) 46

Figure 4.13. Spectral mixing is a consequence of integration of reflected radiation from a spatially mixed IFOV. 48

Figure 5.1. Data sets provided by Consejería de Mediombiente of the Junta de Andalucía. Base layer: raster maps 1:50.000; 2nd layer: digital terrain model with soil sampling points; 3rd layer: mayor roads and villages; 4th layer: distribution of sludge before remediation and borders of the green corridor. 50

Figure 5.2. Soil sample map example from Sobarbina site (left). Soil sampling depth profile (right) 51

Figure 5.3. Soil sampling sites with sludge affected area (average sludge depth deposited after the accident from Consejería de Medio Ambiente 1999).....52

Figure 5.4. Georectified HyMap false colour composite (R = band41 (1.011 µm), G = band17 (0.671 µm), B = band9 (0.549 µm)) showing the full flightline 55

Figure 5.5. Comparison of averaged calibration measurements and averaged image spectra for two sites in 1999.....57

Figure 5.6. Average depth profiles from Sobarbina site for contaminated soils (solid) and uncontaminated soils (dashed). Arsenic (left), cadmium (right).....60

Figure 5.7. Differences in surface concentrations (in percent) between 1999 and 2000 for the sites, where sampling was possible in both years.....64

Figure 5.8. Comparison of soil depth profiles 1999 (triangle) and 2000 (square) and background (cross) from Sobarbina 65

Figure 6.1. Spectra of mixture series of soil sample AZ086 (10 nm) 69

Figure 6.2. Soil AZ086 with 30 weight-% sludge and convex hull fit (dashed) 70

Figure 6.3. Continuum removed spectra of mixture series 71

Figure 6.4. Relationship between absorption depth at 1043 nm and Pb content for 1999 samples. Outliers are marked as triangles (Δ) 72

Figure 6.5. Resampling results for soil sample AZ086. Full spectrum (left), spectral subset with band centres (right). From bottom to top increasing bandwidth (1,5,10,20,50 nm), HyMap spectra on top 74

Figure 6.6. Absorption spectra of examples from mixture series (10 nm). See Figure 6.1 for original reflectance spectra 75

Figure 6.7. Standardised reflectance spectra of examples from mixture series (10 nm). See Figure 6.1 for original reflectance spectra 76

Figure 6.8. Vector standardised reflectance spectra of examples from mixture series (10 nm). See Figure 6.1 for original reflectance spectra 77

Figure 6.9. First derivatives of reflectance spectra of examples from mixture series (10 nm, Savitzky-Golay Method). See Figure 6.1 for original reflectance spectra 80

Figure 6.10. Second derivatives of reflectance spectra of examples from mixture series (10 nm, Savitzky-Golay Method). See Figure 6.1 for original reflectance spectra. 80

Figure 6.11. Correlograms of soil constituents and reflectance spectra (10nm). Trace metal group 81

Figure 6.12. Correlograms of soil constituents and standardised reflectance spectra (10 nm). Trace metal group 83

Figure 6.13: Data arrangement for PLSR (from Wold et al. 2001). The variables are described in the text. 87

Figure 6.14. Artificial neuron. $x_1,...,x_p$ are incoming signals, $w_1,...w_p$ are the corresponding weight factors, F is the transfer function. 89

Figure 6.15. General structure of a MLF network 90

Figure 6.16. Coefficients of determination for the best results obtained with the three methods MLR, PLSR and ANN for the heavy metal group. 100

Figure 6.17. Cross Validation of vector normalised data (10 nm). High values signalise potential outliers 102

Figure 6.18. Scatterplots of predicted vs. measured concentrations. 1:1 line for perfect fit 104

Figure 6.19. Correlogram for vector normalised spectra (10 nm) and HM 106

Figure 6.20. Strongly oxidised surfaces at the Sobarbina site (July 2000) 111

Figure 6.21. Sampling point of a bright crust (AZ 426) 111

Figure 6.22. Comparison of field (left) and laboratory spectra (right) 112

Figure 6.23. Image spectra extracted from HyMap image 2000 at the Sobarbinas site. The spectra show approximately the same surfaces as the field spectra in Figure 6.22 113

Figure 6.24. Linear mixture of two soils and green vegetation for the assessment of vegetation influence on the modelling. AZ001 uncontaminated, AZ021 contaminated 114

Figure 6.25. Linear mixture of two soils and dry vegetation for the assessment of vegetation influence on the modelling. AZ001 uncontminated, AZ021 contaminated 115

Figure 6.26. Prediction results for Pb using PLSR and vector normalised spectra with increasing influence of dry vegetation (0, 5, 10, 20, 30 % from left to right). The first line shows the 1:1 relationship, the second line is the trend line of the predicted data. The plot with 0 % vegetation shows the results of the validation 116

Figure 7.1. General VMESMA scheme 121

Figure 7.2. Application scheme of VMESMA in the present study 122

Figure 7.3. Example of four different types of vegetation (taken from Medspec database (Preissler et al. 1998)): herbaceous (*Asphodelus albus,*△), shrub with some shade (*Euphorbia characias*, ✕), dense coniferous forest canopy (*Pinus brutia*, ✚) and dry shrub (Arbutus unedo, ◇). Reflectance (left) and standardised reflectance (right).....124

Figure 7.4. 2D-scatterplot of data representative of a scene with EMs, which define the mixture space.....125

Figure 7.5. Background EM: green vegetation (◇), dry vegetation (△), soil 1 (✕), soil 2 (✚). Absolute reflectance (left), standardised reflectance (right).....126

Figure 7.6. Example of Spectral Feature Fitting (SFF). Reference spectrum of gypsum (black) is fitted to the field measurement AZ425 (red) using least squares. The SFF score can be calculated from this fit. See Table 7.1 for results. 127

Figure 7.7. Comparison of field measurement and best fitting reference spectrum. The photos on the right show the crusts from which the field spectra were derived. ..129

Figure 7.8. RMS error after the first unmixing. Border of the green corridor for delineation of maximum sludge extension.....130

Figure 7.9. Comparison of original (✚) and modelled (◇)spectra and residuals (△). Pixel in sludge affected area (left) and pixel in non affected area (right)..... 131

Figure 7.10. Sludge abundance map 1999. The affected area (black) superimposed on the HyMap false colour image for better orientation. Sludge abundance within the affected area is scaled from zero (black) to one (white). 132

Figure 7.11. Mineral abundance map 2000. The mixtures of the different EMs can be derived from the colour coded ternary diagram. Red is the pyrite EM, green is the jarosite EM, blue the gypsum EM. 134

Figure 7.12. Field measurements on a typical gypsum patch (bright) in the area. In the foreground some yellow-red patches of jarosite 135

Figure 8.1. Comparison of sludge abundance derived from SMA of the mixture series and sludge weight percentage. A second order polynomial is fitted to the data (R^2 = 0.973). 138

Figure 8.2. Contamination parameters derived from the sludge abundance image for June 1999: residual sludge in g/kg, maximum potential acidification after full oxidation of pyrite in g/kg, neutralisation requirements for full oxidation of pyrite in g/kg and lead contamination in ppm 141

Figure 8.3: Comparison of Pb concentrations for samples analysed in laboratory with concentrations derived from HyMap data. Outliers (△) were not included into the regression. 142

Figure 8.4. Comparison of As concentrations for samples analysed in laboratory with concentrations derived from the HyMap data. Outliers (△) were not included into the regression. Note that the scales of the axes are chosen differently for illustration purposes. 143

Figure 8.5. Comparison of classified As maps based on remote sensing (left) and based on interpolated point measurements (right). The size of the sampling points is related to the measured As concentration. 146

Figure 9.1. Proposed scheme for an integrated assessment and spatial monitoring of metal mining related contamination 153

Figure A.1. Sketch of Sampling Site ‘Mine North’ 174

Figure A.2. Sketch of Sampling Site ‘Mine South’ 175

Figure A.3. Sketch of Sampling Site ‘Sobarbina’ 176

Figure A.4. Sketch of Sampling Site ‘Las Doblas’ 177

Figure A.5. Sketch of Sampling Site ‘Puente Nuevo’ 178

Figure A.6. Vado de Quema 179

Figure E.1. Comparison of soil depth profiles 1999 (triangle) and 2000 (square) and background (cross) from Sobarbina. Part I. 202

Figure E.2. Comparison of soil depth profiles 1999 (triangle) and 2000 (square) and background (cross) from Sobarbina. Part II 203

Figure F.1. Sludge abundance map 1999 for the entire flightstrip. The affected area (black) superimposed on the HyMap false colour image for better orientation. The white rectangle indicates the location of the enlargement. 204

Figure G.1. Mineral abundance map 2000 for the entire flightstrip. The mixtures of the different EMs can be derived from the colour coded ternary diagram. Red is the pyrite EM, green is the jarosite EM, blue the gypsum EM. The white rectangle indicates the location of the enlargement. 205

Figure H.1. Contamination parameters derived from the sludge abundance image for June 1999: residual sludge in g/kg, maximum potential acidification after full oxidation of pyrite in g/kg, neutralisation requirements for full oxidation of pyrite in g/kg.....206

List of tables

Table 1.1. Potential environmental impacts of mining (Sol et al. 1999) 2

Table 3.1. Ranges of natural occurence and critical concentrations of different trace metals (*Bowen H.J.M. 1979, ** Kabata-Pendias & Pendias 1992) 18

Table 3.2. Boundary pH values for beginning mobility of trace metals (Blume & Brümmer 1991) 19

Table 3.3. Landcover types affected by the accident (Coopers & Lybrand 1998) 21

Table 3.4. Average chemical concentrations of the sludge released by the accident. Measurements taken immediately after the accident from different locations (CSIC 1998) 21

Table 5.1. HyMap spectral specifications for 1999 54

Table 5.2. Flight dates, time and altitude for 1999 and 2000 55

Table 5.3. Descriptive statistics (minimum, maximum,mean, standard deviation and coefficient of variance) for all samples from 1999. 59

Table 5.4. Average surface trace metal contaminations 1999 for all sites in ppm (Fe_2O_3 and S in percent). 61

Table 5.5. Correlation matrix of elements 1999. For more clarity only significant correlations (> 0.5, $\alpha = 0.05$) are displayed 62

Table 5.6. Descriptive statistics for all samples from 2000 63

Table 6.1. Resampling width (FWHM) and resulting number of bands 73

Table 6.2. Filter sizes used for calculating first and second order derivatives 79

Table 6.3. Prediction results for MLR (validation set)* 95

Table 6.4. Number of variables selected for optimal prediction (first line) and central wavelength positions [nm] of the selected variables in the order of their selection 96

Table 6.5. Prediction results of ANN (monitoring set)* 97

Table 6.6. Prediction results for PLSR (monitoring set)* 99

Table 6.7. PLSR Prediction results for vector-normalised data with 10 nm FWHM (monitoring set) 100

Table 6.8. Final prediction results after outlier detection for vector-normalised data, 10 nm (validation) using PLSR 103

Table 6.9. Final prediction results of elements related to soil matrix with vector-normalised spectra and 20 nm FWHM 107

Table 6.10. Final prediction results of elements related to organic soil matrix with standardised spectra and 10 nm FWHM 107

Table 6.11. Prediction results for samples 2000 using vector normalised spectra (10nm) from 1999 108

Table 6.12. Comparison of R^2's of prediction results using simulated Hymap full resolution (128 bands) and HyMap reduced band set (110 bands) with laboratory data from 1999 109

Table 6.13. Prediction results for field spectra with HyMap reduced band set resolution using vector normalised spectra of the year 2000 110

Table 6.14. Prediction Results for image spectra 116

Table 7.1. Results of the spectral feature fitting for full range spectra, VIS-NIR and NIR-SWIR 128

Table 8.1. Intervention limits for sensitive and less sensitive areas applied in the green corridor (from Consejería de Medio Ambiente 1998) 144

Table 8.2. Comparison of relative amounts of contamination levels for different data sets 145

Table A.1. Sampling points, coordinates [decimal degrees, WGS84], corresponding soil samples and sampling depth [cm] for 'Mine North' site (non-contaminated samples in blue) 174

Table A.2. Sampling points, coordinates [decimal degrees, WGS84], corresponding soil samples and sampling depth [cm] for 'Mine South' site 175

Table A.3. Sampling points, coordinates [decimal degrees, WGS84], corresponding soil samples and sampling depth [cm] for 'Sobarbina' site. (non-contaminated samples in blue) 176

Table A.4. Sampling points, coordinates [decimal degrees, WGS84], corresponding soil samples and sampling depth [cm] for 'Las Doblas' site 177

Table A.5. Sampling points, coordinates [decimal degrees, WGS84], corresponding soil samples and sampling depth [cm] for 'Puente Nuevo' site. (non-contaminated samples in blue) 178

Table A.6. Sampling points, coordinates [decimal degrees, WGS84], corresponding soil samples and sampling depth [cm] for 'Vado de Quema' site. (non-contaminated in blue, sludge sample in red) 179

Table A.7. Sampling points, coordinates [decimal degrees, WGS84], corresponding soil samples and sampling depth [cm] for sampling campaign 2000. (non-contaminated in blue, sludge sample in red) 180

Table B.1. HyMap band positions 1999 (WL = centre wavelength [nm]; FWHM = Full width at half maximum [nm]) 182

TableB.2. HyMap band positions 2000 (WL = centre wavelength [nm]; FWHM = Full width at half maximum [nm]) 183

Table C.1. Geochemical laboratory analysis for 1999. Part I 184

Table C.2. Geochemical laboratory analysis for 1999. Part II 189

Table D.1. Geochemical laboratory analysis for 2000. Part I 195

Table D.2. Geochemical laboratory analysis for 2000. Part II 198

List of Acronyms

AMD	Acid mine drainage
ANN	Artificial neural network
EM	Endmember
EMR	Electromagnetic radiation
FWHM	Full width half maximum
HM	Heavy metal
MIR	Middle infrared part of the spectrum
MLR	Multiple linear regression
NIR	Near infrared part of the spectrum
PLSR	Partial least squares regression
PRESS	Prediction error sum of squares
RER	Relative error ratio
RMSE	Root mean squared error
RPD	Relative percent difference
SEP	Standard error of prediction
SFF	Spectral feature fitting
SMA	Spectral mixture analysis
SWIR	Short wave infrared part of the spectrum
VIS	Visible part of the spectrum
VMESMA	Variable multiple endmember spectral mixture analysis
VMS	Volcanogenic massive sulphide deposits

Lebenslauf

Vorname, Name: **Thomas Kemper**

Wohnort: **Via Roma 1, 21010 Porto Valtravaglia (Va), Italien**

Geboren am 20.10.1969 in Wickede/Ruhr

Schulbildung

08/1976 – 06/1980	**Albert-Schweitzer Grundschule, Menden**
08/1980 – 05/1989	**Walburgisgymnasium, Menden**

Studium der Angewandten Physischen Geographie (Diplom-Geograph)

von 04/1991 bis 05/1997 an der Universität Trier

Thema der Abschlussarbeit:

Das Potential des Abbildenden Spektrometers MIVIS für die Bestimmung von Bodenparametern - Ein Beispiel aus dem Südlichen Apennin, Italien

Promotionsstudium von 10/1999 bis 03/2003 an der Universität Trier

Berufstätigkeit

07/1998 – 12/2002	**Gemeinschaftliche Forschungsstelle der Europäischen Kommission, Ispra (Italien), Institute for Environment and Sustainability, Soil & Waste Unit;**
	zunächst Promotionstipendium, seit 07/2001 Mitarbeiter im Forschungsprojekt GEORANGE